Effect of Actuation Properties of Multi-Rotor Aerial Vehicles on Their Abilities: Emphasis on Hoverability, Failure Robustness and Trajectory Tracking

Mahmoud Hamandi

To cite this version:

Mahmoud Hamandi. Effect of Actuation Properties of Multi-Rotor Aerial Vehicles on Their Abilities: Emphasis on Hoverability, Failure Robustness and Trajectory Tracking. Robotics [cs.RO]. INSA Toulouse, 2021. English. NNT : . tel-03640626v1

HAL Id: tel-03640626
https://laas.hal.science/tel-03640626v1

Submitted on 25 Oct 2021 (v1), last revised 13 Apr 2022 (v2)

THÈSE

En vue de l'obtention du

DOCTORAT DE L'UNIVERSITÉ DE TOULOUSE

Délivré par :
l'Institut National des Sciences Appliquées de Toulouse (INSA de Toulouse)

Présentée et soutenue le *22/09/2021* **par :**

Mahmoud HAMANDI

Effect of Actuation Properties of Multi-Rotor Aerial Vehicles on Their Abilities: Emphasis on Hoverability, Failure Robustness and Trajectory Tracking

---

JURY

Isabelle FANTONI	Directrice de Recherche CNRS, École Centrale de Nantes, Nantes	Rapporteur
Paolo ROBUFFO GIORDANO	Directeur de Recherche CNRS, IRISA, INRIA, Rennes	Rapporteur
Simon LACROIX	Directeur de Recherche CNRS, LAAS-CNRS, Toulouse	President du Jury
Antonio FRANCHI	Chercheur CNRS, LAAS-CNRS, Toulouse; and Professor, University of Twente, The Netherlands	Directeur de thèse

---

École doctorale et spécialité :
EDSYS : Robotique 4200046
Unité de Recherche :
Laboratoire d'Analyse et d'Architecture des Systèmes (LAAS–CNRS)
Directeur de Thèse :
Antonio FRANCHI
Rapporteurs :
Isabelle FANTONI et *Paolo ROBUFFO GIORDANO*

Abstract

This thesis focuses on the study of the actuation properties of Aerial Vehicles (AV)s, and their ensuing feasible wrench sets and useful abilities. The field of robotics has seen a large expansion over the last decade, with particular emphasis on AVs. These vehicles, that were once used for military purposes, are now more and more employed for civilian tasks such as hobby racing, photography, firefighting, inspection and surveillance, search and rescue, and more recently physical manipulation. With the expansion of the assigned tasks, new designs started emerging, attempting to expand the abilities and wrench capabilities of these vehicles beyond what was initially possible with winged vehicles. As such, new vehicles started emerging beyond the classical quadrotor design, where each group employs a range of techniques to expand the platform's abilities, such as actively tilting propellers while in flight to change the platform's thrust direction, tilting platform's propellers to achieve full actuation, or even optimizing the propeller's placement and orientation to achieve omnidirectional flight. With the vast literature encompassing different designs, it was inevitable that each group of designs follows a specialized nomenclature and design framework. While this approach helped the advancement of these designs, it renders the comparison of the capabilities of different designs a challenging task. Moreover, while each design is demonstrated capable of the tasks it was built for, it would be interesting to define a set of basic abilities that could provide a clear idea of a platform's possible applications.

Unlike fixed wing platforms, AVs are used for their ability to hover in place, i.e., stabilize their position about a desired one over a period of time. From this configuration a platform should have the ability to then move around by following a desired trajectory. While these two abilities have been thoroughly discussed in the literature in an implicit and explicit way, we believe that the conditions for a platform to hover have been discussed either theoretically, or derived for specific platforms. However, a general numerical framework that allows the analysis of this ability was never introduced. Similarly for a platform's ability to fly in an omnidirectional way: while the desired behavior of an omnidirectional platform is intuitively understood, and the conditions to achieve this ability have been discussed in the literature, these conditions usually ignore the platform's actuation limits, and require a case by case analysis of the platform's ability.

From another perspective, AVs are usually equipped with an array of sensors that allow these vehicles to sense their environment and estimate their state. These sensors are the source of the *intelligence* associated with these platforms, and which allows them to navigate autonomously. One of these sensors, that has become crucial for the modern AV, is the Inertial Measurement Unit (IMU). The IMU provides acceleration, angular velocity and possibly magnetometer measurements. These measurements are crucial for the state estimation of the platform when flying indoor or outdoor. In addition to state estimation, new control schemes emerged in the last few years that attempt to benefit from the high frequency of these measurements to fly a quadrotor robustly. While these controllers have allowed quadrotors to achieve interesting performances, they still rely on high frequency measurements of the propeller speeds, and filter the IMU measurements with less than optimal filters.

As such, and following the above introduction,this thesis attempts to provide a plethora of contributions both in the design and control perspective of multi-rotor aerial vehicles as follows:

i) Modeling: provide a unified definition that could describe any multi-rotor aerial vehicle, in addition to a formal definition of the basic abilities that could describe the capabilities of these platforms. Review the majority of multi-rotor aerial vehicle designs from the literature, while comparing the actuation capabilities and abilities of each.

ii) Numerical methods: introduce a numerical method to analyze the hoverability of any platform, in addition to a numerical method to analyze the omnidirectional ability of a platform.

iii) Design: a novel omnidirectional prototype with minimal uni-directional propellers, and a Y-shaped hexarotor.

iv) Trajectory tracking: experimental analysis of the trajectory tracking ability of platforms with different actuation capabilities.

v) IMU: introduction of a novel filter for IMU measurements, and the use of these filtered measurements in a direct acceleration feedback controller.

Each of these contributions is coupled with additional minor contributions, left for the curious reader to find. Finally, each of the theoretical contributions presented in this thesis is coupled with an extensive experimental campaign that demonstrates the stated hypotheses.

Keywords

– Aerial Robotics Control – Aerial Robotics Design – Multidirectional-thrust aerial robots – Robotics – Automatic control

Résumé

Le sujet principal de cette thèse est l'étude des propriétés d'actionnement des Véhicules Aériens (VA), et leurs force/moment réalisables et leurs capacités utiles qui en découlent. Le domaine de la robotique a connu une grande expansion au cours de la dernière décennie, avec un accent particulier sur les VA. Ces véhicules, qui étaient autrefois utilisés à des fins militaires, sont maintenant de plus en plus utilisés pour des tâches civiles telles que les courses de loisir, la photographie, la lutte contre les incendies, l'inspection et la surveillance, la recherche et le sauvetage et, plus récemment, la manipulation physique. Avec l'expansion des tâches assignées, de nouvelles conceptions ont commencé à émerger, tentant d'étendre les capacités de ces véhicules au-delà de ce qui était initialement possible avec des véhicules ailés. En tant que tels, de nouveaux véhicules ont commencé à émerger au-delà de la conception classique du quadrotor, où chaque groupe utilise une gamme de techniques pour étendre les capacités de la plate-forme, telles que l'inclinaison active des hélices en vol pour changer la direction de poussée de la plate-forme, l'inclinaison des hélices de la plate-forme pour obtenir un actionnement complet, ou encore optimiser le placement et l'orientation de l'hélice pour obtenir un vol omnidirectionnel. Avec la vaste littérature englobant différentes conceptions, il était inévitable que chaque groupe de conceptions suive une nomenclature et un cadre de conception spécialisés. Bien que cette approche ait contribué à l'avancement de ces conceptions, elle rend la comparaison des capacités de différentes conceptions une tâche difficile. De plus, alors que chaque conception est démontrée capable des tâches pour lesquelles elle a été conçue, il serait intéressant de définir un ensemble de capacités de base qui pourraient fournir une idée claire des applications possibles d'une plate-forme.

Contrairement aux plates-formes à voilure fixe, les VA sont utilisés pour leur capacité à flotter sur place, c'est-à-dire à stabiliser leur position autour d'une position souhaitée sur une période de temps. A partir de cette configuration, une plate-forme doit avoir la possibilité de se déplacer ensuite en suivant une trajectoire souhaitée. Bien que ces deux capacités aient été discutées en profondeur dans la littérature de manière implicite et explicite, nous pensons que les conditions pour qu'une plate-forme flotte ont été discutées soit théoriquement, soit dérivées pour des plates-formes spécifiques. Cependant, un cadre numérique général permettant l'analyse de cette capacité n'a jamais été introduit. De même pour la capacité d'une plate-forme à voler de manière omnidirectionnelle : alors que le comportement souhaité d'une plate-forme omnidirectionnelle est intuitivement compris et que les conditions pour atteindre cette capacité ont été discutées dans la littérature, ces conditions ignorent généralement les limites d'actionnement de la plate-forme et nécessitent une analyse au cas par cas de la capacité de la plateforme.

D'un autre point de vue, les VA sont généralement équipés d'un ensemble de capteurs qui permettent à ces véhicules de détecter leur environnement et d'estimer leur état. Ces capteurs sont à l'origine de l'*intelligence* associée à ces plateformes, et qui leur permet de naviguer de manière autonome. L'un de ces capteurs, devenu crucial pour les VA moderne, est l'Unité de Mesure Inertielle (UMI). Le UMI fournit des mesures d'accélération, de vitesse angulaire et éventuellement de magnétomètre. Ces mesures sont cruciales pour l'estimation de l'état de la plate-forme en vol intérieur ou extérieur. En plus de l'estimation d'état, de nouveaux techniques de contrôle ont émergé au cours des dernières années qui tentent de beneficier de la fréquence élevée de ces mesures pour piloter un quadrotor de manière robuste. Bien que ces contrôleurs aient permis aux quadrotors d'atteindre des performances intéressantes, ils reposent toujours sur des mesures à haute fréquence des vitesses des hélices et filtrent les mesures d'UMI avec des filtres moins qu'optimaux.

En tant que tel, et suite à l'introduction ci-dessus, cette thèse tente de fournir une pléthore de contributions à la fois dans la perspective de conception et de contrôle des véhicules aériens multi-rotors comme suit :

i) Modélisation : fournir une définition unifiée qui pourrait décrire tout véhicule aérien multi-rotors, en plus d'une définition formelle des capacités de base qui pourraient décrire les capacités de ces plates-formes. Passez en revue la majorité des conceptions de véhicules aériens multi-rotors de la littérature, tout en comparant les capacités d'actionnement et les capacités de chacun.

ii) Méthodes numériques : introduire une méthode numérique pour analyser la capacité de flottage de n'importe quelle plate-forme, en plus d'une méthode numérique pour analyser la capacité omnidirectionnelle d'une plate-forme.

iii) Design : un nouveau prototype omnidirectionnel avec le nombre minimale d'hélices unidirectionnelles et un hexarotor en forme de Y.

iv) Trajectory tracking : analyse expérimentale de la capacité de suivi de trajectoire de plates-formes avec différentes capacités d'actionnement.

v) UMI : introduction d'un nouveau filtre pour les mesures UMI, et utilisation de ces mesures filtrées dans un contrôleur de retour d'accélération direct.

Chacune de ces contributions est couplée à des contributions mineures supplémentaires, laissées au lecteur curieux à trouver. Enfin, chacune des contributions théoriques présentées dans cette thèse est couplée à une vaste campagne expérimentale qui démontre les hypothèses énoncées.

Mots Clés

– Contrôle des robots aérienne – Design des robots aérienne – Robots aériens à poussée multidirectionnelle – Robotique – Contrôle automatique

Acknowledgements

I would like to take advantage of this paragraph to provide gratitude to everyone who has helped me the last few years during my PhD studies. Definitely without everyone I have worked with, and everyone I have encountered, this thesis would have been much harder to accomplish, if not impossible. I am sure that as hard as I try, it is impossible to mention everyone who has actively helped me throughout this journey, however, I will try my best.

Firstly, I am grateful for my advisor Dr. Antonio Franchi. Antonio walked me through my PhD by providing exhaustive academic advise, and spending an extensive amount of time working with me on solving the challenging problems we faced in this thesis. In addition, Antonio was always present to advise me on life issues, and finally, was always there as a friend before being an advisor. In this scope, I would also like to thank Dr. Marco Tognon, who's advise and academic help constituted a seminal part of this thesis, and without which I believe it would have been difficult to produce this manuscript in the way it is now presented.

I would also like to thank the members of the jury for the time and effort they have spent reviewing this thesis, and for their constructive comments. Thank you Dr. Isabelle FANTONI, Dr. Paolo ROBUFFO GIORDANO and Dr. Simon LACROIX.

I would also like to thank the RIS team for all their support during my thesis, boosting me to accomplish the best I could, helping me finance some of the research in this thesis and attending conferences, and most importantly, I need to thank every member of the RIS team for the smiles each one of them greeted me with every time I bumped into any one of them. I would like to thank especially Simon LACROIX for all his academic and personal support during my journey at LAAS. In addition, I would like to thank Anthony MALLET for his continuous support debugging and 'fixing' all the hardware and software I used for the conception of this thesis.

In addition, I would like to dedicate a special thanks for the Aerial Robotics group in RIS and UTwente. You have constituted my family away from home. I would like to thank you for all the long talks, the coffee breaks, the academic debates, the continuous help and collaborations, etc... From this group, I would like to thank each and every member, those that are today at LAAS, those that were in LAAS and already left to new endeavors, and those that are today at UTwente.

I would also like to thank my friends across the globe; those whom I have spent time with at AUB, and whom I still share random conversations with; and those whom I have spent time with at CSU, and whom I couldn't have reached my PhD position without.

Finally I would like to thank my entire family. My parents and brothers who have supported me both emotionally and financially to accomplish my goals in life since the day one. I would also like to thank my parents and brother and sister in law, who have continuously encouraged to keep going. And mostly I would like to thank my wife who have dedicated all the time she could to help me stay focused on my research, and keep me motivated throughout. Finally, I would like to thank my son, whom at the time of this defense would be just 9 months old; despite your age, you have provided me with motivation to finalize this thesis more than you could have imagined.

LAAS–CNRS

Mahmoud

Contents

List of Figures

List of Tables

List of Multimedia

[video01–2020a] **video01**. *Direct acceleration feedback control of quadrotor aerial vehicle*. `https://youtu.be/UKtHYjHEuyM`. 2020 (cited on page 164).

[video01–2020b] **video01**. *Omni-Plus-Seven O7+: Omnidirectional Aerial Vehicle with Minimal Number of Uni-directional Thrusters*. `https://youtu.be/Rv58JE6R2nE`. 2020 (cited on page 104).

[video01–2021a] **video01**. *A Novel Robust Hexarotor Capable of Static Hovering in Presence of Propeller Failure*. `https://youtu.be/GWrOIMyP-UA`. 2021 (cited on page 82).

[video01–2021b] **video01**. *Optimal Tuning of the Lateral-Dynamics Parameters for Aerial Vehicles with Bounded Lateral Force*. `https://youtu.be/yFSonGtvTsM`. 2021 (cited on page 125).

List of Acronyms

AAU	Atomic Actuation Unit
APhI	Aerial Physical Interaction
BLDC	Brushless DC
BLF	Bounded Lateral Force
CoM	Center of Mass
DoF	Degrees of Freedom
ESC	Electronic Speed Controller
FTCS	Fault Tolerant Control System
GC	Geometric Center
GNSS	Global Navigation Satellite System
GPS	Global Positioning System
IMU	Inertial Measurement Unit
INDI	*Incremental Nonlinear Dynamic Inversion*
MAV	Micro Aerial Vehicle
MPC	Model Predictive Control
MRAV	Multi-Rotor Aerial Vehicle
PWM	Pulse Width Modulation
UAV	Unmanned Aerial Vehicle
UKF	Unscented Kalman Filter

Part I

Preliminaries

Chapter 1
Introduction

1.1 Motivation

One of the research fields that are rapidly growing nowadays is the robotics field; with the fourth industrial revolution continuously taking shape ([Techradar–2021]), and changing humanity's perception of robotic systems, the field at large have seen an increased interest from the research community, industry, and general public as a whole. In this context, we define a robotic system as a physical machine that could do autonomous or remotely controlled work, and which contains a certain level of intelligence through the use of software. With this definition, we could encompass a large number of machines that we know of today, such as fixed manipulators (or arm manipulators), Unmanned Ground Vehicles (UGV)s and Unmanned Aerial Vehicles (UAV)s. While each of these three systems seem to be completely different from an application point of view, the three systems (in addition to other robotic systems) actually advance in concurrence. This fact is due to the shared technological concepts in the three from a physical modeling perspective, and from an *intelligence* perspective. It is easy to see that manipulators with a fixed base have the most limited work space in the above three categories. With a fixed base, the manipulator could interact with the environment that is in its surrounding; despite this limitation, these machines have been (and still being) used extensively in industry for tasks such as welding, assembly, and others ([Grau–2017]). The limited work space of fixed base manipulators are overcome in the case of UGVs. Due to their ability to traverse land, their work space becomes practically infinite. As such, research in this field has seen rapid expansion in multiple areas, such as military applications ([Czapla–2013]) and autonomous cars ([Politis–2017]). In addition, UGVs provide the option to place the aforementioned manipulators on a moving platform, and as such expanding their work space. While UGV research have gained increasing popularity in recent years, especially due to the commercialization of autonomous vehicles [Reid–2021], their work space is still theoretically limited as compared to UAVs. UAVs expand the limitations in the work space of UGVs, with a work space that is theoretically infinite, i.e., expanding both land and space.

1.1.1 UAV History

The first occurrence of a UAV that we could find in history, was introduced on July 12^{th} 1849 for a military use, where Austria built autonomous balloons to bombard Venice. The balloons, shown in Fig. 1.1a, were supposed to deliver an explosive charge by electromagnetic means, however, they eventually failed due to unpredicted wind. While many other attempts have been made to construct autonomously flying vehicles since the Austrian balloons, the following design is

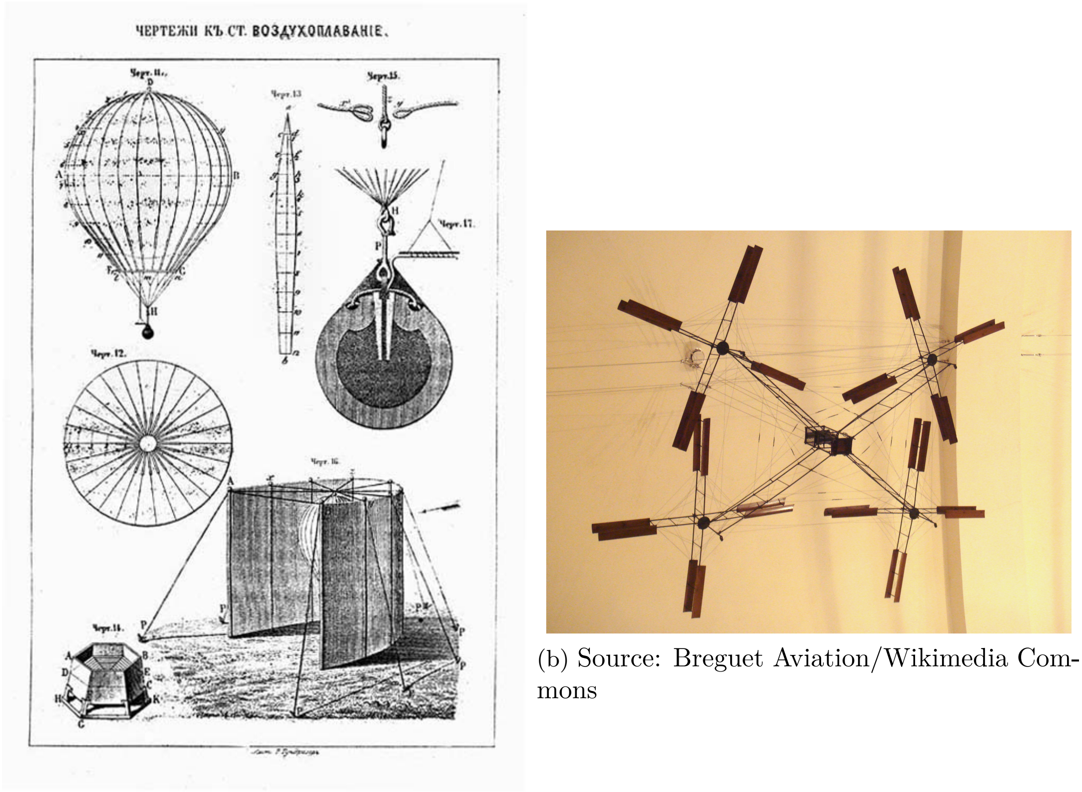

(a) Source: weaponsandwarfare.com

(b) Source: Breguet Aviation/Wikimedia Commons

Figure 1.1 – Showing some of the history of UAVs: left shows the first balloon drone introduced in 1849, and right shows the first quadrotor platform introduced in 1907.

of particular interest for the modern UAV design. The first quadrotor, shown in Fig. 1.1b, was constructed in 1907. Although the design was not yet autonomous, the concept of four fixed propellers carrying the weight of a vehicle was already there. Multiple attempts to automate flying vehicles and present new designs happened afterwards during the first and second world war, mostly for military applications. However, the next big step towards today's UAV technology did not happened until the 1950s, where during the Vietnam war a drone was mounted with a surveillance camera for reconnaissance.

In the 1980s drone technology took another leap forward with the introduction of Global Positioning System (GPS) and Global Navigation Satellite System (GNSS) systems on-board these vehicles, and thus endowing aerial vehicles with another key sensor essential for autonomous navigation. At the same time, during this period drone manufacturing took a leap in the introduction of new techniques and material to render these vehicles more affordable. Following these technological advancements, the military use of UAVs boosted largely in the 1990s and the 2000s, entailing further advancements in the algorithms used for the autonomy of the vehicles, the material used to build drones, and finally, the electronics used on-board to achieve the platforms' intelligence.

In the 2000s, the price-performance ratio of the sensors and processors on-board

(a) Source: dronenodes.com (b) Source: commercialdroneprofessional.com

Figure 1.2 – Two drone applications: left shows a firefighting drone, and right shows a drone inspecting a pipe.

Multi-Rotor Aerial Vehicle (MRAV)s decreased, with a corresponding drop in their size ([Loianno–2015]), entailing a decrease in the size of the manufactured platforms, and allowing an easier public access to the corresponding platforms. As such, and while until 2010 the majority of UAVs were built for military use, after 2010 the field at large saw a boom in the presented designs and the corresponding applications. Such applications vary from search and rescue, surveying, firefighting ([Shakhatreh–2019]), human-robot interaction ([Tognon–2021]) and aerial physical interaction ([Ollero–2018]); some of these applications are shown in Fig. 1.2.

In what follows we will focus only on "micro" aerial vehicles that are designed for commercial use; while the scale of such vehicles is not formally defined, however, we aim at this scale as one with dimensions and weight near the ones of toy robots, or aerial robots used in professional film making. We refer to these platforms as Micro Aerial Vehicle (MAV) or MRAV, given their size, and to emphasize that our focus is on platforms where the main lift is achieved via rotating propellers, each generating a thrust along its axis, and with the orientation of each being either fixed or variable.

1.1.2 MAV Design Evolution

We can see from the above that the first MRAV design was a quadrotor, i.e., a coplanar collinear platform (i.e., all propellers are placed in the same plane (coplanar), and their angular velocities are collinear, i.e., they produce thrusts all oriented in the same direction) with four equally spaced propellers about the Center of Mass (CoM) of the platform. While many other designs have emerged between the modern commercial MAV and the aforementioned design, the use of quadrotors still significantly outweighed the use other designs. This is due to the simplicity of the design from different perspectives: first the design is simple to manufacture due to the symmetry of the platform, and the coplanar collinear assumption. Second, the fact that the propellers' thrust, the on-board Inertial Measurement Unit (IMU), and in most cases the body gravity vector are aligned entails an inherent stability of the platform. Finally, this design is energetically efficient since the majority of the lift is allocated towards opposing the gravity component during hovering. The quadrotor design was soon followed by different coplanar/collinear platforms such as hexarotors and octorotors; while these designs can still only apply forces along the platform's vertical axis, they increase the payload of the platform, thus allowing for heavier attachments to be placed on-board the platform, and allow for the use of the platform for means of payload transport.

While the simplicity of coplanar/collinear platforms allowed it to gain popularity, with many applications relying on the characteristics of coplanar/collinear platforms, its limited force set hinders its use in applications that require a larger force set, or a decoupling between the platform position and orientation. One application that gained popularity in the last decade that could benefit from an improved design is Aerial Physical Interaction (APhI). In this scope, we do note that any MAV is in fact interacting with the environment, may it be in a passive or active way; however, we refer to APhI as the platform's ability to interact with the environment while being physically connected to the object it is interacting with. Such ability includes for example object pick up and drop off, object push and pull, and more generally, interacting with the environment via any physical tool that connects the platform to an external object, such as a manipulator or an inspection probe.

The introduction of the APhI domain introduced many new applications for MAVs; however, at the same time it required MRAV designs with an expanded force set and a decoupling between the platform orientation and position ([Tognon–2019]). As such, new designs started emerging, which attempted to achieve the desired force set and hovering ability. Some of the designs that we found to be very popular are ones were a quadrotor or hexarotor is used with tiled or tiltable propellers. Such designs allow the platform to apply lateral forces independent of the applied lift force and platform orientation, thus decoupling the applied force from the orientation dynamics and as such allow interaction with the environment in a more stable and effective way; these designs could be modeled as Bounded Lateral Force (BLF) platforms as demonstrated in ([Franchi–2018a]). It should be noted that such designs dissipate some of their energy to balance their force induced moments.

Finally, many attempts in the literature introduced platforms that could achieve a force/moment set that allows omnidirectional hovering. Such a design could apply forces in all directions, irrespective of its orientation, and as such, it could have direct APhI applications. Such designs rely either on a small number of tiltable propellers, a large number (8 or more) of 'optimally' fixed propellers, or a large number of actuated propellers.

We can see from the above history that robotic machines started with fixed based manipulators; then to overcome the limitations of a fixed base, these manipulators were fixed on moving ground vehicles; and more recently, these manipulators were attached to flying aerial vehicles to be able to interact with the environment in a theoretically infinite space.

The field of aerial vehicles has seen an extensive expansion in the last decade, with focus on 1) new platform designs that could achieve the desired force and moment sets required by the applications demanded from these vehicles; 2) new control strategies that allow fast maneuvers, and that better exploit the expanded force and moment sets; 3) analyzing the different abilities of the newly designed platforms; 4) in addition to a plethora of demonstrations combining some of the findings in the above listed fields, while advancing these fields to accommodate for the requirements of the presented applications.

1.1.3 The Use of On-board IMU

The majority of modern MAVs are endowed with an on-board Inertial Measurement Unit. Each IMU contains an accelerometer and a gyroscope, and optionally a magnetometer [Ahmad–2013]. The accelerometer provides acceleration measurements along the three principal directions of the platform, the gyroscope provides angular velocity measurements, and finally, the magnetometer is used to measure the direction of the earth's gravity. Most IMU microchips contain a calibration module that combines all these measurements to refine each for possible errors, and to detect any mismatch. IMUs on-board MAVs are most commonly used for state estimation, parameter estimation, or more recently control.

The on-board IMU is a key component for state estimation: the most common strategy for state estimation is to use a Kalman filter (throughout our experiments we use an Unscented Kalman Filter (UKF) (wan2000unscented)). The Kalman filter fuses multiple sensor measurements to estimate the platform position (and orientation) and the corresponding velocities and accelerations, while accounting for the uncertainties in each measurement. The most common sensors used to estimate the platform's pose are GPS measurements of the platform's position in an outdoor environment, height sensor for to detect the distance to the nearest surface, monocular cameras to estimate the platform's velocity and angular velocity, depth camera to estimate in addition the distance to nearby objects, and possibly its position in a map, motion capture system (for indoor use) to detect platform's pose, and finally measurements from the on-board IMU. Each of the above listed sensors provides measurements with different uncertainties and different rates, with the IMU rates being the largest, reaching a rate of 1[kHz] with the sensors used in our lab. A survey on such sensors and fusion techniques can be found in [Lu–2018].

From another perspective, on-board IMUs are important for platform control. From one side, the angular velocity measurements provided by the IMU is important for the stabilization of the platform. More rencently [Ryll–2019] integrated these measurements and the corresponding estimated platform state to compute an estimate of the external wrench applied on the body of the platform. Then, in the last few years, [Smeur–2018b] introduced the Incremental Nonlinear Dynamic Inversion (INDI) controller, used for the robust control of quadrotors with the help of the on-board IMU. The controller was later disucssed and improved in [Tal–2018; Smeur–2015]. The presented controller is a measurement based controller derived from the Taylor expansion of platform dynamics; the controller applies an incremental law that increases (or decreases) the applied propeller rotational speeds to match the desired linear and angular accelerations with the estimated ones. The INDI controller filters all measurements (propeller commands, accelerometer accelerations, and estimated platform angular accelerations) with a classical low-pass filter, where the used filters ensure a synchronyzation between the different filtered measurements. Finally, while the INDI requires the knowledge of the platform control effectivenes matrix, the adaptive version modifies this matrix online to accommodate for errors between desired and estimated platform's angular accelerations.

1.2 Main contribution of the thesis

In this section we detail the main contributions of this thesis. To facilitate the reading of this manuscript, we provide a summary of these contributions in Tab. 1.1. We also report the publications around which this thesis is built in Tab. 1.2 and Tab. 1.3, and report in Tab. 1.4 unpublished contributions that are detailed in this manuscript. As such, we encourage readers who do not wish to read the entire manuscript, to read the corresponding summarizing tables, and skip directly to the section they are most interested in; or if interested, to continue reading the rest of this thesis. It should be noted that while this thesis is built about the different publications listed in tables Tab. 1.2 and Tab. 1.3, it provides additional insights and analyses on different topics related to each of these publications, where this additional material was either conducted after the submission of the corresponding publication, or was omitted in the corresponding publications due to the limited page number allocated in each journal and conference proceedings.

Following the history and literature review from the previous section, we focus in this thesis on the effect of the platform design (i.e., the platform geometry) on its actuation capabilities, abilities and finally, on its measurements. Although there are many works in the literature addressing the different topics studied in this thesis, many of which seminal in the scope of this thesis, there are still numerous open problems that require additional investigation. As such, we attempt to analyze a few of these problems, while proposing clear hypotheses that could explain some of the phenomenon we encountered both in the literature and in real experiments, and proposing adequate solutions which we then evaluate experimentally.

The topic addressed in this thesis is a wide topic, in the sense that the majority of MRAV publications attempt to understand a part of the relation between the platform design and its actuation capabilities. However, in this thesis we focus our attention on modeling the different designs, their capabilities and abilities around the platform's *full allocation matrix*. As such we first introduce a formal modeling of general MRAVs; the aim of the presented modeling is to be general enough to encompass virtually any MRAV design for which actuation is achieved via spinning propellers (possibly re-orientable). In addition to the *full allocation matrix*, this thesis is also build around the platform's force/moment set. As such, we also provide a detailed method for the computation and visualization of these sets for different MRAV designs.

Following the presented modeling, and to demonstrate concretely the relation between different platform designs and their actuation capabilities and abilities, we provide a survey of the majority of MRAV designs from the literature. The survey focuses on the aforementioned relations between the different designs and the different actuation capabilities. The survey is intended as a reference that can be used to

List of the main contributions

1) Formal modeling of general MRAV designs with emphasis on the relation between platform design, the ensuing actuation capabilities and the relation of both to the full allocation matrix. Introduction of methods for the computation and visualization of MRAV force/moment sets for different MRAV designs.(Chapt. 2).

2) Formal definition of MRAV actuation capabilities, and definition of MRAV abilities: hovering, trajectory tracking and aerial physical interaction.(Chapt. 3).

3) Survey of the majority of MRAV designs from the literature, with emphasis on the actuation capabilities of each. Each design is analyzed to understand the corresponding abilities and feasible wrench set (Chapt. 3).

4) Introduction of a novel geometrical method for the analysis of the hoverability of an MRAV. Analysis of the robustness to propeller failure of different coplanar/collinear hexarotor designs. Experimental validation of the analysis conducted on a Y-shaped and a Star-shaped hexarotors with identical components and properties (Chapt. 4).

5) Introduction of a prototype omnidirectional platform with minimal number(7) of uni-directional thrusters. Analysis of the hoverability of the presented design via the introduction of novel metrics that reflect the lift of an omnidirectional platform. Experimental validation of the omnidirectionality of the presented prototype (Chapt. 5).

6) Analysis of the interplay between the parameters of the Bounded Lateral Force controller/platform and the connection between these parameters and the lateral dynamics. Introduction of an optimal gain tuning method for the BLF controller. Experimental campaign that analyzes the parameters interplay/connection with lateral dynamics, and the outcome of the gain tuning method (Chapt. 6).

7) Analysis of vibration noise present in IMU measurements on-board different MRAV platforms, and data-based analysis of the relation between these vibrations and the corresponding platform design. Introduction of a novel zero-phase IMU filter that runs in real time on-board the analyzed MRAV platforms (Chapt. 7).

8) Introduction of a novel direct acceleration feedback controller that closes the loop between desired and measured accelerations. Experimental campaign analyzes the controller robustness to changes in mass, aerodynamic properties and external disturbances (Chapt. 8).

Table 1.1 – Concise list of the main contributions of this thesis.

understand the possible actuation capabilities and platform abilities for platforms with an increasing number of propellers. The survey also provides a visualization of the force set of representative designs to demonstrate more concretely the relation between these designs and the ensuing feasible wrench space. The survey is concluded with the limitations we found in the literature.

Following the definitions made above, we present three studies that aim to fill the gap in the literature on the relation between platform design, and its actuation properties and the ensuing abilities. Each work covers a single actuation property or ability for a specific case, however, it also proposes methods that could be used for a wide range of designs. As such, we first introduced a geometrical method for the analysis of the hoverability of an MRAV; the method relies on the computation of the moment set of the MRAV design, and thus can be computed numerically. As such, the method provides a systematic way to analyze the hoverability of a platform, where previously, such analysis had to be done on a case-by-case basis ([Michieletto–2018]). Following this method, we study the robustness of different coplanar/collinear hexarotor designs to single propeller failure, and show the vulnerability of the classical Star-shaped hexarotor and the robustness of the Y-shaped hexarotor. We also provide a hypothesis that allows a Star-shaped hexarotor to hover following the failure of some of its propellers. We validate the presented analyses via an extensive experimental campaign conducted on a Star-shaped and a Y-shaped hexarotor build with identical components, and similar properties.

Then we tackle trajectory tracking ability of a titled propeller hexarotor, modeled as a Bounded Lateral Force (BLF) platform. With the BLF modeling and controller ([Franchi–2018a]), the platform lays somewhere in-between a Uni-directional Thrust(UDT) platform and an unconstrained Fully Actuated(FA) platform. The parameter that dictates the maximum allowed lateral force ($\overline{f_{xy}}$) that the controller can use is the key to decide whether the platform is closer to behave like a UDT or an FA. To be able to assess the behavior of the platform in response to different values of such parameter, we present a method to auto-tune the parameters of the BLF controller while varying $\overline{f_{xy}}$. Our analysis, in addition to an extensive experimental campaign show that there is a coupling between $\overline{f_{xy}}$ and the different controller gains; moreover, the platform trajectory tracking is strongly affected by the platform $\overline{f_{xy}}$ where as it decreases the platform has to advantage tracking its lateral position on the expense of a decreased ability in tracking its desired orientation.

After studying the above two abilities, we study the effect of a platform design on its actuation property, and more specifically, the effect of a platform's design on its omnidirectional hovering ability. In this chapter we first build a prototype omnidirectional platform with 7 fixed uni-directional thrusters. The platform is the first of its kind, which we prove to be able to hover in different orientations about its CoM. In an aim to build a second version of the platform with a higher level of maturity, we present novel metrics that reflect the omnidirectional hovering ability of any platform. More specifically, the presented metrics reflect the radius of the sphere contained inside the force space of the platform.

Following the analysis of the above three abilities, we present for the first time in the literature an analysis of vibration noise in IMU measurements. We hypothesize that these vibrations are caused by the propellers 'shaking' the platform body. Following the presented hypothesis, we show, through the analysis of the measurements frequency domain, that for a quadrotor platform, the frequency of these vibrations is in the range of the propellers' rotational speed. On the other hand, we show that for a titled propeller hexarotor, in addition to vibrations in the range of the propeller rotational speeds, we could find an additional vibration at a constant frequency. By analyzing the frequency domain of two such platforms constructed with different materials, we conclude that this vibration is due to the platform geometry, while the construction material has a secondary effect on the resulting vibrations.

We leverage the knowledge about the vibration noise by presenting a novel IMU filter that runs on-board in real time. The filter is a regression based filter that assumes the IMU measurements to be a combination of body accelerations modeled as second order polynomial, in addition to vibration noise modeled as a sum of sinusoids at the given vibration frequencies, calculated from the propeller rotational speeds. As opposed to classical low-pass filters, the presented filter is a zero-phase filter; it removes only the signal part related to the vibration frequencies; and finally, it removes completely the vibrations, irrespective of their amplitude, instead of 'just' attenuating them.

Finally, to show the full benefit of the introduced IMU filter, we introduce a direct acceleration feedback controller. The presented controller closes the loop between the desired acceleration and the measured (filtered) one along the vertical axis of a quadrotor. The controller implementation would not have been possible without the proposed IMU filter: if the measurements are not filtered, the high amplitude noise is propagated into the platform controls; on the other hand, if the measurements are filtered with a classical low pass filter, the induced phase causes a mismatch between the compensated and real measurements. As such, a zero-phase IMU filter was required to close the loop between desired and measured accelerations. The presented controller does not require the knowledge of the platform mass, although it can benefit from it; as such, it is robust to changes in the platform mass. Moreover, it is also robust to changes in the aerodynamic lift coefficient, and robust to external disturbances. An extensive experimental campaign was conducted to prove the robustness to the above mentioned variance in the internal parameters and external disturbances, with the campaign showing this robustness following systematic disturbances, and real world scenarios.

Table 1.2 – Summary of publications in Part II and corresponding contribution list.

Part II - MAV Actuation Properties and Abilities	
Publication	**Contribution**
[Hamandi–2020c] **Journal** *accepted* IJRR	Design of Multirotor Aerial Vehicles: a Taxonomy Based on Input Allocation • generalized taxonomy that can encompass all reviewed designs • formal definition of different MRAV actuation capabilities and abilities • review of majority of MRAV designs from the literature
[Baskaya–2021] **Journal** IEEE RAL 2021	A Novel Robust Hexarotor Capable of Static Hovering in Presence of Propeller Failure • introduction of a geometric tool for the analysis of MRAV hoverability • analysis of failure robustness of coplanar/collinear hexarotors • extensive experimental validation conducted with a Y-shaped and a Star-shaped hexarotor with identical components
[Horla–2021] **Journal** IEEE RAL 2021	Optimal Tuning of the Lateral-Dynamics Parameters for Aerial Vehicles With Bounded Lateral Force • study of the interplay between the parameters of the BLF controller • introduction of a detailed method for the optimal auto-tuning of the controller's gains • extensive experimental campaign that analyzes the interplay between the BLF parameters and the auto-tuning method
[Hamandi–2020a] **Conference** IEEE ICUAS 2020	Omni-Plus-Seven (O_+^7): An Omnidirectional Aerial Prototype with a Minimal Number of Unidirectional Thrusters • introduction of a prototype omnidirectional platform with 7 unidirectional thrusters • experimental campaign that demonstrates the omnidirectionality of the platform
[Hamandi–2021] **Conference** *submitted to* IEEE AIRPHARO 2021	Understanding the omnidirectional capability of a generic multi-rotor aerial vehicle • introduction of metrics for the analysis of the omnidirectional property of a generic multi-rotor aerial vehicle • analysis of the omnidirectional property of the prototype from [Hamandi–2020a] • design of a new omnidirectional platform, with geometry similar to the prototype from [Hamandi–2020a], and with different weight and dimensions

Table 1.3 – Summary of the publication around which Part III is built and the corresponding contribution list.

Part III - Effect of IMU on the Robustness of MAV	
Publication	**Contribution**
[Hamandi–2020b] **Conference** IEEE ICRA 2020	Direct acceleration feedback control of quadrotor aerial vehicles • presentation of a novel, real time, zero-phase IMU filter • introduction of a UAV direct acceleration feedback controller • extensive experimental campaign that proves the robustness of the controller to external disturbances and parameter variances

Table 1.4 – Summary of unpublished contributions detailed in this thesis

Part II - MAV Actuation Properties and Abilities
In the scope of the design of coplanar/collinear hexarotors • theoretical analysis of aerodynamic interaction between adjacent propellers • efficiency comparison of coplanar/collinear hexarotors with different angles between adjacent propellers
Part III - Effect of IMU on the Robustness of MAV
In the scope of the design and analysis of the IMU filter • frequency domain analysis of the vibration noise in IMU measurements for three different platforms • application of the introduced IMU filter in [Hamandi–2020b] on tilted propeller hexarotors • frequency domain analysis of the presented IMU filter for the different platforms in question

1.3 Organization of the thesis

In this section we provide a detailed outline of the thesis, describing the content of each part and summarizing the content of each chapter. To make it easier for the reader, we divide this thesis into 4 parts as follows:

Part I is intended to contextualize the thesis w.r.t. the wide area of aerial robotics, and provide some concepts that are necessary for the reader's understanding of the thesis. This part also contains the modeling of MRAV platforms, necessary for the design and control problems discussed throughout the thesis.

Part II presents the main analysis on the relation between platform design and its ensuing actuation properties and abilities. In addition, this part addresses some of the limitations in MRAV designs found in the literature, and analyzes design related concepts. As such, this part starts by defining the actuation properties and abilities. Then it surveys the majority of MRAV designs from the literature, and summarizes the different properties and abilities of each. Then, in this part, we tackle three problems related to the ability of a platform to hover following propeller failure, hover in omnidirectional way, and finally track trajectories. While tackling these problems, we present novel methods to understand numerically a platform's ability to hover while healthy or following propeller failure, a platform's ability to hover in an omnidirectional way, and finally compute the aerodynamic interaction between adjacent propellers of a hexarotor, and the resulting effect on the platform's abilities. All the methods and analyses presented in this part are validated with extensive experimental campaigns on platforms presented in earlier work, or prototype platforms present in this thesis.

Part III presents a filter for IMU measurements, and a controller that attempts to benefit the most from these filtered measurements. This part first analyzes the vibration noise present in IMU measurements, and proposes a novel filter to remove such vibrations from the corresponding measurements. The analysis is conducted on different platforms to understand the relation between platform geometry and the ensuing vibrations. Then it proposes a novel controller that closes the loop between desired and measured accelerations. The controller is hypothesized to be robust to external disturbances and variances in platform parameters. The presented hypothesis is validated experimentally with an extensive experimental campaign.

Part IV finally concludes the thesis by presenting a summary of the different parts, and discusses some of the works that could follow from the presented manuscript.

In the following, we shall provide a brief description of each chapter. Regarding Part I:

Chapt. 2 recalls in a synthetic way the mathematical methodologies used as background for the theoretical analysis conducted in Part II and Part III. In particular, this section provides the basic definitions necessary for the these parts, the general modeling of MRAV designs, and the Newton-Euler formalism applied to different MRAV designs.

Regarding Part II:

Chapt. 3 contains the complete survey of MRAV designs. In this chapter, we provide a thorough analysis of each design, and the corresponding properties, abilities, and wrench set. We conclude the chapter with the limitations we found in the survey, and insights on possible improvements that we believe could advance such designs.

Chapt. 4 contains analysis of the robustness of different coplanar/collinear hexarotors to propeller failure. In addition, it provides a geometrical tool to analyze numerically the hoverability of MRAVs, and an extensive experimental campaign validating the findings on the robustness of Y-shaped and Star-shaped hexarotors.

Chapt. 5 introduces the prototype omnidirectional heptarotor with uni-directional thrusters. The prototype's omnidirectional hovering ability is validated experimentally. The chapter introduces a metric to analyze any platform's ability to hover in an omnidirectional way, and analyzes the feasibility of a new prototype with a higher level of maturity.

Chapt. 6 introduces a method for the auto-tuning of the BLF controller parameters. In addition, it analyzes the interplay between these parameters, and between the parameters and the platform dynamics. Both the auto-tuning method and the aforementioned interplay are analyzed in simulation and experimentally

Regarding Part III:

Chapt. 7 contains frequency domain analysis of the vibration noise in IMU measurements for multiple MRAV designs (a quadrotor and two titled propeller hexarotors composed of different material). In addition, it introduces the real-time on-board zero-phase IMU filter. Different versions of the IMU filter are presented for the different platforms, and its outcome is analyzed in the frequency and time domains. Finally, it is compared to a classical low-pass filter.

Chapt. 8 introduces the direct acceleration feedback controller. The controller is analyzed for robustness against varying parameters and external disturbances; in addition, its advantage against a PID controller is presented. Experimentally, the controller is compared against the PID to show the aforementioned advantage, and it is extensively tested to show its robustness to varying mass, aerodynamic coefficients, and external disturbances (picking up an unknown mass and flying in a turbulent environment).

Regarding Part IV:

Chapt. 9 concludes the thesis by providing a global overview of the manuscript's content. Then briefly provides a few lessons that could be deduced from the thesis, and finally, discusses possible extensions for future work.

Fig. 1.3 provides a visual organization of the thesis.

It should be noted that the different parts of this thesis, while connected, they could be read separately. Part I presents the definitions and equations which are necessary for the rest of the manuscript. For conciseness of the manuscript, throughout the rest of this thesis we only list definitions and equations which were not specified in Part I, and which are specific for the given chapter. While Chapt. 3 defined all the properties and abilities that are necessary for the rest of Part II, on the exception of these definitions, each chapter in Part II could be read independently. And finally, Part III is a chapter that could be read completely on its own following the definitions from Part I. We do note that while this thesis was not carried in any specific project, some of its contributions are conducted within the scope of the H2020 European Project AERIAL-CORE [1]. The project aims to develop novel modules and an integrated cognitive aerial robotics system that could eventually allow the safe and reliable interaction between a MAV and a human coworker.

1.4 Publication note

This thesis grounds on three journal and three conference papers published (or submitted) on major international congresses on robotics and control research. These publications are summarized in Tab. 1.2 and Tab. 1.3. It should be noted that I am a first author or have contributed equally to the first author in all of the six publications listed above. Finally, we do note that while the thesis is built around these publications, it provides additional analyses and findings conducted during or after the publication of each corresponding journal or conference paper, and summarized in Tab. 1.4. As these findings require additional maturation, they are not yet published in peer reviewed conferences or journals, however, it was important to report these findings in this thesis as a continuation of the published contributions.

---

[1] https://aerial-core.eu/

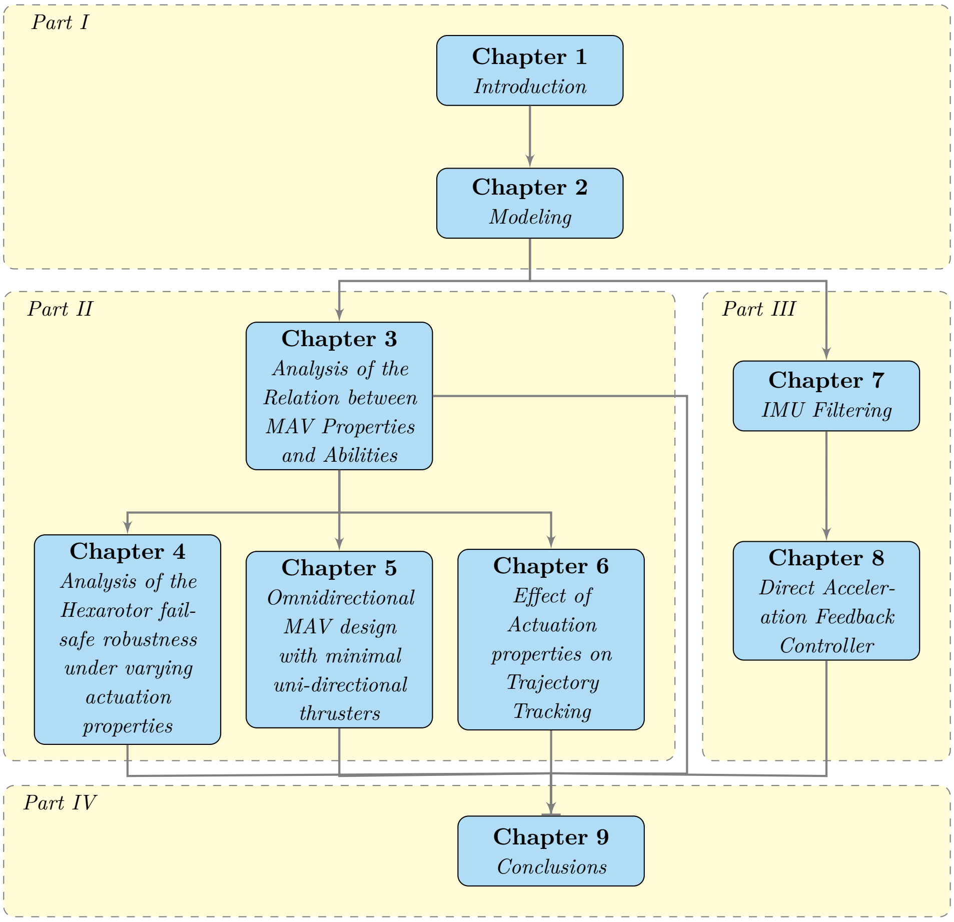

Figure 1.3 – Graphical representation of the thesis organization.

Chapter 2
Modeling

In this chapter we provide a brief review of the theoretical methodologies required for the understanding of the rest of this manuscript. In particular, in this chapter we provide i) the modeling of a generic Multi-Rotor Aerial Vehicle, ii) the analysis of its dynamic properties, and finally, iii) the method used to calculate feasible force and moment set of each platform.

While the following covers the necessary theoretical background to understand all chapters of this manuscript, additional definitions and specifications are provided at the beginning of each of the ensuing chapters when required.

Before providing the modeling of a general Multi-Rotor Aerial vehicle, we note the scope of our modeling as follows. Our focus in this manuscript is on the analysis of multirotor i.e., rotary-wing vehicles, for which the control inputs are solely the spinning velocities of each propeller and, possibly, the propeller orientation. This scope excludes UAV designs where propellers are mixed with wings in which the control input also comprises the wing geometry, i.e., designs in which a subsequent part of the lift is generated by fixed-wing. Some examples are ([Bronz–2017]) or the hybrid designs reviewed in ([Saeed–2015]). The scope of this manuscript also excludes multirotors with variable pitch propeller mechanisms, where the propeller pitch is a control input rather than, or in addition to, the propeller speed, e.g., the quadrotor based design in ([Michini–2011]). Designs in which the motion of weights is used as control input are also excluded, e.g., the quadrotor based design in ([Haus–2016]). Additionally, designs in which the multirotor Center of Mass (CoM) is time varying are also out of the scope of this manuscript. This includes some of the previously mentioned cases but also designs where weight motion participates in the system stabilization. Examples of such stabilization systems can be found in ([Haus–2017]), and in ([Zhao–2017; Anzai–2017]). Nevertheless, to accommodate for manufacturing imperfections and mechanical constraints, we consider the non-moving CoM in a relaxed way, allowing small displacement of the CoM due to the motion of the actuators. Lastly, designs where the weight is partially or totally lifted by means other than the rotating propellers are also excluded. This category includes for example platforms lifted through a gas such as helium or ropes, similar to the design presented in ([KG–2016; Sarkisov–2019]).

Consequently, the considered designs include the control quantities related to:

i) the spinning propellers, each producing mainly a thrust (a lift) and a drag moment, and possibly

ii) the vectorization of their orientation in the body frame.

The modeling of the systems described in this work mainly relies on the Newton-Euler formalism, where a MAV is considered a rigid body floating in space, with its motion fully understood from its gravity force and the forces produced by the sum of its Atomic Actuation Unit (AAU)s.

Tab. 2.1 summarizes the main nomenclature used throughout this manuscript, and Fig. 2.1 provides a visual demonstration of some of these notations. We do note that this list is not exhaustive, however, subsequent variables could be understood from extrapolation of the closest variable in Tab. 2.1.

$\mathcal{B}$	body frame
O_B	rigid body center and axes
$\boldsymbol{x}_B, \boldsymbol{y}_B, \boldsymbol{z}_B$	
$\mathcal{W}$	world frame
O_W	world frame center and axes
$\boldsymbol{x}_W, \boldsymbol{y}_W, \boldsymbol{z}_W$	
N	Number of AAUs in a platform
$\boldsymbol{u} = [\boldsymbol{u}_\lambda^\top \ \boldsymbol{u}_{\boldsymbol{V}}^\top]^\top$	Total control inputs
$\boldsymbol{u}_\lambda$	AAUs thrust control inputs
$\boldsymbol{u}_{\boldsymbol{V}}$	AAUs vectoring control inputs
n_u	Number of control inputs
	composed of $n_u = n_\lambda + n_v$
n_λ	Number of thrust input controls
n_v	Number of thrust-vectoring input controls
$\boldsymbol{v}_i$	Spinning axis of $i-$th AAU expressed in $\mathcal{B}$
α_i, β_i	radial and tangential tilts of the i-th propeller respectively
c_{f_i}, c_{τ_i}	lift and drag coefficients of the i-th propeller respectively
${}^B\boldsymbol{p}_i$	position of the i-th propeller w.r.t. $\mathcal{B}$
$\mathbf{F}$	Full Allocation Matrix
$\mathbf{F}_1$	Force Allocation Matrix
$\mathbf{F}_2$	Moment Allocation Matrix
$\mathbb{U}$	Input control set
$\mathbb{W}$	Feasible wrench set
$\mathcal{F}_1$	Image of the feasible force set on the domain $\mathbb{U}$ subject to zero moment
$\mathcal{F}_2$	Image of the feasible moment set on the domain $\mathbb{U}$
$\mathcal{F}_{2+}$	Image of the feasible moment set on the domain $\mathbb{U}$ at hover

Table 2.1 – This table summarizes the main mathematical notations used in this manuscript.

2.1 Newton-Euler Formalism

The Newton-Euler formalism describes the dynamics of a physical particle when subjected to external forces and moments. This formalism combines the linear mo-

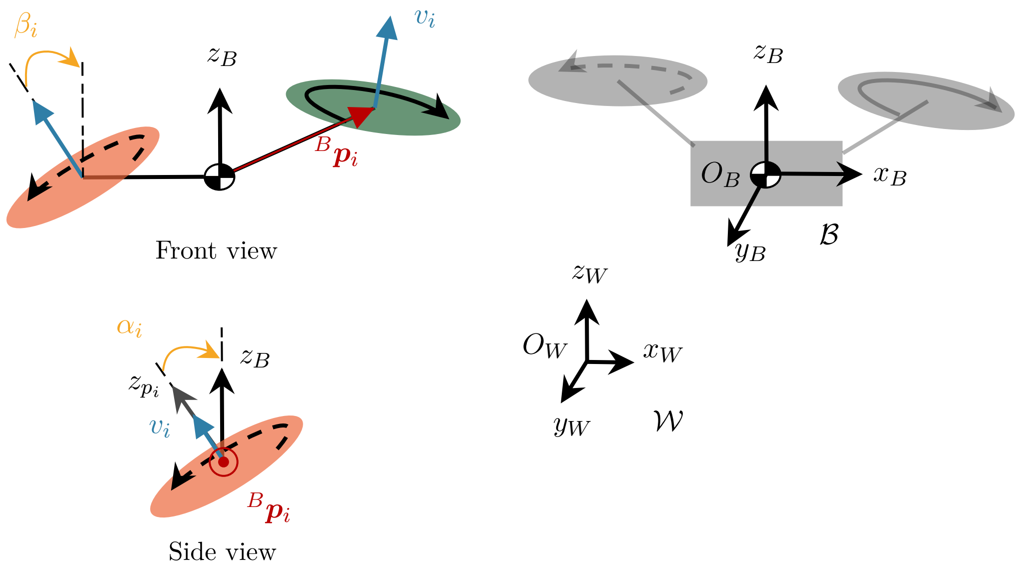

Figure 2.1 – This figure summarizes the main mathematical notations used in this manuscript.

tion dynamics described by Newton, and the corresponding angular motion dynamics described by Euler. The formulation is based on the principal of conservation of momentum, where a system is said to be in a momentum equilibrium unless an external force or moment is applied on its CoM; in mathematical terms, this formulation can be written w.r.t. to the inertial frame as follows:

$$\left.\frac{d(m\boldsymbol{v})}{dt}\right|_I = \boldsymbol{f} \tag{2.1}$$

$$\left.\frac{d(\boldsymbol{J}^I\boldsymbol{\omega})}{dt}\right|_I = \boldsymbol{\tau}, \tag{2.2}$$

where $m \in \mathbb{R}_{>0}$ and $\boldsymbol{J}^I \in \mathbb{R}^{3\times3}_{>0}$ are the mass and inertia matrix of the rigid body respectively, $\boldsymbol{v} \in \mathbb{R}^3$ and $\boldsymbol{\omega} \in \mathbb{R}^3$ are its corresponding linear and angular velocity, and finally, $\boldsymbol{f} \in \mathbb{R}^3$ and $\boldsymbol{\tau} \in \mathbb{R}^3$ are the external forces applied on the rigid body's CoM.

Following the assumptions made in this work, we can specialize the equations Eq. (2.1), Eq. (2.2) as follows:

$$m\left.\frac{d(\boldsymbol{v})}{dt}\right|_I = \boldsymbol{f} \tag{2.3}$$

$$\boldsymbol{J}^I\left.\frac{d(\boldsymbol{\omega})}{dt}\right|_I + \boldsymbol{\omega}\times(\boldsymbol{J}^I\boldsymbol{\omega}) = \boldsymbol{\tau}, \tag{2.4}$$

We refer the reader to the following references for a more exhaustive explanation of the Newton-Euler formalism [Spong–2006; Siciliano–2010; Siciliano–2016; Lynch–

2017].

2.2 Modeling of a generic Multi-Rotor Aerial Vehicle

In this section, we present the modeling of generic Multi-Rotor Aerial Vehicle (MRAV)s starting with the definition of such platforms:

Definition 2.2.1. A *multirotor design* is considered as a rigid body, made of fixed mechanical elements, to which some *Atomic Actuation Units* (AAUs) are attached. The design so defined is completely described by:

i) the number of AAUs, denoted by $N \in \mathbb{N}_{>0}$,

ii) the type of every single AAU, and

iii) the arrangements of the AAUs (position and attitude).

Under the assumptions stated in this thesis, to describe the various possible designs of small multirotors, we propose a general abstract framework defined as follows.

We denote by $\mathcal{B}$ the body frame rigidly attached to the multirotor. Its origin O_B coincides with the rigid body CoM and its main axes are denoted by $\boldsymbol{x}_B, \boldsymbol{y}_B, \boldsymbol{z}_B$, respectively.

2.2.1 Atomic Actuation Units – AAUs

Atomic Actuation Units are the mechatronic components generating thrust. They are the core of each multirotor design. In the literature, they typically consist of a brushless motor with a single propeller.

Considering a generic i-th AAU, we denote by $w_i \in \mathbb{R}$ the *propeller rotational speed* and by[1] $\boldsymbol{v}_i \in \mathbb{S}^2$ the coordinates of the *spinning axis* expressed in $\mathcal{B}$.

Besides, we define a frame $\mathcal{F}_{P_i}$ rigidly attached to the i-th AAU, with origin O_{P_i} coinciding with its CoM, and with axes $\boldsymbol{x}_{P_i}, \boldsymbol{y}_{P_i}, \boldsymbol{z}_{P_i}$ such that $\boldsymbol{z}_{P_i}$ is the spinning axis ($\boldsymbol{z}_{P_i} = \boldsymbol{v}_i$) and $\boldsymbol{y}_{P_i}$ is perpendicular to both $\boldsymbol{z}_{P_i}$ and ${}^B\boldsymbol{p}_i$, where ${}^B\boldsymbol{p}_i \in \mathbb{R}^3$ is the position of O_{P_i} w.r.t. $\mathcal{B}$.

It is convenient to parametrize $\boldsymbol{v}_i$ using two angles α_i and β_i which are defined as follows:

- α_i is the angle needed for a rotation about ${}^B\boldsymbol{p}_i$ to bring $\boldsymbol{z}_B$ into a vector $\boldsymbol{z}'_B$, where $\boldsymbol{z}'_B$ is the projection of $\boldsymbol{z}_B$ into the plane spanned by ${}^B\boldsymbol{p}_i$ and $\boldsymbol{z}_{P_i}$.
- β_i is the angle needed for a rotation about the axis perpendicular to the plane spanned by ${}^B\boldsymbol{p}_i$ and $\boldsymbol{z}_{P_i}$ to let $\boldsymbol{z}'_B$ coincide with $\boldsymbol{z}_{P_i}$.

These two rotations can be combined into a single rotation matrix[2] ${}^B\mathbf{R}_{P_i} \in SO(3)$ defined as ${}^B\mathbf{R}_{P_i} = \mathbf{R}_2(\beta_i)\mathbf{R}_1(\alpha_i)$ where $\mathbf{R}_1(\alpha_i)$ and $\mathbf{R}_2(\beta_i)$ are the two aforementioned rotations, thus obtaining $\boldsymbol{v}_i =^B \mathbf{R}_{P_i}\boldsymbol{e}_3$, where $\boldsymbol{e}_3 = [0\ 0\ 1]^\top$. Notice that

---

[1] $\mathbb{S}^n = \{\boldsymbol{x} \in \mathbb{R}^{n+1} \mid \|\boldsymbol{x}\| = 1\}$

[2] $\mathrm{SO}(3) = \{\mathrm{R} \in \mathbb{R}^{3\times 3} \mid \mathrm{R}^\top \mathrm{R} = \mathrm{I}_3, \det(\mathrm{R}) = 1\}$, where $\boldsymbol{I}_i \in \mathbb{R}^{i\times i}$ is the identity matrix of dimension i.

such rotations are the ones performed by any servomotor controlling the orientation of the corresponding propeller. Furthermore, notice that this parametrization is valid as long as ${}^B\boldsymbol{p}_i$ and $\boldsymbol{z}_{P_i}$ are not parallel, where otherwise (i.e., if $\beta_i = \pm 90°$) the angle α_i has no effect on the thrust direction $\boldsymbol{v}_i$, with this direction being in the same or opposite direction of ${}^B\boldsymbol{p}_i$.

The propeller rotation produces a thrust $\boldsymbol{f}_i \in \mathbb{R}^3$, and a drag moment $\boldsymbol{m}_i \in \mathbb{R}^3$. This force and moment pair applied in O_{P_i} can be expressed w.r.t. $\mathcal{B}$ as follows:

$$\begin{aligned} \boldsymbol{f}_{P_i} &= c_{f_i}|w_i|w_i\boldsymbol{v}_i \\ \boldsymbol{m}_{P_i} &= k_i c_{\tau_i}|w_i|w_i\boldsymbol{v}_i, \end{aligned} \tag{2.5}$$

where $c_{f_i} \in \mathbb{R}_{>0}$ and $c_{\tau_i} \in \mathbb{R}_{>0}$ are positive constants whose value depends on the shape of the corresponding propeller. The term $k_i \in \{-1, 1\}$ accounts for the direction of rotation of the propeller w.r.t. $\boldsymbol{v}_i$. As such, $k_i = -1$ (or $k_i = 1$) if the thrust has the same (or the opposite) direction of $\boldsymbol{v}_i$, and the propeller is consequently considered of CCW (or CW) type.

As normally done in the related literature, in Eq. (2.5) we neglected all the secondary inertia and aerodynamic effects, like centripetal and flapping effects, see ([Mahony–2012]). In fact, in the considered working conditions, these are negligible w.r.t. the main thrust and drag moment contributions.

Assuming that the brushless motor can control w_i, we can define $u_{\lambda_i} = |w_i|w_i \in \mathbb{U}_{\lambda_i} \subset \mathbb{R}$ as one of the controllable inputs for the i-th AAU, where $\mathbb{U}_{\lambda_i}$ is the set of feasible thrust control inputs of the i-th AAU. In particular, this is the input that controls the intensity of the produced force and moment. The equations in Eq. (2.5) can be rewritten w.r.t. $\mathcal{B}$, with the addition of the force-induced moments as follows:

$$\begin{aligned} \boldsymbol{f}_i &= c_{f_i}\boldsymbol{v}_i u_{\lambda_i} \\ \boldsymbol{m}_i &= k_i c_{\tau_i}\boldsymbol{v}_i u_{\lambda_i} +^B \boldsymbol{p}_i \times \boldsymbol{f}_i. \end{aligned} \tag{2.6}$$

For the completeness of the definition of an AAU, we do note that each might produce either uni-directional thrust or bidirectional thrust. Uni-directional thrust propellers can produce thrust in one direction, i.e., $0 \le \underline{w}_i \le w_i \le \bar{w}_i$ where $\underline{w}_i, \bar{w}_i \in \mathbb{R}_{\ge 0}$. On the other hand, bi-directional propellers can produce thrust in both directions, i.e., $\underline{w}_i \le \omega_i \le \bar{w}_i$ where $\underline{w}_i \in \mathbb{R}_{<0}$ and $\bar{w}_i \in \mathbb{R}_{>0}$.

Furthermore, each propeller could have a fixed or actuated spinning axis; we express the spinning axis as follows:

$$\boldsymbol{v}_i = f_{\boldsymbol{v}_i}(\boldsymbol{u}_{\boldsymbol{V}}), \tag{2.7}$$

where $f_{\boldsymbol{v}_i} : \mathbb{R}^{n_v} \to \mathbb{S}^2$ and $\boldsymbol{u}_{\boldsymbol{V}} = [u_1^\top \dots u_{n_v}^\top]^\top \in \mathbb{U}_{\boldsymbol{V}} = \times_{j=1}^{n_v}\mathbb{U}_{\boldsymbol{v}_j} \subset \mathbb{R}^{n_v}$ gathers the angular positions of the shafts of the servo motors that control the orientation of the spinning axis, where we noted by n_v the number of servomotors. Each motor is assumed to be tilted with a maximum number of 2 servomotors, i.e., $n_v \le 2N$. This property can be used to change the vectoring direction of the total thrust produced by the combination of all AAUs without changing their spinning velocities.

In what follows, we consider $\boldsymbol{u}_{\boldsymbol{V}}$ as a state due to its slower dynamics relative to the applied thrust. Instead, we consider its derivative $\dot{\boldsymbol{u}}_{\boldsymbol{V}}$ as the entity controlled by the n_v servo motors, thus the real input.

As such, we assume the existence of a local control loop that controls the rate of change of the platform propeller orientations similar to ([Ryll–2012]), which can be made visible from the dynamic extension of Eq. (2.7) as follows:

$$\dot{\boldsymbol{v}}_i = \frac{d\boldsymbol{v}_i}{dt} = \frac{\partial f_{\boldsymbol{v}_i}}{\partial \boldsymbol{u}_{\boldsymbol{V}}} \dot{\boldsymbol{u}}_{\boldsymbol{V}}. \tag{2.8}$$

2.2.2 Platform Equations of Motion

Let us consider a world frame $\mathcal{W}$, centered in O_W and such that it follows the East-North-Up (ENU) convention. Its main axes are denoted by $\boldsymbol{x}_W, \boldsymbol{y}_W, \boldsymbol{z}_W$, respectively.

Considering the body frame $\mathcal{B}$ previously defined, its position and orientation w.r.t. $\mathcal{W}$ are denoted with ${}^W\boldsymbol{p}_B \in \mathbb{R}^3$ and ${}^W\boldsymbol{R}_B \in \mathrm{SO}(3)$, respectively. To fully describe the state of the vehicle, we also define the linear velocity of the origin of $\mathcal{B}$ by the vector ${}^W\dot{\boldsymbol{p}}_B \in \mathbb{R}^3$ expressed in $\mathcal{W}$, and its angular velocity w.r.t. $\mathcal{W}$ by the vector ${}^B\boldsymbol{\omega}_B \in \mathbb{R}^3$ expressed in $\mathcal{B}$.

For the sake of compactness, we introduce the following notations. Let ${}^B\boldsymbol{P} = [{}^B\boldsymbol{p}_1 \cdots {}^B\boldsymbol{p}_N] \in \mathbb{R}^{3\times N}$ and $\boldsymbol{V} = [\boldsymbol{v}_1 \cdots \boldsymbol{v}_N] \in \mathbb{R}^{3\times N}$ be the concatenation matrices of all AAUs positions and spinning axes, respectively. We define the time derivative of $\boldsymbol{V}$ as $\dot{\boldsymbol{V}} = [\dot{\boldsymbol{v}}_1 \dots \dot{\boldsymbol{v}}_N] \in \mathbb{R}^{3\times N}$. We also denote by $\boldsymbol{u}_\lambda = [u_{\lambda_1} \dots u_{\lambda_N}]^\top \in \mathbb{U}_\lambda \subset \mathbb{R}^{n_\lambda}$ the vector gathering the control inputs relative to the thrust intensity. Notice that $\mathbb{U}_\lambda = \times_{i=1}^N \mathbb{U}_{\lambda_i}$, $n_\lambda = N$. The total control input vector is denoted by $\boldsymbol{u} = [\boldsymbol{u}_\lambda^\top \ \boldsymbol{u}_{\boldsymbol{V}}^\top]^\top \in \mathbb{U} \subset \mathbb{R}^{n_u}$and $\mathbb{U} = \mathbb{U}_\lambda \times \mathbb{U}_{\boldsymbol{V}}$ denotes the set of feasible inputs. Notice that, if the orientation of all the AAUs is fixed, i.e., not actuated, then $\boldsymbol{u} = \boldsymbol{u}_\lambda$ and $n_u = n_\lambda$.

Let us define $\boldsymbol{w} \in \mathbb{R}^6$ as the actuation wrench applied to the platform at O_B expressed in $\mathcal{B}$, and $\mathbb{W}$ as the set of feasible wrenches defined as follows

$$\mathbb{W} = \{\boldsymbol{w}(\boldsymbol{u}) \ \forall \ \boldsymbol{u} \in \mathbb{U}\}. \tag{2.9}$$

Following Eq. (2.6), we can write

$$\boldsymbol{w}(\boldsymbol{u}) = \begin{bmatrix} \boldsymbol{f}(\boldsymbol{u}) \\ \boldsymbol{m}(\boldsymbol{u}) \end{bmatrix} = \sum_{i=1}^{N} \begin{bmatrix} \boldsymbol{f}_i(\boldsymbol{u}) \\ \boldsymbol{m}_i(\boldsymbol{u}) \end{bmatrix}, \tag{2.10}$$

where $\boldsymbol{f} \in \mathbb{R}^3$ and $\boldsymbol{m} \in \mathbb{R}^3$ are the total thrust and moment applied on the platform w.r.t. $\mathcal{B}$.

To characterize $\boldsymbol{w}$, and in particular how an input variation affects $\boldsymbol{w}$, we introduce the *full allocation matrix* $\boldsymbol{F} \in \mathbb{R}^{6\times n_u}$ defined as:

$$\boldsymbol{F}(\boldsymbol{u}) = \frac{\partial \boldsymbol{w}}{\partial \boldsymbol{u}} = \begin{bmatrix} \frac{\partial \boldsymbol{f}}{\partial \boldsymbol{u}_\lambda}(\boldsymbol{u}_{\boldsymbol{V}}) & \frac{\partial \boldsymbol{f}}{\partial \boldsymbol{u}_{\boldsymbol{V}}}(\boldsymbol{u}) \\ \frac{\partial \boldsymbol{m}}{\partial \boldsymbol{u}_\lambda}(\boldsymbol{u}_{\boldsymbol{V}}) & \frac{\partial \boldsymbol{m}}{\partial \boldsymbol{u}_{\boldsymbol{V}}}(\boldsymbol{u}) \end{bmatrix} = \begin{bmatrix} \boldsymbol{F}_1(\boldsymbol{u}) \\ \boldsymbol{F}_2(\boldsymbol{u}) \end{bmatrix}, \tag{2.11}$$

where the first column depends only on $\boldsymbol{u_V}$ due to the linearity of $\boldsymbol{f}$ and $\boldsymbol{m}$ in $\boldsymbol{u}_\lambda$.

We decompose $\boldsymbol{F}$ into $\boldsymbol{F}_1 = \frac{\partial \boldsymbol{f}}{\partial \boldsymbol{u}} \in \mathbb{R}^{3\times n_u}$, and $\boldsymbol{F}_2 = \frac{\partial \boldsymbol{m}}{\partial \boldsymbol{u}} \in \mathbb{R}^{3\times n_u}$ referred to as the *force* and *moment allocation matrices*, respectively.

Following the Newton-Euler formalism, one can derive the dynamic equation of a multirotor as follows:

$$\begin{bmatrix} m^W\ddot{\boldsymbol{p}}_B \\ \boldsymbol{J}^B\dot{\boldsymbol{\omega}}_B \end{bmatrix} = -\begin{bmatrix} mg\boldsymbol{z}_W \\ {}^B\boldsymbol{\omega}_B \times \boldsymbol{J}^B\boldsymbol{\omega}_B \end{bmatrix} + \mathbf{G}\boldsymbol{w}(\boldsymbol{u}), \tag{2.12}$$

where $m \in \mathbb{R}_{>0}$ and $\boldsymbol{J} \in \mathbb{R}^{3\times 3}_{>0}$ are the total mass and the positive definite inertia matrix w.r.t. $\mathcal{B}$ of the flying system, g is the gravitational acceleration constant, and $\mathbf{G}$ rotates the applied wrench (and more specifically $\boldsymbol{f}$) into the world frame for what concerns the translational dynamics, such that

$$\mathbf{G} = \begin{bmatrix} {}^W\boldsymbol{R}_B & \mathbf{0}_{3\times 3} \\ \mathbf{0}_{3\times 3} & \mathbf{I}_{3\times 3} \end{bmatrix}, \tag{2.13}$$

where $\mathbf{I}_{3\times 3}$ is a 3×3 identity matrix.

In the case of a platform where $\dot{\boldsymbol{u}}_{\boldsymbol{V}} = \mathbf{0}$ (i.e., a platform with fixed propellers, or where the propellers are not actively tilting), thanks to the linearity of $\boldsymbol{w}(\boldsymbol{u})$ w.r.t. $\boldsymbol{u}_\lambda$, we can make the *full allocation matrix* appear in Eq. (2.12), where

$$\boldsymbol{w}(\boldsymbol{u}) = \boldsymbol{F}(\boldsymbol{u}) \begin{bmatrix} \boldsymbol{u}_\lambda & \mathbf{0} \end{bmatrix}^\top = \begin{bmatrix} \frac{\partial \boldsymbol{f}}{\partial \boldsymbol{u}_\lambda}(\boldsymbol{u_V}) & \frac{\partial \boldsymbol{f}}{\partial \boldsymbol{u_V}}(\boldsymbol{u}) \\ \frac{\partial \boldsymbol{m}}{\partial \boldsymbol{u}_\lambda}(\boldsymbol{u_V}) & \frac{\partial \boldsymbol{m}}{\partial \boldsymbol{u_V}}(\boldsymbol{u}) \end{bmatrix} \begin{bmatrix} \boldsymbol{u}_\lambda \\ \mathbf{0} \end{bmatrix}. \tag{2.14}$$

In the case where $\dot{\boldsymbol{u}}_{\boldsymbol{V}} = \mathbf{0}$, the second column of $\boldsymbol{F}(\boldsymbol{u})$ has no effect on the output and will not be considered for simplicity. Also note that in the case of fixed propellers, the *full allocation matrix* is constant.

On the other hand, in the case of a platform actively tilting at least one of its propellers, we have to differentiate Eq. (2.12) to make the *full allocation matrix* appear:

$$\begin{bmatrix} m^W\dddot{\boldsymbol{p}}_B \\ \boldsymbol{J}^B\ddot{\boldsymbol{\omega}}_B \end{bmatrix} = \boldsymbol{g}\left({}^W\dot{\boldsymbol{p}}_B, {}^W\boldsymbol{R}_B, \boldsymbol{\omega}_B, {}^B\boldsymbol{P}, \boldsymbol{u_V}\right) + \mathbf{G}\boldsymbol{F}(\boldsymbol{u})\dot{\boldsymbol{u}}, \tag{2.15}$$

where $\boldsymbol{g}\left({}^W\dot{\boldsymbol{p}}_B, {}^W\boldsymbol{R}_B, \boldsymbol{\omega}_B, {}^B\boldsymbol{P}, \boldsymbol{u_V}\right)$ gathers all the terms that do not depend on the inputs $\dot{\boldsymbol{u}}$. For the simplicity of notation, from now on, and unless otherwise specified, we omit the dependency of $\mathbf{F}$ on $\boldsymbol{u}$.

Notice that the model in Eq. (2.12) and correspondingly in Eq. (2.15) is valid under the following assumptions:

i) motor actuators are controlled by a fast high-gain local speed controller, to have a negligible speed transient;

ii) gyroscopic and inertial effects due to propellers and motors are considered second-order disturbances that are neglected in the model and can be compensated by the controller itself, as specified before;

iii) aerodynamic interactions between adjacent propellers are considered negligible, and, again, left to the robustness of the feedback controller,

iv) the counter torque on the body produced by a servomotor rotating a propeller is considered negligible and compensated by the controller.

Remark 2.2.1. For convenience of notation, for the rest of this manuscript we will occasionally omit the reference to $\mathcal{W}$ for ${}^{W}\boldsymbol{p}_B$ and its derivative as well as ${}^{W}\boldsymbol{R}_B$, where we will refer to the former as $\boldsymbol{p}_B$ and to the later as $\boldsymbol{R}_B$ or $\boldsymbol{R}$. In addition, we will omit the reference to $\mathcal{B}$ for ${}^{B}\boldsymbol{\omega}_B$ and its derivative, simplifying the notation to $\boldsymbol{\omega}_B$.

2.3 Actuation Allocation

In this section we will briefly discuss wrench allocation techniques for different MRAV platforms. This discussion will focus on the calculation of control inputs necessary to reach a desired acceleration (or jerk) and a desired angular velocity (or angular acceleration). In this context, we divide platforms into three categories, where a platform is said to be underactuated if its full allocation matrix $\boldsymbol{F}$ is rank deficient, fully actuated (FA) if its full allocation matrix $\boldsymbol{F}$ is full rank, and finally, overactuated (OA) if its full allocation matrix $\boldsymbol{F}$ is a non-square matrix with rank equals 6.

We do note that this section is an introduction of the wide topic of wrench allocation, or control allocation of MRAV platforms, and it serves to give a gist of some of the techniques used for this purpose in the literature and this thesis. However, it does not constitute a comprehensive study of such techniques. Some further examples will be provided later in Chapt. 3 while reviewing the corresponding designs, and specific allocation strategies for the platforms that are used throughout this manuscript will be provided in the corresponding chapters.

Underactuated Platforms The case of underactuated platforms is a particular one, where it was noted that in the literature each design requires a specific allocation strategy, since feedback linearization cannot be directly applied.

For example, the most underactuated platform possible, the uni-rotor platform introduced in ([Zhang–2016]) requires an allocation strategy that takes the desired position and orientation into account, as well as the platform's rotation velocity vector, as the platform is under constant rotation about its CoM. On the other hand, T-shaped bi-rotor (see Sec. 3.3.2) use specifically designed control allocation strategy, where each of its Degrees of Freedom (DoF) is controlled by a combination of propeller allocation. For example, the paper presented in [Papachristos–2011] applies yaw by tilting propellers about opposite α angles, roll by applying different thrust in each propeller, and pitch by tilting both propellers equally in the direction of the desired pitch, where the pitching moment is relative to the tilting angle and the vertical distance between the propellers' CoM and the platform's CoM. Finally, the classical quadrotor (i.e., coplanar/collinear quadrotor with fixed propellers, presented in Sec. 3.3.4) employs a reduced full allocation matrix $\boldsymbol{F}_m$ which consists of only the last four rows of the original full allocation matrix (i.e., moment and thrust along $\boldsymbol{z}_B$), and allocates the propeller commands ([Faessler–2017; Mahony–2012]) as follows:

$$\boldsymbol{u}_\lambda = \boldsymbol{F}_m^{-1}\left(\mathbf{G}^{-1}\left(\begin{bmatrix} m{}^W\ddot{\boldsymbol{p}}_B^\star \\ \boldsymbol{J}{}^B\dot{\boldsymbol{\omega}}_B^\star \end{bmatrix} + \begin{bmatrix} mg\boldsymbol{z}_W \\ {}^B\boldsymbol{\omega}_B \times \boldsymbol{J}{}^B\boldsymbol{\omega}_B \end{bmatrix}\right)\right)_{4\to 6}, \tag{2.16}$$

where ${}^W\ddot{\boldsymbol{p}}_B^\star$ and ${}^B\dot{\boldsymbol{\omega}}_B^\star$ are new virtual control inputs.

Note that in this control law, and due to the underactuation of the platform, only the $\boldsymbol{z}_B$ component of ${}^W\ddot{\boldsymbol{p}}_B^\star$ can be achieved directly (through the control of the total thrust of the platform), while the lateral components of ${}^W\ddot{\boldsymbol{p}}_B^\star$ dictate the roll and pitch components of ${}^B\dot{\boldsymbol{\omega}}_B^\star$. As such, the control law Eq. (2.16) makes only linear and yaw accelerations directly controllable (last four rows of the virtual input).

While we only discuss the above three examples of underactuated platform control strategies, we refer the interested reader for Chapt. 3, where we provide an exhaustive list of such platforms, and provide a brief insight on the corresponding control strategies.

Fully Actuated / Overactuated Platforms If the platform is FA, then the design of the controller is straightforward. In these cases, the full allocation matrix $\boldsymbol{F}$ is full rank and thus invertible. This allows applying simple *static (fixed AAUs) or dynamic (orientable AAUs) feedback linearization.* In case of fixed AAUs, we can define $\boldsymbol{u}_\lambda$ by the inversion of Eq. (2.12) while replacing $\boldsymbol{w}(\boldsymbol{u})$ with Eq. (2.14):

$$\boldsymbol{u}_\lambda = \boldsymbol{F}^{-1}\mathbf{G}^{-1}\left(\begin{bmatrix} m{}^W\ddot{\boldsymbol{p}}_B^\star \\ \boldsymbol{J}{}^B\dot{\boldsymbol{\omega}}_B^\star \end{bmatrix} + \begin{bmatrix} mg\boldsymbol{z}_W \\ {}^B\boldsymbol{\omega}_B \times \boldsymbol{J}{}^B\boldsymbol{\omega}_B \end{bmatrix}\right). \tag{2.17}$$

The control law Eq. (2.17) makes the linear and angular accelerations of a FA platform directly controllable.

In case of orientable AAUs, we can define the dynamic input extension $\dot{\boldsymbol{u}}$ by the inversion of Eq. (2.15):

$$\dot{\boldsymbol{u}} = \boldsymbol{F}^{-1}\mathbf{G}^{-1}\left(\begin{bmatrix} m{}^W\dddot{\boldsymbol{p}}_B^\star \\ \boldsymbol{J}{}^B\ddot{\boldsymbol{\omega}}_B^\star \end{bmatrix} - \boldsymbol{g}\right), \tag{2.18}$$

where ${}^W\dddot{\boldsymbol{p}}_B^\star$ and ${}^B\ddot{\boldsymbol{\omega}}_B^\star$ are new virtual control inputs. The control law Eq. (2.18) makes the linear and angular jerk directly controllable. A possible example of a FA platform with tiltable propellers, and only 6 actuators can be found in ([Odelga–2016]).

In both cases, the virtual inputs can be computed with a simple linear state feedback that makes ${}^W\boldsymbol{p}_B^\star$ and ${}^B\boldsymbol{\omega}_B^\star$ stable.

From another point of view, if the platform is also OA, the moore-penrose pseudo-inverse of $\boldsymbol{F}$ (denoted as $\boldsymbol{F}^\dagger$) should be used instead of the regular inverse;

in addition the null space of $\boldsymbol{F}$ can be employed to optimize some appropriate metrics related to the inputs as done, e.g., in ([Ryll–2015a]).

On the other hand, if the platform is not FA, feedback linearization cannot be directly applied, and particular attention should be dedicated to the design of the control law.

Actuation Limits It should be noted that while the above defined some of the control allocation strategies through feedback linearization for different platforms, it did not take into consideration their actuation limits. As such, these allocation strategies are considered as guidelines for the control of different platforms, which should be complemented by different techniques to account for the actuation limits. Such techniques include geometrical methods that model bounds on the platform's actuation abilities (such as the work in [Castillo–2002] and [Franchi–2018a]), optimal control methods that attempt to allocate the desired virtual control while applying weighted constraints between the desired state and the ability of the platform (such as the work in [Muñoz–2013]), and finally, model predictive control techniques that allocate motor controls to accommodate for the desired trajectory and constraints in an optimal way over a time horizon ([Bicego–2020]).

2.4 Force and Moment Set Representation

To assess the reachable allocation capabilities of platform designs, we present in what follows some methods to compute and visualize the attainable wrench set $\mathbb{W}$.

Since this set is a 6D set which is hard to represent in 3D, we represent, based on the requirement of the corresponding study:

i) the projection of the 6D set $\mathbb{W} \subset \mathbb{R}^6$ on the 3D force space (first three components of the wrench) while applying zero-moment, referred to in the following as $\mathfrak{F}_1 \subset \mathbb{R}^3$,

ii) the projection of the 6D set $\mathbb{W} \subset \mathbb{R}^6$ on the 3D moment space (last three components of the wrench) at hover (i.e., while applying a force in $\mathcal{B}$ to counteract the platform weight, and assuming that $\boldsymbol{z}_B$ and $\boldsymbol{z}_W$ are parallel), referred to in the following as $\mathfrak{F}_{2+} \subset \mathbb{R}^3$.

The choice of the feasible force set with zero-moment and the feasible moment set at hover are of particular interest for multirotors, where both are important for the static hoverability analysis of the platform ([Michieletto–2018]). The former provides an idea of the platform's ability to apply forces while applying zero moment, and thus it provides an idea of the possible forces that the platform could apply while in hover. On the other hand, the second set is important to compute if a platform can hover or not as we will show later in Chapt. 4. The force set will be used throughout the manuscript to classify platforms' actuation abilities (Chapt. 3).

Remark 2.4.1. The analysis of the feasible force set and moment set are calculated in the conditions of Eq. (2.14), where the *full allocation matrix* is either constant, or assumes the direction of all propellers to be constant, i.e., $\dot{\boldsymbol{u}}_{\boldsymbol{V}} = \boldsymbol{0}$.

As such, for tiltable propellers, the feasible force set and moment set are calculated for all possible $\boldsymbol{u_V}$, with its corresponding *full allocation matrix* $\boldsymbol{F}(\boldsymbol{u_V})$. Note that for such platforms, while this does not constitute the entire wrench set, we assume that the change of propeller direction to be done fast enough to consider the part of the wrench set corresponding to the transient phase to be contained in the wrench set with propellers at fixed directions, or that at best, that the wrench set is slightly different from the calculated one. However, the calculation is done in the conditions mentioned in remark 2.4.1 due to the complexity of calculating the wrench set for the transient phase.

For the sake of the representation of $\mathfrak{F}_1$ and $\mathfrak{F}_{2+}$, we detail below the analysis of such sets for three different cases:

Case 1: Fixed propellers In the case of fixed propellers, we note that $\boldsymbol{F}$ is constant. Let $\mathbb{U}_2 = null(\boldsymbol{F}_2) \cap \mathbb{U} \subset \mathbb{R}^N$ and $\mathbf{B}_2 \in \mathbb{R}^{N\times n}$ be the basis of the null space of $\boldsymbol{F}_2$, where $n = N - rank\{\mathbf{F}_2\}$. We denote by $\Lambda \subset \mathbb{R}^n$ the set $\Lambda = \{\boldsymbol{\lambda} \in \mathbb{R}^n \mid \boldsymbol{y} = \boldsymbol{B}_2\boldsymbol{\lambda} \in \mathbb{U}\}$, and subsequently

$$\mathbb{U}_1 = \{\boldsymbol{x} \in \mathbb{R}^N \mid \|\boldsymbol{F}_1\boldsymbol{x}\| \geq m\boldsymbol{g},\ \boldsymbol{x} \in \mathbb{U}\}, \tag{2.19}$$

$$\mathbb{U}_2 = \{\boldsymbol{y} \in \mathbb{R}^N \mid \boldsymbol{y} = \mathbf{B}_2\boldsymbol{\lambda}\ \forall\ \boldsymbol{\lambda} \in \Lambda\}. \tag{2.20}$$

As such, $\mathfrak{F}_1$ and $\mathfrak{F}_{2+}$ can be represented as

$$\mathfrak{F}_{2+} = \{\boldsymbol{x} \in \mathbb{R}^3 \mid \boldsymbol{x} = \boldsymbol{F}_2\boldsymbol{u}\ \forall\ \boldsymbol{u} \in \mathbb{U}_1\}, \tag{2.21}$$

$$\mathfrak{F}_1 = \{\boldsymbol{y} \in \mathbb{R}^3 \mid \boldsymbol{y} = \boldsymbol{F}_1\mathbf{B}_2\boldsymbol{\lambda}\ \forall\ \boldsymbol{\lambda} \in \Lambda\}. \tag{2.22}$$

Due to the linear relations in Eq. (2.20) and Eq. (2.22), $\mathbb{U}_2$ and $\mathfrak{F}_1$ are convex sets, and it is enough to find the extreme points of Λ to represent the convex hull of $\mathfrak{F}_1$.

Similarly, from the linear relations in Eq. (2.19) and Eq. (2.21), $\mathbb{U}_1$ and $\mathfrak{F}_{2+}$ are convex sets, and it is enough to find the extreme points of $\mathbb{U}_1$ to represent the convex hull of $\mathfrak{F}_{2+}$.

The extreme points of Λ are calculated using the algorithm presented in ([Kleder–2020]), where the convex hull of the dual of the polytope ([Genov–2015]) defined by $\mathbb{U}_2$ is computed using ([Barber–1996]), from which the convex hull of the polytope $\mathbb{U}_2$ is then computed. The same method is used to calculate the extreme points of $\mathbb{U}_1$.

For the calculation of the the force and moment spaces in the other two cases, we define f_x, f_y and f_z as the respective components of $\boldsymbol{f}$ along $\boldsymbol{x}_B$, $\boldsymbol{y}_B$ and $\boldsymbol{z}_B$; similarly, we define m_x, m_y and m_z as the respective components of $\boldsymbol{m}$ along $\boldsymbol{x}_B$, $\boldsymbol{y}_B$ and $\boldsymbol{z}_B$.

Case 2: Independently tilting propellers In this case, by a wise change of input coordinates, from $\boldsymbol{u}$ to $\boldsymbol{u}_l$, we can transform the non-linear relation $\boldsymbol{w}(\boldsymbol{u}) = \mathbf{F}(\boldsymbol{V})\boldsymbol{u}$, into a linear one $\boldsymbol{w}(\boldsymbol{u}_l) = \mathbf{F}_l\mathbf{u}_l$. $\mathbf{F}_l$ and $\mathbf{u}_l = [u_{l,1} \ \dots \ u_{l,n_u}]^\top$ are called the augmented allocation matrix and control input, respectively. Notice that $\mathbf{F}_l$ does not depend on $\boldsymbol{u}_{\boldsymbol{V}}$.

Considering the representation of $\boldsymbol{v}_i$ by the angles α_i and β_i, the transformation of input coordinates can be described as follow:

i) For a fixed propeller, $u_{l,i}$ corresponds to $u_{\lambda,i}$.

ii) For a propeller with only radial tilting, $\mathbf{u}_{l,i} = [u_{\lambda,i}\cos(\alpha_i)\ \ u_{\lambda,i}\sin(\alpha_i)]^\top$.

iii) For a propeller with only tangential tilting, $\mathbf{u}_{l,i} = [u_{\lambda,i}\cos(\beta_i)\ \ u_{\lambda,i}\sin(\beta_i)]^\top$.

iv) For a propeller tilting in $\mathbb{S}^2$

$$\mathbf{u}_{l,i} = \begin{bmatrix} u_{\lambda,i}\sin(\alpha_i) \\ u_{\lambda,i}\cos(\alpha_i)\cos(\beta_i) \\ u_{\lambda,i}\cos(\alpha_i)\sin(\beta_i) \end{bmatrix}. \tag{2.23}$$

To find $\mathfrak{F}_1$($\mathfrak{F}_{2+}$), we define a discrete force (moment) search set as follows:

$$\begin{aligned} \mathfrak{F}^d = \{\mathbf{f}^d \in \mathbb{R}^3 | \quad & f_{x,min} \leq f_x^d \leq f_{x,max} \\ & f_{y,min} \leq f_y^d \leq f_{y,max} \\ & f_{z,min} \leq f_z^d \leq f_{z,max} \quad \}, \end{aligned} \tag{2.24}$$

$$\begin{aligned} \mathfrak{M}^d = \{\mathbf{m}^d \in \mathbb{R}^3 | \quad & m_{x,min} \leq m_x^d \leq m_{x,max} \\ & m_{y,min} \leq m_y^d \leq m_{y,max} \\ & m_{z,min} \leq m_z^d \leq m_{z,max} \quad \}, \end{aligned} \tag{2.25}$$

where the range of each force (moment) is the expected one given the platform geometry.

Let us define the desired wrench set for each case as follows:

$$\mathfrak{w}_1^d = \{\boldsymbol{w} \in \mathbb{R}^6 | \boldsymbol{w} = [\mathbf{f}_d^\top, \mathbf{0}_3^\top]^\top \ \forall \ \mathbf{f}_d \in \mathfrak{F}^d\}, \tag{2.26}$$

$$\mathfrak{w}_2^d = \{\boldsymbol{w} \in \mathbb{R}^6 | \boldsymbol{w} = [m\boldsymbol{g}^\top, \mathbf{m}_d^\top]^\top \ \forall \ \mathbf{m}_d \in \mathfrak{M}^d\}. \tag{2.27}$$

Let us consider $\mathbf{u}_d$ as the input required to exert a desired wrench $\boldsymbol{w}_d$, i.e., $\mathbf{u}_d = \boldsymbol{f}_l(\mathbf{F}_l^\dagger \boldsymbol{w}_d)$, where $\boldsymbol{f}_l$ is the map from the augmented control input to the real control input. Then $\mathfrak{F}_1$ ($\mathfrak{F}_{2+}$) is computed as the discrete set of forces(moments) such that $\boldsymbol{w}_d \in \mathfrak{w}_1^d (\boldsymbol{w}_d \in \mathfrak{w}_2^d)$ whose corresponding required input, $\mathbf{u}_d$ is feasible. In details:

$$\mathfrak{F}_1 = \{\boldsymbol{w}_d \in \mathfrak{w}_1^d | \mathbf{u}_d = \boldsymbol{f}_l(\mathbf{F}_l^\dagger \boldsymbol{w}_d) \in \mathbb{U}\}, \tag{2.28}$$

$$\mathfrak{F}_{2+} = \{\boldsymbol{w}_d \in \mathfrak{w}_2^d | \mathbf{u}_d = \boldsymbol{f}_l(\mathbf{F}_l^\dagger \boldsymbol{w}_d) \in \mathbb{U}\}. \tag{2.29}$$

Note that in the case where $n_u > 6$ the pseudo-inverse solution shown above provides one of the infinite solutions to the problem. Due to the nonlinearity in the $\boldsymbol{f}_l$ function, it is not straightforward to find if an adequate solution exists for a specific $\boldsymbol{w}_d$ where the pseudo-inverse solution deems the desired force unfeasible. As such, the corresponding $\mathfrak{F}_1$ ($\mathfrak{F}_{2+}$) solution is a conservative one, while the full solution requires the use of the solution presented below for the jointly tilted propellers.

Case 3: Jointly tilted propellers We represent $\mathfrak{F}_1$ ($\mathfrak{F}_{2+}$) as the discrete set of forces (moments) for which the numerical optimization $\|\mathbf{F}(\boldsymbol{u}_{\boldsymbol{V}})\mathbf{u}_\lambda - \boldsymbol{w}_d\|_2^2$, with the constraint $\mathbf{u} \in \mathbb{U}$ reaches a valid solution, where we limit our search space such that $\boldsymbol{w}_d \in \mathfrak{w}_1^d$ ($\boldsymbol{w} \in \mathfrak{w}_2^d$). To find such a solution, we employ a gradient-based method such as the one presented in ([Byrd–2000]).

Part II

MAV Actuation Properties and Abilities

Chapter 3

Analysis of the Relation between MRAV Properties and Abilities

---

3.1 Motivation

In this chapter we provide an overview of Multi-Rotor Aerial Vehicle (MRAV) designs from the literature while focusing on the actuation properties and abilities of each design. In particular, this chapter i) first studies more thoroughly parameters that characterize a specific Atomic Actuation Unit (AAU), ii) then introduces system property classes, which group platforms based on their actuation properties, iii) and finally, summarizes the majority of designs from the literature while providing their properties and abilities.

For the sake of classifying multirotor platforms according to the properties related to their actuation (*actuation properties*), we consider here only the design parameters directly linked to the vehicle actuation. On the other hand, we do not consider design parameters like total weight, flight electronics, power source, materials, the shape of the structure and so on. Although very important for the final development of an aerial platform, those parameters are tailored by the particular application and do not grant the platform particular properties of interest for this study.

We note that the review of the state-of-the-art in this chapter, while exhaustive is not comprehensive, where the review is to summarize the largest number of original works, while avoiding the inclusion of multiple designs that have similar actuation properties.

3.2 Platform Properties and Abilities

3.2.1 Classifying AAUs:

The parameters required to characterize AAUs, summarized in Tab. 3.1 can be understood as follows:

i) Aerodynamic parameters. The shape of the propeller is an important design factor that defines the lift and drag coefficients, i.e., c_{f_i} and c_{τ_i}, respectively. Those aerodynamic parameters impact the maximum payload and the energy consumption of the vehicle. According to the particular task, the propeller design should be optimized to meet the particular requirements. While in the formulation presented

AAU key param.	Short descrip.	Influence
Aerodynamic param.	Propeller shape	Thrust/drag coefficient
Uni or bidirectional thrust	$\underline{w}_i > 0$ or $\underline{w}_i < 0$	Thrust and drag direction
Fixed or actuated spinning axis	α fixed or actuated β fixed or actuated	Thrust vectoring
Position of O_{P_i}	${}^{B}\boldsymbol{p}_i$	Moment generation

Table 3.1 – Key parameters affecting the impact of platforms' AAUs.

in Chapt. 2 lift and drag coefficients were considered constant, they usually vary throughout their operational range. However, in most applications, propellers are operated in a range where the thrust is constantly proportional to the square of rotational velocity. We make the distinction for bidirectional propellers (propellers rotating in either direction), where the constant coefficients assumption does not hold throughout the propellers' operational range.

ii) Unidirectional or bidirectional thrust.

The second key parameter to consider is the direction of the thrust along the spinning axis. In general, the majority of Unmanned Aerial Vehicle (UAV)s in the literature are designed such that the brushless motor controllers rotate the propellers only in one direction, i.e., $0 \leq \underline{w}_i \leq w_i \leq \bar{w}_i$ where $\underline{w}_i, \bar{w}_i \in \mathbb{R}_{\geq 0}$, making the thrust *unidirectional.* Nevertheless, for some designs with particular brushless motor controllers and propeller profiles, as in ([Brescianini–2016b]), the propellers can generate thrust in both directions. In this case $\underline{w}_i \leq \omega_i \leq \bar{w}_i$ where $\underline{w}_i \in \mathbb{R}_{<0}$ and $\bar{w}_i \in \mathbb{R}_{>0}$, making the thrust *bidirectional.*

Although this solution enlarges the thrust range, it usually results in a lower thrust magnitude w.r.t. to uni-directional propellers for the same spinning velocity. In fact, it requires propeller designs that are symmetric enough to generate thrust in both directions equally.

iii) Fixed or actuated spinning axis. The third key parameter to consider for each AAU is its ability to re-orient its thrust, either actively or passively. This property can be used to change the vectoring direction of the total thrust produced by the combination of all AAUs without changing their spinning velocities.

In this case, and as was mentioned in Chapt. 2, we assume that we can control the velocity of the change of the propeller orientation instead of directly controlling its orientation. Moreover, we have realized throughout our review, that there are two patterns when it comes to the orientation of propellers via servomotors, where i) some designs use one/two servomotors specific for each propeller, and as such, the orientation of each propeller would be independent from the orientation of the other propellers, ii) while other designs use shared servomotors, and as such, the motion of each servomotor controls the orientation of multiple propellers.

3.2.2 System Properties

One of the most important characteristics of a design is the set of the admissible wrenches $\mathbb{W}$. In fact, this affects the controllability of the vehicle (how the platform can control its six Degrees of Freedom (DoF), e.g., in a coupled or independent way), and the set of reachable states. It is noted that the characterization of $\mathbb{W}$ can be deduced from the number of control inputs n_u, the corresponding subset $\mathbb{U}$, and the *full allocation matrix* $\boldsymbol{F}$. According to the properties of $\boldsymbol{F}$, and more in general of $\mathbb{W}$, we can define the following classes of multirotor aerial vehicles which are explained in detail hereafter.

i) Uni-directional thrust (UDT)

ii) Multi-directional thrust (MDT)

iii) Fully actuated (FA)

iv) Over actuated (OA)

v) Omnidirectional (OD).

The interactions between the properties of classes 1) to 5) are depicted in Fig. 3.1.

All the listed classes have properties that extend two basic properties holding for any multirotor design and listed below.

Property 1. The total moment can be varied in any direction of $\mathbb{R}^3$, i.e.,

$$\operatorname{rank}\left\{\frac{\partial \boldsymbol{m}}{\partial \boldsymbol{u}}\right\} = 3. \tag{3.1}$$

This means that for any multirotor design the orientation dynamics is always fully actuated.

Property 2. Nonzero-force and zero-moment are an interior-feasible wrench, i.e.,

$$\operatorname{int}\{\mathbb{W}\} \ni \begin{bmatrix} \bar{\boldsymbol{f}} \\ \boldsymbol{0} \end{bmatrix} \neq \begin{bmatrix} \boldsymbol{0} \\ \boldsymbol{0} \end{bmatrix}. \tag{3.2}$$

The above two properties are sufficient for the platform to re-orient itself in space, and apply a force in at least one direction to counteract its weight without applying any moment (in average), thus remaining in hovering at the equilibrium. Property 2 in particular ensures that the instantaneous change in any direction of the applied wrench around the hovering equilibrium wrench keeps always the wrench in the feasible wrench space. These properties are enough for the platform to hover in place, or to move around while being in the near-hovering mode. However, they do not guarantee any decoupling between the moment and the desired force direction. Further properties extend these two and better characterize $\mathbb{W}$, which we recall is computed by mapping $\mathbb{U}$ through the full allocation matrix $\boldsymbol{F}$. Based on the different properties we formally define the following classes.

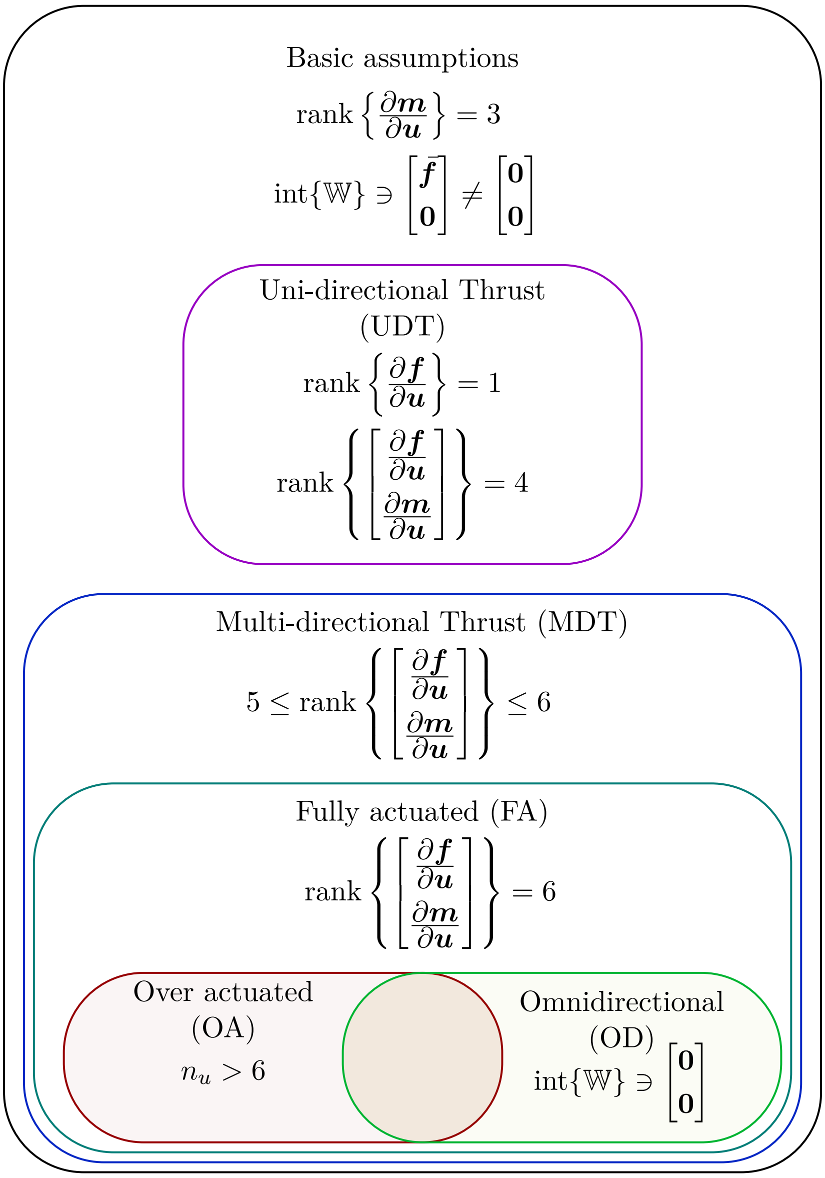

Figure 3.1 – Interaction between thrust related properties for mutlirotor designs.

Uni-directionnal thrust – UDT

This describes platforms for which the total thrust can be varied only along one direction (like, e.g., in coplanar/collinear designs). This property can be expressed as

$$\operatorname{rank}\left\{\frac{\partial \boldsymbol{f}}{\partial \boldsymbol{u}}\right\} = 1 \text{ and } \operatorname{rank}\{\boldsymbol{F}\} = 4, \quad \forall \boldsymbol{u} \in \mathbb{U}. \tag{3.3}$$

Multi-directionnal thrust – MDT

This describes platforms for which the total thrust can be varied along more than one direction independently from the total moment (see e.g., designs like ([Kawasaki–2015])) and can be expressed as

$$5 \leq \operatorname{rank}\{\boldsymbol{F}\} \leq 6, \quad \forall \boldsymbol{u} \in \mathbb{U}. \tag{3.4}$$

Fully actuated – FA

This describes a sub-class of MDT platforms, for which the total thrust can be varied along all directions independently from the total moment.

$$\operatorname{rank}\{\boldsymbol{F}\} = 6, \quad \forall \boldsymbol{u} \in \mathbb{U}. \tag{3.5}$$

Over actuated – OA

This terminology typically describes platforms for which there are more actuation inputs, n_u, than the degrees of freedom of the system. In our proposed nomenclature we limit this definition to only designs which are already FA. This means that a multirotor is OA if the total thrust can be varied along all directions independently from the total moment and with more than one input combination, i.e.,

$$\text{FA and } n_u > 6. \tag{3.6}$$

Omni directional – OD

This describes another sub-class of FA designs, not exclusive from OA, where the total thrust can assume any value in a spherical shell independently from the total moment.

$$\text{FA and } \begin{bmatrix} \bar{\boldsymbol{f}} \\ \boldsymbol{0} \end{bmatrix} \ni \operatorname{int}\{\mathbb{W}\} \; \forall \; \bar{\boldsymbol{f}} \in \operatorname{ball}_{\mathbb{R}^3}(R)/\operatorname{ball}_{\mathbb{R}^3}(r), \tag{3.7}$$

where[1] $R \geq r \geq 0 \in \mathbb{R}$, and r, R depend on the limits of the actuators.

---

[1] $\operatorname{ball}_{\mathbb{R}^3}(R)$ for a certain $R \in \mathbb{R}_{>0}$ is defined such that given a vector $\boldsymbol{x} \in \mathbb{R}^3$, $\boldsymbol{x} \in \operatorname{ball}_{\mathbb{R}^3}(R)$ if $\|\boldsymbol{x}\| \leq R$

The omnidirectional property can also be understood from the attainable wrench set $\mathbb{W}$, where the OD sub-class can be represented as follows:

$$\text{FA and } \begin{bmatrix}\mathbf{0}\\\mathbf{0}\end{bmatrix} \in \operatorname{int}\{\mathbb{W}\}. \tag{3.8}$$

Remark 3.2.1. The basic properties 1 and 2 guarantee $[\mathbf{0}^\top \ \ \mathbf{0}^\top]^\top \in \mathbb{W}$ for any platform, which can be intuitively applied by setting zero control inputs. However, conversely to an OD platform, the zero force and moment point is a boundary point of $\mathbb{W}$, i.e., while applying **0** moment, forces cannot be applied in any direction.

Remark 3.2.2. [Tognon–2018] conducted a theoretical study to characterize OD multirotors with unidirectional propellers and provide algebraic conditions to reach an OD design in the generic case of $N \geq 7$. In particular, it has been proved that for a design with unidirectional propellers, $N = 7$ is the minimal number of propellers to obtain OD. The authors found similarities between omnidirectional multirotors with unidirectional AAUs, called *omniplus* (O_+) , and frictionless contact grasping, ([SGuerrero–2018]).

Remark 3.2.3. The analysis of such properties is very important for the motion control of the vehicle. As mentioned in 2.3, the platform motion is linearly related to the control inputs through $\boldsymbol{F}$. More specifically, the linear and angular accelerations are linearly related to the control input $\boldsymbol{u}_\lambda$ through $\boldsymbol{F}$ in the case of fixed propellers, and the linear and angular jerk are linearly related to the derivative of the control input $\dot{\boldsymbol{u}}$ through $\boldsymbol{F}$.

On the other hand, if the platform is not FA, feedback linearization cannot be directly applied, and particular attention should be dedicated to the design of the control law.

While these properties reflect the ability of the platform to apply forces and moments in certain directions and combinations, it does not directly reflect its ability to maneuver, stabilize its position, or interact with its environment. These abilities are affected by the set of feasible control input $\mathbb{U}$, and by the specific design and hardware extensions added to the platform.

3.2.3 System Abilities

The system abilities are expressed w.r.t. the tasks that can be achieved by the multirotor according to its design. They are all directly related to the attainable wrench set $\mathbb{W}$. We divided these tasks in three representative categories described in the following. These encompass the variety of tasks that can be achieved by multirotor systems.

Hovering Ability

The ability to hover corresponds to the ability of the platform to stay stationary at the desired position. This represents the main advantage of multirotors over fixed-wing UAVs.

In details, in the scope of this manuscript, we define the *static hovering* as the ability of the platform to stabilize its position and orientation for some ${}^{W}\boldsymbol{R}_B \in \mathrm{SO}(3)$ with zero linear and angular velocity (i.e., $({}^{W}\boldsymbol{p}_B, {}^{W}\boldsymbol{R}_B, {}^{B}\dot{\boldsymbol{p}}_B, {}^{B}\boldsymbol{\omega}_B) = ({}^{W}\boldsymbol{p}_B, {}^{W}\boldsymbol{R}_B, \mathbf{0}, \mathbf{0})$). This can be achieved (as described in ([Michieletto–2018])) if at ${}^{W}\boldsymbol{R}_B$

$$\exists\ \mathbf{u}^* \in \mathbb{U} \text{ s.t. } \begin{cases} \boldsymbol{f}(\mathbf{u}^*) = mg\mathbf{e}_3 \\ \boldsymbol{m}(\mathbf{u}^*) = \ \mathbf{0}_3 \\ \mathrm{rank}\{\boldsymbol{F}\} \geq 4 \end{cases} . \tag{3.9}$$

Note that in the case of static hovering, it is assumed that the platform can rotate about its $\boldsymbol{z}_B$ axis, i.e., the platform is able to stabilize its orientation about the desired ${}^{W}\boldsymbol{R}_B$, in addition to any orientation

$$\{\mathbf{y} \mid \mathbf{y} = {}^{W}\boldsymbol{R}_B \mathbf{R}_{\boldsymbol{z}_B}(\gamma)\ \forall\ 0 \leq \gamma \leq 2\pi\}.$$

Finally, we define *dynamic hovering* (or relaxed hovering) as the ability of the platform to keep the position error bounded while varying its linear and angular velocity. In other words, for these platforms static hovering is not feasible, i.e., $\nexists\ \mathbf{u}^* \in \mathbb{U}$ s.t. for ${}^{W}\boldsymbol{R}_B$, $({}^{B}\dot{\boldsymbol{p}}_B, {}^{B}\boldsymbol{\omega}_B) = (\mathbf{0}, \mathbf{0})$, however, an approximate hovering is achieved through continuous movement of the platform around a given point.

Following the above definitions, we define the following categories of hovering:

H.0 hovering not possible (e.g., fixed-wing UAVs)

H.1 dynamic hovering (relaxed hovering)

H.2 hovering in a single orientation (e.g., quadrotor, if one disregards rotations about the vertical axis)

H.3 hovering in several orientations (e.g., the TiltHex design shown in ([Ryll–2017a]))

H.4 hovering in any orientation (e.g., omnidirectional UAVs).

Categories **H.2**, **H.3**, and **H.4** are subclasses of the family of platforms that can achieve static hovering, with the possible orientations spanning an increasingly large space. We remark that each ability from **H.1** to **H.4** includes the previous abilities.

Trajectory Tracking Ability

The ability to follow a trajectory is fundamental for many multirotor applications such as survey, surveillance, and delivery. We propose to categorize the trajectory tracking ability based on the type (position and orientation) and the number of DoF the multirotor can track independently. While some platforms can trade off the tracking in position for its orientation counterpart, in our classification we consider positional tracking to have a higher priority than orientation tracking. As such we consider the 3D position tracking ability as a baseline for the tracking ability classification listed below:

TT.1 Only 3D position tracking is possible. Given a desired acceleration in world frame ${}^{W}\ddot{\boldsymbol{p}}_B$, $\exists \boldsymbol{u}$ s.t. $m{}^{W}\ddot{\boldsymbol{p}}_B = {}^{W}\boldsymbol{R}_B \boldsymbol{f}(\boldsymbol{u})$ for a unique choice of ${}^{W}\boldsymbol{R}_B$.

TT.2 3D position and 1D attitude (rotation along a single axis) tracking are possible. Given a desired acceleration in world frame ${}^{W}\ddot{\boldsymbol{p}}_B$, $\exists \boldsymbol{u}$ s.t. $m{}^{W}\ddot{\boldsymbol{p}}_B = {}^{W}\boldsymbol{R}_B \boldsymbol{f}(\boldsymbol{u})$ for any ${}^{W}\boldsymbol{R}_B$ in a subset of SO(3) with dimension one.

TT.3 3D position and 2D attitude (rotations along two axes) tracking are possible. Given a desired acceleration in world frame ${}^{W}\ddot{\boldsymbol{p}}_B$, $\exists \boldsymbol{u}$ s.t. $m{}^{W}\ddot{\boldsymbol{p}}_B = {}^{W}\boldsymbol{R}_B \boldsymbol{f}(\boldsymbol{u})$ for any ${}^{W}\boldsymbol{R}_B$ in a subset of SO(3) with dimension two.

TT.4 3D position and 3D attitude (rotations along all three axes) tracking are possible. Given a desired acceleration in world frame ${}^{W}\ddot{\boldsymbol{p}}_B$, $\exists \boldsymbol{u}$ s.t. $m{}^{W}\ddot{\boldsymbol{p}}_B = {}^{W}\boldsymbol{R}_B \boldsymbol{f}(\boldsymbol{u})$ for any ${}^{W}\boldsymbol{R}_B$ in a subset of SO(3) with dimension three.

Physical Interaction Ability

We also consider the ability to physically interact with the environment, following the rising trend of Aerial Physical Interaction (APhI) in the last decade. In particular, we decided to separate the possible APhI abilities according to the following classifications:

APhI.0 APhI not possible

APhI.1 suitable for tasks like pushing/pulling

APhI.2 suitable for carrying a load

APhI.3 suitable for manipulation tasks

It should be noted that the APhI abilities require suitable hardware for the specific task, and an adequate level of force and moment decoupling. As explained in ([Michieletto–2018]), the decoupling between force and moment allows a platform to apply forces in one or more directions while applying null moment. This is a requirement to physically interact with a static environment while maintaining hoverability. It should be noted that the force-moment decoupling of a design can be derived from the study of its full allocation matrix $\boldsymbol{F}$ ([Michieletto–2018]). It should also be noted that, and to the best of the authors knowledge, the relation between the allocation matrix and the APhI ability has not been thoroughly studied in the literature, where only the relation between the force-moment decoupling and the APhI ability shown above was presented. However, interesting relations between APhI abilities and the platform's manipulability/maneuverability indexes seems natural and deserve further future study.

As the APhI ability depends not only on the platform property (e.g., full allocation matrix) but also on the externally attached hardware, for each platform, we characterize the APhI ability as demonstrated by the authors of the platform, and not as the platform can theoretically reach if adequate hardware was added to the platform.

Finally, while the level of maturity of each platform from the literature is not an ability, we do classify the level of maturity of each of the reviewed platforms as follows:

Level of Maturity

Given the vast literature on multirotor design, we decided to also stress the level of maturity to distinguish purely theoretical contributions from designs that have been constructed and tested in various scenarios. While the theoretical grounding of any design is of paramount importance, we believe that each should be tested by real experiments verifying the corresponding findings. To this goal, we include in our assessment the level of maturity of each design, where the level can be one of the following:

i) theory,

ii) simulation of the simplified model (simplistic simulation),

iii) simulation with uncertainties and/or second order effects (far from ideal simulation),

iv) prototype, and

v) product.

Results dimmed as theoretical comprise work where the analysis of the design is conducted without any simulation or prototype. On the other hand, we separate simulation proven designs into two categories, where simplistic simulations that serve as a proof of concept are distinguished from realistic ones, which include delays, noise, model discrepancies, external perturbations and so on. The latter reflects a higher degree of maturity of the work and a smaller gap to real experiments. Finally, we label as prototype any work presenting a functional prototype of the proposed design. The final level of maturity would describe designs implemented as commercial products, but we note that such occurrences are rare.

3.3 State of the Art in MAV Design

This section reviews the state-of-the-art in MRAV design from the literature. In addition to a short description of each design, demonstrating its novelty w.r.t. to the state-of-the art, throughout this review, we provide the following:

1) schematic figures that represent each reviewed design along with its actuation capabilities;

2) representative $\mathfrak{F}_1$ sets, where the presented $\mathfrak{F}_1$ sets shown serve to illustrate the different possible actuation properties;

3) summarizing tables that group designs with similar number of thrusters, and provide a quick overview of the properties and abilities possible for each of these groups.

Similarly, we group the reviewed designs based on the number of thrusters in each design to demonstrate the different properties and abilities MRAVs can achieve with each corresponding number of thrusters.

In Tab. 3.2 we summarize the platform components that we use throughout our review to show the corresponding design schematics.

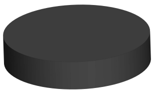	Central body
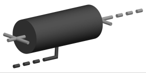	Joint
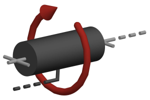	Possibly independently actuated joint
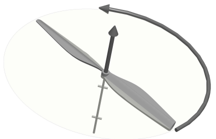	Counter clockwise (CCW) rotating propeller
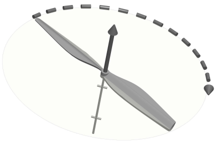	Clockwise (CW) rotating propeller
	Body with a non-tiltable propeller
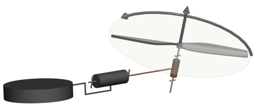	Body with a propeller tiltable radially (angle α)
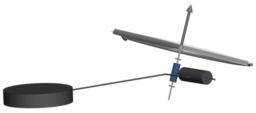	Body with a propeller tiltable tangentially (angle β)
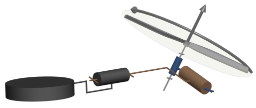	Body with a propeller tiltable in $\mathbb{S}^2$ (both angles α and β)
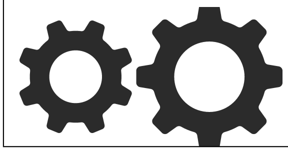	Gears indicating a coupling in the tilting of the corresponding joints

Table 3.2 – Overview of platform design components. This table summarizes the different components used to design a platform. The different component representations are used hereafter to visualize platform designs.

3.3.1 Unirotor (1 AAU)

Even though the case of a multi-rotor composed of a single AAU is a contradiction in itself, it is considered for completeness of the review; in addition, it can represent a configuration reached in the case of extreme failure of multi-rotors. To the best of the authors' knowledge, the only occurrence of such design fitting this paper scope (i.e., excluding moving mass and control surface) can be found in ([Zhang–2016]).

The proposed approach relies on active control and demonstrates a position tracking controller for such a vehicle. Due to its single rotor $n_u = 1$, the vehicle is under constant rotation, however, the prototype was shown to be able to achieve relaxed hovering. The system assessment is shown in Table 3.3.

apparition	properties	abilities	maturity
[Zhang–2016]	none	H.1, TT.1, APhI.0	prototype

Table 3.3 – Recapitulative table for $N = 1$.

3.3.2 Birotor (2 AAUs)

Birotors are composed of only two AAUs as their name suggests. For these designs, hovering can only be achieved if thrust vectoring is controlled, i.e., the total thrust is dynamically oriented during flight. The two AAUs are always rotating in opposing directions to have a zero total drag moment when the propellers spin at the same speed, thus the platform can hover without being subjected to constant rotation. In addition, in most designs, the multirotor CoM is placed between the two AAUs to benefit from a damped pendulum dynamics, such as the work in ([Chowdhury–2012]), where a wing-tail was also added for stabilization as shown in Fig. 3.2. The following designs are summarize in Tab. 3.4.

Tilting in $\mathbb{S}^2$ Designs The fist pioneer work on bi-rotor design was ([Gress–2002]), in which the inertia and gyroscopic characteristics of the multirotor are exploited to control the roll, pitch, and yaw in order to achieve a stable hover. The two AAUs are devised to be tilting in $\mathbb{S}^2$ independently, thus $n_u = 2 + 4$ as shown in Fig. 3.2. Further studies were conducted by [Kendoul–2006] and [Amiri–2011], providing the dynamic model of such designs and introducing some refinements to increase controllability. In the latter, the two AAUs generate unidirectional

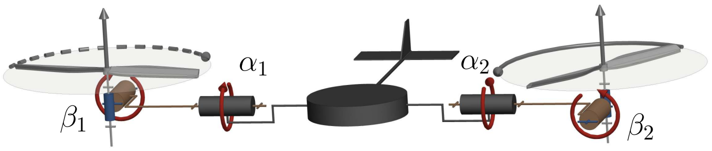

Figure 3.2 – Conceptual 3D kinematic representation of a generic birotor design with wing-tail stabilization.

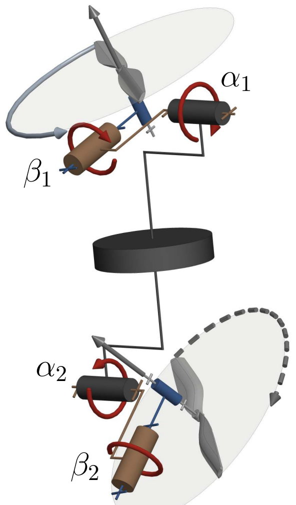

Figure 3.3 – Conceptual 3D kinematic representation of the birotor design presented in ([Prothin–2013]).

thrust actuated independently in $\mathbb{S}^2$. As the resulting dynamic model is highly non-linear and hard to exploit for control purposes, a simplified model is introduced in ([Kendoul–2006]) which allows considering backstepping approaches for control.

Another platform presenting propellers tilting in $\mathbb{S}^2$ was proposed in ([Sanchez–2008]), where the authors consider the same design as in ([Gress–2002]) (Fig. 3.2) while enforcing both AAUs to have the same tilting angles, leading to $n_u = 2 + 2$. This design reduces the computational complexity of the control while still being able to achieve hovering in the conducted experiments.

In [Prothin–2013] the authors present another design, named the 'donut', made of two AAUs aligned vertically along with the center of the multirotor frame, and can be titled independently in $\mathbb{S}^2$ as shown in Fig. 3.3, thus obtaining again $n_u = 2 + 4$. The details of the dynamical model are presented and the authors propose to leverage the tilting to use drift force and moment as control inputs.

Radial and Tangential Tilting Designs A birotor design often found in the literature is presented in [Papachristos–2011] (Fig. 3.2), where the platform has two AAUs placed on an axis above the CoM of the platform, and tilting independently radially about their axis, thus resulting in $n_u = 2 + 2$. This design provides the option to tilt its AAUs almost perpendicularly to the vertical direction, and thus the platform can generate most of its lift laterally to redirect its lift in the desired flight direction. In this design, yaw is achieved by tilting propellers about opposite α angles, roll is achieved by applying different thrust in each propeller, and pitch is achieved by tilting both propellers equally in the direction of the desired pitch, where the pitching moment is relative to the tilting angle and the vertical distance between the propellers' Center of Mass (CoM) and the platform CoM.

A similar design was shown in ([Chowdhury–2012]), where the authors propose a

apparition	n_u	DoF	properties	abilities	maturity	figure
[Gress–2002]	2+4	α_1, α_2, β_1, β_2	MDT	H.3, TT.2, APhI.0	prototype	Fig. 3.2
[Kendoul–2006]						
[Amiri–2011]						
[Sanchez–2008]	2+2	(α_1, α_2) (β_1, β_2)	UDT	H.2, TT.2, APhI.0	prototype	Fig. 3.2
[Donadel–2014]	2+2	β_1, β_2	UDT	H.2, TT.2, APhI.0	realistic simulation	Fig. 3.2
[Prothin–2013]	2+4	α_1, α_2, β_1, β_2	MDT	H.3, TT.2, APhI.0	prototype	Fig. 3.3
[Papachristos–2011]	2+2	α_1, α_2	UDT	H.2, TT.2, APhI.0	prototype	Fig. 3.2
[Chowdhury–2012]	2+2	α_1, α_2	UDT	H.2, TT.2, APhI.0	simplistic simulation	Fig. 3.2
[Blouin–2014]	2+2	α_1, α_2	UDT	H.2, TT.2, APhI.0	prototype	Fig. 3.2
[Cardoso–2016]	2+2	α_1, α_2	UDT	H.2, TT.2, APhI.0	realistic simulation	Fig. 3.2

Table 3.4 – Recapitulative table for the reviewed birotors ($N = 2$).

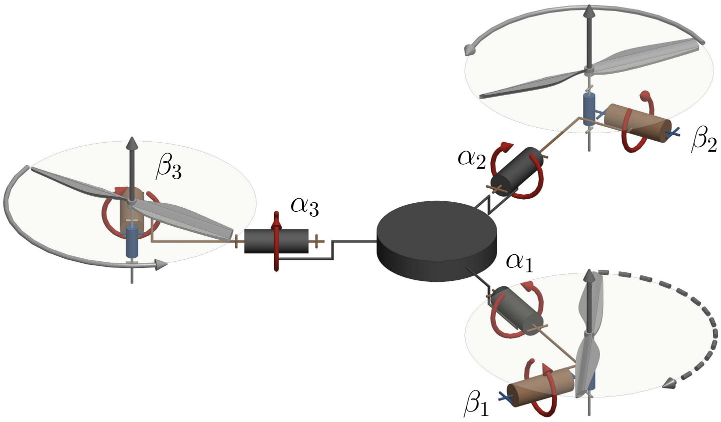

Figure 3.4 – Conceptual 3D kinematic representation of a generic trirotor Δ-configuration design.

controller that changes the tilt angles to achieve desired roll and yaw independently and demonstrate their controller in simulation. Another such controller was proposed in ([Blouin–2014]), however, they test their controller on a prototype. Finally, [Cardoso–2016] present a robust controller for this platform design and showed its path tracking ability in a realistic simulation under external disturbances and model uncertainties.

In ([Donadel–2014]) the authors propose a design where the tangential tiltings are fixed and the two radial tiltings are actuated, hence, again, $n_u = 2 + 2$, with propellers' CoM also above the CoM of the platform as shown in Fig. 3.2 . They propose a control approach relying on optimal H_∞/H_2 techniques, which they validated in realistic simulations.

3.3.3 Trirotor (3 AAUs)

Trirotors are composed of three AAUs. As such, can be considered as an upgrade from birotors, but they pose a challenge due to the unbalanced moment caused by the odd number of propellers. In addition, and similarly to birotors, the few number of actuators imposes limitations on the achievable performance, in particular in the ability to perform stable hovering ([Kataoka–2011]).

One of the first trirotor designs appeared in ([Rongier–2005]), where propellers are tilted at a fixed angle so that a non-collinear thrust is ensured. The control is based on a combination of aircraft gyroscopic effect with a piezosensor to detect the tilt angle (pitch and roll) with respect to the horizontal orientation. However, the lack of control of the yaw angle forces the rotor to constantly rotate about its CoM, thus being unable to achieve the basic static hovering ability (**H.2**). The design is demonstrated on a prototype powered with a cable and shown in Fig. 3.4; as the platform constantly rotates, it stretches the cable causing a failure of the proposed controller.

Multiple designs have been later proposed in the literature that aim to balance the odd shape of the trirotor, which we group into *T-configurations* and Δ-

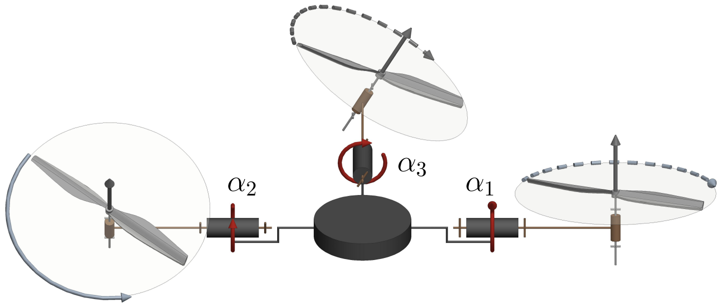

Figure 3.5 – Conceptual 3D kinematic representation of a generic trirotor T-configuration design. The tail propeller (typically smaller and weaker) is depicted on the top while the frontal principal propellers (typically larger and stronger) are on the bottom. The sagittal axis points down in the picture.

configurations. In addition, to overcome the limitation of the number of actuators, which are not enough to achieve the basic **H.2**, several works have proposed to add one or more additional actuators in order to achieve thrust-vectoring, thus making the platform able to gain the **H.2** ability.

T-Configuration This setup is composed by two frontal *principal propellers*, that may be dynamically tilted or fixed, spinning in opposite directions, with a third propeller (typically smaller) mounted on a *tail* as shown in Fig. 3.5. This one, in general, tilts around the radial axis in order to improve pitch and yaw control.

Tail-only tilting propeller this design was presented in ([SalazarCruz–2005]), followed by ([SalazarCruz–2009]). The *tail-propeller* is endowed with a servo motor which allows the control of the yaw motion by tilting about the sagittal axis, and the pitch angle regulating the propeller rotational speed. The two main frontal fixed propellers are in charge of the control of total thrust and roll angle. In total we have $n_u = 3 + 1$. The $\mathfrak{F}_1$ set of this design is represented in Fig. 3.6.

In the mentioned works, the hovering and the forward flight control of this vehicle were achieved using a nonlinear controller based on nested saturations. The same design is instead controlled in ([Yoon–2013]) with an optimal LQR to control the attitude. All these works have been validated with an experimental prototype.

Frontal-propeller tilting In a design presented in ([Papachristos–2013; Papachristos–2014; Papachristos–2016]), the two frontal principal propellers are also able to tilt radially with the same (locked) tilting angle, while the tail rotor can tilt independently, thus obtaining $n_u = 3 + 2$. This approach was adopted to allow the vehicle to apply a push-force (APhI.1) in the sagittal direction. To improve the control scheme and platform stability, in ([Papachristos–2016]) an MPC (Model Predictive Control) approach was implemented.

A commercially available T-configuration trirotor is the *Cerberus Tilt-Rotor*[2].

---

[2] http://skybornetech.com/

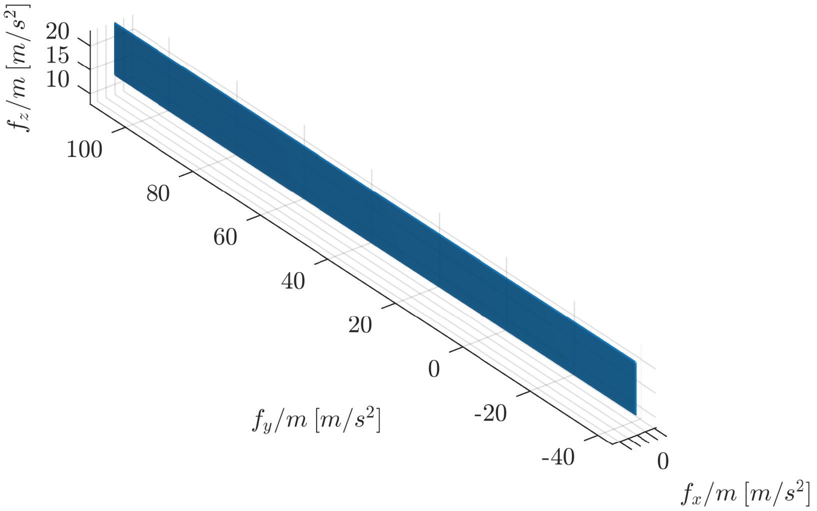

Figure 3.6 – Visualization of the $\mathfrak{F}_1$ set of the design presented in ([SalazarCruz–2009]) normalized by the platform mass. T-shaped trirotor with tail tilting radially and with two fixed main propellers. $N = 3$ and $n_u = 3 + 1$. Profile description: 2D plane perpendicular to the tail rotation plane.

In this product the two frontal principal propellers can tilt radially independently, while the tail propeller is fixed, thus obtaining again $n_u = 3 + 2$. However, its kinematics is different than the previous one. The $\mathfrak{F}_1$ set of the Cerberus Tilt-Rotor is similar to the $\mathfrak{F}_1$ set represented in Fig. 3.6.

Δ-Configuration This design is composed of three propellers of the same dimension arranged on a triangle, with two of them spinning in opposite directions. In addition, in these configurations the thrust is roughly shared equally by all three motors, encouraging the symmetrical placement of the motors on a circle (i.e., every $2\pi/3$) as shown in Fig. 3.4.

One example design was presented in ([Escareno–2008]), where the authors built a $\Delta-$configuration multirotor with all propellers being allowed to tilt radially with the same angle, thus obtaining $n_u = 3 + 1$. While the propellers' tilting is used to directly control the yaw motion, its effect on pitch and roll behavior is compensated as a disturbance. The overall control system is robust with respect to dynamic couplings, in particular gyroscopic effects, and shows a maneuverability similar to that of a quadrotor but with a more compact design as well as a longer autonomy, thanks to the fewer number of motors.

Another $\Delta-$configuration design was presented in [Mohamed–2012], where each propeller can be titled independently in its radial direction in a range of $[-\pi/2, \pi/2]$, thus obtaining $n_u = 3 + 3$. The resulting is a fully actuated vehicle, controlled with

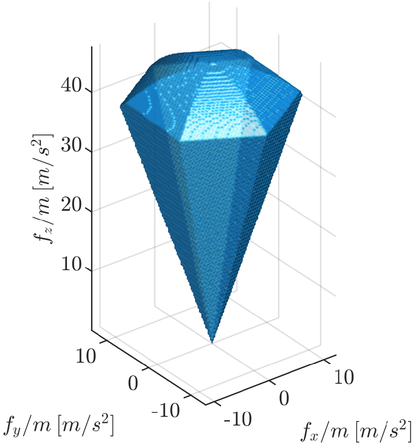

Figure 3.7 – Visualization of the $\mathfrak{F}_1$ set of a $\Delta-$trirotor normalized by the platform mass, where the platform has independent radial tilting of all three propellers; tilting angle limits are chosen at ±30°. $N = 3$ and $n_u = 6$. Profile description: hexagonal pyramid with the tip at zero and with top enclosed with a dome.

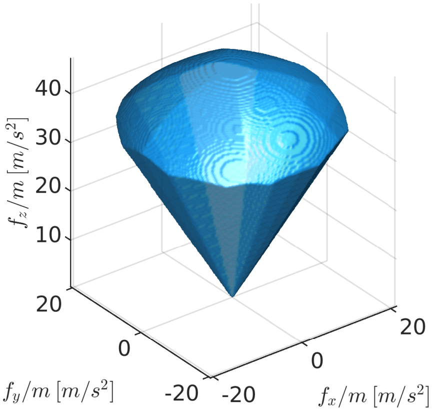

Figure 3.8 – Visualization of the $\mathfrak{F}_1$ set of the design presented in ([Ramp–2015]) normalized by the platform mass. The design consists of a $\Delta-$trirotor with all propellers independently tilting both radially and tangentially; tilting angle limits are chosen at ±30°. $N = 3$ and $n_u = 9$. Profile description: dodecagonal pyramid with the tip at zero and with top enclosed with a dome.

apparition	n_u	DoF	properties	abilities	maturity	figure
[Rongier–2005]	3			H.1, TT.1, APhI.0	prototype	Fig. 3.4
[SalazarCruz–2005]	3+1	α_3	UDT	H.2, TT.2, APhI.0	prototype	Fig. 3.5
[SalazarCruz–2009]						
[Yoon–2013]						
[Papachristos–2013]	3+2	(α_1, α_2), α_3	MDT	H.2, TT.2, APhI.1	prototype	Fig. 3.5
[Papachristos–2014]						
[Papachristos–2016]						
Cerberus RC Tilt-Rotor	3+2	α_1, α_2	MDT	H.3, TT.3, APhI.0	product	Fig. 3.5
[Escareno–2008]	3+1	$(\alpha_1,\alpha_2,\alpha_3)$	UDT	H.2, TT.2, APhI.0	prototype	Fig. 3.4
[Mohamed–2012]	3+3	$\alpha_1,\alpha_2,\alpha_3$	FA	H.3, TT.4, APhI.0	simplistic simulation	Fig. 3.4
[Kastelan–2015]	3+3	$\alpha_1,\alpha_2,\alpha_3$	FA	H.3, TT.4, APhI.0	prototype	Fig. 3.4
[Servais–2015b]	3+3	$\alpha_1,\alpha_2,\alpha_3$	FA	H.3, TT.4, APhI.0	prototype	Fig. 3.4
[Servais–2015a]						
[Ramp–2015]	3+6	$\alpha_1,\alpha_2,\alpha_3$, β_1,β_2,β_3	OA	H.3, TT.4, APhI.0	realistic simulation	Fig. 3.4

Table 3.5 – Recapitulative table for the reviewed trirotors ($N = 3$).

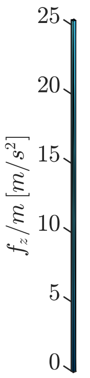

Figure 3.9 – Visualization of the $\mathfrak{F}_1$ set of a fixed coplanar/collinear quadrotor design normalized by the platform mass. $N = 4$ and $n_u = 4$. Profile description: line along the CoM of the platform.

H_∞ loop shaping, and achieving full-pose tracking. Similar designs were studied in ([Kastelan–2015]), ([Servais–2015b]), and ([Servais–2015a]), and the $\mathfrak{F}_1$ set of such designs is represented in Fig. 3.7.

On the other hand, [Ramp–2015] present an overactuated system, where each of the three propellers is allowed to rotate independently in both its tangential and radial directions, thus obtaining $n_u = 3 + 6$. This overactuated system was tested in a realistic simulation, where it proved its ability to achieve full-pose tracking, and we provide its $\mathfrak{F}_1$ set in Fig. 3.8. To find the desired thrust and orientations, the controller is designed to find the desired force vector for each propeller indepentently, which is then achieved by reorienting the propeller to the desired direction and applying the desired thrust.

Table 3.5 summarizes all the presented designs.

3.3.4 Quadrotor (4 AAUs)

This case is of particular interest because for designs with fixed AAUs, $N = 4$ is the minimum number of propellers necessary to achieve the basic actuation assumptions summarized in Eq. (3.1) and Eq. (3.2), in addition to the UDT property and the static hovering ability **H.2**.

The first documented quadrotor design in the literature traces back to 1907 and documented in ([Young–1982]). While this design recorded a few tethered flights, the modern quadrotor design ([Pounds–2002]) traces its origin back to the same platform concept, however, technological advancements within the last century has allowed new platforms to be built with compact electronics and sensors, allowing robust and agile maneuvers.

While the first designs relied on a coplanar/collinear propeller configuration, later modifications were conducted to extend the system properties via thrust-vectoring. All the presented designs consider the AAUs and the CoM to be located roughly on the same plane. We refer to Table. 3.6 as a summary of the presented designs.

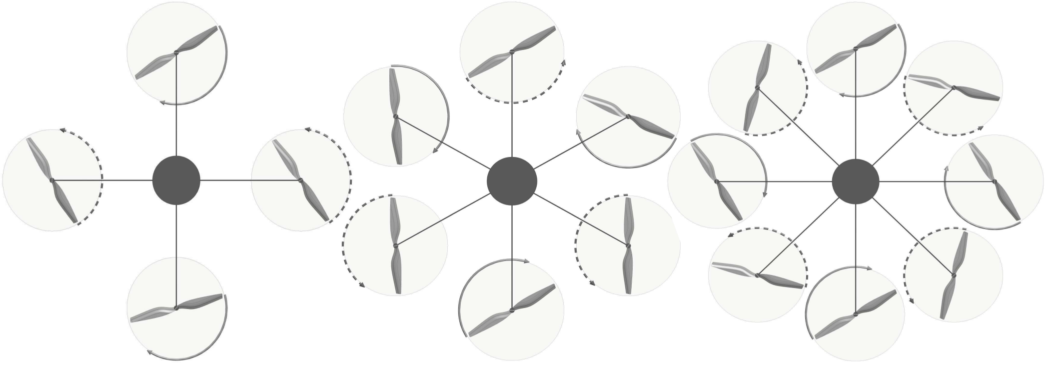

Figure 3.10 – Top view of the conceptual kinematic representation of coplanar/collinear designs with (left to right) 4/6/8 propellers.

Coplanar/collinear Designs For modeling, control and the general theory of classical coplanar/collinear designs one can refer to ([Mahony–2012; Bouabdallah–2004; Bouabdallah–2005; Pounds–2010]), which are three comprehensive references among the vast literature of such designs. We present an example of $\mathfrak{F}_1$ set of such designs in Fig. 3.9. Note that the designs with less than 4 AAUs cannot obtain such nice mono-dimensional shape (UDT ability) because they need at least a tilting rotor to achieve static hovering (H.2). This makes the coplanar/collinear quadrotor the simplest platform of its kind, i.e., with a minimum number of total inputs (servo- and brushless motors) that has decoupled force and moment spaces. Such decoupling significantly simplifies the control problem and is one of the reasons for the success of quadrotors.

Note that the wide attention gathered by coplanar/collinear quadrotors comes from the combination they offer between their simple mechanics and relative easiness of control for trajectory tracking, thanks to the dynamic feedback linearizability (or, equivalently, the differential flatness) of the nonlinear system dynamics ([Mistler–2001]).

This enabled a vast set of applications for coplanar/collinear designs. Innovative modular designs such as the one presented in ([Zhao–2017]), exhibit the same properties as classical coplanar/collinear designs, although they lie outside the scope of this paper due to their varying CoM with each new configuration.

Additionally, coplanar/collinear designs for $N > 4$, shown in Fig. 3.10, (typically $N = 6$ or $N = 8$) will not be discussed hereafter as their properties are the same as the $N = 4$ case. Their coplanar/collinear distribution leads to similar results for all such designs despite the increase of the control inputs. The only notable differences are i) the increase of the control authority due to the increase of AAUs, which translates mostly in an increase of payload, and ii) the possible redundancy, i.e., AAUs failure can be mitigated while preserving the quadrotor properties.

Radial Tilting Designs Some designs consider AAUs which are radially tilted/tilting in order to achieve total thrust vectoring for quadrotors as shown in Fig. 3.11. Within the other two tilting directions, this particular design can be

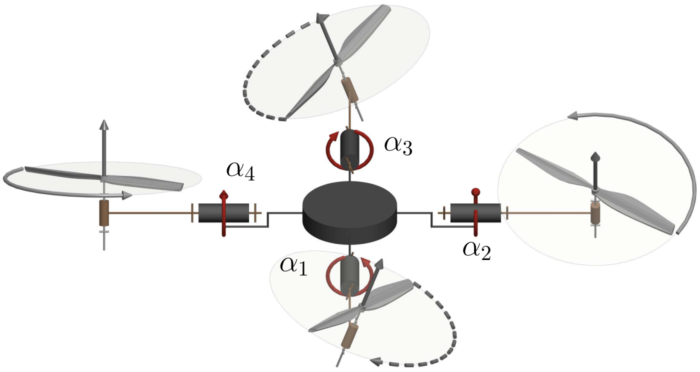

Figure 3.11 – Conceptual 3D kinematic representation of a generic quadrotor with propellers tilting/tilted about their radial axes.

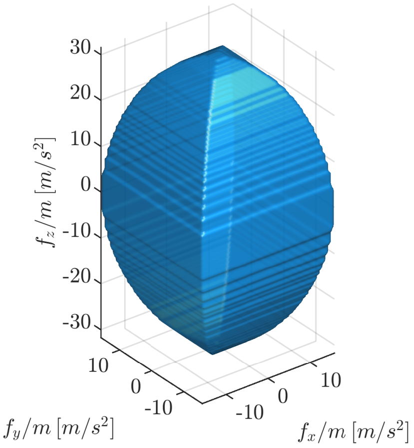

Figure 3.12 – Visualization of the $\mathfrak{F}_1$ set of the design presented in ([Ryll–2012]) normalized by the platform mass. The design consists of a quadrotor with all propellers independently tilting about their corresponding radial axis. $N = 4$ and $n_u = 8$.

considered as the simplest mechanical extension to the coplanar/collinear design achieving thrust vectoring.

[Falanga–2017] presents a quadrotor with propellers tilted 15° radially about their relative axes, i.e., $n_u = 4$. The tilt angle is computed to increase yaw-control, and was tested on a prototype flying through a narrow gap. Fig. 3.11 most closely resembles the described design, however, with the propellers' tilt being constant.

[Ryll–2012] proposed a configuration, further analyzed in ([Ryll–2013]) and ([Ryll–2015a]), where four additional servomotors are used to independently radially tilt the AAUs, thus obtaining $n_u = 4 + 4$, resulting in an over-actuated system, with the corresponding $\mathfrak{F}_1$ set presented in Fig. 3.12. By considering the servo dynamics and the aerodynamic effects, the authors derive and propose a highly coupled system, which proves difficult to manage from a control point of view. To mitigate these shortcomings, the classical approach neglects the servo-motor dynamics and assumes the employment of high gain controllers which can achieve instantaneous tracking. In addition, the aerodynamic effects are modeled in the controller as external disturbances. These simplifications allow the use of feedback linearization techniques with dynamic extension, for a desired trajectory tracking of class $\mathcal{C}^3$. The system's overactuation is dealt with a pseudo-inverse allocation, that is used to obtain a minimum energy thrust generation. The design and corresponding controller have been validated through simulation and experimental implementation.

In ([Falconi–2012]) a similar design was considered with the implementation of an inverse dynamic controller, to compensate for the nonlinear dynamics, and a PD with feedforward to impose a position and attitude trajectory. Similarly to [Ryll–2015a], [Falconi–2012] solved the allocation problem using a pseudo-inverse approach. This approach is more sensitive to model uncertainty due to the complexity of the aerodynamic modeling.

In ([Oosedo–2016]), the authors study a wide range of platform orientations in addition to the transition from horizontal to vertical hovering of the multirotor. Position and orientation are regulated through a PID loop while control allocation techniques for two orientation sets are proposed and experimentally validated.

In ([Yih–2016]) the authors considered the same design subjected to model uncertainties. They propose a robust sliding mode controller for position and orientation tracking, augmented with a chattering suppression block to improve its performance. The proposed model and control law were validated in simulation.

In ([Nemati–2014]) similar radial tilting of the AAUs is considered while constraining paired AAUs to tilt the same angle in opposing directions, thus obtaining $n_u = 4+2$. This results in a fully actuated system (non-overactuated). A trajectory tracking goal has been achieved by PD regulators. In ([Nemati–2016]) the described design is built and tested.

Tangential Tilting Designs Another attempt at extending the classical quadrotor design is to consider tangential tilting of the AAUs, see Fig. 3.13, as in ([Badr–2016]), which has also $n_u = 4 + 4$. To maintain the moment balanced, the AAUs rotation direction is non-standard. Indeed usually CW and CCW AAUs are alternating along the four summits of their square distribution, but in this proposed design they are grouped two by two. This choice allows to have more control au-

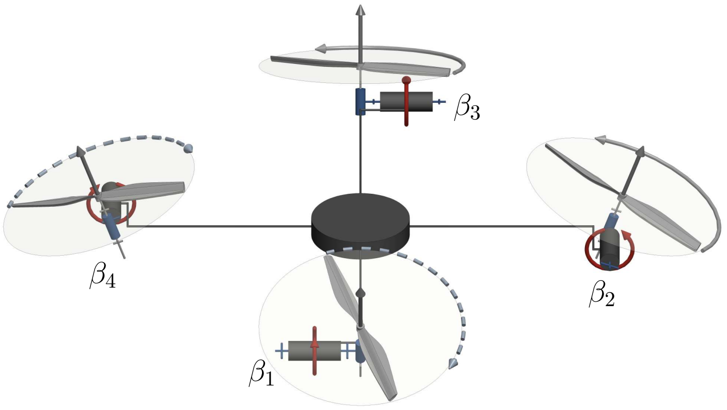

Figure 3.13 – Conceptual 3D kinematic representation of a generic quadrotor with propellers tilting/tilted about their tangential axes.

thority for pitch and roll motions while decoupling roll from the y-translation and pitch from the x-translation. In ([Badr–2016]), the authors develop a controller that resorts to simplifying assumptions based on the trajectory characteristics. This control is tested for a simple trajectory in simulation to validate the decoupling between rotational and translational dynamics. A similar design to the latter was presented by [Devlin–2018], with each propeller rotating independently in the tangential direction, thus obtaining again $n_u = 4 + 4$. The platform is named *ElbowQuad*. The design was tested via real experiments on a prototype of the design.

In ([Scholz–2016]), the authors also study the design shown in Fig. 3.13. To control the platform they synchronized the rotational speed of each of the four AAUs, then derive an input allocation scheme based on heuristics and propose a backstepping approach. The controller tracks the desired orientation, altitude and velocity in the plane, and is robust to unmodeled dynamics. The authors rely on optimization techniques to tune the controller gains. This approach is corroborated with simulation comprising sensor noise.

Another design with tangential tilting of the AAUs can be found in ([Long–2012]), with $n_u = 4 + 4$, and ([Long–2014]), with $n_u = 4 + 3$, named *Omnicopter*. The latter is shown in Fig. 3.14. In this proposed design one main AAU (with either one or two propellers sharing the same axis of rotation with opposed rotation directions) is significantly bigger than the other propellers and is placed in the center of the platform with its thrust direction aligned with the $\boldsymbol{z}_B$ axis of the body frame. The other three AAUs, smaller in size, are distributed around the main one in a triangular distribution and allowed to tilt tangentially.

In ([Long–2012]) a backstepping approach and PID loop are used to achieve decoupled tracking of both orientation and position. The control allocation is achieved by considering a linearization of the system around the functioning point. In ([Long–2014]) the authors proposed the same design with only one central AAU to improve the efficiency of the design. They apply the same control technique for the second design and validate both designs via real experimentations on a prototype.

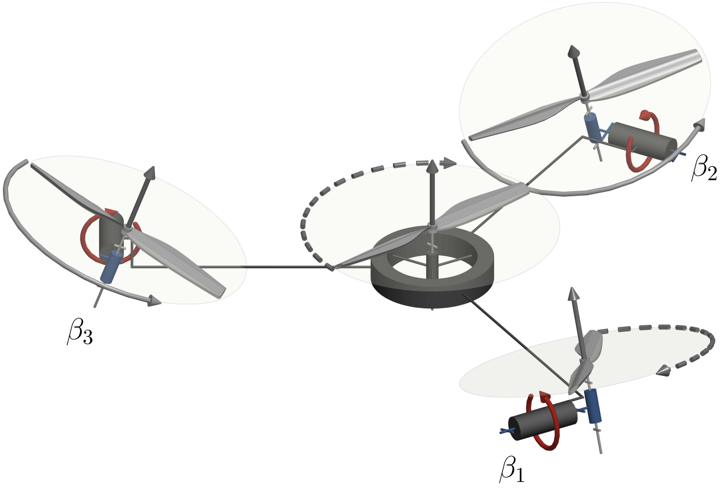

Figure 3.14 – Conceptual 3D kinematic representation of the quadrotor design presented in ([Long–2012; Long–2014]). The three non-central propellers are tilting about their tangential axes independently.

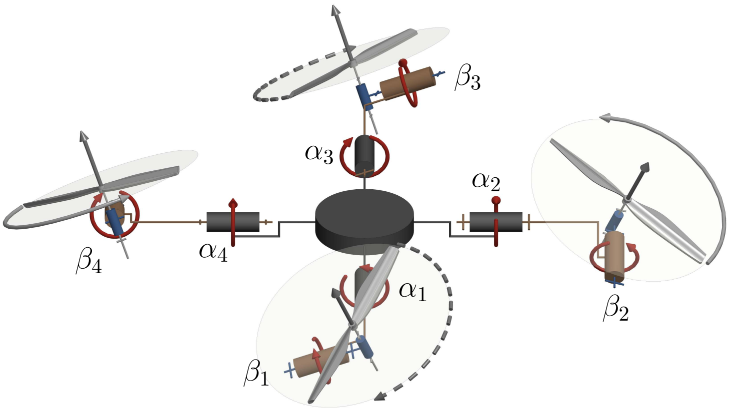

Figure 3.15 – Conceptual 3D kinematic representation of a generic quadrotor with propellers tilting/tilted in $\mathbb{S}^2$, i.e., about both the radial and tangential axes.

Tilting in $\mathbb{S}^2$ Designs The following designs explore the AAUs tilting in $\mathbb{S}^2$ as illustrated in Fig. 3.15, in order to achieve thrust vectoring in all directions for each AAU. Note that due to the mechanical complexity involved in such a design, most of the presented work considering non-fixed AAUs are only theoretical studied.

The first original design can be found in ([Şenkul–2013]) and ([Şenkul–2014]), where the authors consider a classical quadrotor with each AAU being able to tilt both radially and tangentially. In the first work the authors consider all AAUs to tilt independently while rotating at the same speed, hence $n_u = 1 + 8$. Then the full potential of this design is exploited in ([Şenkul–2014]), where the authors allow independent tilting of the propellers, $n_u = 4 + 8$. The authors propose a cascaded PID control loop with adaptive gains to account for the gyroscopic effect arising from the propellers. The above two approaches are validated with simple simulations to show their trajectory tracking ability.

Similarly to [Şenkul–2013], [Hua–2015] propose to study a quadrotor tilting in $\mathbb{S}^2$ as shown in Fig. 3.16, such that the total thrust vectoring is achieved by tilting each AAU equally in the same thrust direction. This scheme allows the platform to apply uni-directional thrust but in a direction that is tiltable in $\mathbb{S}^2$ thus obtaining $n_u = 4 + 2$. The authors propose a control scheme that primarily tracks a reference position or velocity (similar to a coplanar/collinear quadrotor with fixed propellers), then rotates the thrust direction to point in the desired orientation. Position and orientation are proved to be decoupled, which is validated in a simple trajectory tracking simulation.

The same design shown in Fig. 3.16 is explored in ([Odelga–2016]), with the addition of an explicit mechanism design that enforces the angles to rotate equally, while in ([Hua–2015]) it was only theoretically assumed. Full-actuation allows using a standard feedback linearization control with dynamic extension, which is validated by simulation. The introduction of a real mechanism makes explicit the constraints induced by the mechanism limits. Therefore, tracking performances are limited by unidirectional rotors and tilt angle limits, despite the full actuation nature of the design.

[De Martini–2017] also present a quadrotor design with propellers tilting synchronously in $\mathbb{S}^2$ as shown in Fig. 3.15. The synchronization allows the vehicle to fly across a narrow passage, where each pair of propellers are assumed to be tilting about a given axis, with $n_u = 4 + 2$. Furthermore, bidirectional AAUs are considered and physical mechanism constraints are neglected. The proposed control scheme is based on PID and model inversion and validated in a simple simulation. The multirotor orientation is computed in order to allow the navigation through the narrow passage geometry.

The above contributions presented analysis and simulations studying quadrotors with propellers tilting in $\mathbb{S}^2$. In what follows we introduce the contributions that presented a working mechanical system with propellers either tilting in $\mathbb{S}^2$, or tilted about a fixed orientation throughout their flight.

In ([Khoo–2017]), the authors implement a design as shown in Fig. 3.15 that allows independent rotation of all propellers, thus obtaining $n_u = 4 + 8$. The prototype is controlled with a multi-surface sliding mode controller, followed by a pseudo-inverse control allocation.

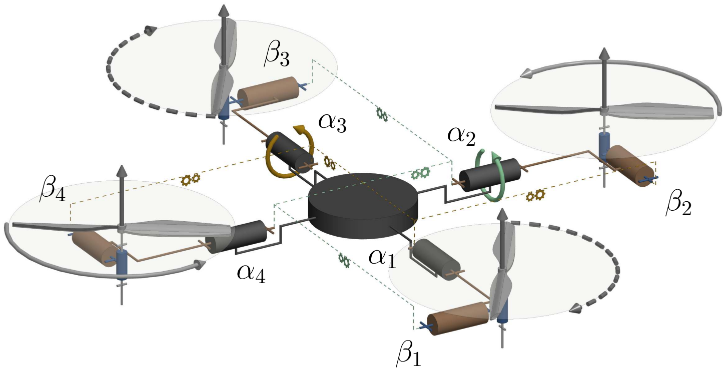

Figure 3.16 – Conceptual 3D kinematic representation of the quadrotor with propellers tilting/tilted in $\mathbb{S}^2$ presented in ([Hua–2015; Odelga–2016]). Highlighted the locked tilting that makes all the propellers point always in the same direction.

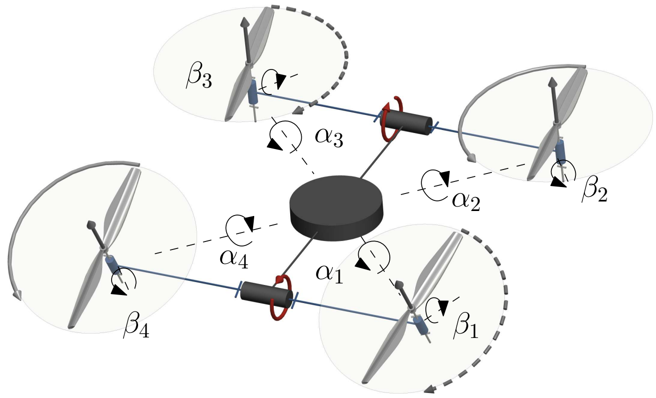

Figure 3.17 – Conceptual 3D kinematic representation of the quadrotor with propellers tilting in $\mathbb{S}^2$ as presented in ([Kawasaki–2015]).

In ([SeguiGasco–2014]) the authors also build a prototype, while considering tilting limits of each AAU in its control. The dynamics of the system are derived while considering the gyroscopic moment produced by the fast tilting AAUs. The authors consider a coplanar/collinear quadrotor controller, with body orientation and total thrust calculated through system linearization and weighted pseudo-inverse. The over-actuation of the system calls for control allocation, which is calculated in an energy-optimal way. The authors validated their approach with a hovering maiden flight, and their design analysis suggested the need for high inertia propellers to increase the produced torque and allow higher vehicle speeds.

Another design with the AAUs tilting in $\mathbb{S}^2$ can be found in ([Kawasaki–2015]), where the authors propose a design such that the AAUs are tilted independently by pairs as shown in Fig. 3.17, where we can see that each pair of propellers are connected to a single axis actuated with a servomotor that can induce an equivalent

apparition	n_u	DoF	properties	abilities	maturity	variety of figure
[Mahony–2012]	4		UDT	H.2, TT.2, APhI.2	product	
[Bouabdallah–2004]						
[Bouabdallah–2005]						
[Falanga–2017]	4		UDT	H.2, TT.2, APhI.0	prototype	Fig. 3.11
[Ryll–2012]	4+4	α_1,α_2,α_3,α_4	OA/OD	H.3, TT.4, APhI.0	prototype	Fig. 3.11
[Ryll–2013]						
[Ryll–2015a]						
[Falconi–2012]	4+4	α_1,α_2,α_3,α_4	OA	H.3, TT.4, APhI.0	simplistic simulation	Fig. 3.11
[Oosedo–2016]	4+4	α_1,α_2,α_3,α_4	OA	H.3, TT.4, APhI.0	prototype	Fig. 3.11
[Yih–2016]	4+4	α_1,α_2,α_3,α_4	OA	H.3, TT.4, APhI.0	realistic simulation	Fig. 3.11
[Nemati–2014]	4+2	(α_1,α_3),(α_2,α_4)	FA	H.3, TT.4, APhI.0	prototype	Fig. 3.11
[Nemati–2016]						
[Badr–2016]	4+4	β_1,β_2,β_3,β_4	FA	H.3, TT.4, APhI.0	simplistic simulation	Fig. 3.13
[Devlin–2018]	4+4	β_1,β_2,β_3,β_4	OA	H.3 TT.4 APhI.1	prototype	Fig. 3.13
[Scholz–2016]	4+2	(β_1,β_2),(β_3,β_4)	FA	H.3, TT.4, APhI.0	simplistic simulation	Fig. 3.13
[Long–2012]	4+4	β_1,β_2,β_3	FA	H.3,TT.4, APhI.0	prototype	Fig. 3.14
[Long–2014]	7	β_1,β_2,β_3				
[Şenkul–2013]	1+8	α_1,α_2,α_3,α_4,β_1,β_2,β_3,β_4	UDT	H.2, TT.2, APhI.0	simplistic simulation	Fig. 3.15
[Şenkul–2014]	4+8	α_1,α_2,α_3,α_4,β_1,β_2,β_3,β_4	OA	H.2, TT.2, APhI.0	simplistic simulation	Fig. 3.15
[Hua–2015]	4+2	(α_1,α_2,α_3,α_4),(β_1,β_2,β_3,β_4)	FA	H.4, TT.4, APhI.0	simplistic simulation	Fig. 3.16
[Odelga–2016]						
[De Martini–2017]	4(Bi)+2	(α_1,α_2,β_1,β_2),(α_3,α_4,β_3,β_4)	FA	H.4, TT.4, APhI.0	simplistic simualtion	Fig. 3.15
[Khoo–2017]	4+8	α_1,α_2,α_3,α_4,β_1,β_2,β_3,β_4	OA	H.3, TT.4, APhI.0	prototype	Fig. 3.15
[SeguiGasco–2014]	4+8	α_1,α_2,α_3,α_4,β_1,β_2,β_3,β_4	OA	H.3,TT.4, APhI.0	prototype	Fig. 3.15
[Kawasaki–2015]	4+2	(α_1,α_3,β_1,β_3),(α_2,α_4,β_2,β_4)	MDT	H.3, TT.3, APhI.1	prototype	Fig. 3.17
[McArthur–2017]	4+1	α_1	MDT	H.2, TT.2, APhI.1	prototype (partially tested)	Fig. 3.18

Table 3.6 – Recapitulative table for the reviewed quadrotors ($N = 4$).

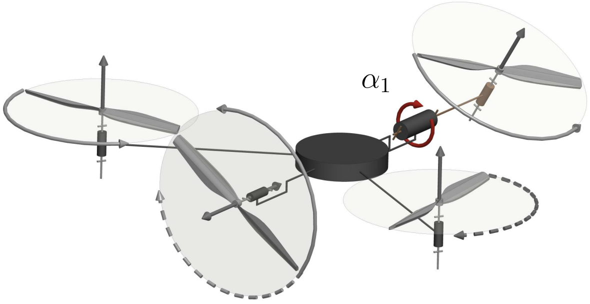

Figure 3.18 – Conceptual 3D kinematic representation of the quadrotor with propellers tilting/tilted radially/tangentially as presented in ([McArthur–2017]).

tilt in both α and β to both propellers, i.e., $n_u = 4 + 2$. The authors propose a control scheme for trajectory tracking which takes into account the effect of the AAUs' airflow interference. The performance of the platform is demonstrated with a prototype while sliding along a surface.

In ([McArthur–2017]) the authors present a quadrotor design based on the composition of a $\Delta-$trirotor (see section Sec. 3.3.3) with an additional tail propeller tangentially tilted to provide thrust in a lateral direction as shown in Fig. 3.18. The design is endowed with this extra propeller to help push an object. All propellers in this design are fixed, except for the trirotor tail which is actively tilted radially, $n_u = 4 + 1$. The proposed design was implemented in a prototype used to validate the extra push abilities in a planar experiment (APhI.1) without flying; in this experiment, the coplanar/collinear propellers were turned off, and an extra propeller was added to control the yaw just during these experiments.

While the quadrotor design was exploited extensively in the literature and allowed platforms to reach OA/OD, the limited number of propellers does not allow the platforms to exhibit more than UDT and **H.2** without any servomotors. While quadrotors are still very popular, many papers from the literature exploit designs with $N > 4$ to exploit actuation properties higher than UDT, especially for applications of APhI, where lateral forces are often required.

3.3.5 Pentarotor (5 AAUs)

The case of $N = 5$ AAUs is not commonly found in the literature, due to its lack of symmetry implied by the odd number of AAUs. Usually, symmetric designs are favored thanks to their ease of control and diagonal inertia matrix.

The only documented non-coplanar/collinear pentarotor design we could find is introduced in ([Albers–2010]) and can be described as a classical coplanar/collinear quadrotor with the addition of a propeller oriented in an orthogonal direction to

apparition	n_u	properties	abilities	maturity	figure
[Albers–2010]	5	MDT	H.3, TT.3, APhI.1	prototype	Fig. 3.19

Table 3.7 – Recapitulative table for the reviewed pentarotor ($N = 5$).

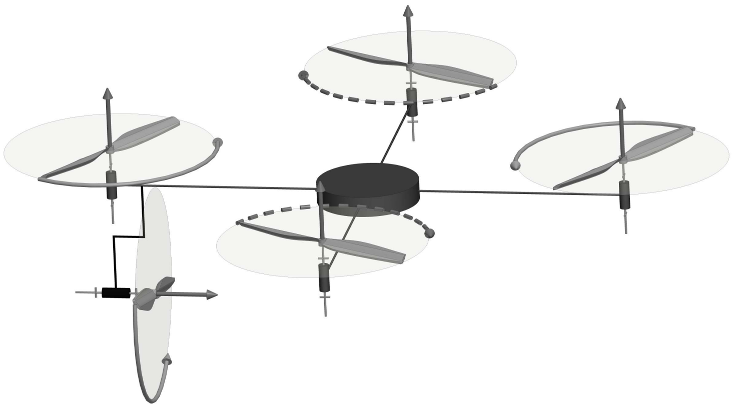

Figure 3.19 – Conceptual 3D kinematic representation of the pentarotor design presented in ([Albers–2010]).

provide extra actuation for attaining the considered tasks; a conceptual design sketch is shown in Fig. 3.19, and the design properties and abilities are listed in Tab. 3.7. The goal is to be able to easily apply a normal force on a wall for tasks such as inspection, cleaning, and painting. All the AAUs orientations are fixed, thus $n_u = 5$. Because of its composition design it holds the same properties as classical coplanar quadrotor, plus the ability to push along one extra translational direction. The proposed design was tested on a prototype, and its $\mathfrak{F}_1$ set is presented in Fig. 3.20.

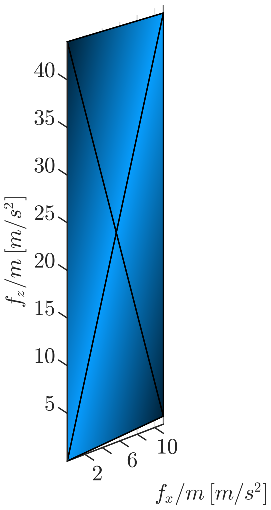

Figure 3.20 – Visualization of the $\mathfrak{F}_1$ set of the design presented in ([Albers–2010]) normalized by the platform mass. The design consists of a quadrotor with an additional propeller pointing in a lateral direction. All propellers are fixed. $N = 5$ and $n_u = 5$. Profile: subsurface of the $\boldsymbol{x}_B\boldsymbol{z}_B-$plane, where we assume the 5th propeller is pointing in the $x-$direction. The surface has the largest height for $x = 0$ and decreases as x increases.

3.3.6 Hexarotor (6 AAUs)

A Hexarotor design has $N = 6$. For Hexarotors, we can group coplanar/collinear designs into two groups, star-shaped and Y-shaped as shown in Fig. 3.21 top and bottom respectively. The former refers to a distribution where each AAU is a vertex of the star, while the latter considers a disposition similar to the delta trirotor, with each pair of propellers sharing the same axis. The system properties and capabilities are the same as for the coplanar/collinear quadrotor, except that the Y-shaped hexarotor is robust to AAU failure, while the star-shaped is not, see ([Michieletto–2018]).

As for hexarotors with tilted AAUs, tilting angles can be chosen so as $\boldsymbol{F}$ is full rank, and thus the platform is fully actuated. In fact, this is the minimal configuration for which it is possible to obtain FA of the 6D pose without any dynamic tilting of the propellers. However, as the AAUs are tilted, part of the energy is dissipated internally to balance the platform while hovering; as such, tilt-angles have to be chosen as a trade-off between propulsive efficiency (i.e., closer to coplanar/-collinear) and maneuverability in the sense of decoupling between actuation force and moment. This choice can be made either based on heuristics or by optimizing a cost function specific to the application at hand. The impact of both radial and tangential tilting, in the case of unidirectional fixed-tilt AAUs for hexarotor, is formally studied in ([Michieletto–2018]). It appears that a sufficient condition to ensure full-rankness of $\boldsymbol{F}$ is to have non-null tangential tilting even in the absence of radial tilting. However, if the tangential tilting is small enough, $\boldsymbol{F}$ is close to loose full-rankness, i.e., has a large condition number, and if the tilting is too important internal forces augment and the design loses energy efficiency. To alleviate that effect, radial tilting can be introduced as a way to lower the condition number

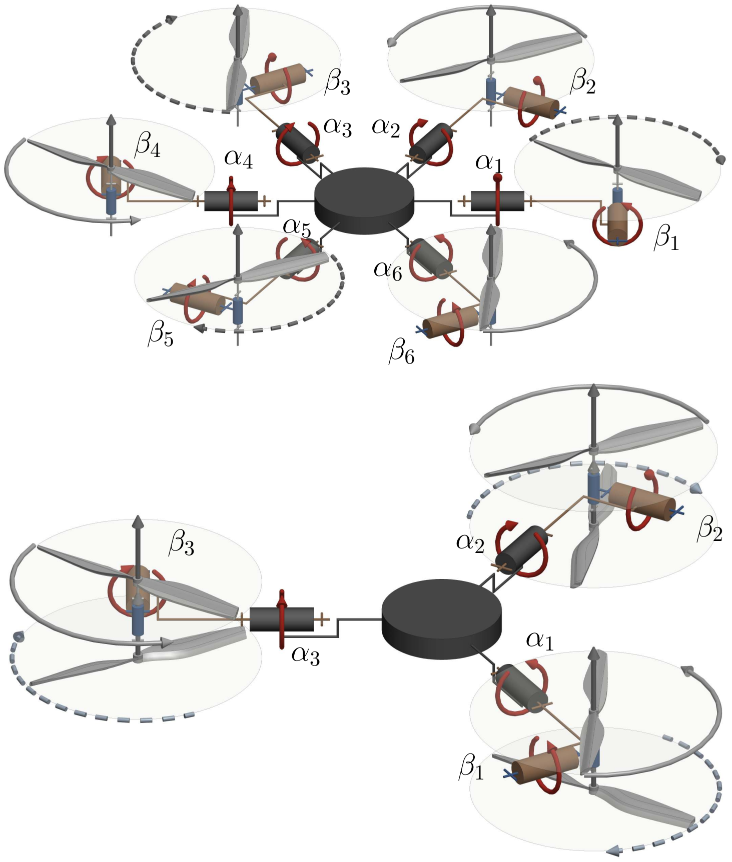

Figure 3.21 – Conceptual 3D kinematic representation of (top) star-shaped hexarotor, (bottom) Y-shaped hexarotor with propellers tilting/tilted in $\mathbb{S}^2$.

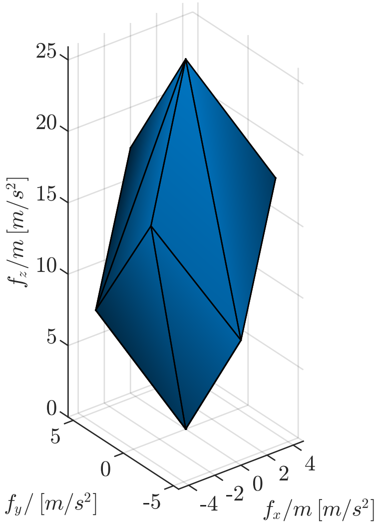

Figure 3.22 – Visualization of the $\mathfrak{F}_1$ set of a hexarotor with propellers equally tilted about a fixed α angle, the $\mathfrak{F}_1$ set is normalized by the platform mass. $N = 6$ and $n_u = 6$. Profile description: trigonal trapezohedron.

for small tangential tilting. It is also proven that hexarotors, for which AAUs are only radially tilted, are *fully vulnerable* to AAU failure (assuming a Star-shaped like distribution of propeller's around the platform's CoM).

As most of the hexarotor designs found in the literature consider unidirectional fixed-tilt AAUs, thus obtaining $n_u = 6$, in what follows AAUs are assumed to have a fixed-tilt unless specified otherwise. Table 3.8 summarizes the properties and abilities of the hexarotor designs reviewed below.

Radial Tilting Designs In ([Jiang–2014]) (and previous work) the design focuses on allowing *force closure*, i.e., the ability to instantaneously resist 6D wrench perturbation such as wind while in contact with the environment. To obtain such a design, AAUs are radially tilted by a constant angle of 20°, obtained considering a manipulability index ([Yoshikawa–1985]); the design is tested on a prototype. The $\mathfrak{F}_1$ set of similar designs is shown in Fig. 3.22.

On the other hand, authors of ([Ryll–2016a]) present a design called *FastHex* where AAUs' radial tilting can be changed simultaneously with a single servomotor for all AAUs as shown in Fig. 3.23, thus obtaining $n_u = 6 + 1$. This allows switching between UDT and FA configurations of the multirotor with only one additional input. This design can be used to optimize between energy efficiency during free-flight (coplanar/collinear AAUs) and an adequate force/moment decoupling during physical interactions. Figure 3.24 illustrates the different possible $\mathfrak{F}_1$ sets at different tilts. Extensive simulations validate the benefits of such a design for a real case scenario, while later [Bicego–2019] also validates these results in real-world expriments.

In ([Kamel–2018]) and ([Elkhatib–2017]), each AAU is equipped with a servomotor (6 in total) to tilt independently, thus obtaining $n_u = 6 + 6$. The design,

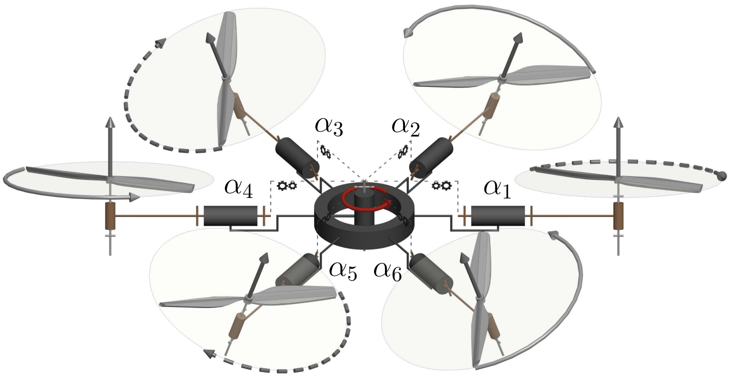

Figure 3.23 – Conceptual 3D kinematic representation of the *FastHex* design presented in ([Ryll–2016a]). The propellers are tilting radially. Highlighted the locked tilting that forces all the propellers to tilt of the same angle α.

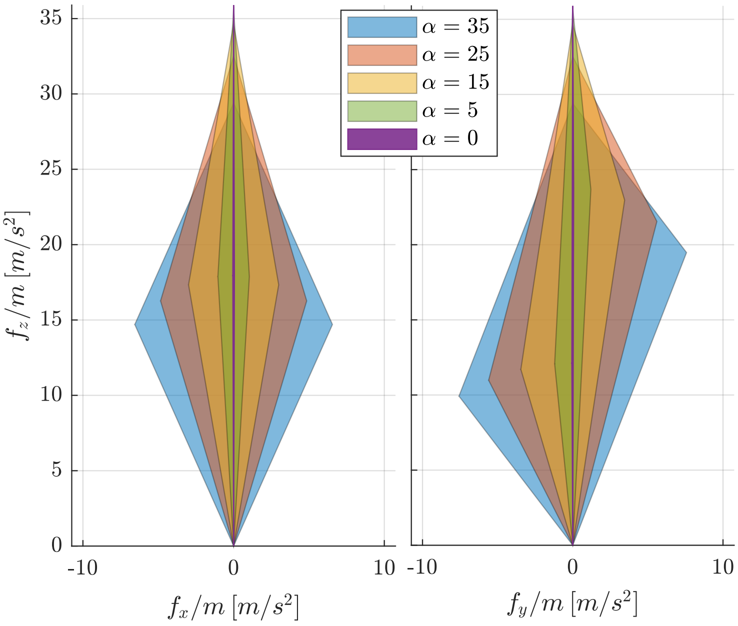

Figure 3.24 – Visualization of the $\mathfrak{F}_1$ set of the *FastHex* design at different propeller tilts α intersection with (right) $x = 0$ plane and (left) $y = 0$ plane. The $\mathfrak{F}_1$ set is similar to coplanar/collinear design for α=0; as α increases, the platform is capable of applying further lateral forces while decreasing the maximum allowable lift.

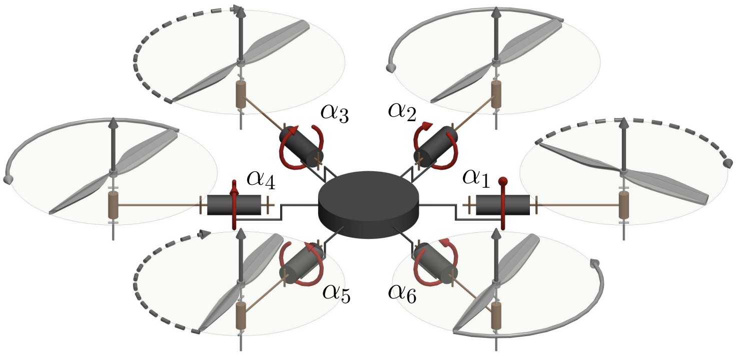

Figure 3.25 – Conceptual 3D kinematic representation of the *Voliro* design presented in ([Kamel–2018]) and ([Elkhatib–2017]). The propellers are tilting radially and all independently.

named *Voliro*, was tested on a prototype showing successful omnidirectional flights and is shown in Fig. 3.25.

Tangential Tilting Designs Differently from the designs in Radial Tilting Designs, [Giribet–2016a] propose a design where the AAUs are tangentially tilted, at a magnitude chosen heuristically at β =13°. Authors have demonstrated the ability of a vehicle with small tilting to be able to face failure in one of its propellers. Trajectory tracking of the platform was validated through simulation with noise and rotor failure.

In ([Pose–2017]) the authors also propose a design relying on tangentially tilted AAUs, where the tilting angle is heuristically chosen in a range that ensures the robustness of the design to failures, at a fixed β =17° for all AAUs. The controller does not exploit the MDT property of the design and focuses on emulating the behavior of coplanar design, by only considering a reduced output vector and finding optimal control allocation to the spinning velocity of the most solicited AAU. This design is shown to be robust to single AAU failure through experiments on a prototype of the design.

The above two designs are mechanically equivalent despite the different choice of tilt angle β, however, the controlled output of each is different, with ([Pose–2017]) not fully exploiting the FA property.

Another design is proposed in ([SGuerrero–2018]), where the authors combine a hexarotor with a hexapod design, mounting each propeller on one of the platform's legs, which can rotate about two axes corresponding to the propeller's arrangement about the CoM, and the propeller's tangential tilt. The platform is able to crawl and fly, and hence it's name *hexapodopter*. The authors prove that their design can achieve FA, and assess their design through simulation.

$\mathbb{S}^2$ Tilting Designs [Crowther–2011] present a hexarotor design where each AAU is allowed to tilt in $\mathbb{S}^2$. [Crowther–2011] describe designs constrained such that the thrusts produced by each pair of AAUs are aligned along 3 orthogonal directions, possible AAUs' orientations and direction are further grouped in 3 classes. The authors validate their feedback linearization based controller in a static experiment on a prototype of one of the detailed classes. This enforced orthogonality ensures that each 6D translation is actuated by a single AAU which comes at the logical corollary cost that each AAU should be able to sustain the full weight of the design. The authors also compare their design to a coplanar design which maximizes propulsive efficiency

Conversely, the following works consider the tilting of the AAUs in a more general way, i.e., not enforcing orthogonality of the individual thrusts. In addition, we note that most works considering generic AAUs orientation in $\mathbb{S}^2$, are interested to find the optimal AAUs orientations and thus consider both radial and tangential tilting in their optimization problem formulation, even if the resultant optimal orientation doesn't always comprise both tiltings.

Another design is proposed in ([Mehmood–2016]), where the tilt angles about $\mathbb{S}^2$ are chosen to optimize maneuverability, defined as the max acceleration reached in a given direction. The paper also investigates the failure of a single propeller and concludes with theoretical contributions.

In ([Tadokoro–2017]) optimal design based on ‘dynamic manipulability measure’ is investigated. It can be understood as omnidirectional acceleration capabilities similar to the manipulator case and is expressed as $\sqrt{\det \boldsymbol{F}\boldsymbol{F}^T}$. This work also proves that it is sufficient to study the planar disposition of the AAUs, as any spatial distribution can be brought to its equivalent plane form (neglecting some mass/inertia changes, and not taking aerodynamic cross-wind into account).

Both methods rely on heavy symmetry constraints imposed on the design, in terms of AAU disposition and tilting. Interestingly the optimal design for these two metrics does not require AAUs to be oriented in $\mathbb{S}^2$, only radial tilting of around 37° and 35° respectively for ([Mehmood–2016]) and ([Tadokoro–2017]). However, we do note that only radial tilting renders the design *fully vulnerable* to AAU failure ([Michieletto–2018]).

The aforementioned maxima are also acknowledged in ([Rajappa–2015]), where the AAUs tilting are adjusted before flight such as to minimize the norm of the control effort upon the desired trajectory. Indeed, it is important to underline that the optimal value of the tilt angles highly depends on the specific trajectory that the UAV has to perform. The problem has been solved searching for an optimal arrangement with respect to a minimum control effort over a desired trajectory. In the end, a feedback linearization technique has been also exploited.

In ([Ryll–2017a]) a design to enable physical interaction is described. AAUs are tilted symmetrically to guarantee a trade-off between maximum lateral forces and losses due to internal forces; the magnitude of the tilting angles are respectively 30° and 10°. The control law is based on an outer-loop admittance controller and an inner loop full-pose geometric controller. Moreover, the interaction forces are estimated by a wrench observer. The effectiveness of the theoretical results has been also tested in real experiments.

[Staub–2018] propose a design, called *OTHex*, tailored to the special case of cooperative beam manipulation. This design is similar to ([Ryll–2017a]), where the AAUs are tilted of fixed angles to allow FA of the multirotor, this is important for cooperative manipulation as it allows the multirotor to resist lateral disturbances without the need for reorienting as in the coplanar case. The OTHex design also considers an AAU distribution less symmetric than ([Ryll–2017a]), allowing a beam to pass through the propellers' volume.

The work by [Morbidi–2018] presents a platform design where the tilting of all propellers is synchronized so as all propellers tilt about the same radial and tangential angles. Their study can be applied for designs with active or passive tilting, thus $n_u = 6 + 2$. The authors determined a minimum-energy trajectory between two predefined boundary states and to achieve this goal an optimal control strategy has been used by including the dynamics of the brushless DC motors in addition to the platform's dynamics. Moreover, a deep analysis of the singularities of the allocation matrix has been presented. The tilting angles (α, β) come from a high-level tilt planner which is pre-computed offline and is known by the optimizer. In some sense, this work is the opposite of ([Rajappa–2015]) where optimal tilt-angles were found to follow a pre-computed trajectory.

The two next works consider bidirectional AAUs. In ([Rashad–2017]) a design aimed at maximizing actuation wrench is proposed while considering bidirectional AAUs. This leads to an OD design that has been validated in simulation with external wrench disturbances. The wrench maximization also results in only radial tilting. Their design was later demonstrated on a prototype with **APhI.1** capabilities in ([Rashad–2019]), however, with unidirectional propellers.

[Myeong–2019] also demonstrate a prototype hexarotor, with the propellers being placed in Y-formation. In their design, two of the motor pairs are placed along a horizontal shaft and can rotate independently in pairs thus obtaining $n_u = 6 + 1$. The design is similar to a T-shaped trirotor with each shaft containing two propellers rotating in opposite directions so as to balance its moment. The platform is endowed with a mechanism that allows it to apply a force on walls to aid in their inspection.

apparition	n_u	DoF	properties	abilities	maturity	variant of figure
[Jiang–2014]	6		FA	H.3, TT.4, APhI.0	prototype	Fig. 3.21(top)
[Ryll–2016a]	6+1	$(\alpha_1,\alpha_2,\alpha_3,\alpha_4,\alpha_5,\alpha_6)$	FA	H.3, TT.4, APhI.0	realsitic simulation	Fig. 3.23
[Bicego–2019]					prototype	
[Kamel–2018]	6+6	$\alpha_1,\alpha_2,\alpha_3,\alpha_4,\alpha_5,\alpha_6$	OD	H.4, TT.4, APhI.0	prototype	Fig. 3.25
│ [Elkhatib–2017]						
[Giribet–2016a]	6		FA	H.3, TT.4, APhI.0	realistic simulation	Fig. 3.21(top)
│ [Pose–2017]						
[SGuerrero–2018]	6+6	$\beta_1,\beta_2,\beta_3,\beta_4,\beta_5,\beta_6$	OA	H.3, TT.4, APhI.1	simplistic simulation	Fig. 3.21(top)
[Crowther–2011]	6+1	$\left(\begin{matrix}\alpha_1, \alpha_2, \alpha_5, \alpha_6, \\ \beta_1, \beta_2, \beta_5, \beta_6\end{matrix}\right)$	OA	H.3, TT.4, APhI.0	prototype	Fig. 3.21(top)
[Ryll–2017a]	6		FA	H.3, TT.4, APhI.1	prototype	Fig. 3.21(top)
[Staub–2018]	6		FA	H.3, TT.4, APhI.3	prototype	Fig. 3.21(top)
[Rajappa–2015]	6		FA	H.3, TT.4, APhI.0	simplistic simlation	Fig. 3.21(top)
[Morbidi–2018]	6+2	$(\alpha_1, \alpha_2, \alpha_3, \alpha_4, \alpha_5, \alpha_6)$, $(\beta_1, \beta_2, \beta_3, \beta_4, \beta_5, \beta_6)$	OA	H.3, TT.4, APhI.0	simplistic simlation	Fig. 3.23
[Rashad–2017]	6(Bi)		OD	H.4, TT.4, APhI.0	realistic simlation	Fig. 3.21(top)
[Rashad–2019]	6		FA	H.3, TT.4, APhI.1	prototype	Fig. 3.21(top)
[Myeong–2019]	6+1	$(\alpha_1, \alpha_2, \beta_1, \beta_2)$	OA	H.3, TT.4, APhI.1	prototype	Fig. 3.21(bottom)

Table 3.8 – Recapitulative table for the reviewed hexarotors ($N = 6$).

3.3.7 Heptarotor (7 AAUs)

This case is of particular interest because for designs that have AAUs with fixed orientations (i.e., $n_u = N$) and all unidirectional thrust propellers, the condition $N \geq 7$ is necessary to achieve OD as proven in ([Tognon–2018]). Despite its OA/OD ability with fixed AAUs, the design is not popular and only two examples of such designs have been found in the literature, summarized in Tab. 3.9.

Arguably, heptarotor designs first appeared in [Nikou–2015], where an optimal design for manipulation tasks with body-fixed end-effector is considered, see Fig. 3.26. The unidirectional AAUs constraint is explicitly considered. The optimization considers the condition number of $\boldsymbol{F}$ to ensure that the wrench produced is not sensitive to small deviations of the AAUs generated thrust. Additionally, the aerodynamic interaction between the AAUs' airflow is considered, and sought to be minimized while keeping the total design volume reasonable. This design is evaluated in a simulation of trajectory tracking, in non-hovering orientation, subjected to disturbances and controlled via a backstepping approach.

In ([Tognon–2018]) the optimization design problem assumes fixed positions of the AAUs, radially around the CoM, and optimize their respective tilting. A major design criterion considered is a minimum allocation-matrix condition number, which aims at an equal sharing of the effort needed to generate wrenches in any direction. Additionally, the notion of 'balanced design' is introduced which guarantees an equal sharing of the extra effort needed to keep all AAUs' individual thrust positive. An associated controller relying on model inversion and PID is proposed alongside. The general optimal design problem is proposed to make the design OD while minimizing the range of required control inputs to hover in any orientation. It is described and applied for $N = 7$, with an extensive realistic simulation of trajectory tracking, with several non-idealities described in the corresponding technical report. The authors hint that minimizing the condition number of $\boldsymbol{F}$, $\kappa(\boldsymbol{F})$, for a balanced design, minimizes the norm of the input. The result of this optimization for $N = 7$ is shown in Fig. 3.27. The $\mathfrak{F}_1$ set of this design is presented in Fig. 3.28. A prototype of the platform will be later discussed in Chapt. 5 to demonstrate the OD ability of the design.

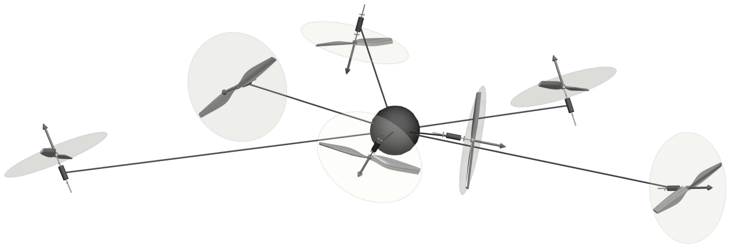

Figure 3.26 – Conceptual 3D kinematic representation of the heptarotor design presented in ([Nikou–2015]).

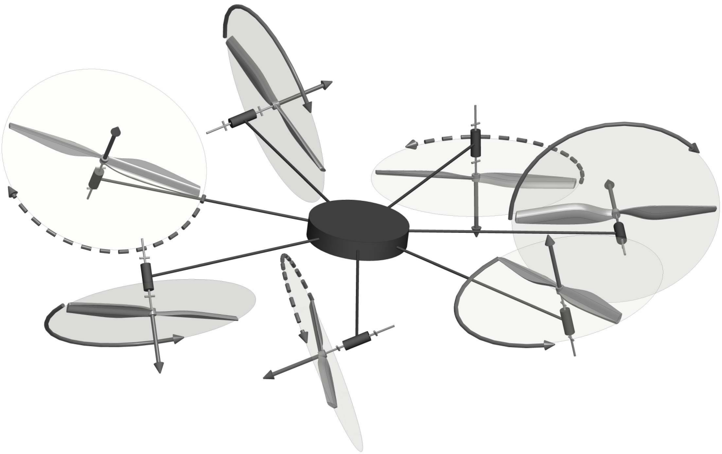

Figure 3.27 – Conceptual 3D kinematic representation of the heptarotor design presented in ([Tognon–2018]).

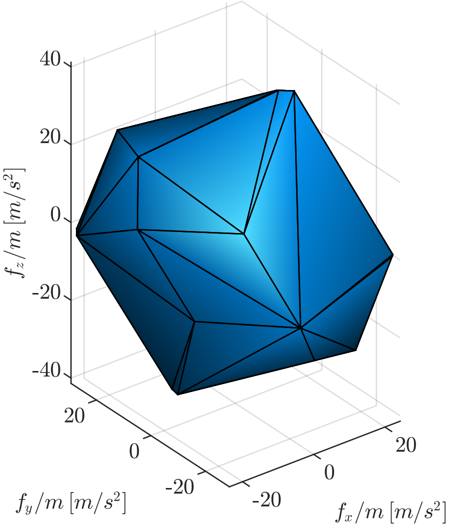

Figure 3.28 – Visualization of the $\mathfrak{F}_1$ set of the design presented in ([Tognon–2018]). The design consists of a heptarotor with fixed unidirectional propellers, with orientations designed to allow ominidirectional flight. $N = 7$ and $n_u = 7$. Profile description: irregular icositetrahedron contained inside a sphere in $\mathbb{R}^3$.

apparition	n_u	properties	abilities	maturity	figure
[Nikou–2015]	7	OA, FA	H.4, TT.4, APhI.3	realistic simulation (TT.4)	Fig. 3.26
[Tognon–2018]	7	OA, OD	H.4, TT.4, APhI.0	realistic simulation (TT.4)	Fig. 3.27

Table 3.9 – Recapitulative table for the reviewed heptarotors ($N = 7$).

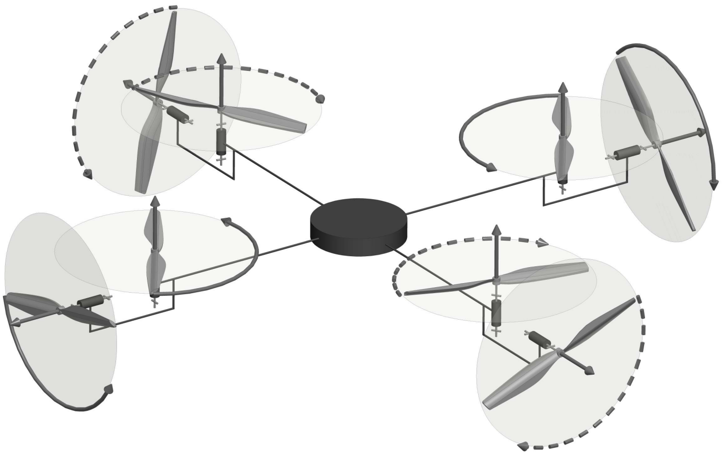

Figure 3.29 – Conceptual 3D kinematic representation of the octorotor design presented in ([Romero–2007a]).

3.3.8 Other Designs with 8 AAUs or more

We group all other platforms with $N \geq 8$ together, where we note that the majority of such designs consist of octorotors. Some notable exceptions are the commercial 'heavy lifter', which are coplanar/collinear multirotor designs. Examples are the ([Aerones–2016]) with $N = 14$, and *Volocopter*[3] with $N = 18$.

The preference of the octorotor design over others in the literature can be explained by the favored symmetric multirotor design with an even number of propellers. Moreover, due to the required compactness of commercial platforms, it becomes important for the design to have the least number of propellers for the given application. A larger number of propellers adds more weight to the platform and requires a larger platform to avoid aerodynamic interactions between adjacent AAUs, and thus is only used when additional thrust is required.

Enhanced Quadrotor design Octorotor designs in this section can be seen as an attempt to overcome the translational under-actuation of coplanar/collinear quadrotors, by adding 4 AAUs with thrust oriented in the non-actuated directions, similarly to the pentarotor in ([Albers–2010]).

In ([Romero–2007a]), a multirotor design based on a quadrotor design is proposed with four additional smaller AAUs, orthogonal to the four main ones. A conceptual kinematic design is shown in Fig. 3.29. The extra AAUs are devoted to controlling the lateral motion of the multirotor. It is interesting to note that the lateral smaller propellers produce an airflow that perturbs the induced wind speed in the main propellers increasing its lift. This term is compensated by a feedforward linearization of the aerodynamic interaction to obtain a full decoupling between the rotational and translational movements. The trajectory tracking problem is then solved by resorting to a mixture of a model-independent PD controller, coupled with a model-dependent compensation of the Coriolis and gyroscopic nonlinear torques.

---

[3] www.volocopter.com

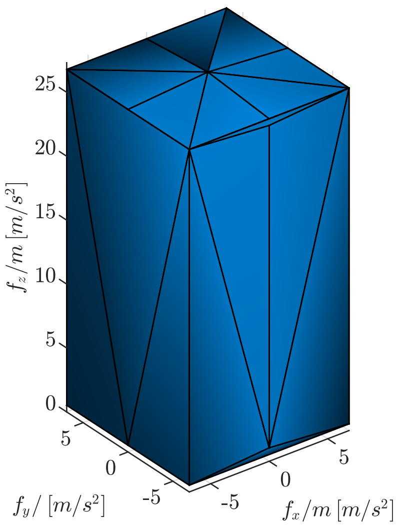

Figure 3.30 – Visualization of the $\mathfrak{F}_1$ set of the design presented in ([Romero–2007a]); the $\mathfrak{F}_1$ set is normalized by the platform mass. The design consists of 8 propellers, with 4 being collinear/coplanar with thrust pointing upwards to provide lift, and the other 4 pointing in the positive and negative x and y directions respectively. $N = 8$ and $n_u = 8$. Profile description: cuboid with square pyramid on top.

The $\mathfrak{F}_1$ set of this design is presented in Fig. 3.30.

In ([Fu–2017]) the AAUs are also tilted in the lateral plane but are located differently, reducing the cross-wind which improved the efficiency; this results again in an FA design.

Optimized Octorotor Designs Following these basic octorotor designs, some more refined designs can be found in the literature.

In ([Park–2016a; Park–2018]) aerodynamic interferences are included in the optimization problem. The goal of the optimization is to find an optimal wrench generation and an optimal rotor location within a maximum allowable volume. The first design was presented in ([Park–2016a]) with $N = 6$, and then a similar design was presented later in ([Park–2018]) with $N = 8$. The final design consists of a longitudinal bar along which propellers are placed in fixed nonsymmetric positions as shown in Fig. 3.31 showing the case with $N = 8$, with $n_u = N$. Eventually, a PID (system-independent) control strategy is implemented. In this case, to obtain bidirectional propulsion, two unidirectional propellers have been stacked together in opposite directions.

An optimized octorotor design with bidirectional propellers is presented in ([Brescianini–2016b]) and shown in Fig. 3.32. The platform is intended to be omnidirectional, and was designed by placing propellers on the edges of an octahedron to have a rotational invariant inertia tensor. Then the rotor disk orientations were chosen to maximize a measure of the platform's agility, i.e., the norm of the maximum attainable force-torque in any direction. As the system is FA, the authors exploit the feedback linearization technique to derive the controller.

In the technical report attached to [Tognon–2018], which has been introduced

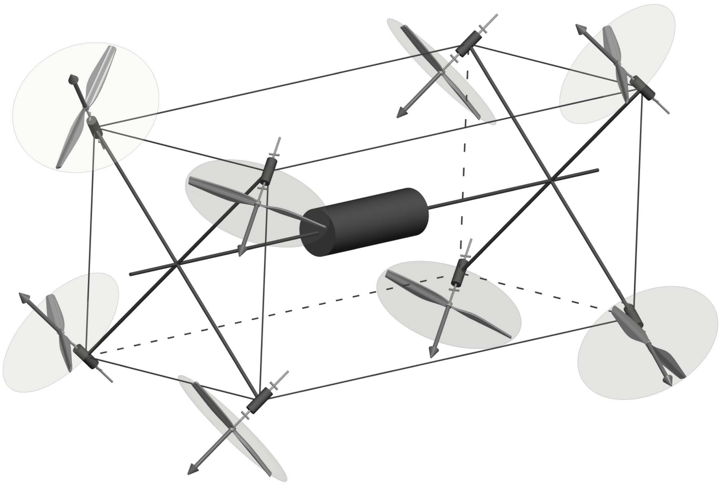

Figure 3.31 – Conceptual 3D kinematic representation of the octorotor design presented in ([Park–2016a; Park–2018]).

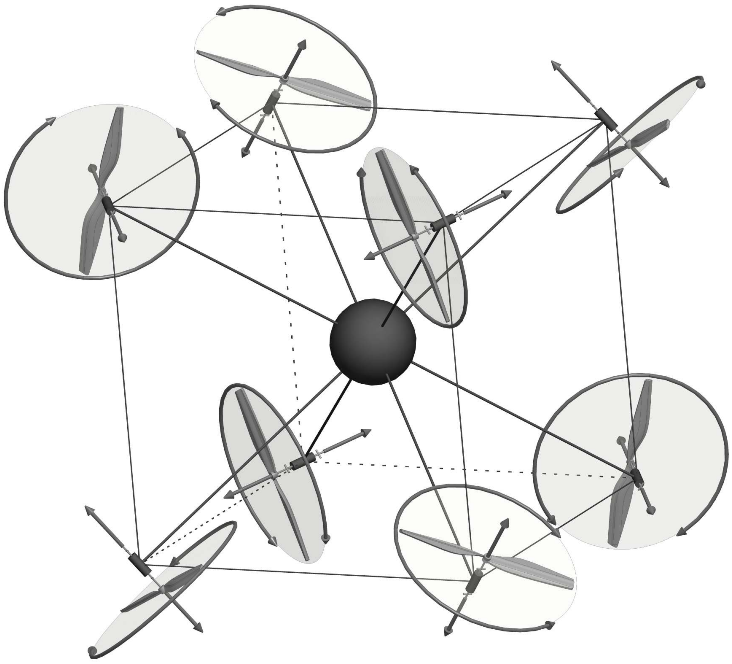

Figure 3.32 – Conceptual 3D kinematic representation of the OD octorotor design presented in ([Brescianini–2016b]).

apparition	n_u	DoF	properties	abilities	maturity	figure
[Romero–2007a][Fu–2017]	8		OA, OD	H.4, TT.4, APhI.0	prototype	Fig. 3.29
[Park–2018]	8		OD	H.4, TT.4, APhI.0	prototype	Fig. 3.31
[Brescianini–2016b]	8(Bi)		OA, OD	H.4, TT.4, APhI.0	prototype	Fig. 3.32
[Allenspach–2020]	12	(α_1, α_2), (α_3, α_4), (α_5, α_6), (α_7, α_8), (α_9, α_{10}), $(\alpha_{11}, \alpha_{12})$	OA, OD	H.4, TT.4, APhI.0	prototype	Fig. 3.25

Table 3.10 – Recapitulative table for the reviewed octorotors and the platforms with more than 8 rotors $N \geq 8$.

in the previous section, an application for $N = 8$ unidirectional propellers is briefly introduced to show the generality of the described design method for fixed unidirectional AAUs.

Finally, [Allenspach–2020] present a dodecacopter that is an upgrade of the *Voliro* design presented in ([Kamel–2018]), where the platform is endowed with 12 propellers, mounted on 6 equally spaced arms in pairs, where each of these pairs share the same spinning axis and rotate in opposing directions. Each arm of the platform can rotate about its radial axis, and thus $n_u = 12{+}6$. The platform is designed to provide position-omnidirectionality, in addition to force-omnidirectionality that is discussed in the paper. The design capabilities are demonstrated with a working prototype.

3.4 Discussion

Throughout the review, we realized a few patterns in the presented designs, such as *i)* the focus on symmetrical designs, *ii)* the use of uni-directional propellers, *iii)* ignoring aerodynamic interaction between propellers, *iv)* and finally system modeling not considering actuation limits.

While these patterns are prevalent, there has been some attempts in the literature to break these renditions. However, the full analysis of each, the corresponding advantages, and their incorporation in future designs is still to be done.

Platform Symmetry We can see that in the presented literature, the majority of designs enforce some symmetry assumptions. These symmetries vary from placing all propellers on a horizontal axis, assuming the same tilt for all propellers (with varying directions), assuming all propellers to be placed on a circumference around the geometric center of the platform, or finally having an even number of propellers. The symmetry is usually done to simplify the mechanical design and the resulting modeling and control, which in turn results in stable platforms and easy to mass-produce designs. However, we have seen that [Tognon–2018] by optimizing the tilt of the propellers about the horizontal axis, independently of any symmetry between the tilts, was able to achieve OD with $N = 7$. Conversely, [Brescianini–2016b] achieved OD with a design where the propellers are no longer placed on a horizontal axis, but rather on the vertices of an octahedron. Finally, [Nikou–2015] removed any symmetry assumption and optimized the location and orientation of all propellers for a given application. As such, we can see that the relaxation of symmetric heuristics, combined with an optimization of the platform based on performance metrics can achieve a wider allocation space, and advance multirotor designs beyond what is currently possible.

Bi-directional propellers We realized throughout the review that the use of bidirectional propellers is scarce, where only a few designs ([De Martini–2017; Rashad–2017; Park–2016a; Park–2018]) and ([Brescianini–2016b])) decided to use such propellers, in spite of the benefit of controlling the thrust produced by the propeller in both directions. One possible motivation is the "singular" behavior near the zero-thrust region ([Park–2018]), where the propeller tends to take longer to reverse their direction of rotation ([Brescianini–2016b]). Commercial solutions for reversible ESCs are scarce and the geometry of the propeller is less energy efficient than the unidirectional counterpart. Lastly, at low speed, the controllability of the exerted forces is very low, thus difficult to be used in practice. The variable pitch propeller can mitigate some of these issues but they come at the expense of additional mechanical complexity and weight, which is also not very practical. Another solution that can be achieved in this part is the use of bidirectioanl propellers while avoiding the allocation near the inversion zone of each propeller. However, proper optimization algorithms must be designed for this regards, in addition to the need for a redundancy resolution in the allocation capabilities.

Aerodynamic Interaction between Propellers The field at large could benefit from further studies on the aerodynamic effects at play, especially the interplay between AAUs cross-wind. The integration of the aerodynamic effects in the model used for control synthesis should permit feed-forward cancellation of these effects. This is of particular importance for the development of platforms endowed with fine force interaction capabilities. Also, a good model of the aerodynamic effects could be leveraged in the design process, extending ([Nikou–2015]) and ([Park–2018]), or benefiting from ([Waslander–2009]).

Actuator Limits Actuator saturation is often dismissed in theoretical studies but plays an important role in practice. Indeed, saturations hinder the multirotor dynamics, and if not taken into account properly, can result in destabilizing the control actions, in particular in dynamical maneuvers or while in physical interaction. While a few papers study the saturation's effect on control ([Franchi–2018b; Invernizzi–2017]), we found only one work that incorporates the actuation limits in their design ([Jiang–2017]). In particular, [Jiang–2017] optimize propeller tilt angles of a tilted hexarotor (similar to Fig. 3.21 on the top) to increase the possible platform lift while increasing the efficiency of the platform.

Chapter 4

Analysis of the Hexarotor fail-safe robustness under varying actuation properties

4.1 Introduction

This chapter studies the robustness of different coplanar/collinear hexarotor designs to a single propeller failure. As was illustrated in Chapt. 3, the set of feasible forces $\mathfrak{F}_1$ of the coplanar/collinear hexarotor is no different than a regular coplanar/collinear quadrotor, consisting of a single line along $\boldsymbol{z}_B$. However, and unlike the quadrotor, a hexarotor has a redundancy in propellers allowing it to withstand, in certain conditions, the failure of at least a single propeller. In this chapter, we illustrate that this robustness to propeller failure could be better understood from the set of feasible moments at hover $\mathfrak{F}_{2+}$ of the platform. As such, in this chapter we will rely on the $\mathfrak{F}_{2+}$ set to study the robustness of different coplanar/collinear hexarotor designs, with a focus on the Star-shaped and Y-shaped designs introduced in Chapt. 3.

Hexarotor Robustness to Propeller Failure in the Literature In the scope of Multi-Rotor Aerial Vehicle (MRAV) failure robustness, we note that [Michieletto–2018] have introduced the notion of robustness to propeller failure, as the ability to statically hover after the loss of any of the multi-rotor propellers. It has been shown in their work that, in order to achieve static hovering robustness for a platform with alternating propeller rotation direction, six propellers are minimally required [Michieletto–2018]. Furthermore, surprisingly, it has been shown that the standard and widespread Star-shaped hexarotors are not robust in such sense. This counterintuitive phenomenon can be seen for example in [Kamel–2015], [Bicego–2020] where simulations and experiments show that the best a model predictive controller is able to achieve in such case is dynamic hovering, even if five propellers are still available[1]. Similar outcomes are obtained from other commercially available platforms[2].

The mathematical reasons for such vulnerability have been deeply analyzed in [Michieletto–2018], where it is explained that in order to achieve robust hexarotor platforms one possibility is to use a Star-shaped platform with tilted propellers [Giribet–2016b; Michieletto–2017]. Exploiting this fact, two new prototypes

---

[1] `https://youtu.be/cocvUrPfyfo`

[2] `https://youtu.be/HQ7wa5cBT_w?t=45`

have been presented. One prototype in [Pose–2020] is a Star-shaped hexarotor platform where one of the propellers can be quickly titled via a servomotor in case of the loss of any of its propellers in order to recover static hoverability. Another prototype, built and experimentally demonstrated in [Michieletto–2018], is a Star-shaped platform with constantly tilted propellers. The robustness of both prototypes have been shown in real experiments.

Another way to obtain robustness, also illustrated theoretically in [Michieletto–2018] is to use a non-Star-shaped hexarotor, like, e.g., the Y-shaped hexarotor [Michieletto–2018]. Such solution is mechanically simpler than the above mentioned designs, because it does not need either the tilting of the propellers or the addition of servomotors or other mechanisms that could affect the platform's reliability. At the best of our knowledge, the robustness of the Y-shaped hexarotor design against propeller failure has never been experimentally tested in the static hovering sense.

It is worth noting that other types of UDT platforms have been tested for robustness in the literature. For example, [Hou–2020] showed that a coplanar collinear quadrotor looses its Yaw control following the failure of any of its propellers. On the other hand, [Saied–2015; Saied–2017] showed that a coplanar collinear octorotor is fully robust to propeller failure. However, since a hexarotor is the minimal configuration for which robustness to propeller failure could be possible ([Mochida–2021]), in this chapter we will only focus on such platforms.

Following the above discussion, this chapter aims to fill this experimental gap and at the same time to provide an extensive corollary of contributions in this field. In particular this chapter is structured as follows: Sec. 4.2 provides an intuitive way (based on geometrical intuition) to understand why the collinear Y-shaped hexarotor design is robust while the collinear Star-shaped hexarotor design is not, and provides also an intuition about the influence of parametric uncertainties on the robustness of the presented platforms; Sec. 4.3 analyzes the efficiency of Y-shaped compared to Star-shaped platforms; the efficiency analysis assumes the only loss of efficiency to be due to the aerodynamic interaction between adjacent propellers. Then Sec. 4.4 carries out a systematic and extensive set of real experiments that compare the Y-shaped and Star-shaped hexarotor designs in the fairest way possible, both from the point of view of robustness and energy efficiency; finally this section demonstrates via real experiments that the Y-shaped hexarotor is a robust platform in the static hovering sense, and therefore it could be used in safety critical environments (e.g., close to buildings and humans). Finally, Sec. 4.5 concludes the chapter. The interested reader is referred to [video01–2021a] for a summarizing presentation of the content of this chapter, in addition to demonstrations of the corresponding experiments.

4.2 Hexarotor Robustness Analysis

Let us first provide the required definitions and modeling necessary for the Robustness Analysis of the Hexarotor. These definitions are to complement the modeling presented in Chapt. 2, which lays the basis of this manuscripts' modeling.

Fig. 4.1 shows modeling schematics of the Y-shaped and Star-shaped hexarotors

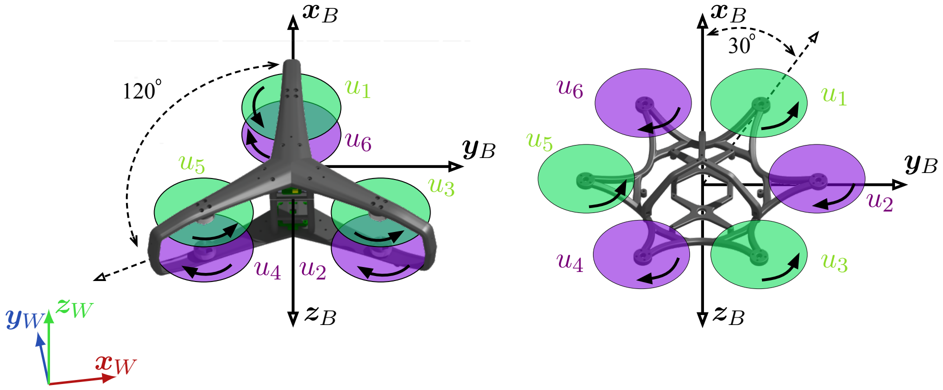

Figure 4.1 – System model and defined frames for Y-shaped (left) and Star-shaped (right) hexarotors.

with the $\mathcal{B}$ frame of each of the two platforms and the world frame $\mathcal{W}$. In this model, we assume propellers to be placed in a circle around the platform Center of Mass (CoM) with radius d, and that each propeller's $\boldsymbol{z}_{P_i}$ is parallel to $\boldsymbol{z}_B$. Moreover, we assume all the propellers of these platforms to be identical, with each propeller rotating in opposite direction to its adjacent; as such, $c_{f_i} = c_f$ and $c_{\tau_i} = \kappa_i c_\tau$, where $c_\tau \in \mathbb{R}_{>0}$ and $\kappa_i = -1(+1)$ denoting respectively a CCW(CW) direction of rotation w.r.t. $\boldsymbol{v}_i$. The position of ${}^B\boldsymbol{p}_i$ in $\mathcal{B}$ is given by

$${}^B\boldsymbol{p}_i = \underbrace{\boldsymbol{R}_z\left(\tfrac{\pi}{6} + (i-1)\tfrac{2\pi}{N} - \tfrac{1}{2}(-1)^i\gamma\right)}_{\boldsymbol{R}_\gamma(i)} \begin{bmatrix} d \\ 0 \\ 0 \end{bmatrix}, \tag{4.1}$$

with $i = 1, \ldots, 6$, where $\boldsymbol{R}_z$ is the canonical rotation matrix about the z-axis. The selection of two different values for the parameter γ allows modeling of both designs considered in this work, and presented in Fig. 4.1, as follows:

1) *Star-shape* hexarotor (Fig. 4.1, right): is a hexarotor platform with $\gamma = 0$. In this configuration, the propellers are the furthest away from each other, and thus do not overlap.

2) *Y-shape* hexarotor (Fig. 4.1, left): is a hexarotor platform with $\gamma = \frac{\pi}{3}$. In this configuration, each pair of propellers share a single rotation axis and are placed on top of each other. In order to make such design physically realizable, the pairs of coinciding propellers have to be displaced along their rotation axis. Such displacement does not affect the computation of the total force and moment because it is done along the direction of the thrust forces.

For any intermediate value of $\gamma \in (0, \frac{\pi}{3})$ one obtains a platform that is 'in between' the two mentioned above.

4.2.1 Feasible Moment Set

In this section we aim to find the feasible moment set for the Y-shaped and Star-shaped hexarotors, and to study the robustness of each of these platforms to propeller failure.

To start, let us plug Eq. (4.1) in Eq. (2.12), then we can write $\boldsymbol{f}_B = \boldsymbol{F}_1 \boldsymbol{u}_\lambda$ and $\boldsymbol{m}_B = \boldsymbol{F}_2 \boldsymbol{u}_\lambda$, where $\boldsymbol{u}_\lambda = [u_{\lambda_1} \ \cdots \ u_{\lambda_6}]^\top \in \mathbb{R}^N$ and the force allocation matrix $\boldsymbol{F}_1$ and moment allocation matrix $\boldsymbol{F}_2$ are defined as

$$\boldsymbol{F}_1 = c_f \begin{bmatrix} 0 & 0 & 0 & 0 & 0 & 0 \\ 0 & 0 & 0 & 0 & 0 & 0 \\ 1 & 1 & 1 & 1 & 1 & 1 \end{bmatrix} \tag{4.2}$$

$$\boldsymbol{F}_2(\gamma) = \begin{array}{l} c_\tau \left[\begin{matrix} rs(\frac{\pi}{6} - \frac{\gamma}{2}) & +rs(\frac{\pi}{2} + \frac{\gamma}{2}) & +rs(\frac{5\pi}{6} - \frac{\gamma}{2}) \\ -rc(\frac{\pi}{6} - \frac{\gamma}{2}) & -rc(\frac{\pi}{2} + \frac{\gamma}{2}) & -rc(\frac{5\pi}{6} - \frac{\gamma}{2} \\ -1 & 1 & -1 \end{matrix}\right. \\ \qquad \left.\begin{matrix} rs(\frac{7\pi}{6} + \frac{\gamma}{2}) & +rs(\frac{3\pi}{2} - \frac{\gamma}{2}) & +rs(\frac{11\pi}{6} + \frac{\gamma}{2}) \\ -rc(\frac{7\pi}{6} + \frac{\gamma}{2}) & -rc(\frac{3\pi}{2} - \frac{\gamma}{2}) & -rc(\frac{11\pi}{6} + \frac{\gamma}{2}) \\ 1 & -1 & 1 \end{matrix}\right] \end{array} \tag{4.3}$$

where $r = (c_f / c_\tau) l$, $s(\cdot) = \sin(\cdot)$, and $c(\cdot) = \cos(\cdot)$.

Specializing Eq. (4.3) for the Y-shaped ($\gamma = \frac{\pi}{3}$) and Star-shaped ($\gamma = 0$) hexarotors one obtains:

$$\boldsymbol{F}_2^Y = \boldsymbol{F}_2(\tfrac{\pi}{3}) = c_\tau \begin{bmatrix} 0 & +r\frac{\sqrt{3}}{2} & +r\frac{\sqrt{3}}{2} & -r\frac{\sqrt{3}}{2} & -r\frac{\sqrt{3}}{2} & 0 \\ -r & +r\frac{1}{2} & +r\frac{1}{2} & +r\frac{1}{2} & +r\frac{1}{2} & -r \\ -1 & 1 & -1 & 1 & -1 & 1 \end{bmatrix} \tag{4.4}$$

$$\boldsymbol{F}_2^S = \boldsymbol{F}_2(0) = c_\tau \begin{bmatrix} +r\frac{1}{2} & +r & +r\frac{1}{2} & -r\frac{1}{2} & -r & -r\frac{1}{2} \\ -r\frac{\sqrt{3}}{2} & 0 & +r\frac{\sqrt{3}}{2} & +r\frac{\sqrt{3}}{2} & 0 & -r\frac{\sqrt{3}}{2} \\ -1 & 1 & -1 & 1 & -1 & 1 \end{bmatrix}. \tag{4.5}$$

Let us assume that each entry of the input $\boldsymbol{u}_\lambda$ is limited between 0 and a maximum value u_{max}, i.e., $\boldsymbol{u}_\lambda \in \mathbb{U} = \bigtimes_{i=1}^{n} [0, u_{max}]$. Consequently we denote the *feasible moment set at hover* of the coplanar/collinear hexarotor parametrized by γ as follows:

$$\mathfrak{F}_{2+}(\gamma) = \{\boldsymbol{m}_B \in \mathbb{R}^3 \mid \exists \boldsymbol{u}_\lambda \in \mathbb{U}_+ : \boldsymbol{m}_B = \boldsymbol{F}_2(\gamma) \boldsymbol{u}_\lambda\}. \tag{4.6}$$

It should be noted for the rest of the derivations in this section that since $\mathbb{U}_+ \subset \mathbb{U}$, then $\mathfrak{F}_{2+} \subset \mathfrak{F}_2$.

The specialized feasible moment sets at hover for the *Y-shaped* and *Star-shaped* hexarotors are noted as $\mathfrak{F}_{2+}^Y = \mathfrak{F}_{2+}(\frac{\pi}{3})$ and $\mathfrak{F}_{2+}^S = \mathfrak{F}_{2+}(0)$, respectively.

The plots in the first column of Figure 4.2 show the feasible moment sets of the *Y-shaped* and *Star-shaped* hexarotors.

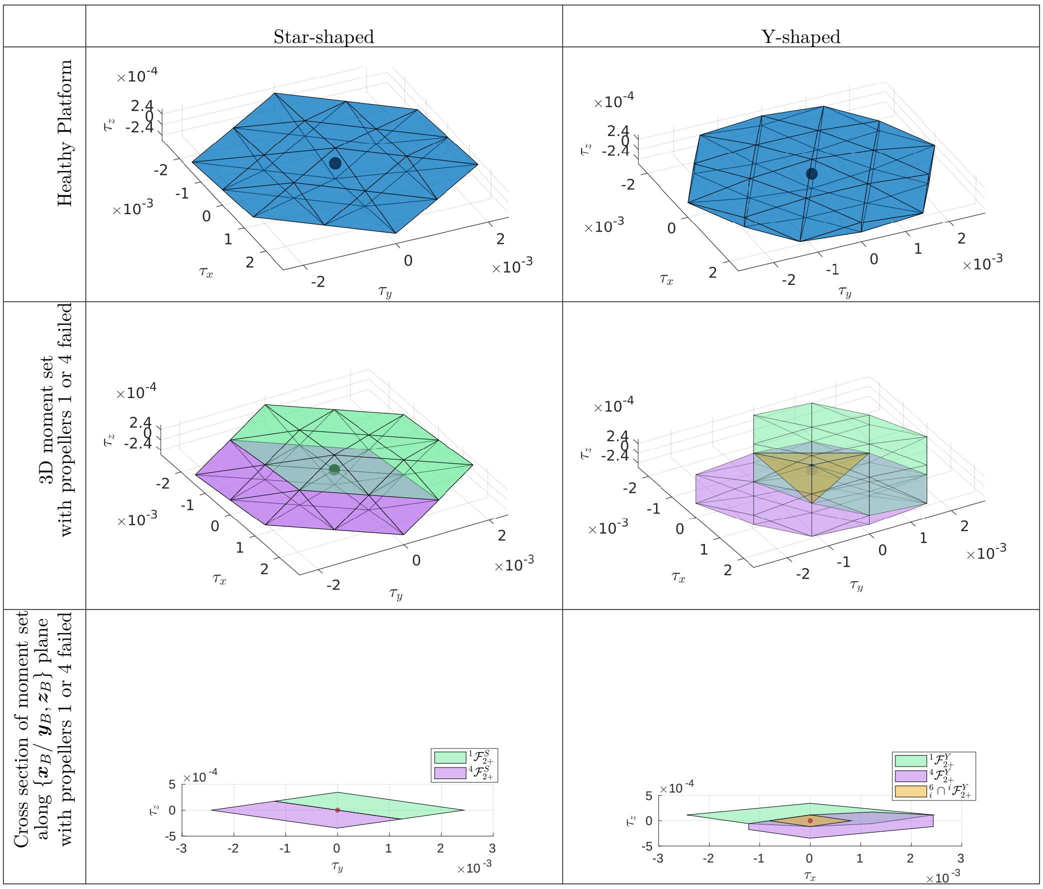

Figure 4.2 – Visualization of the platforms' feasible moment sets at hover.

4.2.2 Static Hovering

The platform is capable of static hovering when it can reach and maintain a constant orientation and position, *i.e.*

$$\dot{\boldsymbol{p}}_B^d \to \mathbf{0}, \qquad \boldsymbol{\omega}_B \to \mathbf{0}, \tag{4.7}$$

As explained in [Michieletto–2018] the following conditions are needed for a platform to posses the static hovering ability

$$rank\{\boldsymbol{F}_2\} = 3 \tag{4.8}$$

$$\exists \boldsymbol{u}_\lambda \in \mathrm{int}(\mathbb{U})\ s.t. \begin{cases} \|\boldsymbol{F}_1 \boldsymbol{u}_\lambda\| \geq m\mathbf{g} \\ \boldsymbol{F}_2 \boldsymbol{u}_\lambda = \mathbf{0} \end{cases} . \tag{4.9}$$

Where $\mathrm{int}(\mathbb{U})$ denotes the interior of $\mathbb{U}$.

Conditions Eq. (4.8) and Eq. (4.9) can be understood geometrically from the feasible moment set at hover $\mathfrak{F}_{2+}$ as follows:

Proposition 4.2.1. A platform can statically hover iff $\mathbf{0} \in \mathrm{int}(\mathfrak{F}_{2+})$.

Proof. It is a straightforward consequence of the continuity of the map $\boldsymbol{F}_2$, where $\mathfrak{F}_{2+}$ having an interior is a sufficient condition to prove Eq. (4.8), and $\mathbf{0} \in \text{int}(\mathfrak{F}_{2+})$ is sufficient to prove Eq. (4.9). $\square$

Corollary 4.2.2. Following Prop. 4.2.1, a platform is deemed unable of static hovering if the origin is on the boundary of $\mathfrak{F}_{2+}$ or an external point of the set.

Lemma 4.2.3. The *Y-shaped* and *Star-shaped* hexarotors can achieve static hovering.

Proof. $rank\{\boldsymbol{F}_2^Y\} = 3$ and $rank\{\boldsymbol{F}_2^S\} = 3$, and any input of the form $\boldsymbol{u}_\lambda = \lambda \mathbf{1} = \lambda[1 \cdots 1]^\top \in \mathbb{R}^N$ with $\lambda \in (0, u_{max})$ belongs to $\text{int}(\mathbb{U})$ and satisfies Eq. (4.9). $\square$

The static hovering ability of both platforms can also be seen from the feasible moment sets at hover (Fig. 4.2), where the origin is indeed an interior point of both $\mathfrak{F}_{2+}^S$ and $\mathfrak{F}_{2+}^Y$.

4.2.3 Rotor Failure

In this subsection we highlight the effect of propeller loss on the static hovering capability of the two hexarotors in exam. We denote by ${}^k\boldsymbol{F}_2(\gamma)$ the moment allocation matrix $\boldsymbol{F}_2(\gamma)$ in which the k^{th} column has been zeroed (or, equivalently, removed). Such matrix represents the moment allocation matrix of a platform in which the k^{th} propeller does not spin anymore after a fault, i.e., $u_k = 0$. We denote by ${}^k\mathfrak{F}_{2+}(\gamma)$ the feasible moment set at hover associated to ${}^k\boldsymbol{F}_2(\gamma)$. The same specializations for the Y-shaped and Star-shaped platforms apply, thus obtaining ${}^k\mathfrak{F}_{2+}^Y$, ${}^k\boldsymbol{F}_2^Y$, ${}^k\mathfrak{F}_{2+}^S$, ${}^k\boldsymbol{F}_2^S$.

Remark. The feasible moment set at hover ${}^k\mathfrak{F}_{2+}^S$ for different k is a rotation about the z-axis of ${}^{k-1}\mathfrak{F}_{2+}^S$, with a flip about the (x, y)-plane.

Proof. It is easy to see following Eq. (4.1) that

$$
{}^k\boldsymbol{F}_2^S = \begin{bmatrix} 1 & 0 & 0 \\ 0 & 1 & 0 \\ 0 & 0 & -1 \end{bmatrix} \boldsymbol{R}_z(\frac{\pi}{3})^{k-1}\boldsymbol{F}_2^S \tag{4.10}
$$

Since all propellers are identical, then the transformation between ${}^k\mathfrak{F}_{2+}^S$ and ${}^{k-1}\mathfrak{F}_{2+}^S$ is the same as between ${}^k\boldsymbol{F}_2^S$ and ${}^{k-1}\boldsymbol{F}_2^S$. $\square$

It was proved in [Michieletto–2018] that the Y-shaped hexarotor – or any collinear coplanar hexarotor with $\gamma \in (0, \frac{2\pi}{3})$ – is still capable of static hovering after the single loss of any of its propellers. On the other hand, [Michieletto–2018] proved that the Star-shaped hexarotor ($\gamma = 0$) loses its ability to perform static hovering as it loses any of its propellers, despite the fact that five propellers are still healthy and available for conttol.

The static hovering ability of the two platforms can be easily understood from the geometrical viewpoint presented earlier. The vulnerability of the Star-shaped hexarotor can be seen from the corresponding feasible moment set at hover ${}^1\mathfrak{F}_{2+}^S$ shown in Figure 4.2, where it is clear that the origin is a point on the boundary of the presented set ; this result is similar for any ${}^k\mathfrak{F}_{2+}^S$ due to Remark 4.2.3. Figure 4.2

also shows that for any ${}^{k}\mathfrak{F}^{Y}_{2+}$, the origin of the feasible moment set at hover is an interior point, and in particular $\mathbf{0} \in \mathrm{int}\{\bigcap_k {}^{k}\mathfrak{F}^{Y}_{2+}\}$.

4.2.4 Effect of Disturbance Moment

If a platform's static hovering is not feasible after the loss of a propeller, but Eq. (4.8) and the first part of Eq. (4.9) are satisfied, then it is possible to shift the origin of the feasible moment set at hover into the interior of ${}^{k}\mathfrak{F}_{2+}$, by adding a external disturbance moment $\boldsymbol{m}_B^{dist}$ such that the control moment $\boldsymbol{m}_B^{c} = -\boldsymbol{m}_B^{dist} \in \mathrm{int}({}^{k}\mathfrak{F}_{2+})$. For the Star-shaped hexarotor, for example, a disturbance moment can be obtained by shifting the CoM of the platform. However, the following negative result holds.

Proposition 4.2.4. It does not exists a unique $\boldsymbol{m}_B^{dist}$ such that

$$-\boldsymbol{m}_B^{dist} \in \mathrm{int}({}^{k}\mathfrak{F}^{S}_{2+}) \quad \forall k \in \{1, ..., N\} \tag{4.11}$$

i.e., there does not exist a single disturbance moment that could be used to shift the origin into the interior of the feasible moment set at hover of the Star-shaped hexarotor in the case of the loss of any of its propellers.

Proof. This result is a consequence of the fact that $\mathrm{int}(\bigcap_k {}^{k}\mathfrak{F}^{S}_{2+}) = \emptyset$. Let us consider a moment $\boldsymbol{m}_B^{1,4} \in {}^{1}\mathfrak{F}^{S}_{2} \cap {}^{4}\mathfrak{F}^{S}_{2}$.

$$\boldsymbol{m}_B{}^{1,4} = c_\tau \begin{bmatrix} +r & +r\frac{1}{2} & -r\frac{1}{2} & -r & -r\frac{1}{2} \\ 0 & +r\frac{\sqrt{3}}{2} & +r\frac{\sqrt{3}}{2} & 0 & -r\frac{\sqrt{3}}{2} \\ 1 & -1 & 1 & -1 & 1 \end{bmatrix} \begin{bmatrix} u_2^1 \\ u_3^1 \\ u_4^1 \\ u_5^1 \\ u_6^1 \end{bmatrix} \tag{4.12}$$

$$= c_\tau \begin{bmatrix} +r\frac{1}{2} & +r & +r\frac{1}{2} & -r & -r\frac{1}{2} \\ -r\frac{\sqrt{3}}{2} & 0 & +r\frac{\sqrt{3}}{2} & 0 & -r\frac{\sqrt{3}}{2} \\ -1 & 1 & -1 & -1 & 1 \end{bmatrix} \begin{bmatrix} u_1^4 \\ u_2^4 \\ u_3^4 \\ u_5^4 \\ u_6^4 \end{bmatrix} \tag{4.13}$$

By simplifying then adding the first and second rows we find $u_4^1 + u_1^4 = -(u_4^1 + u_1^4)$ to be a necessary condition for the intersection between the two sets. The only solution for the above equality is to set $u_1 = u_4 = 0$; as such

$$\nexists \boldsymbol{u}_\lambda > 0 \quad s.t. \quad \boldsymbol{m}_B^{1,4} \in \mathrm{int}({}^{1}\mathfrak{F}^{S}_{2} \cap {}^{4}\mathfrak{F}^{S}_{2}) \tag{4.14}$$

and as such, $\mathrm{int}({}^{1}\mathfrak{F}^{S}_{2} \cap {}^{4}\mathfrak{F}^{S}_{2}) = \emptyset$, and $\mathrm{int}(\bigcap_k {}^{k}\mathfrak{F}^{S}_{2}) = \emptyset$. Since each ${}^{k}\mathfrak{F}^{S}_{2+} \subset {}^{k}\mathfrak{F}^{S}_{2}$ we can conclude that $\mathrm{int}(\bigcap_k {}^{k}\mathfrak{F}^{S}_{2+}) = \emptyset$. ☐

The reasoning behind the previous proof is also visible from Fig. 4.2, where it can be seen clearly that $\mathrm{int}({}^{1}\mathfrak{F}^{S}_{2+} \cap {}^{4}\mathfrak{F}^{S}_{2+}) = \emptyset$.

4.2.5 Effect of Model Uncertainty

While the above modeling considers the nominal geometry of the system, manufacturing uncertainty can slightly change the actuation capabilities of the platform. More specifically, in the nominal model we consider propellers to be mounted with no tilt, i.e., $\alpha, \beta = 0$. As detailed in [Michieletto–2018], any modification in the mounting tilt can affect static hoverability of the platform. Moreover, while we consider lift and drag coefficients c_f, c_τ to be constant, they are a linear fit of the underlying nonlinear model. In addition, different propellers might have varying aerodynamic properties. Finally, in the above formulation the arm length d between the CoM and each propeller is assumed constant, and the CoM is assumed to coincide with the Geometric Center (GC).

In static hovering conditions, the uncertainties mentioned above can be approximated by a lumped disturbance moment ${\boldsymbol{m}_B}^{dist}$; this disturbance has to be compensated so as the resultant moment applied to the platform is equal to zero. This implies that the input moment $\boldsymbol{m}_B$ required for static hovering is equal to $\boldsymbol{m}_B = -{\boldsymbol{m}_B}^{dist}$ instead of zero as it would have been in the nominal case.

The presence of such disturbance ${\boldsymbol{m}_B}^{dist}$ will practically make possible the static hovering of the Star-shaped hexarotor during the loss of some of its propellers; in particular, for any propeller loss whose feasible moment set at hover still contains the origin following the translation by ${\boldsymbol{m}_B}^{dist}$. More formally, the platform can hover upon the loss of any propeller k for which the following condition is verified

$$-{\boldsymbol{m}_B}^{dist} \in \text{int}({}^{k}\mathfrak{F}^{S}_{2+}). \tag{4.15}$$

However, and as suggested in Prop. 4.2.4, for any ${\boldsymbol{m}_B}^{dist}$ there will always exist some propellers whose loss precludes static hovering for the Star-shaped platform.

Remark. In the case of the Y-shaped hexarotor, let us assume that there exists a threshold moment ${\boldsymbol{m}_B}^{threshold}$ such that

$$\forall {\boldsymbol{m}_B}^{dist} \leq {\boldsymbol{m}_B}^{threshold} \; ; -{\boldsymbol{m}_B}^{dist} \in \text{int}(\mathfrak{F}^{Y}_{2+}). \tag{4.16}$$

It is safe to assume that within the manufacturing and operating conditions of our platforms, ${\boldsymbol{m}_B}^{dist} \leq {\boldsymbol{m}_B}^{threshold}$; a similar analogy can be applied to the Y-shaped hexarotor after the failure of any of its propellers.

4.3 Aerodynamic Interactions and Platform Efficiency

This section studies the aerodynamic interaction between adjacent propellers for different γ angles. The objective of this study is to understand the efficiency of different hexarotor designs; as such, the study of the aerodynamic interactions will focus on the interaction's effect on each propeller's lift coefficient. Such interactions have been experimentally studied in ([Theys–2016]), however, we attempt in this section to find a closed form relation that explains the direct relation between the platform efficiency and the angle γ.

To compute such aerodynamic change, let us assume first that the change in

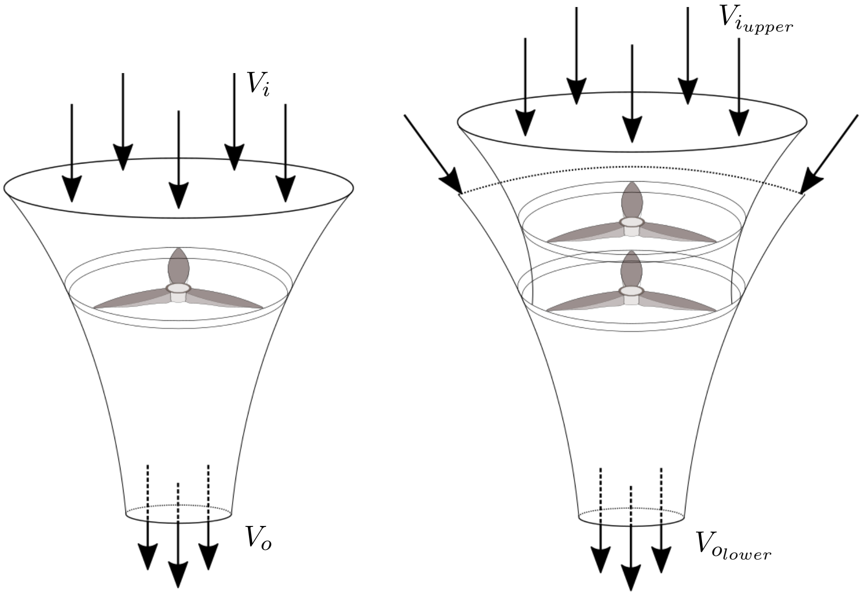

Figure 4.3 – Control volume around single propeller, and interaction between the corresponding control volumes of two propellers placed on top of each other.

efficiency is only significant when two propellers overlap (partially or completely). Let us first define V_i, and V_o as correspondingly the input air velocity to the propeller and the output air velocity exiting the propeller; the control volume showing these entities for a single propeller, and two propellers sharing the same axis are shown in Fig. 4.3. The relation between V_i, V_o and the propeller geometry have been presented in ([Khan–2013]) as follows:

$$c_f = \frac{1}{2}\rho N \sum_{r=R_h}^{R_p} \left[\frac{r^2}{cos\phi} c \left[a(\theta - \alpha_0 - \phi) \right] - C_d tan\phi \right] \Delta r \tag{4.17}$$

where ρ is the density of air in kg/m^3, N is the number of propeller blades, ω is the propeller rotational speed in rad/s, R_h is the hub radius and R_p is the propeller radius, r is a radial location, c is the radial cord, θ is the chordline pitch angle, α_0 is the zero-lift angle of attack, a is the 2-D lift curve slope, C_d is the 2-D drag coefficient, and finally ϕ is the inflow angle. Some of these parameters are illustrated in Fig. 4.4.

As illustrated in ([Khan–2013]), some of these parameters vary for different radii of the propeller, and depend on the input velocity of the propeller. More specifically, it is assumed that a, C_d and ρ are fixed for each propeller, θ and α_0 depend on the propeller radius, and finally, ϕ depend on the propeller radius and the input velocity and the propeller rotational speed.

To find the change in the platform efficiency, let us first assume that the upper propeller is not affected by the lower propeller (i.e., input and output velocity of the upper propeller are not affected). As such, we assume that the upper propeller

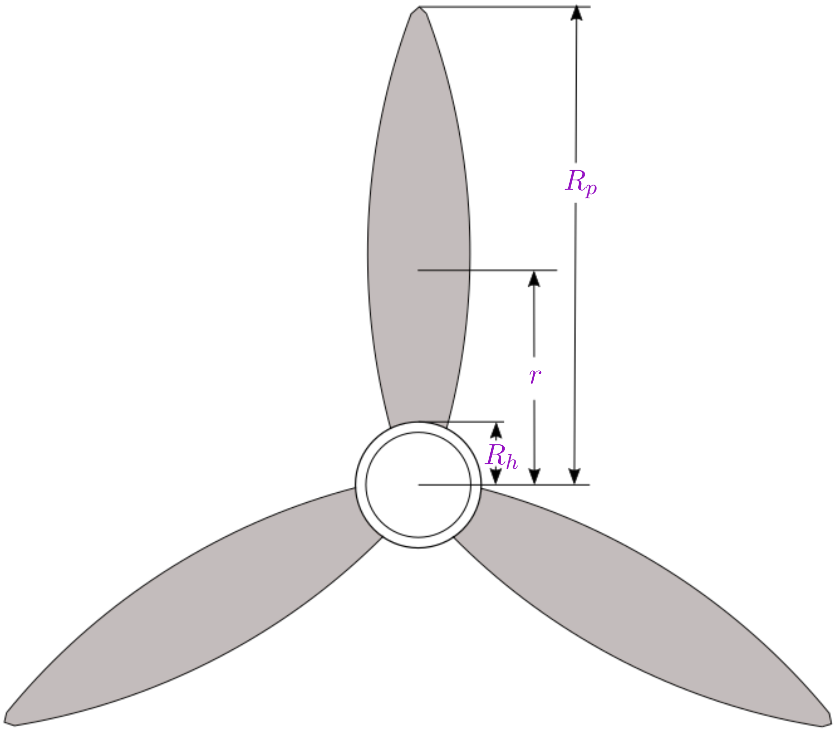

Figure 4.4 – showing top view of a 3 blade propeller, and the corresponding hub radius R_h, propeller radius R_p and intermediate radius r.

withdraws air from the free stream (i.e., $V_{i_{upper}} = 0$). Furthermore, we assume that the input velocity of the lower propeller (at the intersection area) is equal to the output velocity of the upper propeller. However, we assume that the output velocity and input velocity change depending on the propeller radius ([Khan–2013]). Let us assume that the lift is achieved across the entire circle in which the propeller rotates (assuming the propeller is zero depth), and propose the following relation between the lift coefficient and the corresponding sub-surfaces of the propeller circle:

$$c_f = \frac{1}{2}\rho N \sum_{A=1}^{n} \left[\frac{r^2}{cos\phi} c \left[a(\theta - \alpha_0 - \phi) \right] - C_d tan\phi \right] \Delta A \tag{4.18}$$

where n is the number of areas that represent the entire circle. As was done in ([Khan–2013]), the radius of the propeller is discretized, and Eq. (4.17) is computed over different annuli, in which all parameters are assume constant. We augment this assumption to Eq. (4.18) as follows:

i) First, we calculate the output velocity of each of the upper propeller annuli independent of the lower propeller,

ii) then, we find the intersection between each upper propeller annuli and lower

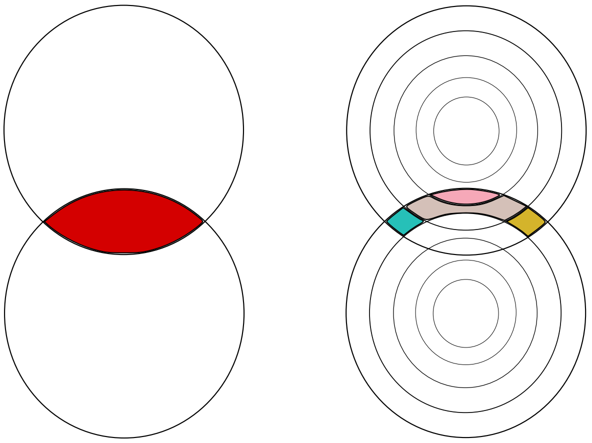
(a) (b)

Figure 4.5 – showing (a) intersection area between two propeller's control area, (b) intersection area between two of the propeller's annuli.

propeller annuli,

iii) in each of these intersections, we calculate the corresponding lift based on the input velocity calculated from the upper propeller's annuli, and the geometry of the lower propeller annuli;

iv) finally, we find the total lift coefficient following Eq. (4.18).

The different annuli are shown in Fig. 4.5.

Following the above formulation, we compute numerically the variance in the lift coefficient while varying gamma and the propeller rotational speeds. We assume the upper and lower propellers to be rotating at the same rotational speeds; this approach provides us with a partial solution, where the full solution would have required varying each propeller speed independently. However, since the full solution is an exhaustive one, we instead only show the solution where both propellers rotate at the same rotational speed (assuming that both propellers share the platform lift equally). The efficiency of a propeller is expressed as follows:

$$\eta(propeller) = \frac{c_f(\gamma)}{c_f(\gamma = 0)}. \tag{4.19}$$

If the calculation of the numerator and denominator of $\eta(propeller)$ is done at the same propeller rotational speeds, then $\eta(propeller)$ is independent of the propeller rotational speeds. The corresponding efficiency of the lower propeller vs the platform γ angle is shown in Fig. 4.6. It should be noted that the platform efficiency can be computed as $\eta(platform) = 1 - \frac{1-\eta(propeller)}{2}$, where this efficiency repre-

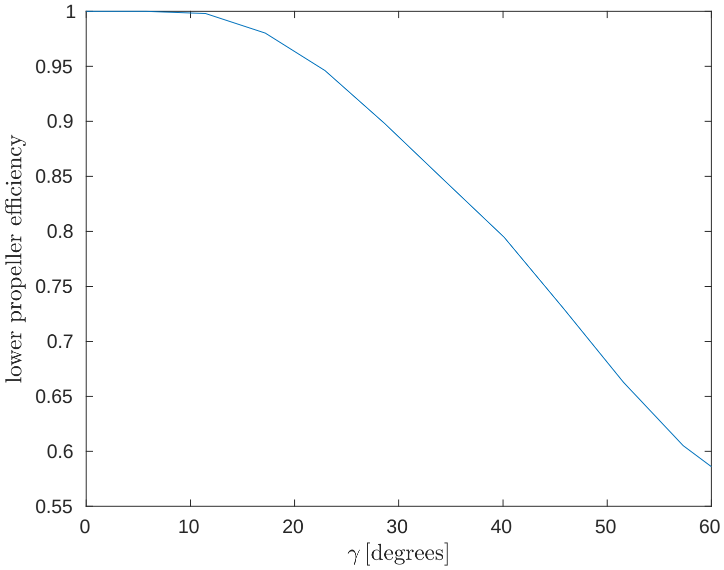

Figure 4.6 – showing the efficiency of the lower propeller vs the platform γ angle.

sents the efficiency between a platform with $\gamma \neq 0$ and the Star-shaped equivalent. Finally, the platform efficiency is directly proportional to the square of the drawn current; following this analysis and Fig. 4.6, we expect the Y-shaped hexarotor to withdraw 11% current more than the corresponding Star-shaped hexarotor.

Remark. The calculated efficiency provides an idea of the flight time efficiency that will be discussed later in this paper, however, we do note that the flight time efficiency also depends on the battery capacity, the battery ratings, the battery temperature, as well as other parameters ([Shepherd–1965]).

4.4 Experimental Validation

4.4.1 Experimental Hardware and Software

To be able to systematically compare the Star-shaped and Y-shaped hexarotors, we designed two platforms with identical components and similar properties, with the corresponding specifications shown in Tab. 4.1. The two platforms, shown in Fig. 4.7, are built via 3D printing technology with Onyx material, and similar off-the shelf components for the propulsion system, telemetry and safety link communication. Finally, the two platforms are flown with the same autopilot and flight controller.

Software: Paparazzi Autopilot and INDI Controller Throughout the flight tests, we have used the Paparazzi Autopilot system [Hattenberger–2014], an open-source autopilot that covers all three segments of the system: ground control, airborne platform control, and the communication link between the two.

Paparazzi has its own flight plan language that allows the platform to follow different reference trajectories; moreover, its middle-ware allows the implementation

Figure 4.7 – The Y-shaped (left) and Star-shaped (right) hexarotor platforms built in-house for the fair comparison.

Table 4.1 – Specifications of the built hexarotor platforms

Specification	Star-Shape	Y-Shape	Units
Center-Motor Distance	0.143	0.130	[m]
Total Mass	0.745		[kg]
Battery Capacity	23.0		[Wh]
Flight time	569	344	[s]
Maximum thrust	60	45	[N]
Structure material	3D printed (Onyx composite)		
Structure components	9 pieces	7 pieces	
Motor & Propeller	T-Motor F40(Kv 2400) & 5T-5147 Prop		
Electronic Speed Ctrl	T-Motor F45A V2.0		
Autopilot	Paparazzi Tawaki v1.1		
Communication	Xbee modem & Futaba SBus Receiver		

of the desired controller on-board the platform.

The autopilot implements the *Incremental Nonlinear Dynamic Inversion* (INDI) controller based on [Smeur–2018b]; the controller is a robust sensor-based (measurement-based) controller which revolves around the control of the angular accelerations in an *incremental* way. As illustrated in [Smeur–2018b], INDI is a robust and reliable controller, capable of dealing with strong wind perturbations and modeling inaccuracies. We refer the interested reader to the corresponding paper for more details on the control law.

We note that while we rely on the INDI as a Fault Tolerant Control System (FTCS), we do not aim to study its advantage over other FTCS from the literature; however, we refer the curious reader to the following literature [Zhang–2013; Mueller–2014; Scaramuzza–2014] for an overview of such systems and their applications.

Throughout our experimental campaign, the INDI controller runs at 500 [Hz] while the trajectory generation is updated at a 16 [Hz] rate.

4.4.2 Experimental Results

To test the robustness and efficiency of the built platforms, an experimental campaign has been carried out at the VTO flight arena[3]. The position and orientation of the vehicles are captured by the motion capture system installed in the arena.

To assess the robustness of the platforms, we introduce the following two metrics

$$\frac{1}{2}\, m \,(\boldsymbol{e}_p^\top \boldsymbol{e}_p + \dot{\boldsymbol{p}}_B^\top \dot{\boldsymbol{p}}_B) \quad \text{(translation motion error)} \tag{4.20}$$

$$\frac{1}{2}\, m \,\omega_\phi^2 \quad \text{(rotational kinetic energy),} \tag{4.21}$$

where $\boldsymbol{e}_p = \boldsymbol{p}_B^d - \boldsymbol{p}_B \in \mathbb{R}^3$ is the positional error and ω_ϕ is the yaw rate. It is easy to show from the underactuated dynamics and differential flatness of both vehicles that such metrics reflect the platform hovering, where both converge to zero if the platform is in static hovering, and diverge otherwise.

Static Hovering Experimental Campaign To test the robustness of each platform, we artificially induce a propeller failure while the platform is in static hovering, and assess the platform's robustness in the wake of the failure.

We note that during these experiments, and unless otherwise specified, the robust controller was not informed about the rotor failure, and rather attempts to fly the platform based on its measurement feedback.

First, we test the Y-shaped hexarotor to verify its robustness to propeller failures as theoretically predicted in Sec. 4.2.1.

Fig. 4.8a shows (top) the position of the Y-shaped hexarotor and (bottom) the hovering metrics of the Y-shaped hexarotor while flying with all propellers working properly and in the wake of the failure of one of each of its six propellers. As expected, the platform recovers its position after the failure of any of its propellers, with the two metrics converging to zero a few seconds after the failure.

A similar experiment was conducted to test the static hovering ability of the Star-shaped hexarotor.

Fig. 4.9a shows (top) the position of the Star-shaped hexarotor and (bottom) the hovering metrics of the Star-shaped hexarotor while flying with all propellers working properly and in the wake of the failure of one of each of its six propellers. It can be seen from Fig. 4.9a that while the healthy platform can hover normally, the Star-shaped hexarotor crashes after the failure of propellers 4-5-6. On the other hand, after the loss of propellers 1-2-3 the platform does not crash, however, it oscillates about the desired position, which can be observed in the large value of the translation motion error. Note that the failure of propellers 2 and 3 showed different behavior during repeatability tests, at worst ending up by crashing.

---

[3] `https://www.enac.fr/en/drone-flight-arena-toulouse-occitanie-0`

While the vulnerability of the Star-shaped hexarotor is expected (Sec. 4.2.1), we repeated the above experiment for the Star-shaped hexarotor while informing the controller of the propeller fault. This is done by providing an updated actuator efficiency matrix to the controller, where the column corresponding to the failed propeller has been zeroed; this provides the controller the knowledge that the corresponding propeller has no effect on the angular rotation of the vehicle.

Fig. 4.9b shows the results of this experiment, where we can see that the Star-shaped hexarotor crashes right after the failure of propellers 4-5-6, while it is capable of static hovering following the failure of propellers 1-2-3. Looking deeper at the control inputs in the cases where static hovering was still possible, we can see that the informed controller was already able to generate required moments without using the corresponding propellers, and as such, the platform's performance was not affected by the corresponding failures.

These experimental results confirm the theoretical prediction presented in Sec. 4.2.5, according to which a nominal Star-shaped hexarotor should become unable of static hovering following the failure of all its propellers, while a real Star-shaped hexarotor should become unable of static hovering after the failure of at least one propeller, but could still be able to statically hover following the failure of one or more propellers, due to the manufacturing uncertainties.

Finally, we test the effect of adding a disturbance moment to the Star-shaped hexarotor on the platform's static hovering ability. The disturbance moment is induced by shifting the location of one of the platform's components in order to shift its CoM. Tab. 4.2 shows the static hovering ability of the Star-shaped hexarotor following the failure of one of each of its propellers while the CoM is placed in the center of the platform, or shifted along $\boldsymbol{x}_B$ or $\boldsymbol{y}_B$. Propeller failures for which repeated tests showed different behaviors are placed in parenthesis. It can be seen that for each of the applied disturbance moments, and as suggested in Sec. 4.2.1, the platform is vulnerable to the loss of some of its propellers, while it can successfully hover following the loss of others. The results of Tab. 4.2 suggest that the nominally built Star-shaped hexarotor has a manufacturing uncertainty equivalent to a shift in its CoM in the Front-Left direction.

Table 4.2 – Effect of CoM shift on the robustness of the Star-shaped hexarotor

Weight position	Controller	No crash when failed	Crash when failed
Front	Not Informed	1-2-(3)	4-5-6
Back	Not Informed	1-2-6	3-4-5
Right	Not Informed	4-5-6	1-2-3
Left	Not Informed	1-2-3	4-5-6
Centered	Not Informed	1-(2)-(3)	4-5-6
Centered	Informed	1-2-3	4-5-6

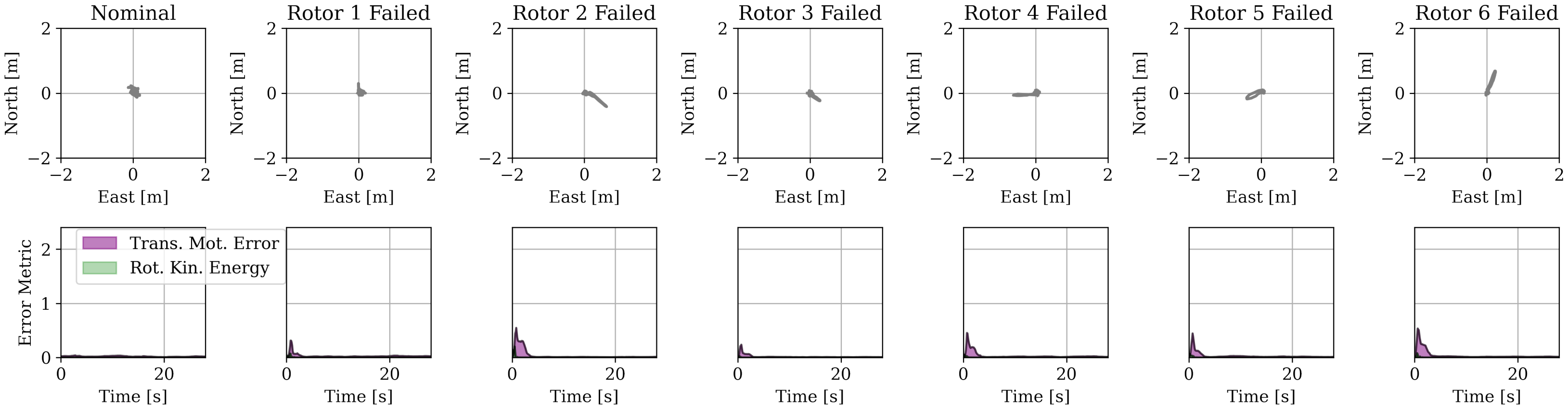

(a) Y-shaped hexarotor flights (controller not informed of the fault)

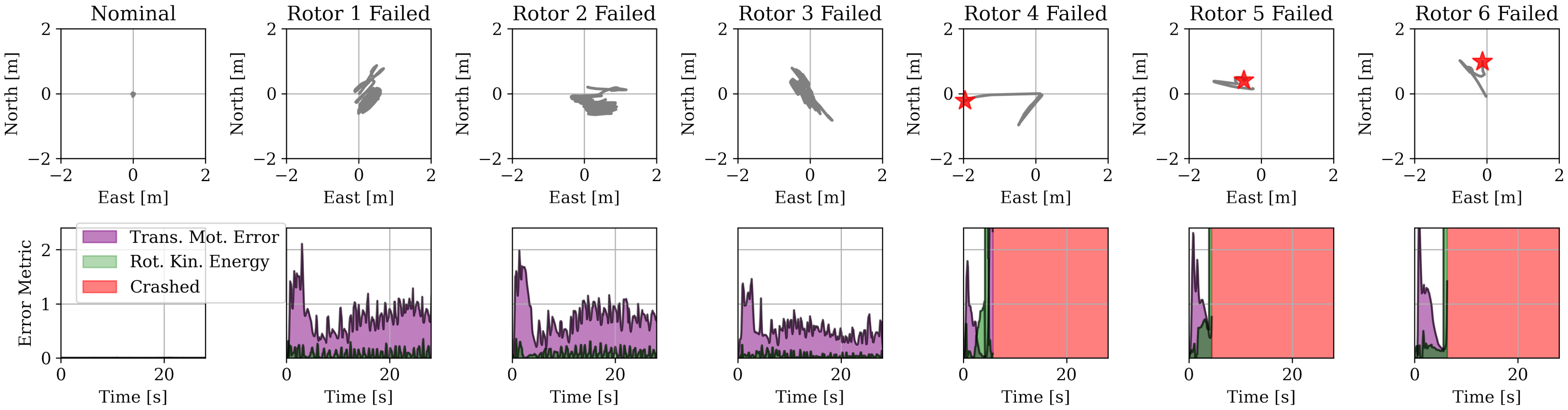

(b) Star-shaped hexarotor flight with the controller not informed of the fault

Figure 4.8 – Experimental campaign studying robustness of Star-shaped and Y-shaped hexarotors. Each of the subfigures shows (top) the North-East projection of the flight trajectory onto the $(\boldsymbol{x}_W, \boldsymbol{y}_W)$ plane, and (bottom) the translation motion error and the rotation kinetic energy of the platform during the corresponding flight.

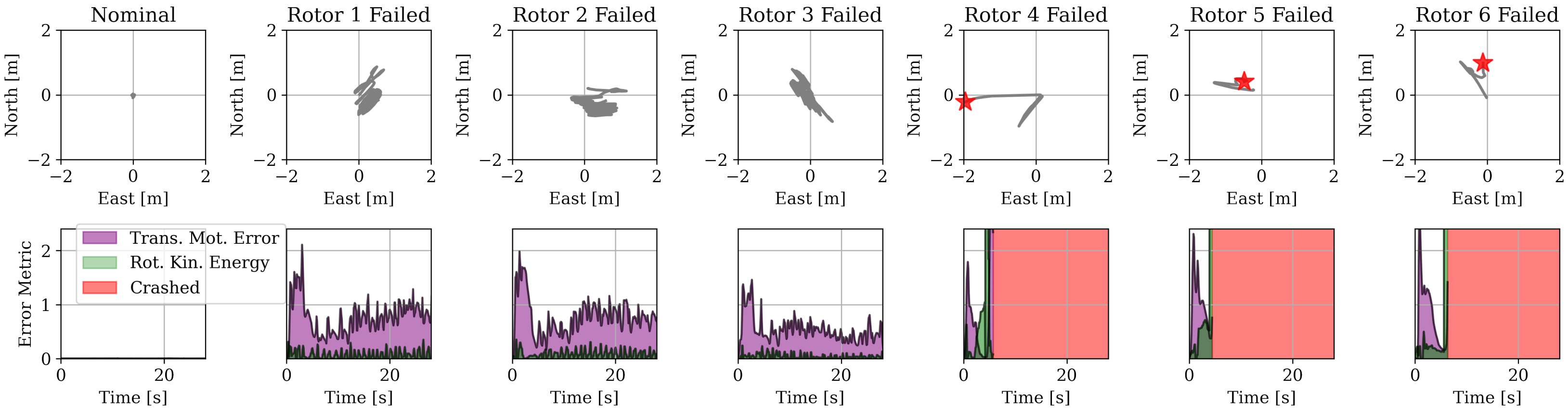

(a) Star-shaped hexarotor flight with the controller not informed of the fault

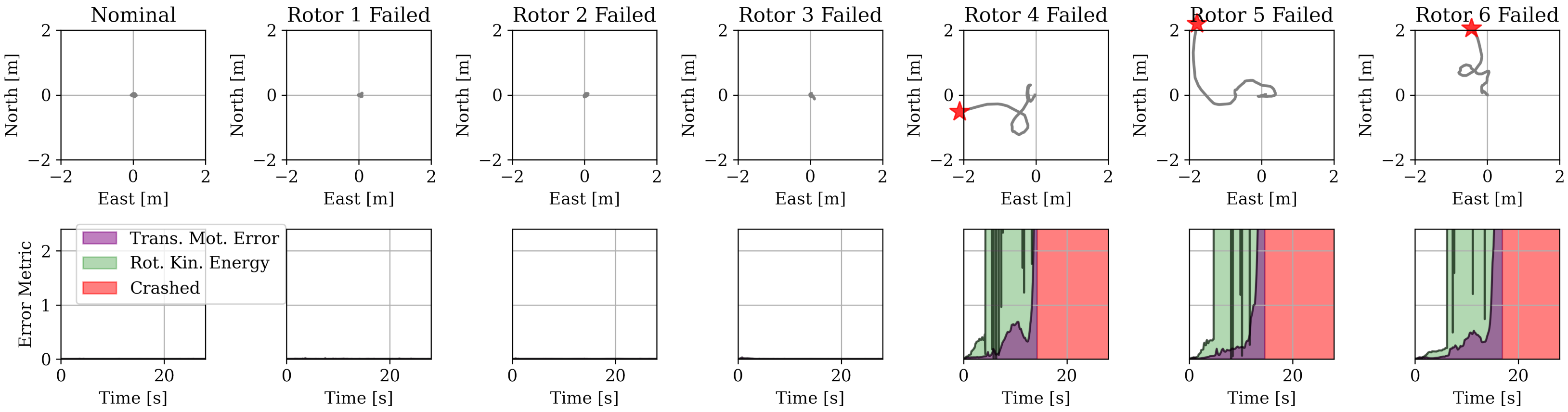

(b) Star-shaped hexarotor flight with the controller informed of the fault

Figure 4.9 – Experimental campaign studying robustness of Y-shaped hexarotor with an informed as compared to an uninformed controller. Each of the subfigures shows (top) the North-East projection of the flight trajectory onto the $(\boldsymbol{x}_W, \boldsymbol{y}_W)$ plane, and (bottom) the translation motion error and the rotation kinetic energy of the platform during the corresponding flight.

Path following after propeller failure To further assess the level of robustness of the Y-shaped hexarotor after propeller failure, the platform was requested to follow a circular path after the recovery from the failure of each of its six propellers. This is essential to show that the Y-shaped hexarotor is not only able to remain still but also to follow a trajectory after a failure. Fig. 4.10 shows the results of these experiments, where it can be seen that the tracking error after propeller failure is bounded and comparable to the corresponding error of the healthy platform.

We omit the plots of the Star-shaped hexarotor circular path tracking following propeller failure, as none of the propeller failures could even satisfy the statically hovering condition.

Energy consumption in healthy condition To assess experimentally the efficiency of the two designs, we compare the power consumption of each platform at hover. To do so, each platform is flown with a fully charged battery (12.6[V]) until the battery voltage reduces to 9.8[V], after which the platform flight becomes unstable due to the battery's current drop. Fig. 4.11 shows the voltage throughout the test flights, where the flight of each platform was repeated twice. It can be seen from this figure that the flight time of the Y-shaped hexarotor is 60% of the corresponding Star-shaped flight time. In addition, the initial voltage drop of the Y-shaped hexarotor (i.e., the voltage drop required for take off) is higher than the corresponding drop in the case of the Star-shaped hexarotor, which suggests a higher drawn current at hover.

It seems that while our efficiency analysis in Sec. 4.3 showed a required current increase of only 11%, the flight time has reduced much more. As the relation between the battery discharge and the required current is a complex relation that depends on multiple factors (battery properties, withdraw current, battery temperature, battery usage), we will not delve more thoroughly into this topic in this thesis, as we believe it deserves a complete work, with extensive experimentations.

Moreover, the reduction in efficiency is expected to be caused in part by the interaction between the co-axial propellers and in part by the increased interaction between the flow of the propellers with the arms connecting the propellers to the platform, given that the arms of the Y-shaped hexarotor are duplicated (i.e., present both below and above propellers) and also made wider than those of the Star-shaped hexarotor, to gain the required structural robustness, as seen in Fig. 4.7.

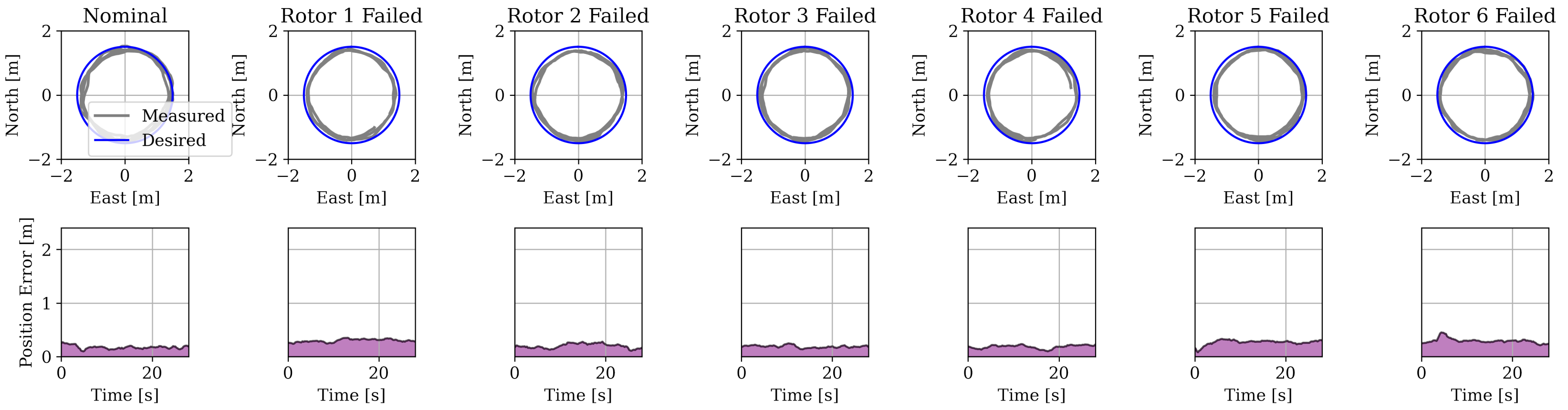

Figure 4.10 – Circular path following of Y-shaped hexarotor in healthy and failed rotor conditions. (Top) shows the North-East projection of the flight trajectory onto the $(\boldsymbol{x}_W, \boldsymbol{y}_W)$ plane, (bottom) shows the norm of the positional error.

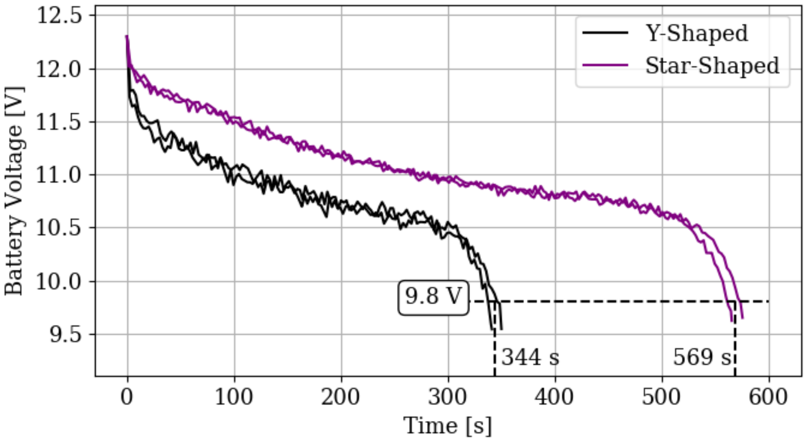

Figure 4.11 – Experimental efficiency analysis of Star-shaped and Y-shaped platforms: measured battery voltage during flight of Star-shaped and Y-shaped hexarotor at hover. Total flight time was recorded twice for each platform as the time for the voltage to drop from 12.6[V] (fully charged battery) to 9.8[V].

4.5 Conclusions

In this chapter we studied the robustness of different coplanar/collinear hexarotor designs, where the focus was mostly on the Y-shaped and Star-shaped hexarotors. The two designs are built with identical components and similar properties to systematically compare the abilities of each. The two platforms rely on the INDI controller to fly robustly even after the failure of any(some) of their propellers respectively.

In addition, we introduced an intuitive geometrical interpretation of the platforms' static hovering ability. Following this geometric interpretation, we showed the vulnerability of the Star-shaped hexarotor to the single failure of some of its propellers and the robustness of the Y-shaped hexarotor to the single failure of any of its propellers.

The static hovering of the two designs is further studied via an extensive experimental campaign that validates the theoretical hypotheses. In addition, their respective efficiency was tested comparing the power consumption of each.

Following the above analysis, we can clearly see that while the Y-shaped hexarotor is robust to the failure of any propeller, it is less efficient than the Star-shaped design. On the other hand, the Star-shaped design is a more efficient design, while it is vulnerable to the failure of some of its propellers.

The study of a platform that can benefit from the efficiency and robustness of each of the two designs is an interesting research line that is left as a future work.

CHAPTER 5

Omnidirectional MAV design with minimal uni-directional thrusters

---

5.1 Introduction

The objective of this chapter is to introduce a prototype omnidirectional multirotor platform with seven fixed unidirectional propellers. As was demonstrated in [Tognon–2018] and mentioned in Chapt. 3, the minimum number of fixed unidirectional propellers to achieve OD is $N = 7$. As such, in this chapter we aim to build such a platform and demonstrate through real experiments its OD property.

Then we will analyze more in depth the OD property of the platform through the analysis of the platform's force set $\mathfrak{F}_1$, to show the limitations of building an OD platform with $N = n_u = 7$. Since the $\mathfrak{F}_1$ set takes into consideration the propeller limits, in addition to the platform geometry, it allows a better analysis of its properties.

State-of-the-art Omnidirectional Platforms The most common UAV in the literature is the quadrotor [Mahony–2012; Faessler–2018], which can apply unidirectional forces and three-dimensional moments. While the use of the classical quadrotor lead to many contributions in the field of Multi-Rotor Aerial Vehicle (MRAV) design, control and trajectory tracking, the platform is still an underactuated platform that cannot apply apply lateral forces and therefore needs to tilt to move laterally.

As such, multiple designs from the literature presented platforms that exploit the full six-dimensional wrench space, aiming to decouple the platform's forces from its orientation. The works in [Ryll–2019] and [Romero–2007b] use tilted unidirectional thrusters to apply 3-dimensional forces independently from the applied moment. However, these platforms cannot apply forces in any direction, and are usually limited to force directions in the upper hemi-sphere.

Conversely, [Ryll–2016b; Ryll–2015b; Long–2013] actively tilt the propellers to achieve omnidirectional flight: [Ryll–2016b] synchronizes the tilt angle of the propellers of a hexarotor, [Ryll–2015b] actively tilts the angles of a quadrotor independently about their radial axes, and [Long–2013] actively tilts the propellers of a trirotor, while adding a fixed central propeller to carry the weight of the vehicle. While popular in the literature, actuated propellers add weight to the platform due to the extra actuators. In addition, propeller tilting is achieved via servo motors, which cannot guarantee instantaneous force exertion due to the time required to re-orient the propellers.

On the other hand, [Brescianini–2016a; Park–2016b; Dyer–2019] achieve omnidirectional flight with 6 or 8 bidirectional thrusters. While their solutions are very interesting, as illustrated in Chapt. 3, bidirectional thrusters exhibit a singularity near the zero thrust region. Moreover, commercial hardware solutions for bidirectional thrusters are not satisfactory, where commercial Electronic Speed Controller (ESC)s allowing the control of bidirectional propellers are scarce at the moment in which this thesis is written. Additionally, bidirectional propellers provide typically less thrust than their uni-directional equivalent at the same rotational speed.

As such, in this chapter we aim to design an omnidirectional platform with fixed, uni-directional propellers. Moreover, we aim to design a minimal design, i.e., with the minimal number of required fixed uni-directional propellers to achieve the desired property. The interested reader is referred to [video01–2020b] for a summarizing presentation of the content of this chapter, in addition to demonstrations of the corresponding experiments.

5.2 O_+^7 design

This section aims to introduce the design approach of an O_+^7 (O-plus-seven, or omni-plus-seven) platform, and demonstrate the production of a working prototype, where we refer to O_+^7 as any omnidirectional platform with 7 uni-directional propellers.

5.2.1 Optimization of the Design

Let us first assume that all propellers in our design are identical, and as such, and following the nomenclature from Chapt. 2, we can define a fixed propeller aerial vehicle design as the tuple $\mathcal{T} = (N, m, \boldsymbol{V}, {}^B\boldsymbol{P}, \boldsymbol{\kappa}, c, u_{min}, u_{max})$ representing the number of propellers N, the platform mass m, the thrust direction and position of all propellers in $\mathcal{B}$ – $\boldsymbol{V}$ and ${}^B\boldsymbol{P}$, respectively – the rotation direction of the corresponding propellers $\boldsymbol{\kappa}$, the aerodynamic drag to lift coefficient c, and minimum and maximum thrust of each propeller, u_{min} and u_{max}, where $0 \leq u_{min} < u_{max}$.

While u_{min} and u_{max} are not mentioned in [Tognon–2018], they are crucial for the prototype design to guarantee the feasibility of a desired wrench $\boldsymbol{w}_d \in \mathbb{W}$, where $\mathbb{W}$ is the set of desired wrenches necessary for the platform's flight. As such, we can write the following condition for the wrench space of an omnidirectional platform:

$$\forall\, \boldsymbol{w}_d \in \mathbb{W} \quad \exists\, \boldsymbol{u}_\lambda^d \quad s.t. \quad \boldsymbol{w}_d = \boldsymbol{F}\boldsymbol{u}_\lambda^d \quad and \quad \boldsymbol{u}_\lambda^d \in \mathbb{U}, \tag{5.1}$$

where $\mathbb{U}$, the set of allowable control thrust, is defined as the N-dimensional hypercube s.t. $\mathbb{U} = \bigtimes_{i=1}^{N} [u_{min}, u_{max}]$.

We denote with $\mathbf{1}$ the column vector with all ones. Its size is understood from the context. Given two vectors $\boldsymbol{x}$ and $\boldsymbol{y}$, the notations $\boldsymbol{x} \geq \boldsymbol{y}$, $\boldsymbol{x} > \boldsymbol{y}$ are intended component-wise.

Definition 5.2.1. a design tuple $\mathcal{T}$ is said to be OmniPlus (O_+) if one of the following equivalent conditions holds [Tognon–2018]

$$\forall \boldsymbol{w} \in \mathbb{R}^6 \quad \exists \boldsymbol{u}_\lambda \geq u_{min}\mathbf{1} \quad s.t. \quad \boldsymbol{F}\boldsymbol{u}_\lambda = \boldsymbol{w} \tag{5.2}$$

$$\forall \boldsymbol{w} \in \mathbb{R}^6 \quad \exists \boldsymbol{u}_\lambda \geq \mathbf{0} \quad s.t. \quad \boldsymbol{F}\boldsymbol{u}_\lambda = \boldsymbol{w} \tag{5.3}$$

$$rank(\boldsymbol{F}) = 6, \quad \exists \boldsymbol{b} = [b_1 \ldots b_n]^\top > \mathbf{0} \quad s.t. \quad \boldsymbol{F}\boldsymbol{b} = \mathbf{0} \tag{5.4}$$

Allocation Strategy Given an O_+ design and a desired wrench, following *condition* Eq. (5.4), one may calculate the thrust $\boldsymbol{u}^*_\lambda \quad s.t. \quad \boldsymbol{u}^*_\lambda = \boldsymbol{F}^\dagger \boldsymbol{w}_d$ where $\boldsymbol{F}^\dagger$ is the *Moore-Penrose* pseudo inverse of $\boldsymbol{F}$. As was proven in [Tognon–2018], $\boldsymbol{u}^*_\lambda$ always has at least a negative entry, and as such violates *condition* Eq. (5.2).

Let us consider an ellipsoid that represents the attainable wrench space $S_w = \{\boldsymbol{w} \in \mathbb{R}^6 | \boldsymbol{w}^\top \Sigma \boldsymbol{w} \leq \mathbf{1}\} \subset \mathbb{R}^6$, where $\Sigma \in \mathbb{R}^{6\times6}$ is a positive definite matrix. The set U_w maps S_w through the linear transformation $\boldsymbol{F}$ such that $U_w = \{\boldsymbol{u}_\lambda \in \mathbb{R}^N | \boldsymbol{w} = \boldsymbol{F}\boldsymbol{u}_\lambda, \forall \boldsymbol{w} \in S_w\}$. U_w maps S_w one to one, however, as stated in the previous paragraph, not all solutions $\boldsymbol{u}^*_\lambda \in U_w$ have all positive entries, and as such $U_w \not\subset \mathbb{U}$.

Let's define a vector $\boldsymbol{b} \in null(\boldsymbol{F}) \cap \mathbb{R}^N_+$, then $\boldsymbol{b} \perp \boldsymbol{u}^*_\lambda$. Any solution such that $\boldsymbol{u}^{**}_\lambda = \boldsymbol{u}^*_\lambda + \lambda \boldsymbol{b}$ with $\lambda > 0 \in \mathbb{R}$ satisfies $\boldsymbol{w}_d = \boldsymbol{F}\boldsymbol{u}^{**}_\lambda$. As such, the objective of the allocation strategy would be to find λ such that $\boldsymbol{u}^{**}_\lambda \in \mathbb{U}$ as follows:

$$\lambda = \underset{\boldsymbol{u}^{**}_\lambda \in \mathbb{U}}{\operatorname{argmin}} \|\boldsymbol{u}^{**}_\lambda(\boldsymbol{u}^*_\lambda, \boldsymbol{b})\| = \underset{\boldsymbol{u}^{**}_\lambda \in \mathbb{U}}{\operatorname{argmin}} \|\boldsymbol{u}^*_\lambda + \lambda \boldsymbol{b}\|. \tag{5.5}$$

The control thrust found in Eq. (5.5) satisfies $\boldsymbol{u}^{**}_\lambda \in U^*_w$, where $U^*_w = U_w \cap \mathbb{U}$. It is noted that U^*_w also maps S_w one to one, and as such, in what follows we refer to $\boldsymbol{u}^{**}_\lambda(\boldsymbol{w})$ as the control thrust in U^*_w that allows the platform to apply wrench $\boldsymbol{w}$.

Definition 5.2.2. an O_+ design is said to be optimal if its space U^*_w has minimum eccentricity, and if its propellers equally share the effort to keep $\boldsymbol{u}^{**}_\lambda \in \mathbb{U}$ calculated in Eq. (5.5).

Minimizing the eccentricity of U^*_w allows the platform to apply lower maximum thrust for each desired wrench since the platform will be sharing the load equally among its propellers; this problem can be solved by minimizing the condition number of $\Sigma^{-1}\boldsymbol{F}$. On the other hand, to satisfy the second condition of *Definition* 5.2.2, it is easy to be convinced that the best choice is to have $\boldsymbol{b} = \mathbf{1}$. For more details we refer the reader to [Tognon–2018].

5.2.2 Parameter Optimization

In this subsection we detail the choice of parameters that allow the design $\mathcal{T}$ to satisfy the conditions and requirements mentioned above. First, we make the following assumptions:

- the platform dimensions are chosen separately and fixed throughout the optimization,
- all motors and propellers used in the platform are identical,
- motor and propeller choice is made separately from this optimization problem,

- propeller rotation directions are chosen prior to the optimization, with these directions alternating between one propeller and the next, i.e., $\kappa_i = (-1)^i$ for $i = 1 \dots N$.

With these assumptions, we can clearly see that the *etero-vectoring* part of $\mathcal{T}$ (N, m, ${}^{B}\boldsymbol{P}$, $\boldsymbol{\kappa}$, c, u_{min}, u_{max}) is fixed, in addition to the norm of the vectoring part $\|\boldsymbol{v}_i\|$ for $i = 1 \dots N$, while the optimization problem should choose the direction of the vectoring part ($\boldsymbol{V}$). It is noted that $\|\boldsymbol{v}_i\| = 1$ as the allocation matrix $\boldsymbol{F}$ is assumed to map wrench $\boldsymbol{w}$ to propeller thrust $\boldsymbol{u}_{\lambda}$.

To highlight the optimization problem, let us rewrite $\boldsymbol{F}_1$ and $\boldsymbol{F}_2$ as follows:

$$\boldsymbol{F}_1 = [\boldsymbol{I}_3\boldsymbol{v}_1 \dots \boldsymbol{I}_3\boldsymbol{v}_N] \tag{5.6}$$

$$\boldsymbol{F}_2 = [(S({}^{B}\boldsymbol{p}_1) + \kappa_1 c\boldsymbol{I}_3)\boldsymbol{v}_1 \dots (S({}^{B}\boldsymbol{p}_N) + \kappa_N c\boldsymbol{I}_3)\boldsymbol{v}_N]. \tag{5.7}$$

Then we can rewrite the second part of Eq. (5.4) as:

$$\underbrace{\begin{bmatrix} \boldsymbol{I}_3 b_1 & \dots & \boldsymbol{I}_3 b_N \\ (S(\boldsymbol{d}_1) + \kappa_1 c\boldsymbol{I}_3)b_1 & \dots & (S(\boldsymbol{d}_n) + \kappa_N c\boldsymbol{I}_3)b_N \end{bmatrix}}_{\boldsymbol{A}(N, {}^{B}\boldsymbol{P}, \boldsymbol{\kappa}, c, \boldsymbol{b})} \boldsymbol{V} = \boldsymbol{0}, \tag{5.8}$$

where $\boldsymbol{I}_i$ is the i-by-i *identity matrix.*

Following this formalism, the O_{+} parameter optimization can be written as follows:

$$\min \; cond(\Sigma^{-1}\boldsymbol{F}) \tag{5.9}$$

subject to the following constraints

$$\boldsymbol{V}^{\top}\boldsymbol{D}_1\boldsymbol{V} = 1, \; \dots, \boldsymbol{V}^{\top}\boldsymbol{D}_N\boldsymbol{V} = 1 \tag{5.10}$$

$$rank(\boldsymbol{F}(\boldsymbol{\kappa}, c, {}^{B}\boldsymbol{P}, \boldsymbol{V})) = 6 \tag{5.11}$$

$$\boldsymbol{A}(N, {}^{B}\boldsymbol{P}, \boldsymbol{\kappa}, c, \boldsymbol{1})\boldsymbol{V} = \boldsymbol{0} \tag{5.12}$$

where $\boldsymbol{D}_i = diag(\boldsymbol{D}_{i1} \dots \boldsymbol{D}_{iN})$ is a $3N$-by-$3N$ diagonal matrix, with $\boldsymbol{D}_{ij} = 0$ if $j \neq i$ and $\boldsymbol{D}_{ii} = \boldsymbol{I}_3$ otherwise.

We note that in the choice of the propeller placements, we chose all propellers to be coplanar, placed in a star shape with the first propeller arm along $\boldsymbol{x}_B$, i.e., ${}^{B}\boldsymbol{p}_1 = [d, 0, 0]^{\top}$, and ${}^{B}\boldsymbol{p}_i = {}^{B}\boldsymbol{p}_1\boldsymbol{R}_{\boldsymbol{z}}(2\pi(i-1)/N)$ for $i = 2 \dots N$, where d is the norm of the arm connecting O_B to the Center of Mass (CoM) of any propeller, and $\boldsymbol{R}_{\boldsymbol{z}}$ is the transformation matrix corresponding to the rotation about $\boldsymbol{z}_B$.

In the aim to build an omnidirectional platform, it is desired that the force and moment ellipsoids to resemble a sphere, where the platform will be invariant to its flight direction. As such we choose Σ of the form

$$\Sigma = \begin{bmatrix} \sigma_{\boldsymbol{f}}\boldsymbol{I}_3 & \boldsymbol{0}_{3\times3} \\ \boldsymbol{0}_{3\times3} & \sigma_{\boldsymbol{m}}\boldsymbol{I}_3 \end{bmatrix} \tag{5.13}$$

where $\sigma_{\boldsymbol{f}}, \sigma_{\boldsymbol{m}} \in \mathbb{R}_{>0}$.

Finally, we analyze the maximum propeller thrust u_{max}^{d} while the platform is in hover, where we define

Definition 5.2.3. hovering (or *static hovering*) as the ability of the platform to stabilize its position and orientation for some orientation $\boldsymbol{R}_d \in SO(3)$ with zero linear and angular velocity, i.e., $(\boldsymbol{p}_B^d, \boldsymbol{R}_d, \dot{\boldsymbol{p}}_B^d, \boldsymbol{\omega}_B^d) = (\boldsymbol{p}_B^d, \boldsymbol{R}_d, \boldsymbol{0}, \boldsymbol{0})$.

Hovering is of particular interest for the design as it is a base point for the platform to apply forces and moments in any direction. The analysis of u_{max}^{d} is required for the motor choice and it is an important feature to study the feasibility of the design.

The chosen Σ, and the ensuing minimization of $cond(\Sigma^{-1}\boldsymbol{F})$, enforces a uniformity in the platform's generated force (moment) about its corresponding directions, and as such guarantees invariance of the platform to ${}^{W}\boldsymbol{R}_B$ at hovering.

While hovering, the thrust of each propeller can be calculated as

$$\boldsymbol{u}_{\lambda,d}(\boldsymbol{R}_d) = \boldsymbol{u}_{\lambda,d}^{**}\left(\begin{bmatrix} m\, g\, \boldsymbol{R}_d\, \boldsymbol{e}_3 \\ \boldsymbol{0}_3 \end{bmatrix}\right) \tag{5.14}$$

Due to the invariance of the platform to its hovering direction and to the chosen optimization constraints, it is straight forward to prove that

$$u_{max}^{d} = \max\ \boldsymbol{u}_{\lambda,d}(\boldsymbol{R}_d) = \max\ \boldsymbol{u}_{\lambda,d}(\boldsymbol{I}), \tag{5.15}$$

where the right hand part of the equality is for hovering at an identity rotation matrix. While in theory maximum propeller thrust should be the same irrespective of the hovering orientation, in practice the condition number never reaches unity, and as such there is always a difference between the max $\boldsymbol{u}_{\lambda,d}(\boldsymbol{R}_d)$ at different $\boldsymbol{R}_d$, and as such, u_{max}^{d} is found with a grid search algorithm over possible orientations.

5.3 O_{+}^{7} Protoype

For our prototype we chose to construct a platform with $N = 7$, the least number of uni-directional propellers necessary to achieve omnidirectional thrust. The platform, shown in Fig. 5.1, is built to be the smallest possible to increase its stability by reducing any possible oscillations in the arms connecting the motors to the body; as such, we chose an arm length $d = 0.16$ [m]. We then chose 5" propellers, as it is the largest diameter that can be installed on the platform without any collision between adjacent propellers. The propellers we chose enforced a drag to lift coefficient $c = 0.002$ [m], and a lift coefficient $c_f = 0.5e-4[\text{N/Hz}^2]$. Finally, the wrench ellipsoid was chosen such that $\Sigma = diag([1, 1, 1, 0.5, 0.5, 0.5])$. We estimated the platform mass before the platform construction to be around 1.1 [kg] following the component-wise weight estimation shown in Tab. 5.1.

5.3.1 Numerical Optimization

The O_{+} optimization algorithm calculated the vectoring part of the design, and reached a minimum condition number of $cond(\Sigma^{-1}\boldsymbol{F}) = 2.052$, with a vectoring

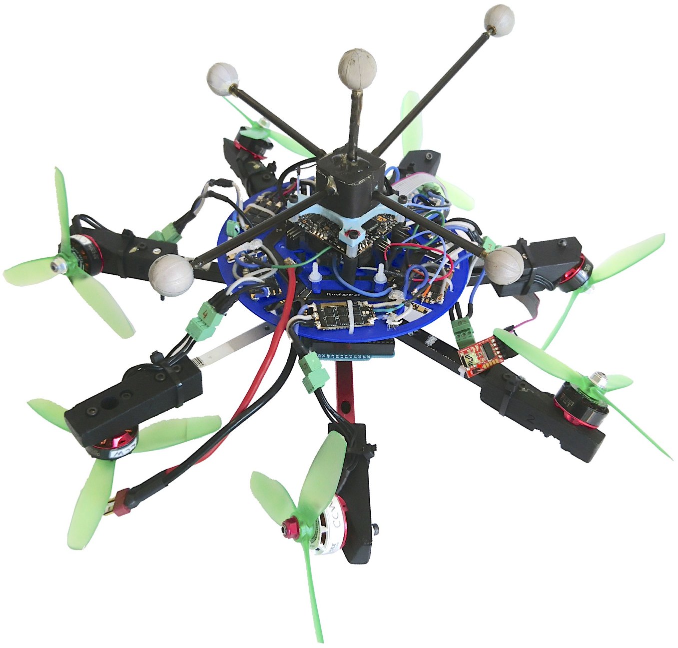

Figure 5.1 – O^7_+ prototype: the built prototype showing the motor assembly, the electronics assembly and the motion capture tracking markers.

Component	weight per unit [g]	# units	weight [g]
Motors	40	7	280
Propellers	5	7	35
Electronics	200	–	200
Mechanical parts	350	–	350
Battery	214	–	214
Total			1079

Table 5.1 – Weight estimation of the O^7_+ prototype prior to its final design and construction. It should be noted that the weight of parts that are certainly used were reported as they are, while others are estimated.

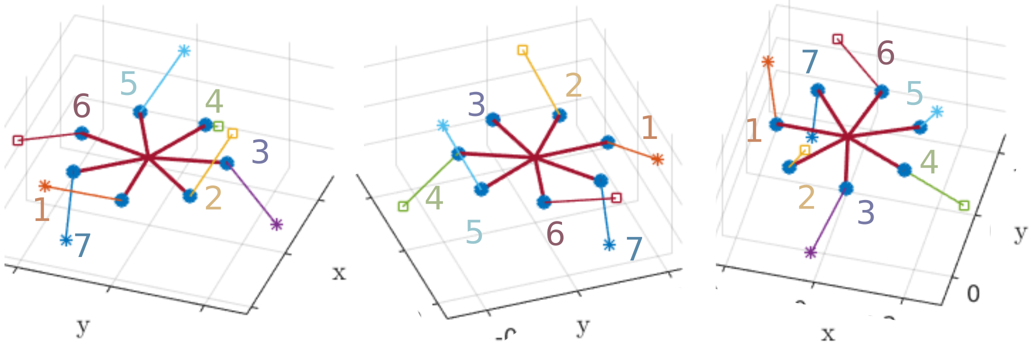

Figure 5.2 – Optimized propeller direction of the O_{+}^{7} design, with $N = 7$, $d = 0.16\,[m]$ and $c = 0.002\,[m]$ at $cond(\Sigma^{-1}\boldsymbol{F}) = 2.052$.

part as follows:

$$\boldsymbol{v} = \begin{bmatrix} 0.36 & -0.35 & 0.29 & -0.81 & -0.37 & 0.78 & 0.10 \\ -0.90 & 0.44 & 0.76 & -0.12 & 0.45 & -0.57 & -0.07 \\ 0.25 & 0.83 & -0.58 & -0.58 & 0.81 & 0.26 & -0.99 \end{bmatrix}. \tag{5.16}$$

The above thrust directions are illustrated in Fig. 5.2.

With the current parameters, the maximum propeller thrust was found to be $u_{max}^{d} = 11.18\,[\mathrm{N}]$, corresponding to a maximum rotational speed of $w_{max} = 472\,[\mathrm{Hz}]$ for the chosen propellers; as such we chose a motor that can provide a peak thrust of 14 [N] with the chosen propellers, at which the motor is required to rotate at 530 [Hz].

The chosen motor is controlled in Pulse Width Modulation (PWM) via an ESC, i.e., , the motor is controlled in open-loop, where the thrust generated at each PWM was identified with a force-torque sensor. Finally, the PWMs delivered to the ESCs are generated using an onboard microcontroller.

5.3.2 Platform Implementation

The platform body is constructed with 7 identical aluminum bars connecting the CoM of the platform to the CoM of the propellers. Each propeller is connected with a separate arm to ensure the stability of the platform. Aluminum bars are fastened together using $3D$ printed plates connected to one of their edges, while the second edge is connected to a $3D$ printed adapter that ensures the motors' connection at the calculated directions. Fig. 5.3 shows the CAD drawing of one of the adapters, while Fig. 5.4 shows the CAD drawing of the body frame assembly.

Finally, the necessary electronics and motion capture markers are placed on top

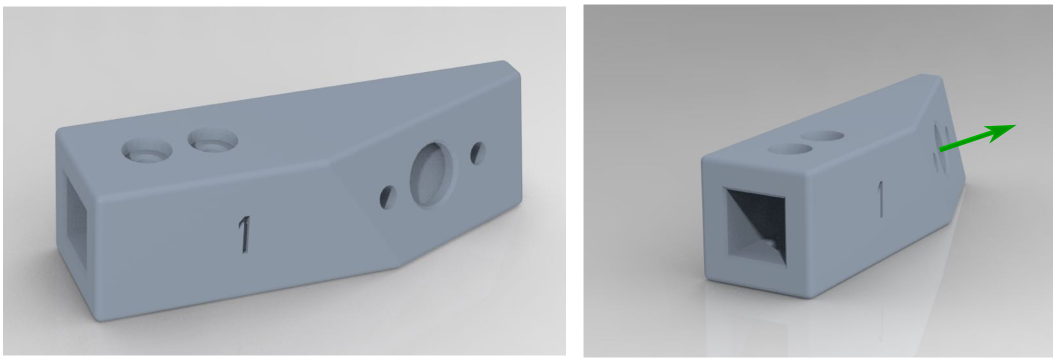

Figure 5.3 – CAD design of the motor adapter for the O^7_+ prototype motor # 1. The adapter is designed to fasten the motor to the body frame at position ${}^{B}\boldsymbol{p}_1$ and orientation $\boldsymbol{v}_1$ in $\mathcal{B}$.

of the platform, with the full prototype shown in Fig. 5.1.

The final weight of this setup without a battery is measured at $m = 0.835$ [kg].

5.3.3 Design Drawbacks

The platform prototype as presented above exhibits the following drawbacks that can affect its performance:

- Propeller open-loop control: as the propellers are controlled in open-loop, the propeller speed is not guaranteed, and correspondingly the individual motor thrust. Therefore, the applied wrench can differ from the desired one.
- Propeller airflow cylinder intersection. We define the airflow cylinder as the cylinder containing the corresponding propeller, of radius equal to the propellers', and direction similar to the corresponding propeller. Since the propellers are placed close to each other, with each producing thrust in *any* direction, it is impossible for the airflow cylinders of adjacent propellers not to intersect as shown in Fig. 5.5. This intersection affects their aerodynamics, as propellers have to withdraw air from the inflow/outflow of their adjacent propellers instead of withdrawing air from the free stream assumed static. It should be noted that it is difficult to estimate the effect of this intersection, as the change in the thrust produced by each propeller will depend on the amount of thrust provided by the adjacent propeller, and due to the nonlinearity of the corresponding intersection, as opposed to the study in Sec. 4.3.

While these drawbacks can induce an error in the applied wrench, we assume it equivalent to an external disturbance that can be compensated by the feedback controller shown in Sec. 5.5.1.

5.4 Omnidirectional hoverability of the O^7_+ design

This section aims to assess the omnidirectional hoverability of the built O^7_+ prototype, and the hoverability of platforms with similar propeller number and config-

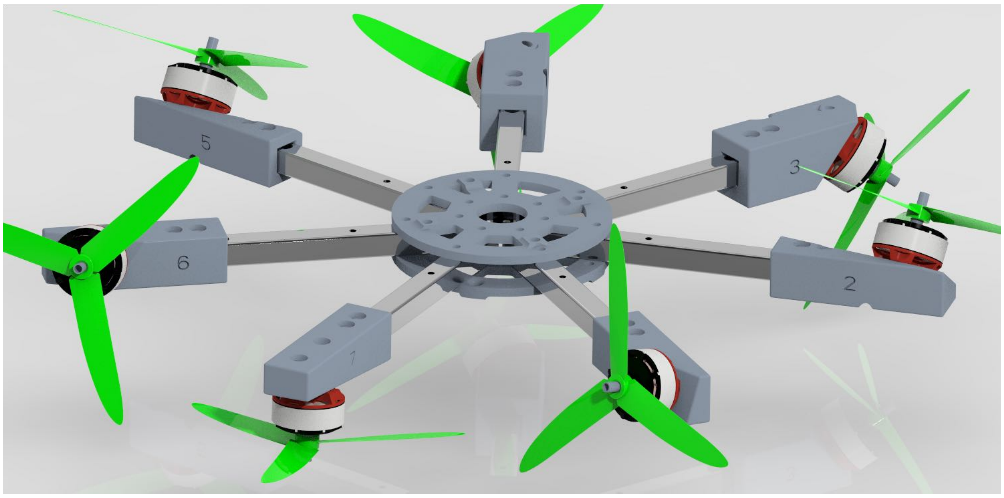

Figure 5.4 – CAD design showing the O^7_+ prototype body assembly. The body assembly shows the motors and propellers connected to the body frame with aluminum bars, where each motor was fastened to the corresponding bar with a CAD designed adapter similar to the one shown in Fig. 5.3. Each of the shown adapters was designed to fit the corresponding orientation $\boldsymbol{v}_i$ in $\mathcal{W}$.

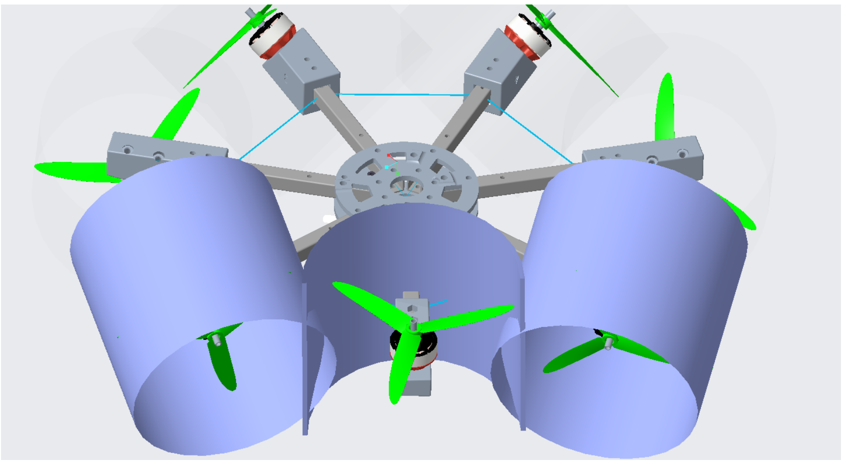

Figure 5.5 – O^7_+ prototype: example intersection between adjacent propeller airflow cylinders, showing the intersection between 7th propeller airflow cylinder with the airflow cylinders of the 1st and 6th propeller.

urations. Furthermore, this chapter studies the possibility of building a platform that can mitigate the drawbacks mentioned in Sec. 5.3.3.

The analysis done in this chapter relies on the $\mathfrak{F}_1$ set introduced in Chapt. 2, where it is used to understand the relation between the possible force in any direction in relation with the propeller maximum thrust u_{max}.

5.4.1 Omnidirectionality Metrics

The computation of the $\mathfrak{F}_1$ set is conducted as illustrated in Chapt. 2 using the fixed propellers case. The objective of this study is to understand the maximum possible lift that can be applied by the platform for a given u_{max}, while fixing the platform vectoring as illustrated above in Sec. 5.3.1.

While for coplanar/collinear platforms such as quadrotors the total lift can be easily calculated from the sum of u_{max} of all propellers, the total lift in an O_+^7 platform is more difficult to calculate due to i) the orientation of propellers in different directions rendering the maximum lift in a certain direction a complex trigonometric relation that can be deduced from Eq. (5.6) and Eq. (5.7) and the u_{max} of each propeller; ii) the requirement to calculate the possible lift in all directions, where an omnidirectional platform should be able to lift its weight in all directions in a sphere around its CoM.

While we did introduce conditions for a platform to achieve the omnidirectional property in Eq. (3.8), the corresponding conditions do not take into consideration the balance between the actuation limits and the platform mass. In this scope, we note that an omnidirectional platform is a platform that, in addition to the condition in Eq. (3.8), could apply a lift in any direction that is at least equal to its weight. More formally,

Proposition 5.4.1. A platform is omnidirectional if it is fully actuated and it can lift its weight in any direction about the origin, i.e.,

$$\text{FA and } \forall\ \bar{\boldsymbol{f}} \in \text{ball}_{\mathbb{R}^3}(\|m * \boldsymbol{g}\|),\ \bar{\boldsymbol{f}} \ni \mathfrak{F}_1 \tag{5.17}$$

As such, and given the $\mathfrak{F}_1$ set of a platform, we introduce the following metrics that allow the assessment of the omnidirectional property of a platform:

1) Omnidirectional Lift (ODL): this metric reflects the maximum lift that can be applied in any direction, and can be computed as the radius of the maximum inscribed sphere inside the $\mathfrak{F}_1$ set, centered at the origin.

2) Maximum-Directional Lift (MDL): this metric reflects the maximum lift that can be applied along at least one direction, and can be computed as the radius of the minimum circumscribed sphere about the $\mathfrak{F}_1$ set, centered at the origin.

To analyze the Omnidirectional property of a platform, one has to analyze the ODL for the given design and chosen propellers when compared to the platform mass. However, in some cases a platform could achieve a partial-Omnidirectional property, where we define this subclass of platforms as follows:

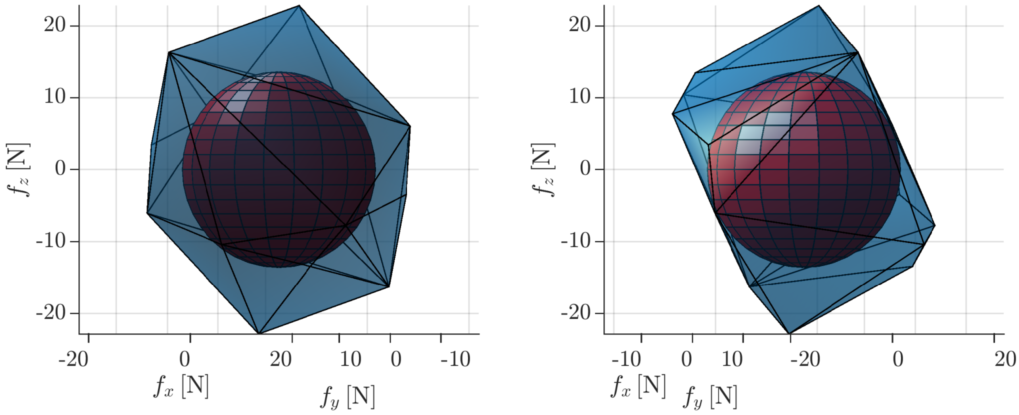

Figure 5.6 – $\mathfrak{F}_1$ set of the presented O^7_+ prototype, showing in red the maximum inscribed sphere, representing the ODL metric.

Definition 5.4.2. A partial-Omnidirectional platform is a platform that has the following conditions:

$$\text{FA and } \begin{bmatrix} \mathbf{0} \\ \mathbf{0} \end{bmatrix} \in \text{int}\{\mathbb{W}\}, \tag{5.18}$$

$$\text{ODL} \leq mg \leq \text{MDL}. \tag{5.19}$$

To facilitate the analysis of different platform designs, in what follows, we refer to the above two metrics (ODL and MDL) as the corresponding metrics normalized by the gravity constant g; as such, these metrics reflect directly the allowable platform mass given the platform design and u_{max}, and their corresponding unit is the [Kg].

Omnidirectional Hoverability of our Prototype Fig. 5.6 shows the inscribed circle in the $\mathfrak{F}_1$ set of our prototype platform. We can calculate that for our prototype the ODL $= 1.37$ [Kg] and the MDL $= 2.34$ [Kg] . As such, our prototype is a full omnidirectional platform which can lift its mass for any direction/orientation.

5.5 Experimental validation

The objective of this section is to assess experimentally the omnidirectional hoverability of our built prototype.

5.5.1 Controller

Given a desired position and orientation $\boldsymbol{p}_B^d(t)$ and $\boldsymbol{R}_d(t)$, the control strategy is straightforward as the allocation matrix $\boldsymbol{F}$ is full rank. The desired wrench is calculated as the one that brings the platform to the desired position and orientation (along with their corresponding derivatives) while compensating for gravity and gyroscopic moments. As such the desired wrench can be written as follows:

$$\boldsymbol{w}^d = \boldsymbol{G}^{-1} \begin{bmatrix} m(g\boldsymbol{e}_3 + \ddot{\boldsymbol{p}}_B^d) \ + \boldsymbol{K}_P \boldsymbol{e}_p + \boldsymbol{K}_V \dot{\boldsymbol{e}}_p + \boldsymbol{K}_{IP} \int_0^t \boldsymbol{e}_p \\ \boldsymbol{\omega}_B \times \boldsymbol{J}\boldsymbol{\omega}_B + \boldsymbol{K}_{\boldsymbol{R}} \boldsymbol{e}_{\boldsymbol{R}} + \boldsymbol{K}_\omega \boldsymbol{e}_\omega + \boldsymbol{K}_{I\boldsymbol{R}} \int_0^t \boldsymbol{e}_{\boldsymbol{R}} \end{bmatrix} \tag{5.20}$$

where $\boldsymbol{G}$ maps the desired wrench from $\mathcal{B}$ to $\mathcal{W}$ and can be written as follows:

$$\boldsymbol{G} = \begin{bmatrix} \boldsymbol{R} & \mathbf{0}_{3\times3} \\ \mathbf{0}_{3\times3} & \mathbf{I}_{3\times3} \end{bmatrix}, \tag{5.21}$$

$\boldsymbol{K}_P, \boldsymbol{K}_V, \boldsymbol{K}_{IP}, \boldsymbol{K}_{\boldsymbol{R}}, \boldsymbol{K}_\omega$ and $\boldsymbol{K}_{I\boldsymbol{R}}$ are diagonal positive definite matrices $\in \mathbb{R}^{3\times3}$ representing the controller tunable gains. $\boldsymbol{e}_p = \boldsymbol{p}_B^d - \boldsymbol{p}_B$, $\boldsymbol{e}_\omega = \boldsymbol{\omega}_B^d - \boldsymbol{\omega}_B$ and $\boldsymbol{e}_{\boldsymbol{R}} = 1/2(\boldsymbol{R}_d^\top \boldsymbol{R} - \boldsymbol{R}^\top \boldsymbol{R}_d)^\wedge$, where $[.]^\wedge$ is the inverse skew symmetric operator. Then for each desired wrench, a control thrust is calculated as described earlier in Eq. (5.5).

5.5.2 State Estimation

The platform is endowed with an IMU that captures the platform's specific linear acceleration and angular velocity. Furthermore, its position and orientation are tracked with a motion capture system.

All measurements from the IMU are filtered with the regression-based filter introduced later in Chapt. 7. The filter is designed to reduce the noise caused by the propellers' vibration; however, as the motors are controlled in open-loop (i.e., propeller rotational velocities are not measured), the filter fit the second order polynomial to the IMU signal without separation between its signal and noise constituents. While the filter was not designed for such use, it performed acceptably well in this situation; this behavior is expected to be due to the high frequency propeller rotational speeds as compared to the acceleration and and angular velocity frequencies.

Both filtered IMU measurements and motion capture measurements are fused using an Unscented Kalman Filter (UKF) [Wan–2000] to retrieve the full pose estimate of the platform.

5.5.3 Preliminary Tests

Dynamic Simulation To further assess the performance and flyability of the prototype described in section Sec. 5.3, we simulated its dynamical system in Matlab/Simulink with the estimated mass. The simulation is made closer to reality with the addition of measurement noise and signal delays.

Fig. 5.7 shows the performance of the platform's flight with $\boldsymbol{z}_B$ circling the unit radius sphere. This figure shows that the platform is able to fly while in a variety of orientations. The simulation also shows that the platform can apply independent force and moments, and as such, orient $\mathcal{B}$ independently of its translation, while the propeller rotational velocities are kept within the allowable range.

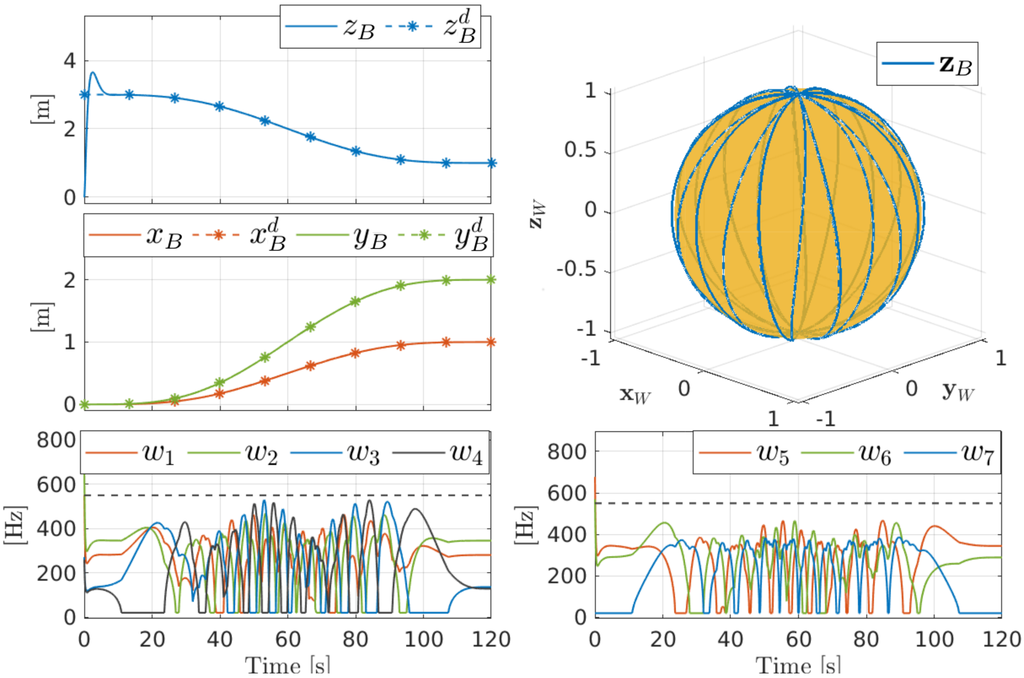

Figure 5.7 – Tracking results of the simulated O^7_+ platform while following a desired position and orientation. The platform orientation is chosen such that $\boldsymbol{z}_B$ circles the unit sphere multiple times, while the position is chosen to change smoothly and simultaneously on all axes. The desired and actual $\boldsymbol{z}_B$ are superimposed in the top right plot. A step change in the z-position is required at time $t = 0s$, where the platform is required to lift from the height of 0 [m] to 4 [m]. The figure also shows the propeller rotational velocities w_i for $i = 1 \ldots 7$, where the dashed line constitutes the limiting maximum velocity.

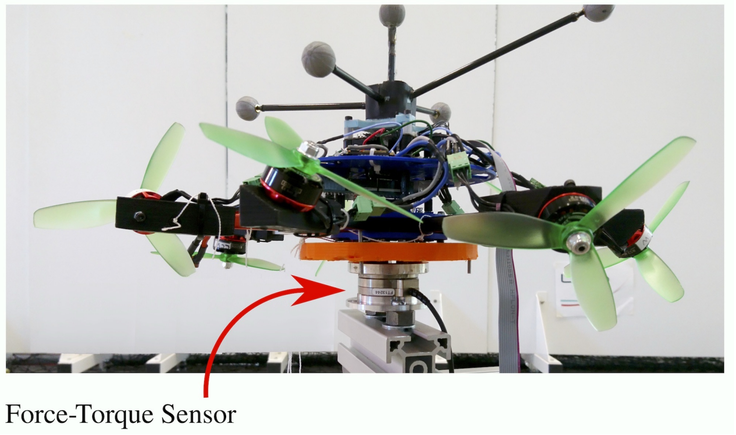

Figure 5.8 – O^7_+ prototype platform fixed to the force-torque sensor.

test	$\boldsymbol{f}_d$ [N]	$\boldsymbol{ferror}$ [N]	$\boldsymbol{m}_d$ [N.m]	$\boldsymbol{merror}$ [N.m]
1	[0 0 8]	[0.4 + 0.0 − 0.2]	[0 0 0]	[−0.1 + 0.1 + 0.1]
2	[4 2 8]	[0.0 − 0.1 − 0.3]	[0 0 0]	[−0.1 + 0.3 − 0.2]
3	[0 4 8]	[0.2 − 0.3 − 1.1]	[0 0 0]	[−0.3 + 0.1 + 0.0]
4	[0 0 8]	[0.6 − 0.1 − 0.6]	[0.2 0 0]	[−0.1 + 0.1 + 0.1]
5	[0 0 8]	[0.3 − 0.3 − 0.4]	[0 0.2 0]	[−0.0 − 0.1 + 0.1]
6	[0 0 8]	[0.3 − 0.1 − 0.4]	[0 0 0.2]	[−0.0 + 0.1 − 0.0]

Table 5.2 – Analysis of the nominal and measured wrench of the O^7_+ prototype platform. This table represents the nominally applied force $\boldsymbol{f}_d$ and moment $\boldsymbol{m}_d$, and their respective measured error.

Wrench Tests To assess the discrepancy between the ideal model and the built prototype, a force-torque sensor was used to measure the generated wrench in a static experiment as shown in Fig. 5.8. Tab. 5.2 shows the force and moment constituents of the desired nominal wrench $\boldsymbol{w}_d$ and the corresponding error between the measured and nominal wrench $\boldsymbol{w}_{error} = \boldsymbol{w}_{measured} - \boldsymbol{w}_d$.

We can observe from the data in Tab. 5.2 an error between the measured and nominal values of the applied wrench; it can also be observed that the value of this error changes depending on the desired nominal wrench. While we could not identify clearly the cause of these errors, they were expected due to the motor speed control and aerodynamic interaction between adjacent propellers, in addition to manufacturing imperfections (see Sec. 5.3.3).

5.5.4 Flight Experiments

System Setup As stated in Sec. 5.5.2, the platform is endowed with an IMU, which exports the raw specific linear acceleration and angular velocity measure-

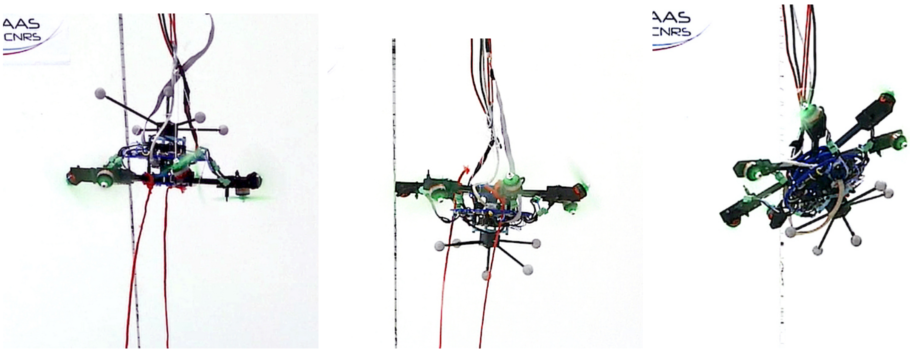

Figure 5.9 – Preliminary hovering tests of the O_{+}^{7} prototype platform: a) platform hovering horizontally, b) platform hovering upside down, c) platform hovering at a tilted orientation such that $\phi_d = 130°$.

ments at 1 [kHz]; in addition, the platform position and orientation are tracked with a motion capture system at 100 [Hz]. Both measurements are fused by a UKF running at 1 [kHz], and providing an estimate of the platform state. The platform controller is implemented in Matlab/Simulink at 500 [Hz], while the onboard microcontroller delivers the desired PWM to the ESCs. Most software (excluding the controller), including those used for the communication between Matlab and the platform, are developed in C++ using Genom3 [Mallet–2010], a code generator and formal software component description language that allows assembling middleware-independent components in a modular system. These software can be found here: `https://git.openrobots.org/projects/telekyb3`

The platform is top-connected to a power supply cable, in addition to multiple data cables allowing the back and forth communication with the off-board controller PC.

Hovering To preliminarily test the omnidirectional flight ability of the platform, we ask the vehicle to lift off from its hanged position and hover in place in multiple orientations as shown in Fig. 5.9. The performance of the platform in each of the desired orientations is shown in Fig. 5.10 through Fig. 5.12. These figures show that the platform is able to hover horizontally, upside down, and at a tilted angle.

Remark. In all these experiments, the propeller rotational velocities are within the acceptable range. Moreover, the maximum propeller rotational velocity is around 380 [Hz], far from the maximum allowed rotational velocity of 550 [Hz].

Remark. While the platform is able to hover at these orientations, there is a noticeable tracking error in all experiments even if the controller gains have been tuned specifically for each experiment to reduce tracking error while assuring the platform's stability.

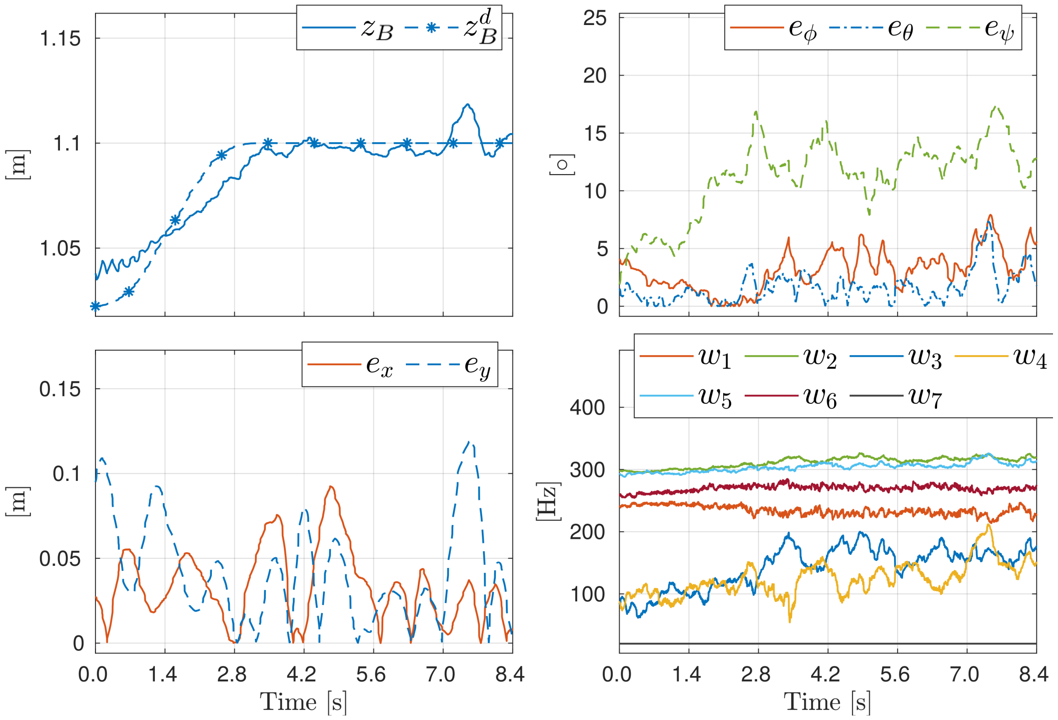

Figure 5.10 – Performance of the O_+^7 prototype platform while hovering horizontally: (top-left) shows the desired and estimated platform height, (top-right) shows the angular errors, (bottom-left) shows the norm of the xy error, and (bottom-right) shows the propeller desired rotational velocities.

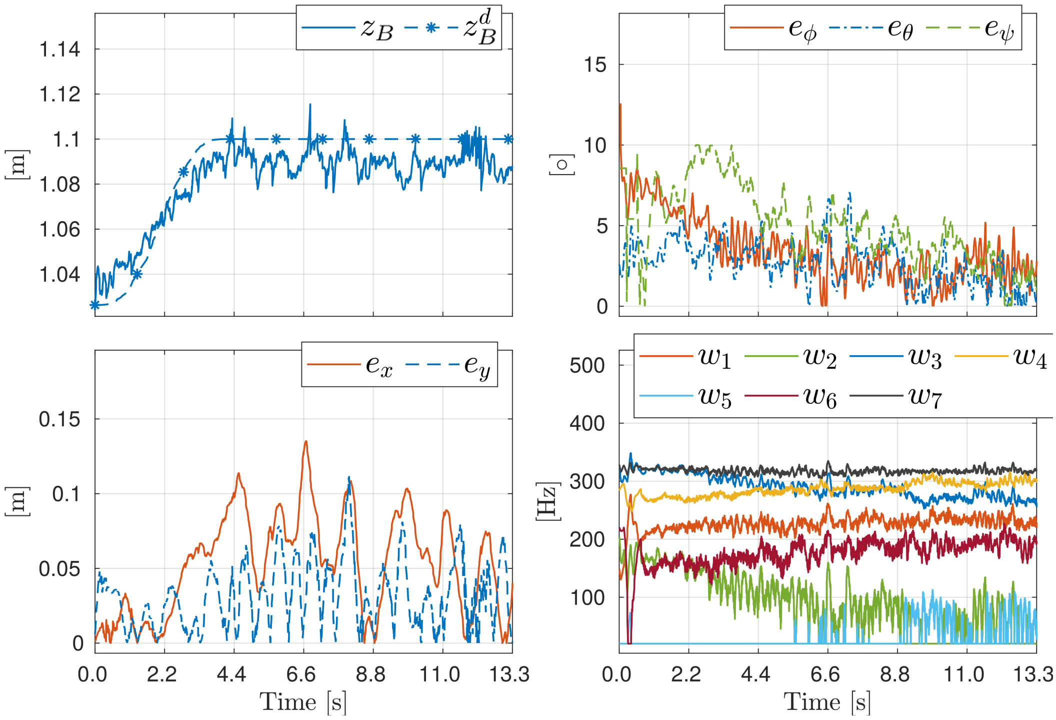

Figure 5.11 – Performance of the O^7_+ prototype platform while hovering with $\boldsymbol{z}_B$ pointing in the negative $\boldsymbol{z}_W$ direction, i.e., , $\phi_d = 180°$: (top-left) shows the desired and estimated platform height, (top-right) shows the angular errors, (bottom-left) shows the norm of the xy error, and (bottom-right) shows the propeller desired rotational velocities.

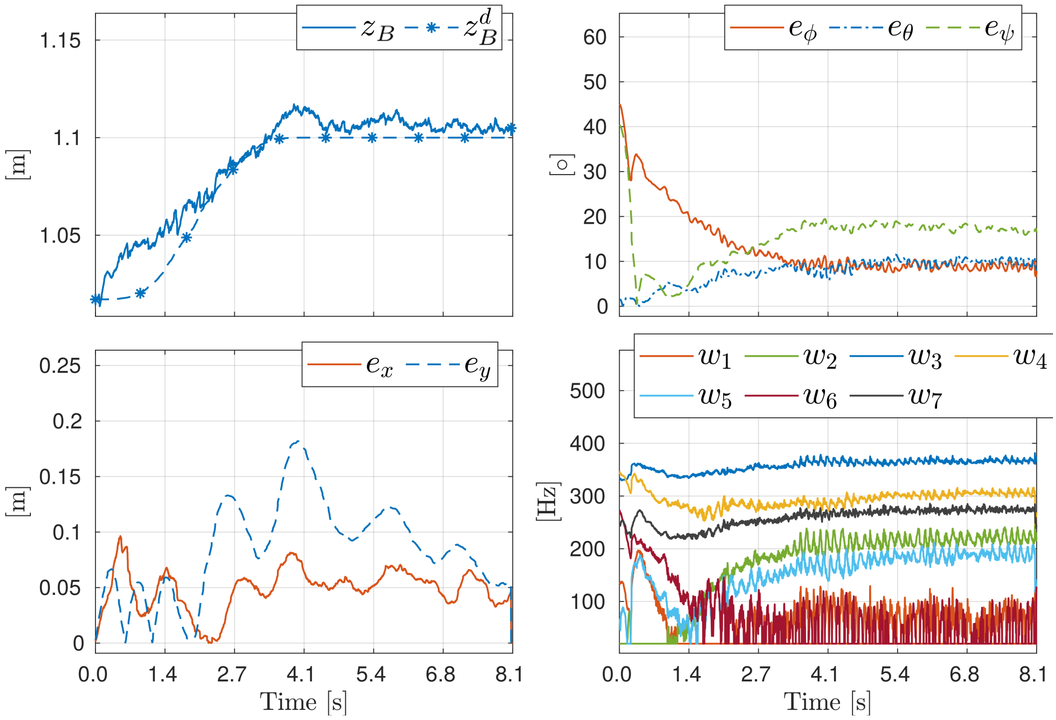

Figure 5.12 – Performance of the O_{+}^{7} prototype platform while hovering at a tilted orientation such that $\phi_d = 130°$, $\theta_d = 0°$ $\psi_d = 90°$: (top-left) shows the desired and estimated platform height, (top-right) shows the angular errors, (bottom-left) shows the norm of the xy error, and (bottom-right) shows the propeller desired rotational velocities. The platform starts its maneuver while being oriented near upside down, i.e., $\phi(t = 0s) \approx 180°$.

5.6 Upgraded O_+^7 design

In this section we attempt to study the feasibility of a new O_+^7 design that overcomes two of the drawbacks of the design presented above. The first drawback that we aim to overcome is the aerodynamic interaction between adjacent propellers. While this drawback was not formally diagnosed, we believe that a platform with larger arms could allow better spacing between adjacent propellers, and as such, eliminate the chance of such interactions. At the same time, we aim to overcome the drawback of the required propeller high angular velocity. As stated before, this high velocity required the control of the corresponding propellers in open-loop. At the same time, we do note that such high velocity causes human discomfort if the platform is eventually operated in the proximity of a human operator, in addition to the increased danger it could cause. To reduce the required rotational speeds, we rely on designing a platform with propellers larger than the ones used in the prototype shown in Fig. 5.1. We do note that the larger propellers also require a longer arm length.

Possible Propeller Dimensions in an O_+^7 design The aim of the new design is to maximize the platform lift while avoiding propellers' aerodynamic interaction. To accomplish this task, we have to use the largest propellers that could fit on the platform without any interaction between ajacent propellers. In this regards, we mention two approaches for the calculation of the maximum propeller diameter in terms of the arm length:

1) Coplanar propellers: in this case all propellers are placed in the same plane as the CoM of the platform, and equally spaced about the CoM; as such, the maximum allowable propeller diameter is equal to the circle cord it can occupy:

$$\text{maximum diameter} = 2d \sin\frac{\pi}{7} \tag{5.22}$$

2) Propellers placed on a sphere: in this case we assume propellers to be placed equally spaced on the surface of a sphere centered at the platform's CoM. In this case, the maximum allowable propeller diameter is equal to the minimum cord length of the sphere between two adjacent propellers' CoMs. The placement of the propellers is done in a way to maximize the distance between adjacent propellers using the Bauer's spiral method [Arthur–2015], and the minimum distance is computed numerically. Following this method, the maximum propeller diameter is such that:

$$\text{maximum diameter} = d \tag{5.23}$$

Following the above propeller diameter calculations, an additional safety factor has to be considered to avoid propeller tip collision, and to avoid lateral aerodynamic interactions between adjacent propellers.

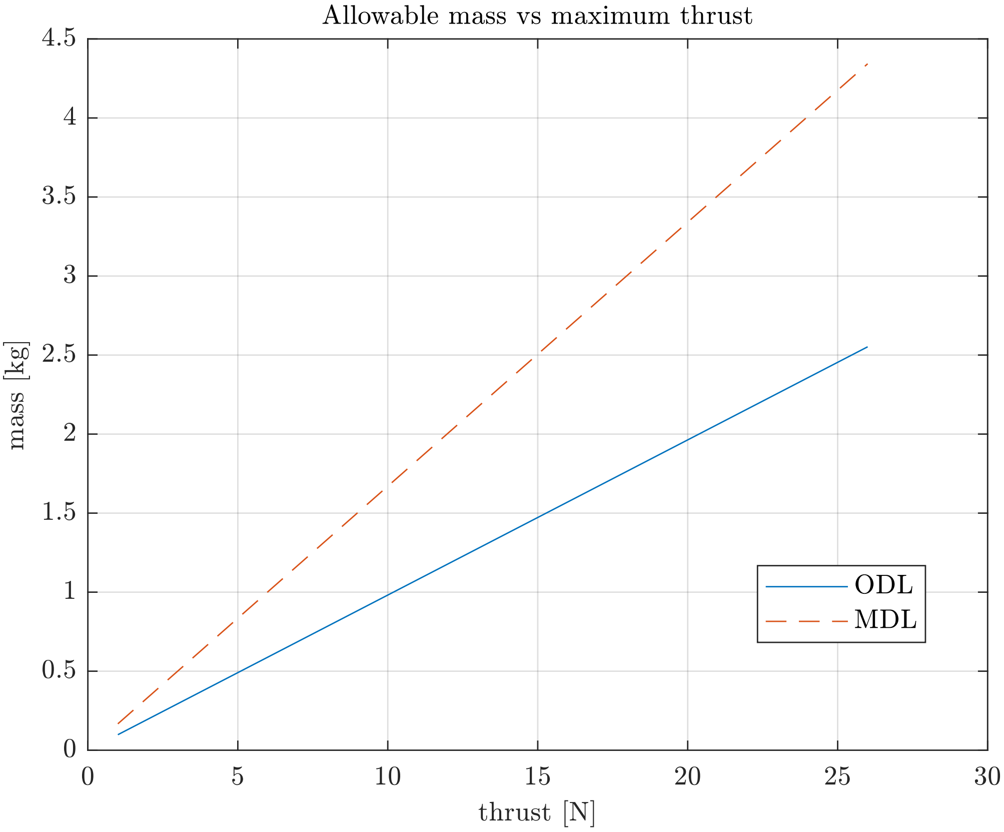

Figure 5.13 – Graph showing the relation, in the presented O_+^7 design, between the propellers' maximum lift u_{max}, and the maximum lift mass [Kg] following the ODL metric and the MDL metric (normalized by g). The data from this graph was calculated based on the design presented in Sec. 5.3.

Maximum Lift of an O_+^7 Platform Following the above, we calculated the lift metrics introduced in Sec. 5.4.1 for different u_{max} while fixing the vectoring part of our O_+^7 design as shown in Sec. 5.3. The results of this analysis are shown in Fig. 5.13, which shows that for a fixed design, the relation between the ODL and MDL metrics and the maximum propeller lift is linear.

Upgraded O_+^7 design Following this analysis, we can estimate the weight of our new platform from the components used in the FiberTHex platform (App. A) as shown in Tab. 5.3. It should be noted that in this design we are using MK3644 motors from MikroKopter, instead of the MK3638 used in the FiberTHex due to the difference in the required power. In addition, we do note that the ESCs used in the FiberTHex (along with the embedded controller) can spin each motor with a maximum rotational speed of 120 [Hz]; as such, the Upgraded O_+^7 design might require a different ESC, however, we assume that the ESCs that should be used on this design to have equal weight to the ones used in the FiberTHex.

Following the estimated weight of the new O_+^7 platform, the required u_{max} per propeller needed to achieve omnidirectional hoverability of the platform(i.e., ODL

Component	weight per unit [g]	# units	weight [g]
Motors	111	7	777
Propellers	15	7	105
Motor Mountings	22	7	154
Electronics	391	–	391
Mechanical parts	549	–	549
Battery	398	–	398
Total			2374

Table 5.3 – O_+^7 estimated new design: weight estimatation of each of the platform components based on the components used for the FiberTHex platform (App. A).

metric equals the platform estimated mass) is estimated at $u_{max} = 24.5$[N].

Moreover, the arm length of the platform is set at $d = 0.4\,$[m]. In this case, the maximum propeller radius that could fit the platform geometry is 13.7” for the coplanar case and 15.75” for the sphere placement case. We will assume that for safety and to avoid collisions, we can use 13” and 15” propellers respectively for the coplanar and the sphere cases.

The lift coefficient of each of these propellers is rated at 12.19 (14.41) $\times 10^{-4}$ [N/Hz^2] for the 13” (15”) propellers. Note that the lift coefficient of the 15” propeller is an estimate based on various propellers’ lift coefficients.

As such, the estimated required maximum propeller rotational speed is $\omega_{max} =$ 142 [Hz] and 130 [Hz] for the coplanar and sphere case respectively.

Conclusion Following the above analysis, we can conclude that it is possible to design an upgraded O_+^7 platform with propeller rotational speeds significantly lower than the ones required by the built prototype. This large difference is due to the relation between the platform’s dimension, weight, propeller size and required lift.

While the relation between the platform dimension and propeller size (and the possible lift it can generate) is linear, the relation between its dimension and weight is not linear. The latter is due to the fixed weight of some of the platform’s components (electronics), which constitute a significant part of the weight of smaller platforms as compared to larger ones.

We can also conclude that the ESCs that were used on the FiberTHex indeed cannot be used for the O_+^7 designed with similar dimensions to the FiberTHex, due to the required maximum propeller speeds.

5.7 Conclusions

In this chapter we have presented a novel prototype of an O_+ UAV with 7 unidirectional propellers. To our knowledge, the design is the first of its kind. We conducted an experimental campaign to assess the model and the prototype. Our experiments show that the platform is able to hover in many directions. From our tests, we have realized that there is a discrepancy between the nominal desired wrench and the one actually applied by the platform. This discrepancy is expected to be caused by: i) the open-loop control of the propeller rotational velocities, ii) and the aerodynamic interactions between adjacent propellers due to the small size of the frame. While the aerodynamic interactions are caused by the proximity between the propellers, the open-loop control of the propellers is necessary to ensure such high speed rotational velocity of the propellers, where off the shelf ESCs providing closed loop speed control at the required rotational speed are still rare.

We assessed the omnidirectional hoverability of the presented prototype, and showed that the platform is able to hover in any direction about the platform CoM, while using the open-loop motors.

Finally, we computed the required parameters for an upgraded design with larger dimensions and propellers. We showed that for the chosen dimensions the required propeller rotational speeds are decreases drastically as compared to the presented prototype. The construction of the new prototype is left as future work, where we do note that it is desirable in the upgraded prototype to use closed-loop ESCs to control the propeller rotational speeds, while none of the ESCs used in our lab could provide closed-loop control of the propellers at the required rotational speeds.

Chapter 6

Effect of Actuation properties on Trajectory Tracking

6.1 Introduction

In this chapter we aim to understand the effect of actuation properties on platforms' trajectory tracking. To facilitate the experimental study of trajectory tracking using different actuation properties, we rely on the use of a FA platform (the Tilt-Hex Fig. 6.1) controlled with the Bounded Lateral Force (BLF) controller. This controller allows us to easily modulate the behavior of the Tilt-Hex between the one of a FA platform and of a UDT platform, and thus allows us to experimentally test the trajectory tracking of the platform with different actuation properties. In what follows we will introduce more thoroughly the BLF controller, while discussing its robustness to external disturbances.

To be able then to fairly compare the behavior of the controller for different actuation properties, we will introduce the optimal tuning of the controller gains, that guarantees a consistent desired behavior across our experiments.

We will then show the results of our experimental campaign, followed by a summarizing conclusion.

The interested reader is referred to [video01–2021b] for a summarizing presentation of the content of this chapter, in addition to demonstrations of the corresponding experiments.

6.2 Introduction of the Bounded Lateral Force Model

The BLF abstract class was firstly introduced in [Franchi–2018a], as a grouping of all the platforms that can apply bounded lateral forces in body frame. Unlike the more popular quadrotors, these platforms can apply a lateral force in their body frame thanks to tilted propellers, similar to the example platform we will use in this chapter, shown in Fig. 6.1. For such platforms position and orientation dynamics are decoupled, and as such they can move laterally without the need of tilting, tilt without the need of moving laterally, and interact with the environment while maintaining an independent desired orientation. In its simplest and more effective representation, among the ones introduced in [Franchi–2018a], a BLF platform's feasible force set is modeled as a cylinder which radius, summarized by the parameter $\overline{f_{xy}}$ representing the maximum allowable lateral force in any horizontal direction, in body frame, however the model encompasses a much broader set of possible cases, in which the lateral bound can have virtually any shape.

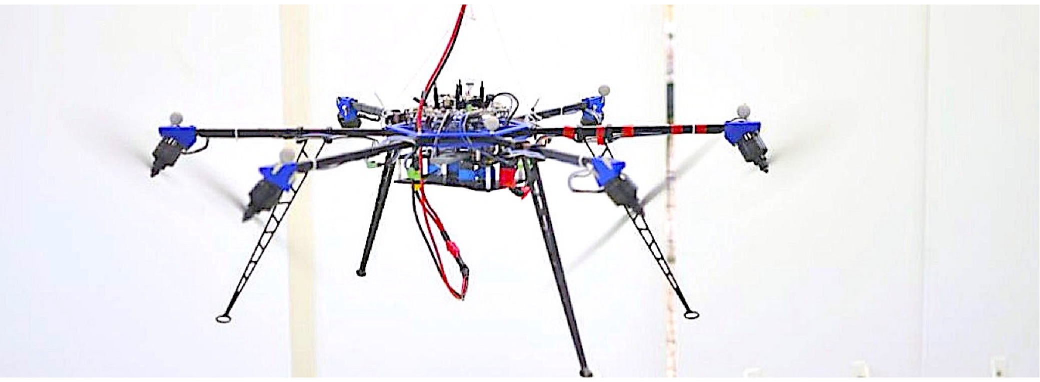

Figure 6.1 – The considered hexarotor with tilted propellers (Tilt-Hex).

The geometric controller presented in [Franchi–2018a] requires the inertial parameters of the platform, and tuned gains of its attitude and position controllers; similar controllers have also been proposed in the literature, such as the controller presented in [Invernizzi–2018]. The inertial parameters of the platform can be easily estimated from the platform's geometry, and do not depend on the controller gains. Similarly, the attitude controller has a larger authority than the position controller, and thus can be tuned using standard methods, independently of the chosen position controller. The position controller merits further explanation, in fact, as can be seen from Fig. 6.2, the lateral force limits are coupled with the applied lift force. Therefore a single parameter $\overline{f_{xy}}$ is an estimate of the actual maximum lateral force allowed by the platform for the current lift, where it is difficult to choose the best value for this parameter a priori.

Furthermore, the choice of $\overline{f_{xy}}$ can substantially affect the platform's performance, where if chosen to be near zero, the platform acts as an underactuated one, with a strong coupling between the position and attitude dynamics. If $\overline{f_{xy}}$ is chosen to be large enough, the platform behaves as a fully-actuated one, and the position and attitude dynamics become decoupled; special consideration has to be given as not to exceed platform's physical limits at the applied lift.

In this chapter, we aim to study experimentally the above-mentioned interplay between the chosen maximum lateral force and the position dynamics, while systematically tuning the controller gains. Let us first introduce the BLF controller equations. Note that these equations complement the equations of motion from Chapt. 2.

Let us define the control force and moment applied in body frame at the origin O_B respectively as $\boldsymbol{m}_B \in \mathbb{R}^3$, and $\boldsymbol{f}_B = [u_x,\, u_y,\, u_z]^\top \in \mathcal{U}_f \subset \mathbb{R}^3$ where $\mathcal{U}_f$ represents the *set of feasible forces* in the body frame (note that $\mathfrak{F}_1$ is a subset of $\mathcal{U}_f$ where the platform applies zero moment). The particular class of BLF vehicle considered here is characterized by the cylindric structure of the set $\mathcal{U}_f$, namely, $\mathcal{U}_f = \mathcal{U}_{xy} \times \mathbb{R}_{\geq 0}$, where $\mathcal{U}_{xy}$ is the *set of feasible lateral forces* defined as

$$\mathcal{U}_{xy} = \{[u_x,\, u_y]^\top \in \mathbb{R}^2 \mid u_x^2 + u_y^2 \leq \overline{f_{xy}}^2\}. \tag{6.1}$$

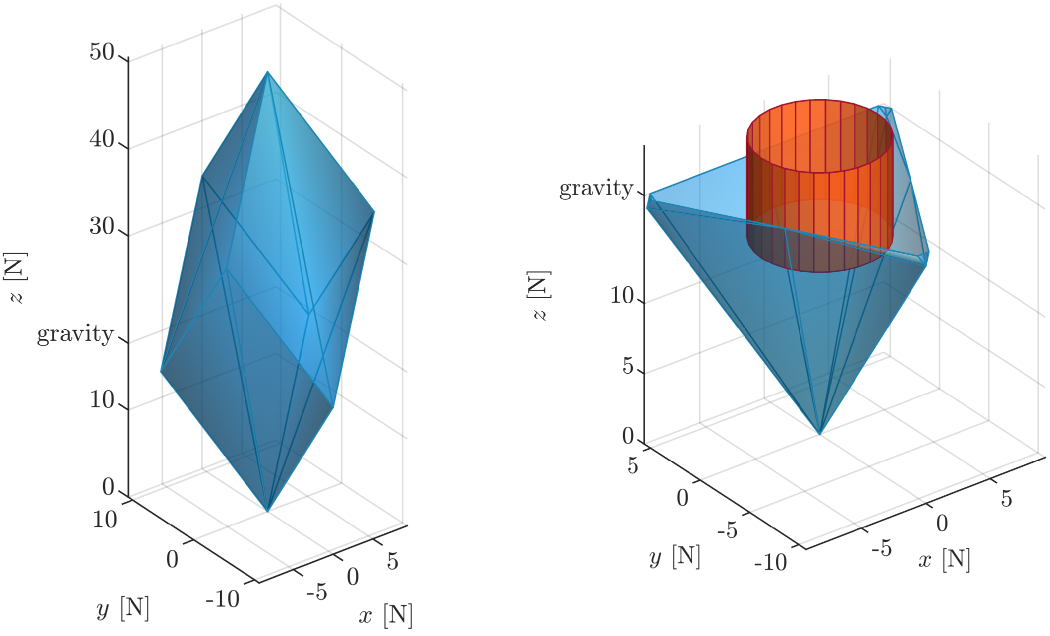

(a) (b)

Figure 6.2 – (a) Feasible force set of the platform $\mathfrak{F}_1$ in Fig. 6.1 at hover. (b) The same feasible force set with cross section at the gravity compensation plane. The figure also shows the BLF cylinder for the platform applying a lift force ±20% of the gravity-opposing lift.

As such, and following the allocation strategy from [Franchi–2018a], if the required lateral force $\notin \mathcal{U}_{xy}$, the controller prioritizes the position controller and tilts the platform differently from the reference attitude trajectory so as to include the lateral force $\in \mathcal{U}_{xy}$. The smaller $\overline{f_{xy}}$, the closer the BLF vehicle resembles an underactuated multirotor (e.g., a quadrotor) and as a consequence, the more coupled its lateral motion and attitude dynamics are – e.g., a lateral acceleration requires a non-zero tilting of the vehicle. The larger $\overline{f_{xy}}$, the more decoupled its orientation and lateral motion can be – e.g., the BLF vehicle can accelerate laterally with a small tilting and can tilt with lateral acceleration close to zero.

The BLF model has two advantages over more accurate models of the particular multi-rotor aerial vehicle at hand: i) the BLF model is much simpler and requires the identification and use of only one actuation parameter – namely $\overline{f_{xy}}$; ii) the BLF model can be made asymptotically stable using a controller (see [Franchi–2018a]) that is analytically proven to converge and it has been experimentally demonstrated to effectively stabilize real multirotor platforms modeled as BLF, such as the platform shown in Fig. 6.1. More accurate models can be introduced [Bicego–2020], however, they require the complex identification of many parameters, which may be impractical in some cases. Furthermore, due to their complexity, they can be controlled only resorting to numerical optimization-based control, which typically requires a high computational power that may not be available on-board. Last but not least, such numerical methods do not typically have an analytical guarantee of asymptotic stabilization.

A BLF vehicle can be stabilized along a time-varying and full-pose reference trajectory $\boldsymbol{q}^r(t) = (\boldsymbol{p}^r_B(t), \boldsymbol{R}_r(t))$ using the analytically-proven control law presented in [Franchi–2018a], which has the following form:

$$\boldsymbol{f}_B = \mathrm{sat}_{\mathcal{U}_{xy}}\Big((\boldsymbol{f}_r^\top \boldsymbol{R}_B \boldsymbol{e}_1)\boldsymbol{e}_1 + (\boldsymbol{f}_r^\top \boldsymbol{R}_B \boldsymbol{e}_2)\boldsymbol{e}_2\Big) + (\boldsymbol{f}_r^\top \boldsymbol{R}_B \boldsymbol{e}_3)\boldsymbol{e}_3\,, \tag{6.2}$$

$$\boldsymbol{m}_B = \boldsymbol{\omega}_B \times \boldsymbol{J}\boldsymbol{\omega}_B - \boldsymbol{K}_{\boldsymbol{R}}\boldsymbol{e}_{\boldsymbol{R}} - \boldsymbol{K}_\omega \boldsymbol{e}_\omega \tag{6.3}$$

$$\qquad - \boldsymbol{J}\Big([\boldsymbol{\omega}_B]_\times \boldsymbol{R}_B^\top \boldsymbol{R}_d \boldsymbol{\omega}^d_B - \boldsymbol{R}_B^\top \boldsymbol{R}_d \dot{\boldsymbol{\omega}}^d_B\Big)\,, \tag{6.4}$$

where

$$\boldsymbol{f}_r = m(\ddot{\boldsymbol{p}}^r_B + g\boldsymbol{e}_3) - \boldsymbol{K}_P \boldsymbol{e}_p - \boldsymbol{K}_V \dot{\boldsymbol{e}}_p\,, \tag{6.5}$$

where $\boldsymbol{K}_P$ and $\boldsymbol{K}_V$ are proportional and derivative positional controller gains, and $\boldsymbol{e}_p$ and $\dot{\boldsymbol{e}}_p$ are the position and velocity errors in world frame.

Considering the goal of this paper, we omit further details about the controller for the sake of compactness and readability, and we refer the reader to [Franchi–2018a] for the exact definition of all the terms in the controller as well as its stability proof, and for Sec. 6.5 for the robustness analysis of the controller. In the next section, we focus on the discussion of the parameters used in this control law.

The BLF model described above has three parameters: m, $\boldsymbol{J}$, and $\overline{f_{xy}}$, which are all used in the corresponding controller in Eq. (6.2)–Eq. (6.5) together with the four additional sets of parameters representing the control gain matrices $\boldsymbol{K}_P$, $\boldsymbol{K}_V$, $\boldsymbol{K}_{\boldsymbol{R}}$, and $\boldsymbol{K}_\omega$. In the following, we analyze each parameter from the point of view of interdependency and easiness of identification with methods available in the state-of-the-art.

Inertial Parameters The inertial parameters m and $\boldsymbol{J}_B$ have clear physical meaning and their offline identification or online estimation is rather straightforward and established (see, e.g., [Wüest–2019] and [Spica–2013]). Furthermore, their nominal values are typically accurate because they can be retrieved from the CAD model of the system. Therefore, one can safely assume their values to be identifiable with good accuracy using standard methods.

Gains of the Attitude Control loop The gain matrices $\boldsymbol{K}_{\boldsymbol{R}}$ and $\boldsymbol{K}_\omega$ appear in Eq. (6.4) and affect the attitude dynamics, which is independent of the rest of the vehicle dynamics (the position dynamics) and contains only the parameter $\boldsymbol{J}_B$, which, as explained before, can be fairly assumed to be known with good accuracy. Furthermore, the attitude dynamics is fully-actuated and no limits in the control moments appear in the BLF model. As a consequence, the gains $\boldsymbol{K}_{\boldsymbol{R}}$ and $\boldsymbol{K}_\omega$ can be easily tuned independently from the other control parameters by using standard PD tuning methods such as the one presented in [Wu–2014]. Therefore, we can also in this case safely assume that $\boldsymbol{K}_{\boldsymbol{R}}$ and $\boldsymbol{K}_\omega$ are tuned with state-of-the-art methods and do not require special attention.

Maximum magnitude of the Lateral Force In a real multi-rotor platform, see [Bicego–2019], the maximum magnitude of the lateral force depends on the applied vertical component of the force and the applied full moment. Such lateral bound is typically larger when the requested vertical force exactly compensates for the gravity force and the total moment is zero. The farther the vertical force and the moment are from such two neutral conditions, the smaller the lateral bounds on the horizontal component of the force. Fig. 6.2 shows an example of a feasible force set at hover and a corresponding BLF model calculated when applying a vertical force opposing gravity (static hovering has been formally defined in Chapt. 4.

In the cylindric BLF model considered here, on the contrary, $\overline{f_{xy}}$ is a lumped constant value. If $\overline{f_{xy}}$ is set too small, then the controller will let the platform behave too close to an underactuated platform, while if $\overline{f_{xy}}$ is set too large, it could lead to suboptimal behaviors because it may not represent well the lateral bounds induced by the moment and vertical force required by the task.

In conclusion, the parameter $\overline{f_{xy}}$ plays the role of a 'lateral-actuation modulator' which has to be tuned in order to optimize the behavior of the real controlled platform for the particular task at hand. Such a need calls for an automated tuning algorithm that can optimize the value of $\overline{f_{xy}}$ based on the controller performance.

Gains of the Position Control loop The gain matrices $\boldsymbol{K}_P$ and $\boldsymbol{K}_V$ appear in Eq. (6.5) and affect the position dynamics. It is standard to assume a diagonal structure of $\boldsymbol{K}_P$ and $\boldsymbol{K}_V$ considering the symmetry of the model and in order to avoid an unnecessary cross-direction coupling induced by the controller. Furthermore, thanks to the horizontal symmetry of the model and controller, one can assume that the corresponding first two entries of each diagonal are equal. Therefore, it is reasonable to assume the following structure for $\boldsymbol{K}_P$ and $\boldsymbol{K}_V$:

$$\boldsymbol{K}_P = \operatorname{diag}\{k_p,\, k_p, k_{pz}\}\,, \tag{6.6}$$

$$\boldsymbol{K}_V = \operatorname{diag}\{k_v,\, k_v, k_{vz}\}\,. \tag{6.7}$$

The choice of k_{pz} and k_{vz} affects the closed-loop vertical dynamics along which the system has a large control authority and is not influenced by the rest of the dynamics. Therefore – similarly to $\boldsymbol{K}_{\boldsymbol{R}}$ and $\boldsymbol{K}_\omega$ – the gains k_{pz} and k_{vz} can be tuned independently, e.g., letting the vehicle move up and down and using standard PD tuning techniques [Wu–2014].

The remaining parameters, namely k_p and k_v, cannot be chosen independently from $\overline{f_{xy}}$, because there is a nonlinear saturation on the lateral dynamics that depends on $\overline{f_{xy}}$ (see Eq. (6.2)). Therefore, k_p and k_v have to be chosen in a way that lets the system behave optimally in the lateral motion, while well coping with the saturation induced by $\overline{f_{xy}}$.

To provide an insight into the complexity of such an interplay, let us first consider the two extreme cases. If $\overline{f_{xy}}$ is chosen very small, the platform lateral dynamics is in practice underactuated and the platform needs to tilt in order to move laterally. Therefore, the gains k_p and k_v have to be optimized to let the position dynamics be as fast as possible but ‘slower’ than the attitude dynamics, following a time-scale separation principle, as in a quadrotor. On the contrary, if $\overline{f_{xy}}$ is large, the system can move laterally (up to a certain acceleration) without tilting, therefore there is virtually no need to take the attitude dynamics into account and obeying a time-scale separation principle in the tuning of k_p and k_v. On the other side, there is still the dynamics of the motor/propeller to consider. In fact, lateral motions without tilting require a much more ample range of propeller spinning velocities compared to the case in which the system moves laterally by tilting (with small $\overline{f_{xy}}$). This phenomenon can be easily appreciated looking at the experiments reported in [Franchi–2018a]. Therefore, for large $\overline{f_{xy}}$, the dynamics to consider is the motor/propeller one, which has of course different characteristics than the attitude one.

For intermediate values of $\overline{f_{xy}}$, a mixture of attitude and motor dynamics influences the optimal choice of the gains k_p and k_v in a way that is hard to predict a priori.

Conclusions From the discussion carried out above, it emerges that there are two different types of control parameters in Eq. (6.2)–Eq. (6.5). The first type, namely m, $\boldsymbol{J}_B$, $\boldsymbol{K}_{\boldsymbol{R}}$, $\boldsymbol{K}_\omega$, k_{pz} and k_{vz} can be tuned mostly independently and resorting to state-of-the-art methods such as, e.g., physical parameter identification using least squares approach or PD tuning. The second type, namely $\overline{f_{xy}}$, k_p, and k_v, are tightly coupled, and their effects on the system behavior are coupled and nonlinear and one cannot use straightforward methods like PD tuning to tune these parameters. In particular:

i) different values of $\overline{f_{xy}}$ may be chosen depending on the motion task at hand, where there is no clear ’best value’ until the task is specified;

ii) for each value of $\overline{f_{xy}}$ it is expected to obtain different optimized values for k_p and k_v, due to the nonlinear interplay explained before.

Therefore, in the remaining part of this chapter, we focus our attention on the *optimal tuning of* k_p *and* k_v *for different values of* $\overline{f_{xy}}$ *in real platforms modeled and controlled as BLF.*

6.3 Optimization of the Bounded Lateral Force Controller Gains

The optimization algorithm that is used to tune the gains k_p and k_v, for a given value of the parameter $\overline{f_{xy}}$, is an instantiation of the model-free OPTIM-tune algorithm presented in [Giernacki–2019] and requires only a measurable metric of the performance of the controller in order to work. The overall method is a combination of two nested loops: *i)* an outer loop, described in Algorithm 1, and *ii)* an inner loop, also called *single parameter tuning*, described in Algorithm 2.

Algorithm 1 (the outer loop) receives as input: *i)* the maximum lateral force $\overline{f_{xy}}$ (which is kept constant during the tuning), *ii)* the two sets $\mathfrak{D}^{(1)}_{k_p}$, $\mathfrak{D}^{(1)}_{k_v}$ that

Algorithm 1: Tuning of controller gains k_p and k_v for a fixed $\overline{f_{xy}}$ value.

```
**Data:** $\overline{f_{xy}}$, $\mathfrak{D}_{k_p}^{(1)}$, $\mathfrak{D}_{k_v}^{(1)}$, $N$ and $N_b$
**Result:** optimized $k_p^\star \in \mathfrak{D}_{k_p}^{(1)}$, $k_v^\star \in \mathfrak{D}_{k_v}^{(1)}$
$i \leftarrow 1$
**while** $i \leq N_b$ **do**
    $k_v \leftarrow \overline{\mathfrak{D}}_{k_v}^{(i)}$
    $\mathfrak{D}_{k_p}^{(i+1)} \leftarrow \text{Algorithm}_2(\mathfrak{D}^{(1)} = \mathfrak{D}_{k_p}^{(i)}, \xi = k_v, \overline{f_{xy}}, N)$
    $k_p \leftarrow \overline{\mathfrak{D}}_{k_p}^{(i+1)}$
    $\mathfrak{D}_{k_v}^{(i+1)} \leftarrow \text{Algorithm}_2(\mathfrak{D}^{(1)} = \mathfrak{D}_{k_v}^{(i)}, \xi = k_p, \overline{f_{xy}}, N)$
    $i \leftarrow i + 1$
**end**
$k_p^\star = \overline{\mathfrak{D}}_{k_p}^{(N_b)}$
$k_v^\star = \overline{\mathfrak{D}}_{k_v}^{(N_b)}$
```

represent the intervals over which the gains k_p and k_v are optimized, and *iii)* two integers, N_b and N, representing the number of iterations in the outer and inner loop, respectively.

Algorithm 2 (inner loop, or single parameter tuning) receives as input: *i)* $\overline{f_{xy}}$ and N (the same of Algorithm 1), *ii)* the starting set, denoted with $\mathfrak{D}^{(1)}$, in which one of the two gains (either k_p or k_v) will be optimized, and *iii)* the value of the other parameter (either k_v or k_p) that is kept fixed during the execution of Algorithm 2, denoted with ξ. The algorithm provides a new set $\mathfrak{D}^{(N)}$ as output, which is a contraction of $\mathfrak{D}^{(1)}$ and which is guaranteed to contain the optimum value of the corresponding parameter.

Algorithm 1 executes a basic iteration N_b times, in which two instances of Algorithm 2 are performed sequentially to contract $\mathfrak{D}_{k_p}^{(i)}$ and $\mathfrak{D}_{k_v}^{(i)}$. In the first instance, k_v is kept fixed at its current estimate and the set to which the optimal k_p belongs is contracted, thus generating an improved estimate of k_p. In the second instance – symmetrically – the new estimate of k_p is kept fixed while the set to which the optimal k_v belongs is contracted, thus generating a new improved estimate of k_v. At the end of Algorithm 1 the optimized values of the gains are returned in the form of the mid-values of the intervals generated by the contractions of the last (N_b-th) iteration, i.e., $\mathfrak{D}_{k_p}^{(N_b)}$ and $\mathfrak{D}_{k_v}^{(N_b)}$. Such mid-values are denoted with $\overline{\mathfrak{D}}_{k_p}^{(N_b)}$ and $\overline{\mathfrak{D}}_{k_v}^{(N_b)}$, respectively.

Algorithm 2 performs the set contraction implementing N smaller consecutive contraction steps. Each step executes two flight tests with the vehicle, using $\overline{f_{xy}}$ as lateral force bound and ξ as the temporarily-fixed gain. The goal of each flight test is to evaluate the effect of a new candidate for the upper and lower bound of the set containing the gain to be optimized. A new upper bound candidate ${}^{+}\hat{\theta}^{(i+1)}$ is tested in the first flight test, while a new lower bound candidate ${}^{-}\hat{\theta}^{(i+1)}$ is tested in the second one. Each flight test is followed by the evaluation of a cost function f that depends on the state error $\boldsymbol{s}_e$, i.e., the vector describing the error between the

Algorithm 2: Generic single parameter tuning.

```
Data: $\mathfrak{D}^{(1)} = [{}^-\theta^{(1)}, {}^+\theta^{(1)}]$, $\xi$, $\overline{f_{xy}}$, and $N$
Result: $\mathfrak{D}^{(N)} = [{}^-\theta^{(N)}, {}^+\theta^{(N)}]$
$i \leftarrow 1$
while $i \leq N$ do
    calculate contraction factor $\rho_i$
    calculate candidate $(i+1)$ bounds:
        $ {}^-\hat{\theta}^{(i+1)} =^- \theta^{(i)} + \rho_i({}^+\theta^{(i)} - {}^-\theta^{(i)})$
        $ {}^+\hat{\theta}^{(i+1)} =^- \theta^{(i)} + (1-\rho_i)({}^+\theta^{(i)} - {}^-\theta^{(i)})$
    execute flight test with params $\xi$, ${}^-\hat{\theta}^{(i+1)}$, and $\overline{f_{xy}}$
    ${}^-f \leftarrow f(\boldsymbol{s}_e)$
    execute flight test with params $\xi$, ${}^+\hat{\theta}^{(i+1)}$, and $\overline{f_{xy}}$
    ${}^+f \leftarrow f(\boldsymbol{s}_e)$
    if ${}^-f < {}^+f$ then
        $\mathfrak{D}^{(i+1)} \leftarrow [{}^-\hat{\theta}^{(i+1)}, {}^+\theta^{(i)}]$
    else
        $\mathfrak{D}^{(i+1)} \leftarrow [{}^-\theta^{(i)}, {}^+\hat{\theta}^{(i+1)}]$
    end
    $i \leftarrow i+1$
end
```

desired and the measured state of the system during the execution of a flight test. The candidate bound that corresponds to the test which returned the lower value of f is used as new upper or lower bound for the set of the estimated parameter, thus producing the sought contraction for the particular step. This process is repeated N times. The last obtained set $\mathfrak{D}^{(N)}$ is returned as the result of the algorithm.

In our specific case, the goal is to find the optimal controller gains that ameliorate the lateral trajectory tracking while the platform remains as much as possible horizontal – thus exploiting at best the lateral force capability of BLF platforms. In line with such goal, and assuming that the position trajectory of a flight test is composed by N_c reference points, the corresponding cost function f is defined as follows:

$$f(\boldsymbol{s}_e) = \underbrace{\sum_{k=1}^{N_c} |\boldsymbol{e}_k|}_{f_{\mathbf{e}}} + \frac{1}{Q} \underbrace{\sum_{k=1}^{N_c} |\phi_k|}_{f_\phi} = \sum_{k=1}^{N_c} J_k \,, \tag{6.8}$$

where $|\boldsymbol{e}_k|$ is the norm of the lateral position error, $|\phi_k|$ is the norm of the tilt angular error and J is the weighted error per reference point. The parameter Q is used to weight the contribution of the angular error in the overall performance index, giving more or less importance to the fact that the platform remains horizontal while following the position trajectory.

6.4 Experimental validation

We validate the proposed approach with the BLF platform presented in [Franchi–2018a]; the platform is referred to as the Tilt-Hex and is shown in Fig. 6.1. The platform is a hexarotor constructed from six 12”-wide tilted propellers equally-spaced about the platform Center of Mass (CoM). The platform has a mass of 1.8 kg, and an inertia tensor $\boldsymbol{J}_B = \mathrm{diag}\{11.5,\ 11.4,\ 19.4\} \cdot 10^{-6}\,\mathrm{kg} \cdot \mathrm{m}^2$.

In addition, the platform is endowed with an Inertial Measurement Unit (IMU) providing acceleration and angular velocity measurements at 1 kHz, and is tracked with a motion capture system at 100 Hz. Both measurements are fused with an Unscented Kalman Filter (UKF) running at 1 kHz, providing an estimate of the platform state. The motion controller runs on-board at 1 kHz, and brushless motor controllers (Brushless DC (BLDC) Electronic Speed Controller (ESC)) regulate the propeller speeds using an in-house developed closed-loop speed controller [Franchi–2017]. Most of the software is developed in C++ and runs on an on-board PC, with the exception of the gain tuning algorithm which runs in MATLAB/Simulink on a ground PC. Most of the on-board software are open source, and can be found at `https://git.openrobots.org/projects/telekyb3`.

A simulation and an experimental campaign have been carried out, in which the task has been to tune the controller gains, for the selected values of $\overline{f_{xy}}$ and different Q ratios. In all the experiments and simulations, the maximum lateral acceleration of the reference trajectory has been set at $1.5\,\mathrm{ms}^{-2}$, jerk at $10\,\mathrm{ms}^{-3}$, lateral velocity at $2\,\mathrm{ms}^{-1}$, to bring the platform to its lateral motion limits. During each of the tuning experiments, the initial domains of the controller gains have been chosen such that $\mathfrak{D}_{k_p}^{(1)} = [10,\ 30]$ and $\mathfrak{D}_{k_v}^{(1)} = [5,\ 15]$, and each domain has been contracted $N = 12$ times by the inner loop in each of the $N_b = 2$ outer loop iterations.

Finally, to stress the lateral position tracking and horizontality of the platform (zero tilt), the reference trajectory has been chosen as a back and forth path parallel to $\boldsymbol{x}_W$.

6.4.1 Simulative Analysis of the Cost Function Landscape

To study the cost function landscape, we simulated the above-mentioned platform with the corresponding controller, and computed the different components of the cost function while varying the controller positional gains k_p and k_v over a discretized grid of $\mathfrak{D}_{k_p}^{(1)}, \mathfrak{D}_{k_v}^{(1)}$.

Fig. 6.3 shows the contour plots of the two components of $f(\mathbf{s}_e)$ at $\overline{f_{xy}} = 2\,N$ and $\overline{f_{xy}} = 8\,N$. The functions $f_{\mathbf{e}}$ and f_ϕ are shown separately to understand the effect of each on the performance of the presented tuning scheme. This figure shows that as $\overline{f_{xy}}$ is increased from $2\,N$ to $8\,N$, the lateral position error component $f_{\mathbf{e}}$ decreases slightly for almost all values in the given range, and the number of local minima slightly increases as the position changes moderately. On the other hand, f_ϕ shows a different behavior, where it can be seen that the number of local minima increases substantially for $\overline{f_{xy}} = 8\,N$. In addition, as $\overline{f_{xy}}$ is increased, the values of f_ϕ decrease substantially; this can be seen from the different scales of the corresponding contour plots. As such, as $\overline{f_{xy}}$ is increased the effect of the angular component on the overall

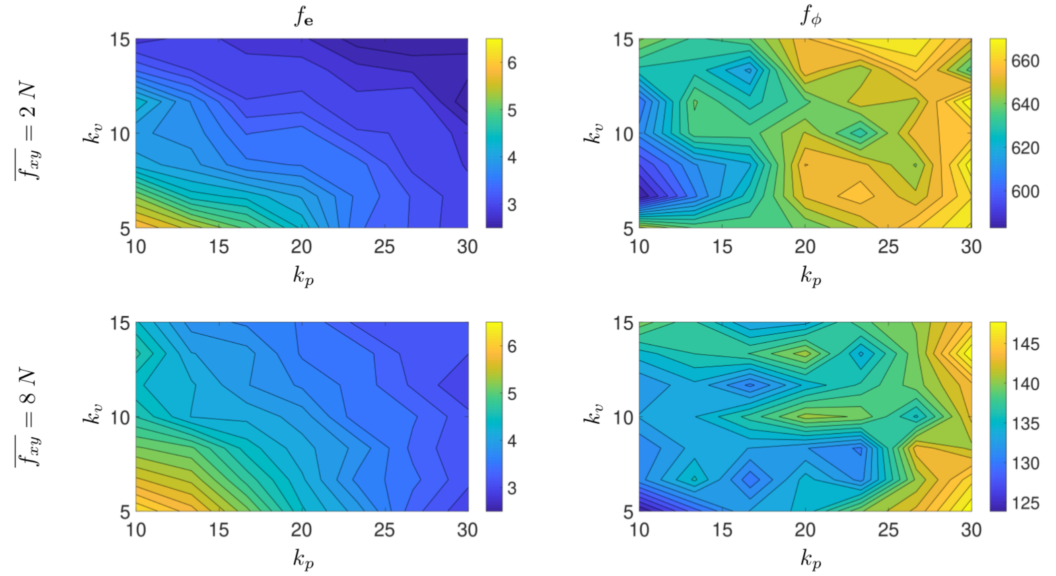

Figure 6.3 – Contour plots of $f_{\mathbf{e}}(k_p, k_v)$ and $f_{\phi}(k_p, k_v)$ for two different values of $\overline{f_{xy}}$ computed via simulation on a discretization of the ranges $\mathfrak{D}^{(1)}_{k_p}, \mathfrak{D}^{(1)}_{k_v}$.

cost function decreases; this is similar to an increase in the Q value. This shows the decreased effect of f_{ϕ} (and correspondingly the angular dynamics) on the tuning of the position controller gains as $\overline{f_{xy}}$ increases, even when Q is kept constant.

6.4.2 Experimental Test of the Tuning Algorithm

We conduct an experimental campaign to demonstrate the tuning of the proposed algorithm and to show the relation between the chosen $\overline{f_{xy}}$ and the optimized controller gains.

Fig. 6.4 shows the average of the optimized controller gains and standard deviation of each for different values of $\overline{f_{xy}}$ and Q, where the optimization at each $\overline{f_{xy}}$ and Q value have been repeated thrice. This figure depicts that as $\overline{f_{xy}}$ increases, the optimized k_p increases and the optimized k_v decreases for both Q values. In the case of $Q = 300$, the contribution of f_{ϕ} is reduced substantially leading to higher optimized k_p and k_v values as the optimization allows for more aggressive position tracking without taking the angular tracking error into consideration.

In order to get an improved understanding of how the algorithm operates, we show the evolution of the optimization for two of the above optimization cases, corresponding to $\overline{f_{xy}} \in \{2\,N, 8\,N\}$ and at a constant $Q = 50$. Fig. 6.5 shows the corresponding evolution for $\overline{f_{xy}} = 2\,N$ and $\overline{f_{xy}} = 8\,N$. This figure depicts the evolution of the controller gains and the resulting performance index for each of the two $\overline{f_{xy}}$ values. These experiments clearly show the improved trajectory tracking of the controller with the optimized gains, and that while the initial controller gains are the same for both experiments, the optimized gains vary substantially for different values of $\overline{f_{xy}}$, supporting the interdependence of such parameters that is claimed in this work.

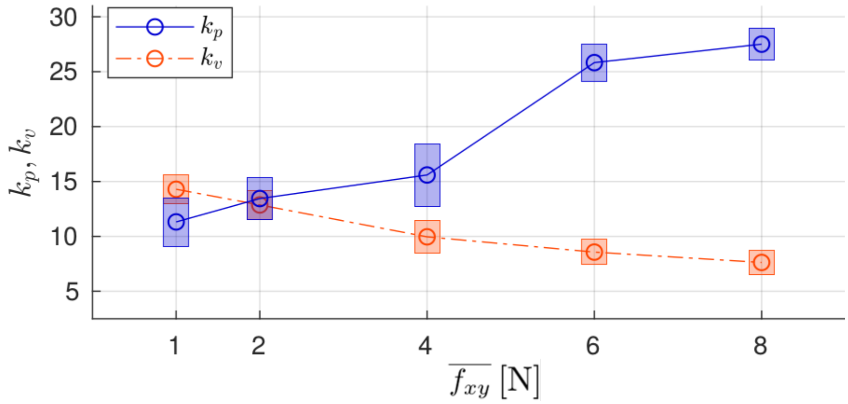

(a) $Q = 50$

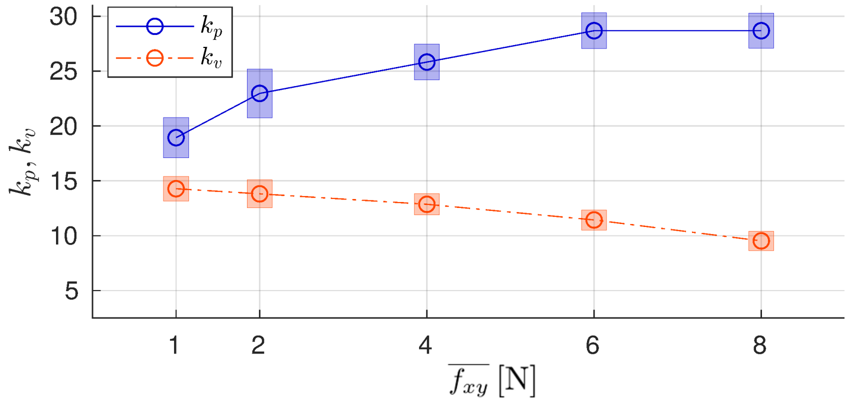

(b) $Q = 300$

Figure 6.4 – Optimized gains (k_p, k_v) of the position controller versus $\overline{f_{xy}}$ for two values of the weighting ratio Q. For each optimized gains, we show the average value and the standard deviation bar computed from three repetitions of each experiment.

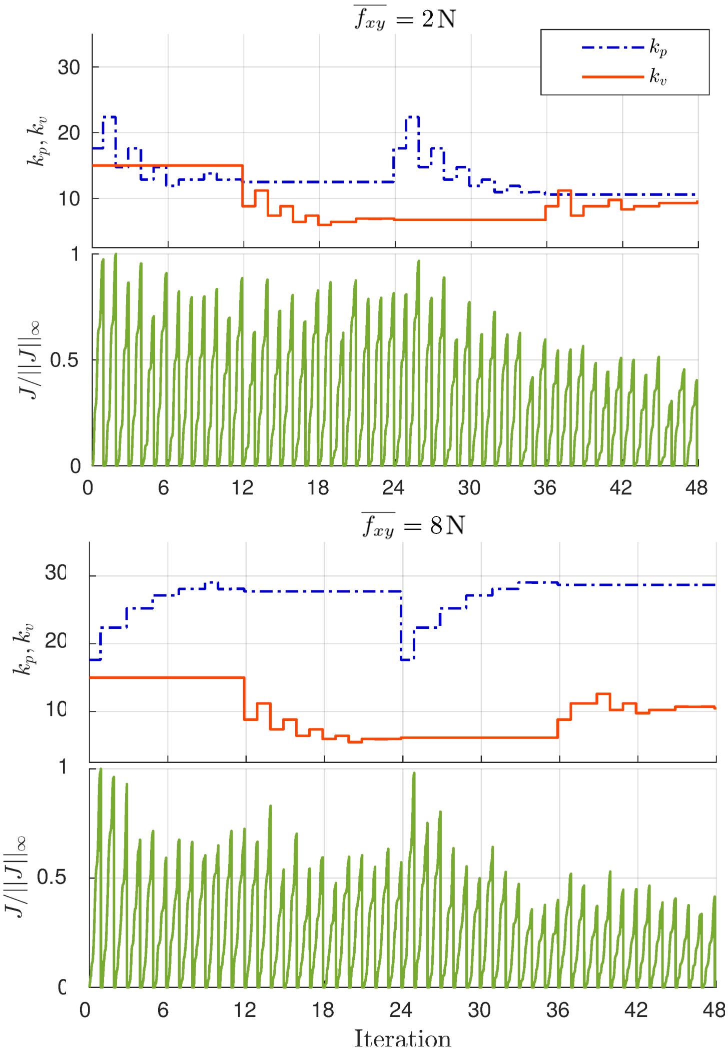

Figure 6.5 – Evolution of the gain tuning algorithm for $\overline{f_{xy}} = 2\,N$ and $\overline{f_{xy}} = 8\,N$ while $Q = 50$ showing the controller gains k_p, k_v, and the weighted error per step J_k for $N = 12$ and $N_b = 2$.

6.5 Bounded Lateral Force Controller Robustness

While the OPTIM-tune method does not require any knowledge of the UAV model, it does require an initial range of gains in which it tries to find the optimal value, and in which the closed-loop system is assumed to perform in a stable manner. These may result either from initial test flights, or through the analysis of simulation-based flights. As such, we the optimization algorithm assumes the platform performance to be stable in this range.

However, since the tuning above was conducted in "near-perfect" environment, where the tracking was done with a motion tracking system, and the optimization was done on a repeated trajectory, the optimized gains are not guaranteed to result in a robust performance when faced with external disturbances or unmodeled uncertainties. As such, in what follows we conduct a formal robustness analysis of the resulting controller in two cases: i) the first case is when the platform mass is different from the nominal one, ii) and the second case is when the platform is subjected to an external disturbance.

As such, in what follows, we assess the stability of the used control system [Franchi–2018a] against external disturbances when the optimized gains are used.

First, let us linearize the system around the working points from the presented problem. To do so, let us first recap the used notations while making some adjustments for an ease of readability as follows:

notation	definition	dimension
$\mathbf{R}$	rotation matrix of $\mathcal{B}$ in $\mathcal{W}$	$\mathbb{R}^{3\times3}$
θ	rotation angle about $\boldsymbol{y}_W$	$\mathbb{R}$
θ_d	desired rotation angle about $\boldsymbol{y}_W$	$\mathbb{R}$
$\boldsymbol{e}_p$	position error in $\mathcal{W}$	$\mathbb{R}^3$
$\boldsymbol{e}_v$	linear velocity error in $\mathcal{W}$	$\mathbb{R}^3$
$\boldsymbol{e}_R$	angular error in $\mathcal{W}$	$\mathbb{R}^3$
$\boldsymbol{e}_\omega$	angular velocity error in $\mathcal{B}$	$\mathbb{R}^3$
$\boldsymbol{J}_B$	Inertia Matrix in $\mathcal{B}$	$\mathbb{R}^{3x3}$
e_{px}	position error in $\boldsymbol{x}_W$	$\mathbb{R}$
e_{vx}	linear velocity error in $\boldsymbol{x}_W$	$\mathbb{R}$
$\mathbf{K}_p$	position gain matrix	$\mathbb{R}^{3\times3}$
$\mathbf{K}_v$	linear velocity gain matrix	$\mathbb{R}^{3\times3}$
$\mathbf{K}_\omega$	angular velocity gain matrix	$\mathbb{R}^{3\times3}$
$\mathbf{K}_R$	angular gain matrix	$\mathbb{R}^{3\times3}$

Further, we assume all gain matrices to be diagonal matrices as follows: $\mathbf{K}_p = diag(k_p, k_p, k_{pz})$, $\mathbf{K}_v = diag(k_v, k_v, k_{vz})$, $\mathbf{K}_\omega = diag(k_{\omega x}, k_{\omega y}, k_{\omega z})$, and $\mathbf{K}_R = diag(k_{Rx}, k_{Ry}, k_{Rz})$. Similarly, we assume the inertia matrix to be a diagonal matrix such that $\boldsymbol{J}_B = diag(J_{11}, J_{22}, J_{33})$. Finally, $\boldsymbol{f}_r$ is divided about the different axes of $\mathcal{W}$ axes such as $\boldsymbol{f}_r = \{f_{rx}, f_{ry}, f_{rz}\}$ and ω is divided about the different axes of

$\mathcal{B}$ such as $\omega = \{\omega_x, \omega_y, \omega_z\}$.

6.5.1 Mass uncertainty

In the following formulation, we assume a constant reference consisting of a motion along the $\boldsymbol{x}_W$ axis, and rotation about the roll angle θ, while assuming the motion and rotation about all other axes to be negligible, and $\mathbf{R}_r = \mathbf{I}$. Following the above assumptions, the attitude controller boils down to the stabilization of the following error term:

$$e_\theta = \theta - \theta_d \,. \tag{6.9}$$

Geometrically, to check if $\boldsymbol{f}_r \in \mathcal{U}_{xy}$ (condition (33) from [Franchi–2018a]) it is enough to check the following:

$$\text{find } \theta \text{ such that } \mathbf{R}_y(\theta)\boldsymbol{f}_r\mathbf{e}_1 \leq \overline{f_{xy}}. \tag{6.10}$$

If Eq. (6.10) holds, $\theta_d = 0$ and $e_\theta = \theta$, otherwise, the optimization problem from [Franchi–2018a] will reduce to finding an equality from Eq. (6.10), such as:

$$\mathbf{R}_y(\theta_d)\boldsymbol{f}_r\mathbf{e}_1 = \overline{f_{xy}}\,, \tag{6.11}$$

$$f_{rx}\cos(\theta_d) + f_{rz}\sin(\theta_d) = \overline{f_{xy}}\,, \tag{6.12}$$

$$\theta_d = 2\tan^{-1}\left(\frac{f_{rz} \pm \sqrt{||\boldsymbol{f}_r||^2 - \overline{f_{xy}}^2}}{f_{rx} + \overline{f_{xy}}}\right). \tag{6.13}$$

Let $f_{rx} = -k_p e_{px} - k_v e_{vx}$ and $f_{rz} = mg - k_{pz}e_{pz} - k_{vz}e_{vz}$ (as previously defined). By assuming that $k_{pz}e_{pz} + k_{vz}e_{vz}$ to be negligible compared to mg, we can simplify f_{rz} such as $f_{rz} = mg$. As such

$$\theta_d = 2\tan^{-1}\left(\frac{mg \pm \sqrt{(mg)^2 + k_p^2 e_{px}^2 + k_v^2 e_{vx}^2 - \overline{f_{xy}}^2}}{-k_p e_{px} - k_v e_{vx} + \overline{f_{xy}}}\right). \tag{6.14}$$

A regulation task is considered, thus to have stable hovering it must hold that $e_{px} = p_x - p_{dx} = p_x$, $e_{vx} = v_x - v_{dx} = v_x$, and θ_d should be expanded around $p_x = 0$, $v_x = 0$, to obtain

$$\hat{\theta}_d \;\; = \;\; a + b_1 p_x + b_2 v_x \,. \tag{6.15}$$

Thus, the plant and controller state space model can be written as follows:

$$\begin{aligned}
\dot{\boldsymbol{p}} &= \underline{v}\,, && (6.16)\\
\dot{\boldsymbol{v}} &= -\frac{1}{m}\mathbf{R}\mathbf{K}_p p_x - \frac{1}{m}\mathbf{R}\mathbf{K}_v v_x\,, && (6.17)\\
\dot{\mathbf{R}} &= \mathbf{R}\left[\boldsymbol{\omega}\right]_\times\,, && (6.18)\\
\dot{\boldsymbol{\omega}} &= -\boldsymbol{J}_B^{-1}\mathbf{K}_R\begin{bmatrix}0\\ \theta - a - b_1 p_x - b_2 v_x\\ 0\end{bmatrix} + \\
&\quad -\boldsymbol{J}_B^{-1}\mathbf{K}_\omega\boldsymbol{\omega}\,, && (6.19)
\end{aligned}$$

where a, b_1 and b_2 result from a Taylor series expansion. Following the previously stated assumptions, $\mathbf{R} = \mathbf{R}_y(\theta)$,

$$\mathbf{R} = \begin{bmatrix}\cos(\theta) & 0 & \sin(\theta)\\ 0 & 1 & 0\\ -\sin(\theta) & 0 & \cos(\theta)\end{bmatrix} = \begin{bmatrix} r_1 & 0 & r_2\\ 0 & 1 & 0\\ -r_2 & 0 & r_1\end{bmatrix}. \qquad (6.20)$$

In addition to the previous assumptions, let us consider that the platform is near hover. Following the above assumptions, θ and ω_2 are assumed to be near zero, while ω_1 and ω_3 are assumed negligible. As such, $r_1 \approx 1$, $r_2 \approx \theta$, $\omega_1 = \omega_3 = r_1\omega_3 = 0$. Moreover, we can assume $p_y = v_y = v_z = 0$, and $e_z = e_y = 0$. As such, the state space model of the plant and controller can be reduced to the following:

$$\begin{aligned}
\dot{p}_x &= v_x\,, && (6.21)\\
\dot{v}_x &= -\frac{1}{m}\left(k_p p_x + k_v v_x\right), && (6.22)\\
\dot{v}_z &= 0\,, && (6.23)\\
\dot{r}_1 &= 0\,, && (6.24)\\
\dot{r}_2 &= \omega_2\,, && (6.25)\\
\dot{\omega}_1 &= -\frac{k_{\omega x}}{J_{11}}\omega_1\,, && (6.26)\\
\dot{\omega}_2 &= -\frac{k_{\omega y}}{J_{22}}\omega_2 + \frac{k_{Rx}}{J_{22}}\left(a + b_1 p_x + b_2 v_x - \theta\right), && (6.27)\\
\dot{\omega}_3 &= -\frac{k_{\omega z}}{J_{33}}\omega_3\,. && (6.28)
\end{aligned}$$

Following the above linearization of the system, we introduce a parametric uncertainty in the mass of the UAV; the uncertainty is modeled in m such as $\frac{1}{m} = \frac{1}{m^\circ(1+p_m\delta_m)}$, where m° is a nominal mass, p_m defines a range for uncertain mass and δ_m is an uncertainty of unknown magnitude (usually $|\delta_m| < 1$). The derivation will consider x axis terms.

In order to test its robust stability, the influence that the considered uncertainty can exert on the relations in the system is examined. Let the two signals be

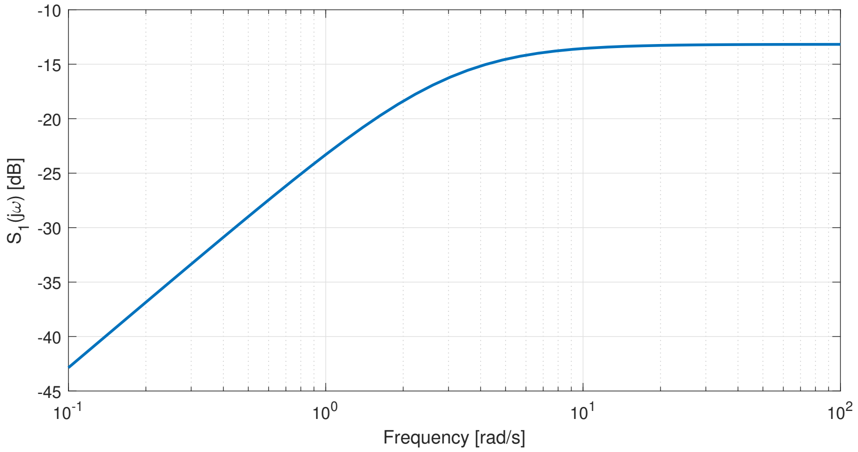

Figure 6.6 – Log-magnitude plot of M (small-gain theorem)

introduced, u_Δ as the input to the uncertainty, and y_Δ as its output,

$$\dot{p}_x = v_x \,, \tag{6.29}$$

$$\dot{v}_x = \frac{1}{m^\circ p_m} u_\Delta \,, \tag{6.30}$$

$$u_\Delta = -p_m k_p p_x - p_m k_v v_x - p_m y_\Delta \,, \tag{6.31}$$

$$y_\Delta = \delta_m u_\Delta \,. \tag{6.32}$$

Having assumed zero initial conditions, and doing the Laplace transform

$$M(s) = \frac{U_\Delta(s)}{Y_\Delta(s)} = \frac{-m^\circ p_m s^2}{m^\circ s^2 + k_v s + k_p} \tag{6.33}$$

$$\frac{1}{1 - M(s)\delta_m} = \frac{m^\circ s^2 + k_v s + k_p}{m^\circ(1 + p_m\delta_m)s^2 + k_v s + k_p} \tag{6.34}$$

Since Eq. (6.34) is proper, we concur that there is no destabilizing uncertainty, as per Routh stability criterion $m^\circ(1 + p_m\delta_m) > 0$, $k_p > 0$, $k_v > 0$ at all times.

Since $1 - M(s)\delta_m$ has a proper and stable inverse for all $\delta_m \in \Delta$, where Δ describes the uncertainty set, then the controller robustly stabilizes the considered uncertain plant against Δ [Zhou–1996]. Equivalently, since there exists r such that $\|M\|_\infty \leq \frac{1}{r}$ holds, with $|\delta_m| < r$ and $\delta_m \in \Delta$, then $1 - M(s)\delta_m$ has a proper and stable inverse for all $\delta_m \in \Delta$, as per small gain theorem (see Fig. 6.6, with $r = 1$, $m = 1$, $k_p = 20$, $k_v = 10$, $p_m = 1$).

For larger values of k_p and k_v (which define the first two diagonal terms in $\mathbf{K}_p$ and $\mathbf{K}_v$) the left part of the plot moves up, which means we have lower capability to reject possible low-frequency uncertainties, what forms a natural bound expressed by reducing robustness against such uncertainties. As the range of gains remains unknown, there is a need to optimize them for a given $\overline{f_{xy}}$. In addition, as the method allows one to feed a reference primitive with selected dynamics, OPTIM-tune can find optimized controller gains to improve tracking. Shaping the loop to have narrow-bandwidth like properties, resembles the results obtained from robustness issues optimization.

6.5.2 Sensitivity vs. complementary sensitivity

On the basis of the first-order Taylor expansion of Eq. (6.13) at $e_{x0} = e_{v0} = 0$, one gets

$$\begin{aligned}
a &:= 2\tan^{-1}\left(\frac{mg \pm \sqrt{(mg)^2 - \overline{f_{xy}}^2}}{\overline{f_{xy}}}\right), && (6.35)\\
b_1 &:= \frac{2k_p\left(mg \pm \sqrt{(mg)^2 - \overline{f_{xy}}^2}\right)}{\overline{f_{xy}}^2 + \left(mg \pm \sqrt{(mg)^2 - \overline{f_{xy}}^2}\right)^2}, && (6.36)\\
&= \frac{k_p}{mg} && (6.37)\\
b_2 &:= \frac{2k_v\left(mg \pm \sqrt{(mg)^2 - \overline{f_{xy}}^2}\right)}{\overline{f_{xy}}^2 + \left(mg \pm \sqrt{(mg)^2 - \overline{f_{xy}}^2}\right)^2}, && (6.38)\\
&= \frac{k_v}{mg}. && (6.39)
\end{aligned}$$

Now, having assumed that $\theta \approx 0$ we get $\sin(\theta) \approx \theta$, $\cos(\theta) \approx 1$, and by additionally assuming $\omega_2 \approx 0$, our equations simplify to the following:

$$\boldsymbol{u} = [u_x,\, u_y]^T\,. \tag{6.40}$$

$$\begin{aligned}
\dot{p}_x &= v_x\,, && (6.41)\\
\dot{v}_x &= -\frac{1}{m}u_x - \frac{1}{m}u_v\,, && (6.42)\\
\dot{r}_{13} &= \omega_2\,, && (6.43)\\
\dot{\omega}_1 &= -\frac{k_{\omega x}}{J_{11}}\omega_1\,, && (6.44)\\
\dot{\omega}_2 &= -\frac{k_{ry}}{J_{22}}r_2 - \frac{k_{\omega y}}{J_{22}}\omega_2\\
&\quad + \frac{b_1 k_{ry}}{J_{22}k_p}e_{px} + \frac{b_2 k_{ry}}{J_{22}k_v}e_{vx} + \frac{a k_{ry}}{J_{22}}\,, && (6.45)\\
\dot{\omega}_3 &= -\frac{k_{\omega z}}{J_{33}}\omega_3\,. && (6.46)
\end{aligned}$$

As per $\dot{\theta} = \dot{r}_2 = \omega_2$ and

$$\boldsymbol{u} = \mathbf{K}_x \boldsymbol{e}_x = \begin{bmatrix} k_p & 0 \\ 0 & k_v \end{bmatrix} \begin{bmatrix} e_{px} \\ e_{vx} \end{bmatrix}, \tag{6.47}$$

the system reduces to ($\omega_1 = 0$, $\omega_3 = 0$)

$$\begin{aligned}
\dot{p}_x &= v_x \,, &(6.48)\\
\dot{v}_x &= -\frac{1}{m} u_x - \frac{1}{m} u_v \,, &(6.49)\\
\dot{\theta} &= \omega_2 \,, &(6.50)\\
\dot{\omega}_2 &= -\frac{k_{\omega y}}{J_{22}} \omega_2 - \frac{k_{ry}}{J_{22}} \theta \\
&\quad + \frac{b_1 k_{ry}}{J_{22} k_p} u_x + \frac{b_2 k_{ry}}{J_{22} k_v} v_x + \frac{a k_{ry}}{J_{22}} \,, &(6.51)
\end{aligned}$$

where a, b_1, b_2 result from Taylor expansion of θ_d.

Let us consider a triplet of external disturbances acting on the system as: an additive linear force, an additive torque, and a another one to model the term $\frac{a k_{ry}}{J_{22}}$, in the form

$$\Delta_v, \quad \Delta'_\omega, \quad \Delta_a \,, \tag{6.52}$$

respectively, where each is norm-bounded (infinity norm) to 1. Our system of equations can thus be rewritten in the following form:

$$\begin{aligned}
\dot{p}_x &= v_x \,, &(6.53)\\
\dot{v}_x &= -\frac{1}{m} u_x - \frac{1}{m} u_v + \delta_v \Delta_v \,, &(6.54)\\
\dot{\theta} &= \omega_2 \,, &(6.55)\\
\dot{\omega}_2 &= -\frac{k_{\omega y}}{J_{22}} \omega_2 - \frac{k_{ry}}{J_{22}} \theta + \frac{b_1 k_{ry}}{J_{22} k_p} u_x + \frac{b_2 k_{ry}}{J_{22} k_v} u_v + \\
&\quad + \delta_{\omega'} \Delta_{\omega'} + \delta_a \Delta_a \,. &(6.56)
\end{aligned}$$

Having assumed zero initial conditions, and incorporating $\delta_{\omega'} \Delta_{\omega'} + \delta_a \Delta_a$ into $\delta_\omega \Delta_\omega$, with $e_{vx} = \dot{e}_{px}$, it holds that

$$\begin{aligned}
s P_x(s) &= V_x(s) \,, &(6.57)\\
s V_x(s) &= -\frac{1}{m} U_x(s) - \frac{1}{m} U_v(s) + \delta_v \Delta_v(s) \,, &(6.58)\\
s \Theta(s) &= \Omega_2(s) \,, &(6.59)\\
s \Omega_2(s) &= -\frac{k_{\omega y}}{J_{22}} \Omega_2(s) - \frac{k_{ry}}{J_{22}} \Theta(s) + \frac{b_1 k_{ry}}{k_p J_{22}} U_x(s) \\
&\quad + \frac{b_2 k_{ry}}{k_v J_{22}} U_v(s) + \delta_\omega \Delta_\omega(s) \,. &(6.60)
\end{aligned}$$

where $u_v = k_v e_{vx} = k_v \dot{e}_{px} = k\dot{u}_x$ with $k = \frac{k_v}{k_p}$.

The above system can be reduced as follows:

$$\begin{aligned} V_x(s) &= -\frac{ks+1}{sm}U_x(s) + \frac{\delta_v}{s}\Delta_v(s)\,, && (6.61) \\ s\Omega_2(s) &= -\frac{1}{J_{22}}\left(\frac{k_{ry}}{s} + k_{\omega y}\right)\Omega_2(s) + \\ &\quad + \frac{1}{k_p J_{22}}\left(s b_2 k_{ry} + b_1 k_{ry}\right)U_x(s) \\ &\quad + \delta_\omega \Delta_\omega(s) && (6.62) \end{aligned}$$

and

$$\begin{aligned} V_x(s) &= -\frac{ks+1}{sm}U_x(s) + \frac{\delta_v}{s}\Delta_v(s)\,, && (6.63) \\ \Omega_2(s) &= \frac{s^2 b_2 k_{ry} + s b_1 k_{ry}}{s^2 k_p J_{22} + s k_p k_{\omega y} + k_p k_{ry}}U_x(s) + \\ &\quad + \frac{s k_p J_{22}\delta_\omega}{s^2 k_p J_{22} + s k_p k_{\omega y} + k_p k_{ry}}\Delta_\omega(s)\,. && (6.64) \end{aligned}$$

The above equations can be presented as a multi-input multi-output system as follows:

$$\begin{bmatrix} V_x(s) \\ \Omega_2(s) \end{bmatrix} = \begin{bmatrix} -\frac{ks+1}{sm} & \frac{\delta_v}{s} & 0 \\ \frac{s^2 b_2 k_{ry} + s b_1 k_{ry}}{s^2 k_p J_{22} + s k_p k_{\omega y} + k_p k_{ry}} & 0 & \frac{s k_p J_{22}\delta_\omega}{s^2 k_p J_{22} + s k_p k_{\omega y} + k_p k_{ry}} \end{bmatrix} \begin{bmatrix} U_x(s) \\ \Delta_v(s) \\ \Delta_\omega(s) \end{bmatrix}\,. \qquad (6.65)$$

Then the connection between $U_x(s)$ and $V_x(s)$ can be written as follows:

$$\begin{aligned} L_1(s) &= \frac{V_x(s)}{U_x(s)} = -k_P\frac{ks+1}{sm} && (6.66) \\ T_1(s) &= \frac{L_1(s)}{1+L_1(s)} = -\frac{k_P\frac{ks+1}{sm}}{1-k_P\frac{ks+1}{sm}} = && (6.67) \\ &= -\frac{k_P(ks+1)}{ms - k_P(ks+1)} = \frac{k_v s + k_p}{(k_v - m)s + k_P}\,, && (6.68) \\ S_1(s) &= \frac{1}{1+L_1(s)} = -\frac{sm}{(k_v - m)s + k_p}\,, && (6.69) \end{aligned}$$

and the connection between $U_x(s)$ and $\Omega_2(s)$ can be written as follows:

$$L_2(s) = \frac{\Omega_2(s)}{U_x(s)} = k_v \frac{sb_2k_{ry} + b_1k_{ry}}{s^2k_pJ_{22} + sk_pk_{\omega y} + k_pk_{ry}} \,, \tag{6.70}$$

$$T_2(s) = \frac{L_2(s)}{1+L_2(s)} = \frac{k_v \frac{sb_2k_{ry}+b_1k_{ry}}{s^2k_pJ_{22}+sk_pk_{\omega y}+k_pk_{ry}}}{1 + k_v \frac{sb_2k_{ry}+b_1k_{ry}}{s^2k_pJ_{22}+sk_pk_{\omega y}+k_pk_{ry}}} = \tag{6.71}$$

$$= \frac{sk_vb_2k_{ry} + k_vb_1k_{ry}}{s^2k_pJ_{22} + sk_pk_{\omega y} + k_pk_{ry} + sk_vb_2k_{ry} + k_vb_1k_{ry}} = \tag{6.72}$$

$$= \frac{sk_vb_2k_{ry} + k_vb_1k_{ry}}{s^2k_pJ_{22} + s(k_pk_{\omega y} + k_vb_2k_{ry}) + k_{ry}(k_p + k_vb_1)} \,, \tag{6.73}$$

$$S_2(s) = \frac{1}{1 + k_v \frac{sb_2k_{ry}+b_1k_{ry}}{s^2k_pJ_{22}+sk_pk_{\omega y}+k_pk_{ry}}} = \tag{6.74}$$

$$= \frac{s^2k_pJ_{22} + sk_pk_{\omega y} + k_pk_{ry}}{s^2k_pJ_{22} + s(k_pk_{\omega y} + k_vb_2k_{ry}) + k_{ry}(k_p + k_vb_1)} \,. \tag{6.75}$$

At this point, naturally the following constraints appear, related to Routh stability criterion:

$$k_v - m > 0 \quad , \tag{6.76}$$

$$k_p > 0 \quad , \tag{6.77}$$

$$k_p + k_vb_1 > 0 \,, \tag{6.78}$$

$$k_pk_{\omega y} + k_vb_2k_{ry} > 0 \,, \tag{6.79}$$

as

$$k_v > m \quad , \tag{6.80}$$

$$k_p > 0 \quad , \tag{6.81}$$

giving natural bounds on controller gains. Please note that the transfer functions are of second-order, and as per Nyquist stability criterion, the closed-loop system has simple stability conditions.

In the potential analysis, and following [Zhou–1996], a MULTIPLICATIVE uncertainty $\Delta(s)$ acting at a plant $P(s)$ output can be included; the transfer function between the output of the uncertainty and its input equals $-T_1(s)$ or $-T_2(s)$. By the small gain theorem, these sub-systems remain stable for

$$\|\Delta(j\omega)\|_\infty \|T(j\omega)\|_\infty < 1 \tag{6.82}$$

what corresponds to all the plants in the form $P(s)(1+\Delta(s))$ for $\|\Delta(j\omega)\|_\infty < r$ where $\|T(j\omega)\|_\infty < \frac{1}{r}$.

Considering an ADDITIVE uncertainty $\Delta(s)$ acting on the plant $P(s)$, the transfer function between the output of the uncertainty and its input equals $C(s)S_1(s)$ or $C(s)S_2(s)$, where the plant is given by $P(s)+\Delta(s)$ and $C(s)$ is the transfer function

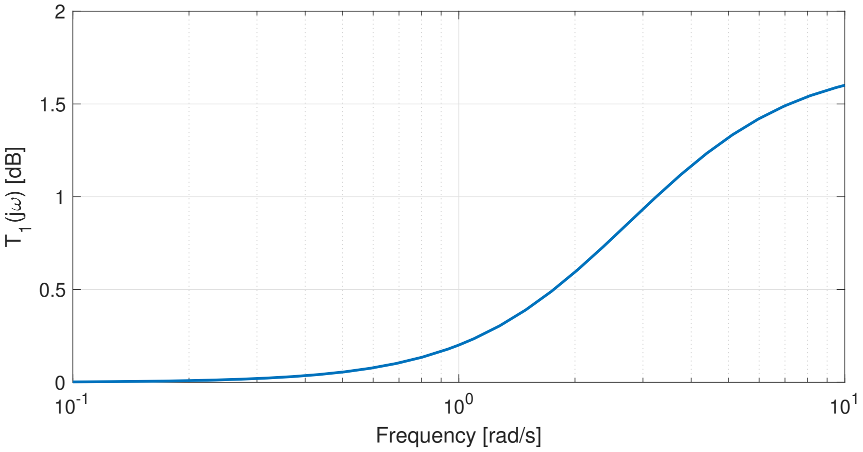

Figure 6.7 – Complementary sensitivity function $T_1(j\omega)$ for $\overline{f_{xy}} = 4$, $k_p = 25$, $k_v = 10$

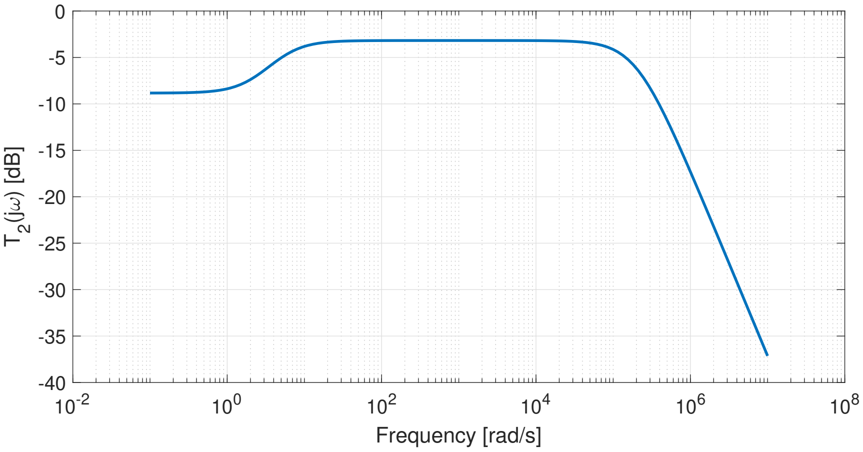

Figure 6.8 – Complementary sensitivity function $T_2(j\omega)$ for $\overline{f_{xy}} = 4$, $k_p = 25$, $k_v = 10$

of the controller. By the small gain theorem, these sub-systems remain stable for

$$\|\Delta(j\omega)\|_\infty \|C(j\omega)S(j\omega)\|_\infty < 1\,. \tag{6.83}$$

Abiding by these constraints, the closed-loop system remains stable whenever in the model ($m = 1.8$, $k_{ry} = 7$, $k_{\omega y} = 0.7$, $J_{22} = 11.4 \cdot 11^{-6}$) it holds that $k_p > 0$ and $k_v > m$.

It can be seen from Fig. 6.7 and Fig. 6.8 that $\|T_1\|_\infty$ and $\|T_2\|_\infty$ are always norm-bounded, $\|T_2\|_\infty$ is always below 1, while $\|T_1\|_\infty$ is below 1 for low frequencies. As such, the linear controller is robust to the aforementioned external disturbances, while the attitude controller is robust to these disturbances only when these disturbances have a low frequency.

6.6 Conclusions

In this chapter, we studied the interplay between the parameters and gains of the BLF controller. We showed that the optimally-chosen position control gains rely largely on the estimated lateral force limit.

While one can fix the estimated lateral force limit at one of its extreme values, we discussed the effect of these extremes, where if the limit is chosen small enough the platform behaves as an underactuated one, while if chosen large enough, it might exceed the physical capabilities of the platform, and thus the controller could behave sub-optimally.

We then presented a detailed method for the auto-tuning of the position control gains for different estimated lateral force limits, and showed how these optimized gains vary accordingly. However, the choice of this parameter is still an open question, where for each application, different values of the lateral force limit should be chosen. Moreover, based on the applied lift force, this parameter has to be changed with the corresponding optimized gains.

While the optimization was done in "near-perfect" conditions, we provided a formal study of the robustness of the presented optimized controller to variances in the platform's mass and its robustness to external disturbances. This study shows that while the position controller is robust to external disturbances in any frequency range, the attitude controller is only robust to slowly varying external disturbances. Finally, this study also showed that the controller is robust to a bounded low frequency variance in the platform mass.

To conclude, this study shows how the trajectory tracking capability of a platform is affected following its actuation properties, which is directly affected by its geometry. While the current study was conducted on a single platform, it allowed us to test different actuation capabilities from UDT to FA, and showed that a UDT platform (with zero lateral force) can only track a **TT.2** trajectory, while as it approached FA (non-zero lateral forces) it can track trajectories with high Degrees of Freedom (DoF).

Part III

Effect of IMU on the Robustness of MAV

Chapter 7

IMU Filtering

7.1 Introduction

In this chapter we aim to understand the noise profile present in Inertial Measurement Unit (IMU)s placed on-board Multi-Rotor Aerial Vehicle (MRAV)s, and present a novel IMU filter for control purposes.

While IMUs on-board MRAVs have a noise profile that is affected by the propellers vibrating the platform, these sensors are generally filtered with a general purpose low pass filters. General purpose low pass filters add delay and phase shift to the measurements, in addition to removing high frequency components of the signal. As such, the aim of this chapter is to introduce a specific filter, that extracts *only* noise frequencies caused by the propellers, which we will refer to as vibrations.

In what follows, while our analysis will only show the study of acceleration measurements, we do note that the same analysis applies for the gyroscope measurements in terms of vibration analysis and used filter, however, we will omit it to avoid redundancy.

7.2 Vibration Frequency Analysis

This section analyzes IMU measurements of a quadrotor platform and a tilted propeller hexarotor referred to as the FiberTHex (App. A). We expect the vibration noise on-board the platforms to be directly caused by the propellers, where we hypothesize that as the propellers pass above (or below) the platforms' arms (the rod connecting the platform's Center of Mass (CoM) to the propellers' CoM) it creates a negative (or positive) pressure which lets the arms oscillate; this oscillation is then propagated through the platform body to the mounted IMU. As such, we expect the platform geometry or material to also affect the characteristics of the vibration noise.

Our analysis relies on the frequency domain analysis of each measurement, in an attempt to understand the connection between the vibration noise frequency w.r.t. the platforms' propeller velocity commands.

We compare the IMU measurements with a ground truth constructed from a motion capture system (optiTrack system) data. First, let us define the IMU acceleration measurements as $\boldsymbol{a}_{imu} \in \mathbb{R}^3$; the IMU provides the specific acceleration of the platform, i.e., if we assume IMU accelerations measurements to be ideal (noise and vibration free) they could be written as follows:

$$\boldsymbol{a}_{imu} = {}^{W}\boldsymbol{R}_B^{\top}({}^{W}\ddot{\boldsymbol{p}}_B - \boldsymbol{g}) \tag{7.1}$$

from which one can get a direct measure of the acceleration

$$^{W}\ddot{\boldsymbol{p}}_B = {}^{W}\boldsymbol{R}_B \boldsymbol{a}_{imu} + \boldsymbol{g} \tag{7.2}$$

On the other hand, the motion capture system provides only position measurements in $\mathcal{W}$ (in addition to orientation measurements). As such, the collected motion capture data is post processed offline to find the corresponding specific accelerations. Formally, let us note by $\boldsymbol{p}_{opti}(t) \in \mathbb{R}^3$ as the position measurement at time instance t of frame O_B in $\mathcal{W}$ as measured by the motion capture system. Moreover, let us assume that the platform's acceleration is constant over a window of motion capture measurements $[\boldsymbol{p}_{opti}{}^{\top}(t-nT)\ \boldsymbol{p}_{opti}{}^{\top}(t-(n-1)T)\ \dots\ \boldsymbol{p}_{opti}{}^{\top}(t+(n-1)T)\ \boldsymbol{p}_{opti}{}^{\top}(t+nT)] \in \mathbb{R}^{3(2n+1)}$, where $n \in \mathbb{N}_{>0}$ and $T \in \mathbb{R}_{>0}$ is the sampling period. Then we can estimate the corresponding acceleration $\boldsymbol{a}_{opti}(t) \in \mathbb{R}^3$ of O_B in $\mathcal{W}$ through second order linear regression, such that

$$\boldsymbol{p}_{opti}(j)_{j=t-nT}^{t+nT} = \boldsymbol{\theta}_{\boldsymbol{p}_{opti},0} + \boldsymbol{\theta}_{\boldsymbol{p}_{opti},1} j + \frac{1}{2}\boldsymbol{\theta}_{\boldsymbol{p}_{opti},2} j^2, \tag{7.3}$$

where the estimated motion capture specific acceleration can be computed from the second order polynomial factor such as

$$\boldsymbol{a}_{opti}(t) = {}^{W}\boldsymbol{R}_B^{\top}(\boldsymbol{\theta}_{\boldsymbol{p}_{opti},2} - \boldsymbol{g}). \tag{7.4}$$

Finally, the IMU measured acceleration $\boldsymbol{a}_{imu}$ is compared to the motion capture one $\boldsymbol{a}_{opti}$ in the frequency domain, where the frequency domain in computed using the Fast Fourier Transform technique from [Frigo–1998].

The resulting frequency domain analysis for the quadrotor platform is shown in Fig. 7.1 and the one for the FiberTHex platform is shown in Fig. 7.2. These figures also show the propeller commands in the corresponding time window. In these figures we will refer to the vibration ground truth (GT) as the difference between the frequency domain of $\boldsymbol{a}_{imu}$ and $\boldsymbol{a}_{opti}$. We can observe from Fig. 7.1 that the GT vibrations have frequencies in the same range of the propeller commands throughout the platform's flight, in addition to vibrations with frequencies in the range of the first harmonic of the propeller commands. On the other hand, we can observe for the FiberTHex, Fig. 7.2, that we have two peak frequencies in the range of the propeller commands (i.e., one peak near 50 [Hz] and one near 65 [Hz]), in addition to their first harmonics; in addition to these peaks, the GT vibrations contain a peak that is not in the range of the propeller commands (at 37 [Hz]). We do note that this last peak in the FiberTHex GT vibrations is 'always' present even when sub-windows of the data are analyzed.

The difference between the two behaviors is expected to be caused by some of the following:

1) The quadrotor have propellers producing thrust only along $\boldsymbol{z}_B$, while the propellers in the FiberTHex produce thrust each along a different direction.

2) The quadrotor's arms connecting the platform CoM to the propellers' CoMs are constructed from aluminum, while the arms of the FiberTHex are con-

structed from carbon fiber (note that aluminum material has a lower damping ratio than the carbon fiber material).

3) Finally, the IMU in the FiberTHex is mounted on a damper, while it is mounted directly on the quadrotor's body frame.

To understand which of the above differences is causing the 37 [Hz] vibration, we analyze the spectrum of another tilted propeller hexarotor: the TiltHex presented in [Ryll–2017b]. The TiltHex platform has the same geometry as the FiberTHex (i.e., same arm length, propeller disposition and orientation); however, the TiltHex is constructed from aluminum bars, similarly to the quadrotor, and its IMU is mounted on the platform's body without the use of a damper. As such, the only difference between the quadrotor and the TiltHex is the platform's geometry and number of propellers.

Fig. 7.3 shows the resulting frequency domain analysis of the TiltHex flight. We can see from this figure that the 37 [Hz] vibration is present in the TiltHex vibration analysis, similar to the FiberThex case. However, and unlike the FiberTHex case, the other vibrations that are in the range of the propeller commands are distributed over a larger range, while in the FiberTHex case they were gathered around two peaks. This suggests that the 37 [Hz] vibration is caused by the platform geometry, while the material used in the FiberTHex is dampening the vibration generated by the propellers.

As such, the difference between the GT vibrations in these figures show that different platform geometry (and number of propellers) and/or material can affect differently the vibration noise. Moreover, our analysis suggests that the relation between the vibration noise and the propeller commands in a quadrotor to be directly related to propeller commands. As such, in what follows we will propose a method to extract such noise vibrations from a quadrotor while assuming these vibrations to be a sum of vibrations in the range of the propeller rotational commands and vibrations in the range of their first harmonics. Then we will analyze the same method for the FiberTHex case and suggest an intuitive extension to the quadrotor case to filter the IMU measurements of the FiberTHex.

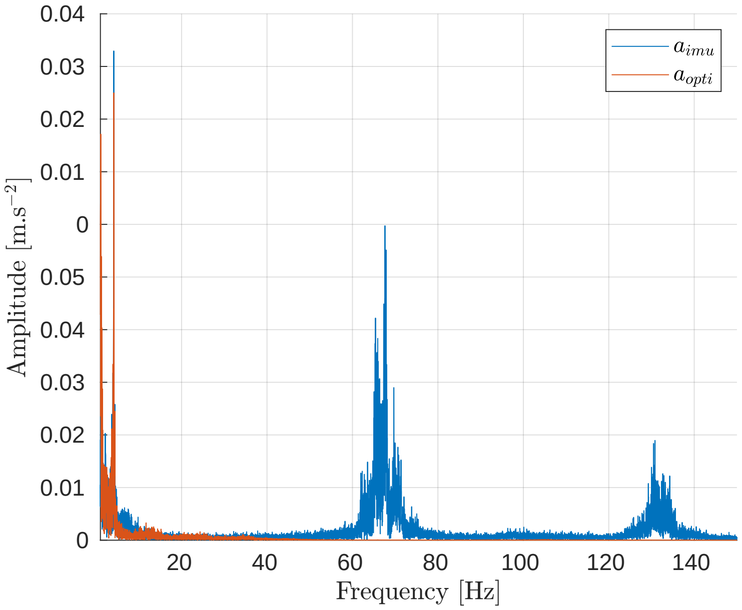

(a) Acceleration measurements frequency domain

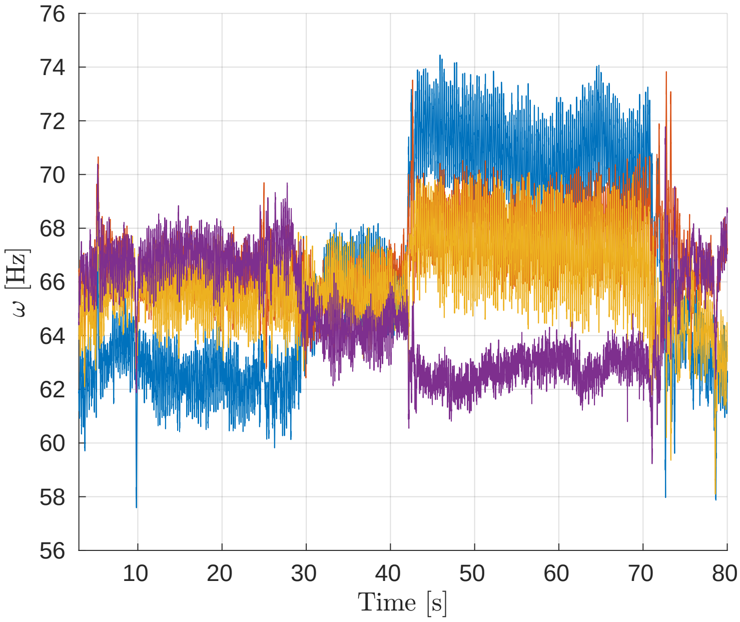

(b) Propeller rotational commands

Figure 7.1 – Acceleration measurements frequency domain and propeller rotational commands on-board the quadrotor platform.

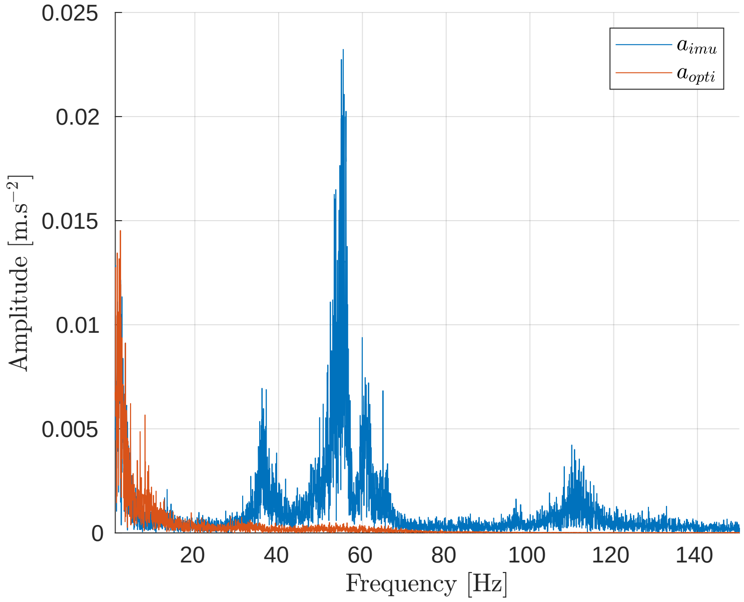

(a) Acceleration measurements frequency domain

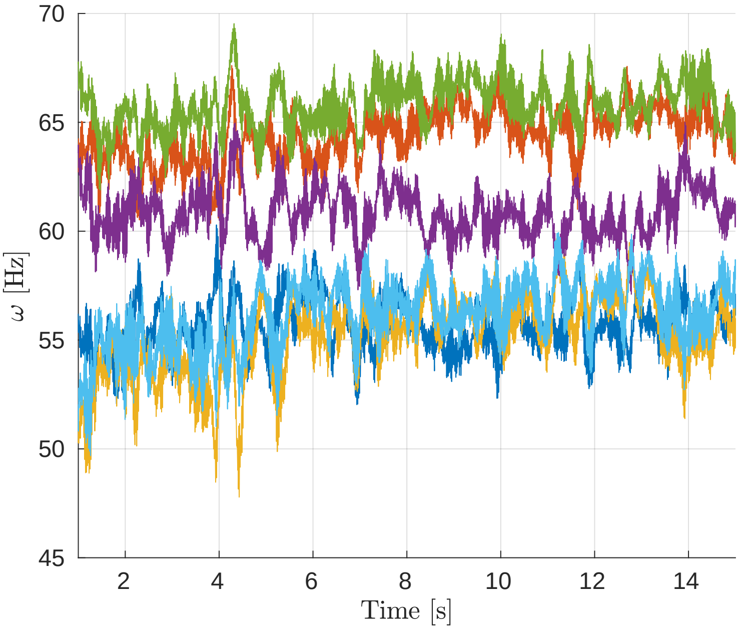

(b) Propeller rotational commands

Figure 7.2 – Acceleration measurements frequency domain and propeller rotational commands on-board the FiberTHex platform.

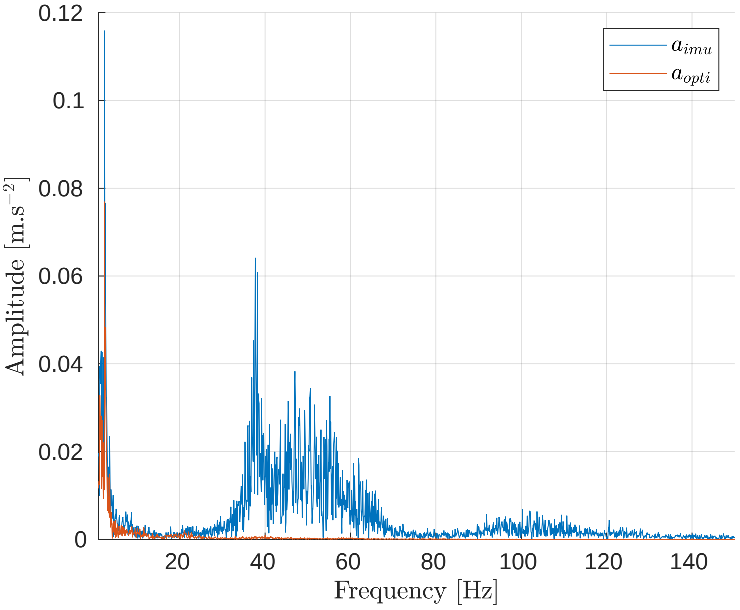

(a) Acceleration measurements frequency domain

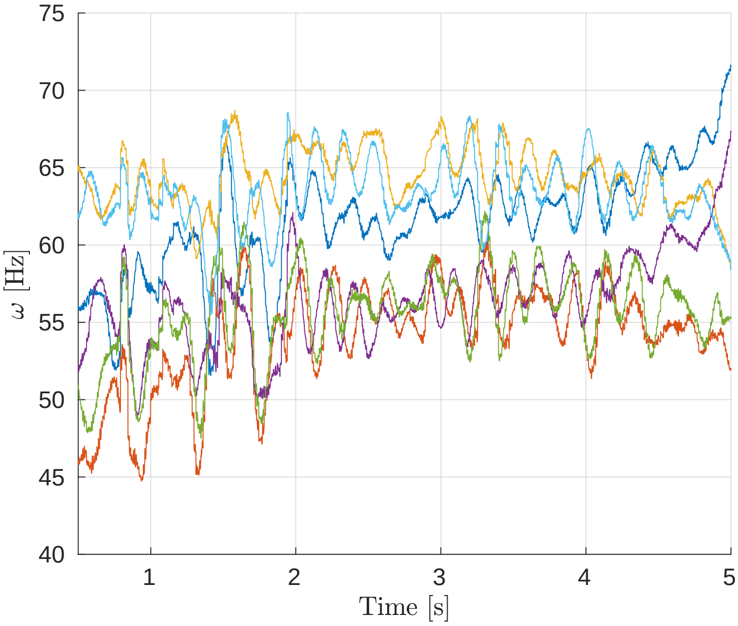

(b) Propeller rotational commands

Figure 7.3 – Acceleration measurements frequency domain and propeller rotational commands on-board the TiltHex platform.

7.3 Quadrotor IMU Filter

The raw accelerometer measurements are practically unusable for control applications such as the one presented later in Chapt. 8 due to high amplitude noise, mostly coming from the vibrations of the propellers. The most common technique to extract the body acceleration is to use a low-pass filter, which introduces frequency dependent delay and phase shift, and can remove high frequency components of the signal. Moreover, low-pass filters are linear filters that only attenuate high frequency noise proportionally to its amplitude, instead of completely removing it, regardless of its amplitude. As such, a high amplitude noise can still show up significantly in the linearly filtered signal. On the other hand, classical notch filters could be designed to remove only vibrations at the corresponding frequencies, however, they share the same drawbacks of the classical low pass filter, i.e., they only attenuate proportionally the vibration noise and add a phase shift as well. Moreover, it is very difficult to design a notch filter that is narrow enough that it does not affect signal frequencies that could be found near vibration frequencies.

To overcome the above limitations, and leverage the knowledge of the vibration frequencies, we designed an adaptive and regression-based notch filter that allows to reject multiple frequency components, without adding any delay or phase shift, and that at the same time remains computationally simple enough to be implement in real time on a low power CPU. In addition, as our filter is regression-based, it is able to find the amplitude of the noise signal and virtually remove it completely from the acceleration signal, regardless of its amplitude, where a linear filter could only attenuate it as explained before.

Considering what has been presented so far, we can modify the ideal accelerometer model in Eq. (7.1) into:

$$\boldsymbol{a}_{imu} = \dot{\boldsymbol{v}}^S + \boldsymbol{\delta} + \boldsymbol{\sigma}, \tag{7.5}$$

where $\dot{\boldsymbol{v}}^S = \boldsymbol{R}_B^\top \left({}^W\ddot{\boldsymbol{p}}_B - \boldsymbol{g}\right)$ is the *true* specific acceleration of the main body, the one that we would like to estimate, $\boldsymbol{\delta}$ represents the vibrations induced by spinning propellers, and $\boldsymbol{\sigma}$ represents all the additional noise, assumed gaussian distributed with zero mean.

Let us consider a certain time window of $n \in \mathbb{N}_{>0}$ acceleration samples, $\tilde{\boldsymbol{a}}_{imu}(t) = [\boldsymbol{a}_{imu}^\top(t)\ \ \boldsymbol{a}_{imu}^\top(t-T)\ \ \dots\ \ \boldsymbol{a}_{imu}^\top(t-nT)]^\top \in \mathbb{R}^{3n}$, where $T \in \mathbb{R}_{>0}$ is the sampling period. The different components and assumptions for the presented filter are shown in Fig. 7.4. The first step to estimate $\dot{\boldsymbol{v}}^S(t)$ given $\tilde{\boldsymbol{a}}_{imu}(t)$ is to model the components of $\boldsymbol{a}_{imu}$. For the specific acceleration we use a Taylor/polynomial approximation:

$$\dot{\boldsymbol{v}}^S(t) = \sum_{i=0}^{p} \theta_{\boldsymbol{v}i} t^i, \tag{7.6}$$

where $p \in \mathbb{N}_{>0}$ is the degree of the polynomial which has to be chosen a priori and depends on the variability signal $\dot{\boldsymbol{v}}^S$ over the time window $[t - nT, t]$ (as a rule of thumb, in general, the larger the time window the larger p), and $\theta_{\boldsymbol{v}i} \in \mathbb{R}$ is the generic unknown i-th coefficient of the polynomial to be estimated. We model $\boldsymbol{\delta}$ as

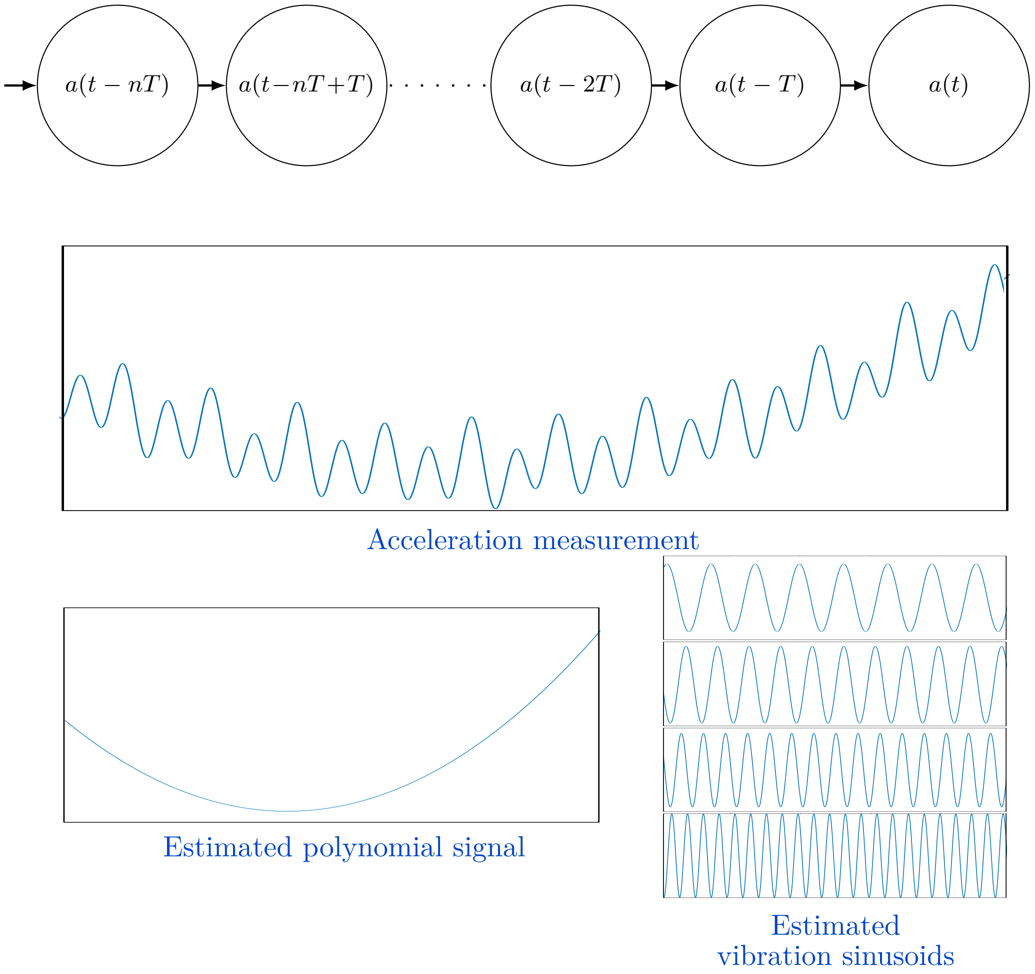

Figure 7.4 – Schematic of the assumptions made for the regression based filter proposed in this chapter. The regression based filter fits into the last n acceleration measurements a regression model, where the signal is a sum of the signal, assumed as a polynomial, and sum of sinusoids.

a sum of q shifted sinusoidal functions:

$$\boldsymbol{\delta}(t) = \sum_{j=0}^{q} \theta_{\boldsymbol{\delta}j} \sin\left(\omega_{\boldsymbol{\delta}j} t + \phi_{\boldsymbol{\delta}j}\right), \tag{7.7}$$

where $\theta_{\boldsymbol{\delta}j} \in \mathbb{R}$ and $\phi_{\boldsymbol{\delta}j} \in \mathbb{R}$ are the amplitude and phase shift of the generic j-th sinusoidal, again to be estimated. We assume that the pulsation $\omega_{\boldsymbol{\delta}j}$ of the j-th sinusoidal is known since it is directly linked to the spinning frequency of the propellers and its harmonics. There are several ways to choose q and $\omega_{\boldsymbol{\delta}j}$ according to the current frequency of the propellers. In general, it is a good practice to choose q as small as possible to avoid over-fitting. Following this guideline, we choose $q = 4$ for the quadrotor case taking $\omega_{\boldsymbol{\delta}1}$ and $\omega_{\boldsymbol{\delta}2}$ as the minimum spinning frequency among the propellers (in the considered time window) and its first harmonic, respectively.

Similarly, we take $\omega_{\boldsymbol{\delta}3}$ and $\omega_{\boldsymbol{\delta}4}$ as the maximum spinning frequency among the propellers (in the considered time window) and its fist harmonic, respectively.

Noticing that $\sin(\omega_{\boldsymbol{\delta}j}t + \phi_{\boldsymbol{\delta}j}) = \cos(\phi_{\boldsymbol{\delta}j})\sin(\omega_{\boldsymbol{\delta}j}t) + \sin(\phi_{\boldsymbol{\delta}j})\cos(\omega_{\boldsymbol{\delta}j}t)$ we can rewrite Eq. (7.7) as

$$\boldsymbol{\delta}(t) = \sum_{i=0}^{q} \theta_{cj} \sin(\omega_{\boldsymbol{\delta}j}t) + \theta_{sj} \cos(\omega_{\boldsymbol{\delta}j}t), \tag{7.8}$$

which is now linear in the new parameters $\theta_{cj} = \theta_{\boldsymbol{\delta}j}\cos(\phi_{\boldsymbol{\delta}j})$ and $\theta_{sj} = \theta_{\boldsymbol{\delta}j}\sin(\phi_{\boldsymbol{\delta}j})$.

Notice that the minimum requirement is $N \geq p + 2q$. In addition, in order to clearly identify all the sinusoidal components, it is desirable that $\tilde{\boldsymbol{a}}_{imu}$ contains at least a full period of the slowest sinusoidal signal.

Finally, in order to remove the additional second order noise $\boldsymbol{\sigma}$ (i.e., the ‘small’ residual noise that is not model by the regression) from ${}^{S}\hat{\boldsymbol{v}}$ we use a discrete adaptive high-bandwidth low-pass filter. Let ${}^{S}\hat{\boldsymbol{v}}[k]$ be the regressed estimation of the specific acceleration at the discrete-time $t_k = kT$, where $k \in \mathbb{N}^+$. Then the adaptive high-bandwidth low-pass filter can be expressed as:

$${}^{S}\hat{\boldsymbol{v}}_f[k] = (1 - \kappa[k])\,{}^{S}\hat{\boldsymbol{v}}_f[k-1] + \kappa[k]\,{}^{S}\hat{\boldsymbol{v}}[k], \tag{7.9}$$

where ${}^{S}\hat{\boldsymbol{v}}_f[k]$ is the low-pass filtered value of ${}^{S}\hat{\boldsymbol{v}}[k]$, and $\kappa[k]$ is an adaptive gain computed as:

$$\kappa[k] = min\left(1, \left|\frac{{}^{S}\hat{\dot{\boldsymbol{v}}}[k]}{\ddot{\boldsymbol{v}}^{th}}\right|\right), \tag{7.10}$$

where $|.|$ represents the absolute value, ${}^{S}\hat{\dot{\boldsymbol{v}}}[k]$ is an estimation of the rate of change of $\dot{\boldsymbol{v}}^S$ calculated from the regressed derivative of ${}^{S}\hat{\boldsymbol{v}}$, and $\ddot{\boldsymbol{v}}^{th}$ is a threshold rate such that if ${}^{S}\hat{\dot{\boldsymbol{v}}}[k] \geq \ddot{\boldsymbol{v}}^{th}$ the filter would behave as a zero-phase all-pass filter.

The chosen adaptive gain allows the filter to have low bandwidth when $\dot{\boldsymbol{v}}^S$ is slowly varying (a case in which the effect of $\boldsymbol{\sigma}$ is more visible), thus effectively filtering the second order noise, and a very high bandwidth when $\dot{\boldsymbol{v}}^S$ is rapidly varying (a case in which the effect of $\boldsymbol{\sigma}$ is almost negligible compared to the variation of the signal) to obtain non-delayed tracking.

Filter Results In this paragraph we demonstrate the outcome of the filter to understand its behavior, and better understand its advantage over the classically used second-order Butterworth filter ([Tal–2018]). As such, we will first show the frequency domain analysis of the filtered signal to demonstrate that our filter can indeed remove the vibration noise frequencies. Then we will show time domain plots to demonstrate the behavior of the filter against the classical controller.

In Fig. 7.5 we show the frequency domain of the original IMU signal $\boldsymbol{a}_{imu}$, and the corresponding estimated specific acceleration ${}^{S}\hat{\boldsymbol{v}}$, i.e., filtered with our regression-based filter. Fig. 7.5 shows clearly that the filtered signal attenuates

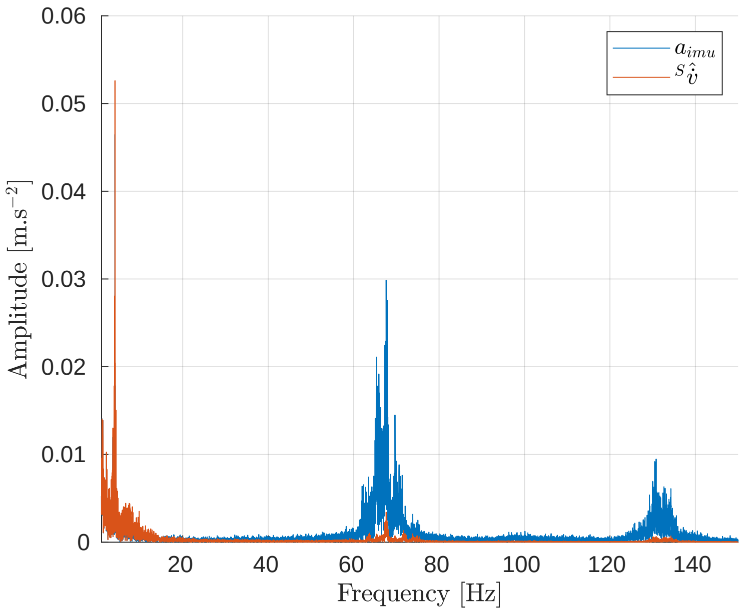

Figure 7.5 – Frequency domain of the measured IMU signal $\boldsymbol{a}_{imu}$ and the regression-based filter estimated specific acceleration ${}^S\hat{\boldsymbol{v}}$.

significantly the vibration noise, while data at frequencies outside of the filtering region is still intact. This suggests that the filter can in fact remove the vibration noise, while accurately estimating the body acceleration.

In Fig. 7.6 we show time domain comparison between the estimated specific acceleration using different techniques: 1) the proposed regression-based filter, defined by the symbol ${}^S\hat{\boldsymbol{v}}$; 2) a second-order Butterworth filter with cutoff frequency 30 [Hz] (same setup used in [Tal–2018]), defined by the symbol ${}^S\hat{\boldsymbol{v}}_{\text{butt30}}$; 3) and finally, a second-order Butterworth filter with cutoff frequency 13 [Hz], defined by the symbol ${}^S\hat{\boldsymbol{v}}_{\text{butt13}}$. From Fig. 7.6 it is evident that the proposed regression-based filter is the one able to suppress the vibrations (see Fig. 7.6 on the right) while minimizing the delay when the signal changes rapidly (see Fig. 7.6 on the left). On the other hand, using a second-order Butterworth filter with cutoff frequency 30 [Hz], the delay with respect to the real signal is small (although still larger than using the proposed regression-based filter) but the vibrations are still there (see Fig. 7.6 on the right). In order to almost completely suppress the vibrations with a second-order Butterworth filter, one has to set a cutoff frequency of 13 [Hz]; However, by doing so the induced delay becomes much larger. This clearly shows the advantage of the proposed regression-based filter over the classically used Butterworth filter for IMU measurements filtering in the quadrotor case.

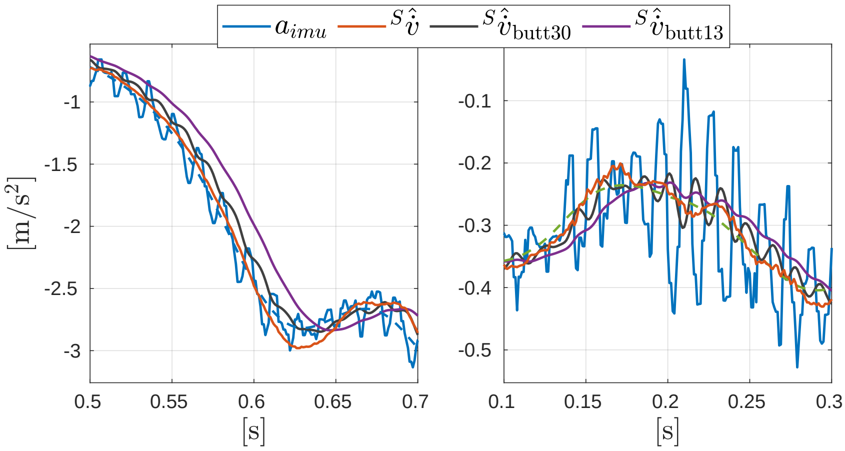

Figure 7.6 – Comparison of different types of filters on the raw accelerometer data $\boldsymbol{a}_{imu}$, where ${}^{S}\hat{\boldsymbol{v}}$ is the output of the proposed regression-based filter, ${}^{S}\hat{\boldsymbol{v}}_{\text{butt30}}$ is the output of a second-order Butterworth filter with cutoff frequency 30 [Hz], and ${}^{S}\hat{\boldsymbol{v}}_{\text{butt13}}$ is the output of a second-order Butterworth filter with cutoff frequency 13 [Hz].

7.4 FiberThex IMU filter

As discussed in Sec. 7.2, the vibration in the IMU measurements on-board the FiberTHex platform contains components in the range of the propeller commands and their harmonics, in addition to an extra vibration that is outside these ranges. As mentioned in Sec. 7.2, this vibration frequency is constant even in sub-windows of IMU acceleration measurements. As such, for the FiberTHex IMU filtering we use the same filter as the one used for the quadrotor, however, while filtering for 5 vibration frequencies (i.e., $q = 5$) instead of 4. The first two frequencies $\omega_{\boldsymbol{\delta}1}$ and $\omega_{\boldsymbol{\delta}2}$ correspond to the minimum spinning frequency among the propellers (in the considered time window) and its first harmonic, respectively. The second two frequencies $\omega_{\boldsymbol{\delta}3}$ and $\omega_{\boldsymbol{\delta}4}$ correspond to the maximum spinning frequency among the propellers (in the considered time window) and its first harmonic, respectively. Finally, the fifth frequency $\omega_{\boldsymbol{\delta}5}$ is a fixed frequency set at 37 [Hz].

Fig. 7.7 shows the frequency domain analysis of the proposed filter on-board the FiberTHex. This figure shows that the proposed filter reduces largely the vibration noise from the IMU signal, while estimating correctly the specific platform acceleration.

We should note that different calibration methods were tested to find such fixed frequencies for "any" MRAV platform; however, our analysis did not reach any satisfactory solutions, and thus none were shown. As such, this analysis is left as a future work.

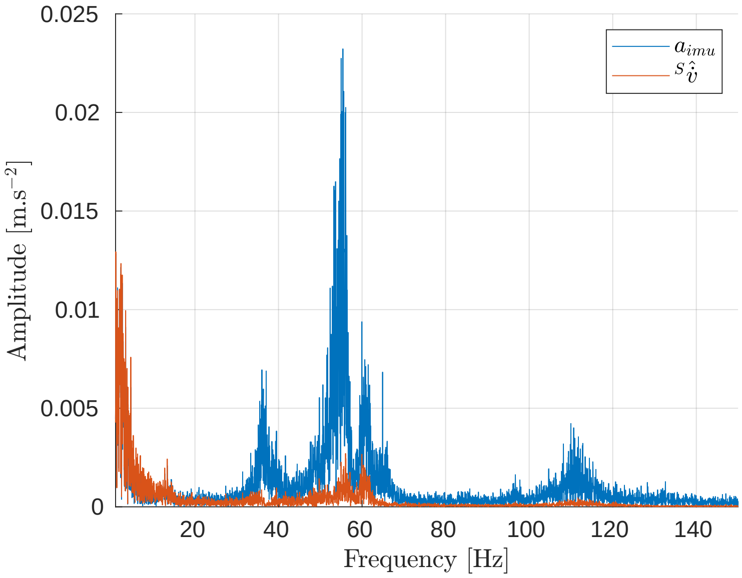

Figure 7.7 – Frequency domain of the measured IMU signal $\boldsymbol{a}_{imu}$ and the regression-based filter estimated specific acceleration ${}^S\hat{\boldsymbol{v}}$, on-board the FiberTHex.

7.5 Conclusion

In this chapter we have analyzed the noise profile in IMU measurements on-board quadrotor platforms, and on-board two tilted propeller hexarotors. Our frequency domain analysis shows that part of the noise in these measurements is due to vibrations caused by the rotating propellers. As such, these vibrations show up in the IMU measurements as signals with frequencies in the range of the propeller rotational commands. For the tilted propeller hexarotors, we observed an additional vibration noise at a fixed frequency, unrelated to the propeller rotational commands. We showed that this frequency is due to the platform's geometry, and is independent of the platform's material.

While we showed that for a quadrotor propeller induced vibrations are a sum of signals with frequencies only in the range of the propeller rotational commands and their harmonics, the cause of this effect is still ambiguous in this work. We believe this phenomenon to be caused by one of the platform's geometry characteristics as follows: 1. the quadrotor has four propellers placed in a 'plus' shape about the platform CoM; 2. and the quadrotor has all propellers generating thrust along $\boldsymbol{z}_B$. It is important, to better understand the vibration profile for different platforms, to analyze the cause of quadrotor's vibration profile. While we leave this study as future work, this analysis should show one of the following: 1. if the second cause mentioned above is the cause of the vibration profile, this profile will be the same for any coplanar/collinear platform. 2. While if the first cause is the root of the vibration profile, any quadrotor platform that has the 'plus' shape, even if the propellers are tilted, will have the same vibration profile.

Following the vibration analysis in this chapter, we proposed a regression-based IMU filter which uses the information about the commanded propeller speeds, and extracts *vibration-free* body acceleration. We showed that our regression based method removes the vibrations from the IMU acceleration signal while introducing a much smaller delay than classical low pass filters, and while adding virtually no phase shift to the signal.

The presented filter will be used later in Chapt. 8 as a crucial part of the direct acceleration feedback controller, where the controller cannot work without the presented filter. This filter was also used for the feedback control of the omniheptarotor prototype presented in Chapt. 5. We do note that we did not account for the platform propeller rotational commands in the case of the heptarotor, however, since the platform's required high velocity propeller commands, the acceleration signal could be easily fit as a second order polynomial in the measurement IMU signal without accounting for the propeller rotational speeds.

Chapter 8

Direct Acceleration Feedback Controller

8.1 Introduction

Following the Inertial Measurement Unit (IMU) filtering presented in Chapt. 7, in this chapter we leverage the filtered IMU measurements to achieve a robust quadrotor position controller, with a direct acceleration feedback control strategy.

For the purpose of designing the position controller, a quadrotor can be considered as a point mass whose acceleration is the sum of mass-normalized forces such as gravity, wind, and a control force produced by the propellers. The control force can be parameterized in two components 1) its *intensity* which is the total thrust provided by the sum of propeller forces, and 2) its *orientation* which normally corresponds to the vertical axis attached to the vehicle body frame. In its most common form, the motion control of the Center of Mass (CoM) of a quadrotor vehicle boils down to two control loops, the outer and inner loops (see, e.g., [Mahony–2012; Faessler–2018] and references therein). The outer loop (position control) computes a desired thrust and orientation (roll and pitch) from a blending of the acceleration reference and a feedback based on the CoM position and velocity measurements. The inner loop (attitude control) computes the desired torques to reorient the platform to the desired orientation. Finally, both the desired force and torques are provided to a low level module that computes rotational speed of each propeller necessary to reach the calculated thrust and orientation.

While each control part is affected by wrongly estimated parameters and external disturbances, this paper focuses on the improvement of the position control, which we shall show to be enough to mitigate disturbances such as uncertain mass and external forces, in addition to uncertain aerodynamic parameters in the low level motor control loop.

To put our controller into perspective, we further divide the position controller into a position feedback loop that computes the desired accelerations based on the measured and desired states, and into a thrust controller that calculates the desired thrust based on the desired accelerations; this second part is commonly implemented in open-loop by applying an inverse of the platform model. To cope with the non-perfect control of the CoM acceleration due to the open-loop nature of the thrust controller, the most common strategy is to make the position feedback loop more robust to input disturbances and parameter uncertainties. Classical solutions resort to different robust controllers (integral position feedback, adaptive control [Antonelli–2018], sliding mode [Besnard–2012], Model Predictive Control (MPC) [Alexis–2011], etc.), or try to compensate for the inaccurate acceleration control using a disturbance observer [Yüksel–2019; Ryll–2019; Tomić–2017].

Another approach that is gaining popularity in the literature is the *Incremental Nonlinear Dynamic Inversion* (INDI) [Tal–2018; Smeur–2015; Smeur–2018a], which exploits the accelerometer measurement to robustify the quadrotor control. The controller is based on an incremental law computed from the Taylor expansion of the dynamics. The robustness of INDI against external disturbances has been proven by real experiments. However, in spite of its robustness, INDI requires the knowledge of the *input effectiveness* (i.e., knowledge of the mass and aerodynamic parameters), and propeller rotational measurements. In addition, INDI low-pass-filters the accelerometer measurements; this introduces a frequency-dependent delay and removes high-frequency components that might be relevant, e.g., in the presence of impacts or rapid changes of acceleration due, e.g., to fast changes in the mass and propeller effectiveness.

In this chapter, we propose an alternative solution to the problem; our main idea is rather simple but at the best of our knowledge, it has never been explored in this form in the related literature. Rather than partially relying on the open-loop model inversion, we want to transform the thrust control into a proper feedback control which is based on the direct acceleration measurement. To do so, we exploit the specific acceleration measurement provided by the accelerometer enriching the position controller with an acceleration feedback compensator. The goal is to steer to zero the error between the desired acceleration commanded by the position feedback loop and the measured acceleration coming from the accelerometer. This idea is clearly inspired by torque-feedback-based joint controller for standard manipulators [Vischer–1995], where the electric motor input is commanded in order to steer the measured torque to the desired one. Furthermore, we prove theoretically and experimentally that our controller does not require the knowledge of the mass, propeller rotational speed measurements, and is robust to large variances in the aerodynamic parameters. Finally, to get the most out of the accelerometer measurements, we leverage the IMU filter introduced in Chapt. 7 as a zero delay notch filter, that can run in real-time on-board the platform. We do note that the presented controller was not possible without the use of the presented IMU filter, where the use of low-pass-filtered measurements induces delays into the system; as the controller employs the IMU data for feedback compensation, with the low pass-filter the controller tries to compensate for accelerations that have already passed instead of more recent measurements. On the other hand, if the IMU measurements were not filtered, the vibrations in the measurements are propagated by the controller, which in turn lets the platform oscillate and the controller to fail.

The interested reader is referred to [video01–2020a] for a summarizing presentation of the content of this chapter, in addition to demonstrations of the corresponding experiments.

8.2 Controller Design

To define our controller, let us first consider the quadrotor model, where the motion can be controlled acting on four inputs: $f_B \in \mathbb{R}$ and $\boldsymbol{m}_B = [m_{B,x} \ m_{B,y} \ m_{B,z}]^T \in$

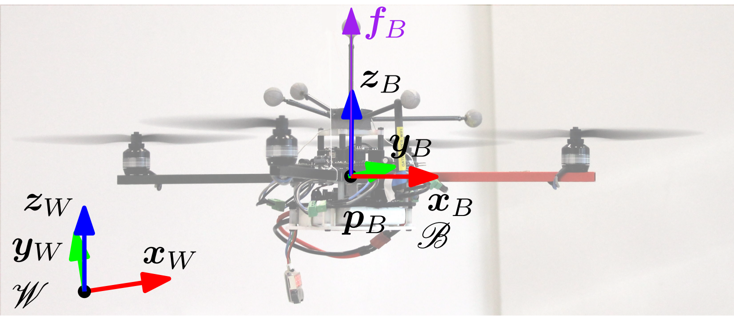

Figure 8.1 – System model and main variables.

$\mathbb{R}^3$, where f_B is the magnitude of the thrust force $f_B = \boldsymbol{f}_B \boldsymbol{z}_B$ applied at O_B and parallel to $\boldsymbol{z}_B$, and $\boldsymbol{m}_B$ is the 3D control moment expressed in $\mathcal{B}$. An example of the system and its main variables is shown in Fig. 8.1.

Applying the standard Newton-Euler equations one obtains the following vehicle equations of motion:

$$\ddot{\boldsymbol{p}}_B = \frac{\boldsymbol{f}_B}{m} - \boldsymbol{g} + \frac{\boldsymbol{f}_e}{m} \tag{8.1}$$

$$\dot{\boldsymbol{R}}_B = \boldsymbol{S}(\boldsymbol{\omega}_B)\boldsymbol{R}_B \tag{8.2}$$

$$\boldsymbol{J}_B\dot{\boldsymbol{\omega}}_B = -\boldsymbol{S}(\boldsymbol{\omega}_B)\boldsymbol{J}_B\boldsymbol{\omega}_B + \boldsymbol{m}_B, \tag{8.3}$$

where $\boldsymbol{f}_e \in \mathbb{R}^3$ is any external force (wind gust, model inaccuracy, aerodynamic effects, etc.) expressed in $\mathcal{W}$ and $\boldsymbol{f}_B \in \mathbb{R}^3$ is the total force applied by the propellers on $\mathcal{B}$ at O_B expressed in $\mathcal{W}$. $\boldsymbol{S}(\star)$ is the skew operator defined as $\boldsymbol{S}(\star) : \mathbb{R}^3 \to \mathbb{R}^{3\times 3}$ such that $\boldsymbol{S}(\boldsymbol{x})\boldsymbol{y} = \boldsymbol{x} \times \boldsymbol{y}$ for every $\boldsymbol{x} \in \mathbb{R}^3$ and $\boldsymbol{y} \in \mathbb{R}^3$.

The motion control problem addressed here is to design a feedback law for the control inputs f_B and $\boldsymbol{m}_B$ that steers the position of the vehicle CoM along a sufficiently smooth desired trajectory $\boldsymbol{p}_B^d(t) : \mathbb{R} \to \mathbb{R}^3$. It is well known that for a quadrotor, one can also independently control the rotation along the thrust direction, commonly called *yaw angle*. Since the accelerometer cannot improve the control of this quantity, the latter is done using standard techniques [Mahony–2012].

As already discussed, the typical control structure for a quadrotor aerial vehicle is composed of two high level controllers (the position controller and attitude controller) and one low level controller that controls the propeller velocities. In the following, we shall show this standard control law and how we intend to modify the position control part in order to enhance the robustness against unknown parameters and external disturbances, using the direct accelerometer feedback. In what follows we will briefly discuss the attitude controller that calculates desired torques, and we refer curious readers to [Mahony–2012; Faessler–2018] for further details on the attitude controller. Then we will also briefly discuss the motor controller that calculates desired propeller rotational speeds that would achieve the desired thrust and moments.

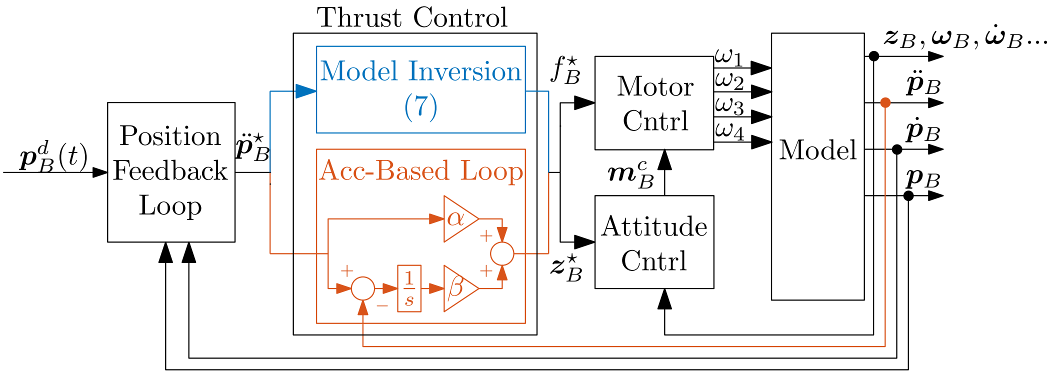

Figure 8.2 – Block diagram of the quadrotor controller with the two variants of the thrust controller.

Attitude Controller The attitude controller calculates the desired torques $\boldsymbol{m}_B$ to track the desired orientation; in addition, since the quadrotor is a **UDT** platform, the attitude controller is also used to allow the platform to apply the desired lateral forces. To present our attitude controller, given a desired force $\boldsymbol{f}_B$ and yaw angle error e_ψ, let us first denote locally by $\boldsymbol{x}_d$, $\boldsymbol{y}_d$ and $\boldsymbol{z}_d$ as the corresponding first to third columns of $\boldsymbol{R}_d$; in addition, let us define $\boldsymbol{y}_{\psi,d} = [-sin(\psi_d)\ cos(\psi_d)\ 0]$ as the second column of a rotation matrix that represents the desired yaw; then our attitude control strategy is as follows:

$$\boldsymbol{z}_d = \frac{\boldsymbol{f}_B}{f_B} \tag{8.4}$$

$$\boldsymbol{x}_d = \frac{\boldsymbol{y}_{\psi,d} \times \boldsymbol{z}_d}{\|\boldsymbol{y}_{\psi,d} \times \boldsymbol{z}_d\|} \tag{8.5}$$

$$\boldsymbol{y}_d = \boldsymbol{z}_d \times \boldsymbol{x}_d \tag{8.6}$$

Then the corresponding orientation error can be calculated as follows:

$$\boldsymbol{e}_{\boldsymbol{R}} = \frac{1}{2}(\boldsymbol{R}_B^\top \boldsymbol{R}_d - \boldsymbol{R}_d^\top \boldsymbol{R}_B)^\vee, \tag{8.7}$$

where $[\star]^\vee$ is the inverse skew symmetric operator; the corresponding angular velocity error is as follows:

$$\boldsymbol{e}_\omega = \boldsymbol{R}_B^{\top W}\boldsymbol{\omega}_B^d - \boldsymbol{\omega}_B, \tag{8.8}$$

and the resulting desired moment can be computed as follows:

$$\boldsymbol{m}_B = \boldsymbol{K}_{\boldsymbol{R}}\boldsymbol{e}_{\boldsymbol{R}} + \boldsymbol{K}_\omega \boldsymbol{e}_\omega + \boldsymbol{\omega}_B \times \boldsymbol{J}_B \boldsymbol{\omega}_B, \tag{8.9}$$

where ${}^W\boldsymbol{\omega}_B^d$ is the desired angular velocity of $\mathcal{B}$ w.r.t. $\mathcal{W}$ which can be 1) calculated from a derivative of the desired trajectory, 2) set to zero to use $\boldsymbol{e}_\omega$ as a damping factor, 3) or calculated using a controller such as the one introduced in [Faessler–2017].

Motor Controller The motor controller specifies the propeller rotational velocity required to achieve the desired thrust and moments. We assume these rotational velocities to be applied instantaneously through a further low level controller in the Electronic Speed Controller (ESC)s described in [Franchi–2017].

To find the propeller speeds we can write the control allocation matrix for a quadrotor in the following form:

$$\begin{bmatrix} f_B \\ m_{B,x} \\ m_{B,y} \\ m_{B,z} \end{bmatrix} = c_f \begin{bmatrix} -1 & -1 & -1 & -1 \\ 0 & l & 0 & l \\ l & 0 & l & 0 \\ c & c & c & c \end{bmatrix} \begin{bmatrix} \omega_1^2 \\ \omega_2^2 \\ \omega_3^2 \\ \omega_4^2 \end{bmatrix} \tag{8.10}$$

where c_f, c and l are correspondingly the propellers' lift coefficient, drag to lift ratio and distance between platform's CoM and propellers and ω_i is the rotational velocity of the $i-$th propeller.

From the above, it is straight forward to see that the relation between the sum of the squared of ω_i's and f_B is linear in c_f.

8.2.1 Position feedback loop

The position feedback loop is designed considering the dynamics of the vehicle CoM virtually as a double integrator. Let us note $\ddot{\boldsymbol{p}}_B^\star \in \mathbb{R}^3$ as a controllable virtual input, then in an ideal situation:

$$\boldsymbol{p}_B = \int \dot{\boldsymbol{p}}_B = \int \int \ddot{\boldsymbol{p}}_B^\star, \tag{8.11}$$

Since the position feedback loop is a linear system any stabilizing controller that steers $\boldsymbol{p}_B(t)$ to $\boldsymbol{p}_B^d(t)$ can be used. The simplest implementation is a PD controller:

$$\ddot{\boldsymbol{p}}_B^\star = \ddot{\boldsymbol{p}}_B^d + k_p \boldsymbol{e}_p + k_v \dot{\boldsymbol{e}}_p, \tag{8.12}$$

where $\boldsymbol{e}_p = \boldsymbol{p}_B^d - \boldsymbol{p}_B$, and $k_p, k_v \in \mathbb{R}_{>0}$ are positive scalars. We remark that any other more sophisticated controller can be used such as PID, robust controller, sliding mode, etc. However, if we can steer $\ddot{\boldsymbol{p}}_B$ to $\ddot{\boldsymbol{p}}_B^\star$, even the simple PD control law Eq. (8.12) will asymptotically steer $\boldsymbol{p}_B(t)$ to $\boldsymbol{p}_B^d(t)$.

Then the role of the thrust controller and the attitude controller is to compute the real control inputs f_B and $\boldsymbol{m}_B$ such that Eq. (8.11) is verified.

8.2.2 Classical thrust controller

The classical way to make $\ddot{\boldsymbol{p}}_B = \ddot{\boldsymbol{p}}_B^\star$ is to apply a partially open-loop controller based on the inversion of the dynamics. In particular, the thrust vector, $\boldsymbol{f}_B^\star$, is computed inverting Eq. (8.1):

$$\boldsymbol{f}_B^\star = m\left(\ddot{\boldsymbol{p}}_B^\star + \boldsymbol{g}\right) - \boldsymbol{f}_e. \tag{8.13}$$

As we showed above, the total thrust vector is controlled by the thrust intensity and the full-body orientation. Along the current thrust direction, $\boldsymbol{z}_B^\top \boldsymbol{f}_B^\star$ can be instantaneously applied setting the thrust intensity control input similar to [Lee–2010]:

$$f_B = \boldsymbol{z}_B^\top \boldsymbol{f}_B^\star. \tag{8.14}$$

A schematic representation of the controller along the thrust direction is shown in Fig. 8.2. In order to properly apply the other two components (lateral forces), it should be that $\boldsymbol{z}_B = \boldsymbol{z}_B^\star$ where $\boldsymbol{z}_B^\star$ is computed as

$$\boldsymbol{z}_B^\star = \boldsymbol{f}_B^\star / \|\boldsymbol{f}_B^\star\|, \tag{8.15}$$

where $\|\star\|$ is intended as the *Euclidean norm.* To attain Eq. (8.15), the desired thrust direction, together with the desired rotation along the latter (desired yaw angle), are used as a reference by the attitude controller that steers $\boldsymbol{z}_B$ to $\boldsymbol{z}_B^\star$ and the yaw angle to the desired one.

In the practical implementation of Eq. (8.14) and Eq. (8.13), one typically uses the nominal values of the system parameters such as the mass $\hat{m}$, the gravity $\hat{\boldsymbol{g}}$, and an estimation of the external disturbance, $\hat{\boldsymbol{f}}_e$; concurrently, it is estimated that the lift coefficient applied in the allocation strategy is constant at its nominal value $\hat{c}_f$. By replacing the nominal values into Eq. (8.13), and placing equation Eq. (8.13) and Eq. (8.14) into Eq. (8.1), we can write the closed-loop dynamics along the thrust direction (the most important one for the quadrotor motion control) as follows:

$$\boldsymbol{z}_B^\top \ddot{\boldsymbol{p}}_B = \boldsymbol{z}_B^\top \left(\frac{1}{m} \left(\boldsymbol{f}_e - \hat{\boldsymbol{f}}_e \frac{\hat{c}_f}{c_f} \right) - \boldsymbol{g} + \frac{\hat{m}\hat{c}_f}{m c_f} \hat{\boldsymbol{g}} + \frac{\hat{m}\hat{c}_f}{m c_f} \ddot{\boldsymbol{p}}_B^\star \right) \tag{8.16}$$

It is clear that, if the nominal and estimated quantities are equal to the real values, i.e., $\hat{m} = m$, $\hat{\boldsymbol{g}} = \boldsymbol{g}$, $\hat{\boldsymbol{f}}_e = \boldsymbol{f}_e$ and $\hat{c}_f = c_f$, then $\boldsymbol{z}_B^\top \ddot{\boldsymbol{p}}_B = \boldsymbol{z}_B^\top \ddot{\boldsymbol{p}}_B^\star$, and the control objective is achieved at least along the thrust direction. Nevertheless, as soon as there are model uncertainties and estimation errors, which is the normal situation in practice, such a goal is not met. In the next subsection, we shall show how the use of the accelerometer allows to attain the control objective even in those non-ideal conditions.

8.2.3 Accelerometer-based thrust controller

The majority of quadrotor platforms are equipped with an IMU including an accelerometer and a gyroscope. The two are normally used for the estimation of the vehicle position and attitude [Mahony–2012; Martin–2010]. Here we shall show how the acceleration measurement can also be used to make the (partially open) position loop controller a (fully) closed-loop one. This allows achieving the control objective Eq. (8.11) even with model uncertainties and unknown external disturbances.

The accelerometer measurements, defined by the vector $\boldsymbol{a}_{imu} \in \mathbb{R}^3$, provide the specific acceleration, i.e.,

$$\boldsymbol{a}_{imu} = \boldsymbol{R}_B^\top \left(\ddot{\boldsymbol{p}}_B - \boldsymbol{g}\right), \tag{8.17}$$

from which one can get a direct measure of the acceleration

$$\ddot{\boldsymbol{p}}_B = \boldsymbol{g} + \boldsymbol{R}_B \boldsymbol{a}_{imu}. \tag{8.18}$$

In what follows, instead of using the direct acceleration measurement $\boldsymbol{a}_{imu}$, the formulation will assume that we are using the filtered version $\dot{\boldsymbol{v}}^S$ in Eq. (8.18) instead.

As done in the previous section let us focus on the dynamics along the thrust direction. To simplify the notation we define $y = \boldsymbol{z}_B^\top \ddot{\boldsymbol{p}}_B$, $u = \boldsymbol{z}_B^\top \boldsymbol{f}_B = f_B$, $a = (c_f/(m\,\hat{c}_f))$ and $b = \boldsymbol{z}_B^\top \left(\boldsymbol{f}_e/m - \boldsymbol{g}\right)$. We can then rewrite Eq. (8.1) along the thrust direction as

$$y = au + b. \tag{8.19}$$

We consider a and b as unknown variables. More in general, the quantity a, also called *input effectiveness*, includes different sources of uncertainties: 1) the platform mass, and 2) the thrust intensity which might be not precisely known. The latter might even change over time due to aerodynamic effects, e.g., ground and ceiling effects [Powers–2013]. The quantity b represents any external disturbance applied to the robot (e.g., wind gusts, the additional weight of a load, unmodeled drag, etc.), including the gravity. The control objective is to steer y to $y^\star = \boldsymbol{z}_B^\top \ddot{\boldsymbol{p}}_B^\star$ with a and b unknown. To attain this purpose we propose the following controller based on the acceleration input

$$u = \alpha y^\star + \beta \int e_y dt, \tag{8.20}$$

where $e_y = y^\star - y$ is the acceleration error, $\beta \in \mathbb{R}$, and $\alpha \in \mathbb{R}$ is an estimation of $1/a$. We shall show that the term $\alpha y^\star$ improve the control performance if α is a decent approximation of $1/a$. However, if a good estimation of a is not available, α can be set arbitrarily and the controller is still applicable. A schematic representation of the controller along the thrust direction is shown in Fig. 8.2.

We can verify that e_y has a stable behavior analyzing its dynamics:

$$\dot{e}_y \;\;=\;\; \dot{y}^\star - (a\dot{u} + \dot{a}u + \dot{b}) = -a\beta e_y + \tilde{a}\dot{y}^\star - \dot{a}u - \dot{b}, \tag{8.21}$$

where $\tilde{a} = 1 - a\alpha$. The equilibrium point is clearly $\bar{e}_y = \left(\tilde{a}\dot{y}^\star - \dot{a}u - \dot{b}\right) / (a\beta)$ and is asymptotically stable if $a\beta > 0$, while assuming $\dot{a}$ to be zero. Even if a is unknown, its sign is normally known and the sign of β can be chosen accordingly. Without loss of generality, we can assume that $a > 0$. The equilibrium point $\bar{e}_y$ is then asymptotically stable for any $\beta > 0$, a and b.

Remark. Notice that if $\dot{y}^\star = \dot{a} = \dot{b} = 0$, as in many of the practical cases, the error will asymptotically converge to zero. One can also observe that knowing precisely the input effectiveness, (*i.e.,* $\alpha = 1/a$, $\tilde{a} = 0$) the part of the error due to

$\dot{y}^\star$ vanishes. It is not surprising that knowing the feed-forward term will improve the performance. Nevertheless we remark that for the Direct Acceleration (DA) controller a precise knowledge of a is not actually needed. In fact, increasing β, one can make the steady-state error $\bar{e}_y$ very small, independently of the unknown parameter and disturbance. Unfortunately, β cannot be arbitrarily large otherwise $\dot{u}$ will be too large and the system will not be able to provide the corresponding u.

8.2.4 Discussion on the Comparison with PID

Let us assume that a standard PD position feedback loop controller is applied. We can then replace Eq. (8.12) into Eq. (8.20), where we recall that $y^\star = \boldsymbol{z}_B^\top \ddot{\boldsymbol{p}}_B^\star$:

$$u = \alpha \left(\ddot{p}^d_{Bt} + k_p e_{Bt} + k_v \dot{e}_{Bt} \right) \tag{8.22}$$

$$+ \beta \left(\dot{e}'_{Bt} + k_v e'_{Bt} + k_p \int e_{Bt} dt \right). \tag{8.23}$$

where $\ddot{p}^d_{Bt} = \boldsymbol{z}_B^\top \ddot{\boldsymbol{p}}^d_B$, $e_{Bt} = \boldsymbol{z}_B^\top \boldsymbol{e}_p$ and similarly for its derivatives. Furthermore, $e'_{Bt} = \int (\dot{p}^d_{Bt} - \dot{p}_{Bt}) dt$ and $\dot{e}'_{Bt} = \int (\ddot{p}^d_{Bt} - \ddot{p}_{Bt}) dt$ with $\dot{p}_{Bt} = \boldsymbol{z}_B^\top \dot{\boldsymbol{p}}_B$ and similarly for its derivatives. While it is clear that Eq. (8.23) resembles a PID, it turns out from the experimental comparisons (see Fig. 8.8) that the step response against an external disturbance can be made faster for the proposed acceleration-based thrust controller plus a PD position feedback loop controller when compared to the PID controller. The experiment has been conducted with the two controller gains tuned at best[1].

To investigate this discrepancy, we notice that the PID in Eq. (8.23) relies on the high frequency accelerometer measurements 1 [KHz], in addition to the low frequency position and velocity measurements required in a normal PID.

In the following, we analyze a simplified system that still encapsulates the main properties, in order to better explain why high-frequency acceleration feedback shows better stability than an equivalent controller based on slower sampled measurements. Let us consider the dynamic system

$$\dot{x}_1 = x_2, \quad \dot{x}_2 = u, \tag{8.24}$$

where $u = -k_1 x_1 - k_2 x_2$ is a simple PD controller with $k_1, k_2 \in \mathbb{R}_{>0}$. For this system we analyze two cases:

1) both x_1 and x_2 in u are sampled with period $T \in \mathbb{R}_{>0}$;
2) only x_1 in u is sampled with period T, while x_2 is sampled at a much higher frequency such that it can be considered continuous.

In our parallelism, case 1) corresponds to the standard PID based on low-sampled measurements, while case 2) corresponds to the proposed acceleration-based thrust controller.

---

[1] We consider the best gains as the maximum gains that preserve the stability of the system. Higher gains would make the system unstable.

For case 1), from the theory of digital control [Landau–2007], it is well known that the proportional gain k_1 cannot be increased arbitrarily (aiming at a better performance). On the contrary, its maximum value is bounded depending on the sampling time T. The higher T the lower k_1 has to be in order to guarantee stability.

For case 2) the measurement of x_2 can be considered continuous time with respect to the sampling of x_1. Then, the control input u can be written as

$$u = -k_1 \bar{x}_1 - k_2 x_2, \tag{8.25}$$

where $\bar{x}_1$ is the sampled measurement of x_1. In the continuous-time we can write $\bar{x}_1(t) = x_1(t) - \Delta x_1(t)$ where $\Delta x_1(t) \in \mathbb{R}$ is the error at time t due to the sampling of the signal. Notice that $\Delta x_1(t) = 0$ if $t = iT$ for a certain i. Let us now consider the following Lyapunov function:

$$V(x_1, x_2) = \frac{1}{2}\left(k_1 x_1^2 + x_2^2\right), \tag{8.26}$$

which is clearly positive semi-definite, and $V(x_1, x_2) = 0$ if $x_1 = x_2 = 0$. The time derivative of $V(x_1, x_2)$ is

$$\begin{aligned} \dot{V}(x_1, x_2) &= k_1 x_1 x_2 + x_2\left(-k_1 \bar{x}_1 - k_2 x_2\right) \\ &= x_2\left(k_1 \Delta x_1 - k_2 x_2\right). \end{aligned} \tag{8.27}$$

Considering the Taylor approximation of Δx_1 around the time iT for a certain i, we can bound Δx_1 with $x_2 T$. Therefore, it is easy to verify that

$$\dot{V}(x_1, x_2) \leq -x_2\left(k_2 - k_1 T\right) x_2 \tag{8.28}$$

which is negative semi-definite if k_2 is chosen such that $k_2 - k_1 T > 0$. Using the LaSalle principle [Khalil–2001], we can prove the stability of the system. This implies that, whatever is the sampling period of x_1, one can choose k_1 arbitrarily large, and then k_2 such that $k_2 > k_1 T$. For case 2), thanks to the high sampling frequency of x_2, one can obtain a fast convergence of the state to zero independently from the sampling rate of x_1.

8.3 Experimental Campaign

The validation experiments have been conducted with a quadrotor platform, with software running on-board in real-time. The experiments are conducted indoor with conditions emulating outdoor settings as detailed below. The quadrotor platform used for the experiments weights about 1 [Kg]. The vehicle is endowed with an IMU, which exports the raw accelerometer and gyroscope measurements at 1 [KHz], and four brushless motor controllers (Brushless DC (BLDC) ESC) regulating the propeller speed using an in-house developed closed-loop speed controller [Franchi–2017]. A motion capture system reads the position and orientation of the vehicle and an Unscented Kalman Filter (UKF) component performs the sensor fusion to retrieve the full state of the platform. To ensure consistency with the typical sensor

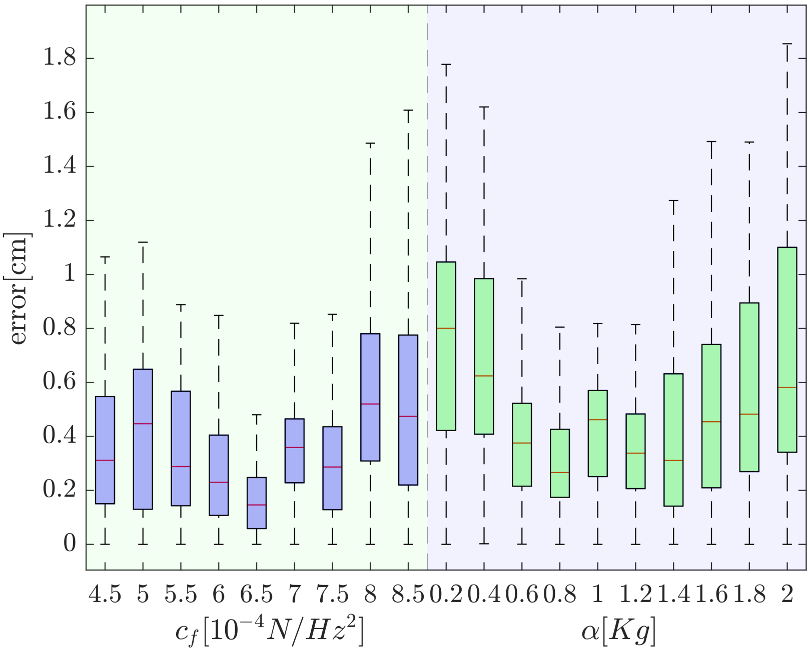

Figure 8.3 – showing error distribution of the platform while taking off and landing with a wrong c_f or α.

frequencies available in an outdoor setting endowed with, e.g., a standard vision-based localization system, we sample the position and velocity measurements from the UKF at 20 [Hz]. Most of the software components (including the controller) have been developed in C++ and run on an on-board PC (odroid XU4) at 1 [KHz]. As for most of the robotics software at LAAS-CNRS, software components have been developed using GenoM3 [Mallet–2010], a code generator and formal software component description language that allows assembling middleware-independent components in a modular system. Most of this software is available on the *openrobots* repository at `https://git.openrobots.org/projects/telekyb3`

8.3.1 Flight with unknown parameters

This section shows experiments where the platform takes off and lands with different values of the lift coefficient c_f and α provided to the attitude controller and the thrust controller respectively.

- In the first flight we vary $\alpha \in [0.2, 2][Kg]$, while its nominal value is $\frac{1}{a} = 1[Kg]$.
- In the second flight we vary the estimated lift coefficient $c_f \in [4.5e^{-4}, 8.5e^{-4}][N/Hz^2]$, while its identified nominal value is $\hat{c}_f = 6.5e^{-4}[N/Hz^2]$.

Fig. 8.3 shows the distribution of the platform's error while following the above maneuver with the chosen parameters. The figure shows that the platform is able to fly for the given α and c_f range. We note that the tested c_f range is one that might be encountered during regular flights (such as ground effect [Bernard–2018]), however, we acknowledge that our controller does not guarantee stability for larger variances in c_f due to the presence of the attitude controller. In addition, we

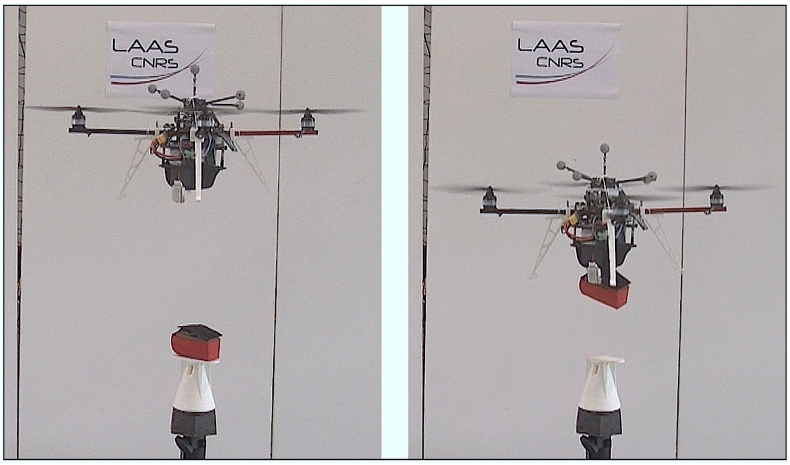

Figure 8.4 – The quadrotor picking up an unknown mass with a hook-and-loop. Left: the platform descending to pick up the object. Right: the platform ascending after it had fastened and picked up the object.

note from Fig. 8.3 that the performance improves if α is an exact estimate of $\frac{1}{a}$, however, the controller is still stable even when α is set arbitrarily as explained earlier in remark 8.2.3.

8.3.2 Use of DA in Two Practically Relevant Scenarios

In this section we assess the performance of the proposed DA controller while completing two real world tasks involving unknown and time-varying changes in the quadrotor dynamical model: *i)* hook-and-loop fasten and pick an unknown-mass object, and *ii)* take-off and maneuver in an air-turbulent environment

In the first experiment, shown in Fig. 8.4, the platform is commanded to pick up an object whose 0.4 [Kg] mass is unknown to the controller. Despite the unknown mass, the platform was able to follow the desired position while approaching and lifting the object.

Fig. 8.5 shows the actual-vs-desired quadrotor altitudes before and after hook-and-loop fastening and picking up the object with the unknown mass. The top surface of the object is taken as a reference point. The platform is commanded to go below the object surface as seen in the hook-and-loop fastening and pick up section of Fig. 8.5. This experiment shows that while the weight of the object is unknown to the controller, and there is a phase in which the motion is even hindered, the platform's performance is smooth, stable, and indistinguishable before and after the pick up, with less than 0.008 [m] error in both phases.

In the second experiment, shown in Fig. 8.6, the platform flies underneath a flying hexarotor weighting about 2.5 [Kg]; due to the configuration of its propellers, the hexarotor creates a turbulent environment for the quadrotor. Despite the turbulence, the quadrotor is able to lift off ground, hover in place, then approach the hexarotor and retract back to its original position.

Fig. 8.7 shows the performance of the DA controller in the presence of this

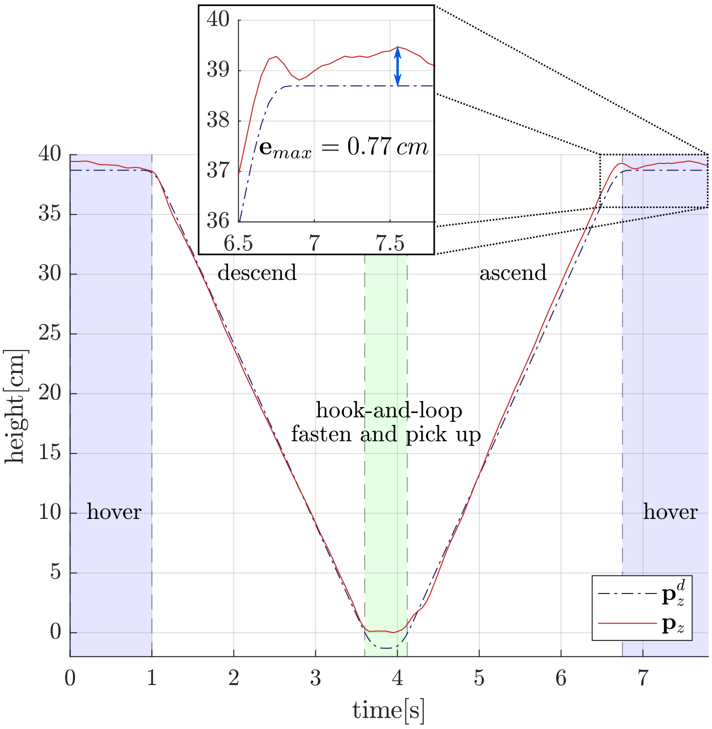

Figure 8.5 – position tracking of the quadrotor before and after hook-and-loop fasten and pick up of an object whose 0.2 [Kg] mass is unknown to the controller.

turbulence created by flying near ground and underneath the flying hexarotor. The platform first lifts off from ground and hovers in place, then it increases its altitude to approach the bottom of the hexarotor, and then it goes back to hover in the previous altitude. The DA controller in Fig. 8.7 shows complete resilience to the existing turbulence while following its desired trajectory, with less than 0.01 [m] maximum error. It has to be noted that during take off there is an initial error caused by the quadrotor's safety starting procedure which imposes the motor speeds to follow a 2.5 [s] saturation ramp from 0% to 100% which prevents the execution of the DA commanded forces. The DA controller lets the platform behave smoothly and stably despite such additional unmodeled obstruction to the actuation system.

Figure 8.6 – The quadrotor flying stabiliy beneath a 2.5 [Kg] hexarotor.

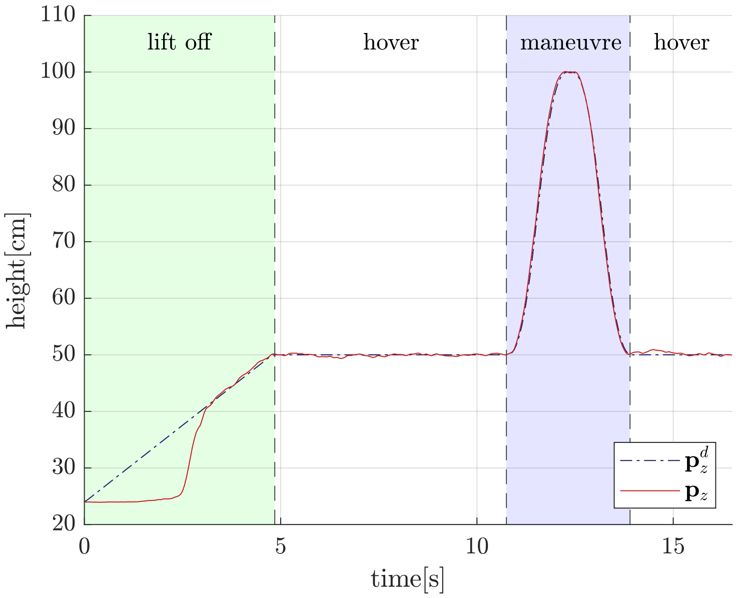

Figure 8.7 – position tracking of the quadrotor flying beneath a 2.5 [Kg] hexarotor. The plot shows a lift off phase, followed by a hover phase, a maneuvre phase, and finally another hover phase. During the first 2.5 [s], the platform follows a safety procedure imposing a ramp on the motor speeds, irrespective of the controller commands.

8.3.3 Comparing the Best DA and PID Performances

We assess the performance of DA against a PID controller with equivalent gains as described in Eq. (8.23). Gains k_p and k_v were tuned to ensure a desirable transient performance, and a near zero steady state error: $k_p = 27.5$ and $k_v = 18$. The acceleration gain β was varied to study its effect on the performance of each controller; as seen from Eq. (8.20), the increase in β increases the reactiveness of the controller to e_y, and correspondingly its reactiveness to external disturbances.

Fig. 8.8 shows a statistical representation of repeated experiments demonstrating a comparison between the DA controller and a PID following a step disturbance of 4 [N] – equivalent to $\simeq 0.407$ [Kg], i.e., 40% of the platform mass. This experiment highlights the performance of the controllers in scenarios such as sudden lifting of an unknown mass, or a very quick change in the aerodynamic properties of the platform's actuators, due, e.g., to a sudden wind gust. The same figure shows the difference between the controllers for different values of the acceleration gain β.

We observe that both controllers can achieve a zero steady state error before and after the step disturbance, however with varying transient performances. As we increase β, both controllers reach steady state in a shorter time, and achieve a smaller maximum error post the step response; these last two observations suggest that an increase in β induces a faster reaction to external disturbances.

We can also observe from Fig. 8.8 that the performance of both controllers is similar for the same β, with the PID lagging slightly from the DA controller. However, we can see that at $\beta = 4$ the PID controller lets the error oscillate and eventually diverge, while the DA controller can still achieve stable flight. At $\beta = 12$ the DA controller shows small oscillations – while still achieving a stable flight – with a maximum error of 2 [cm], while the PID's best error was around 4 [cm], with $\beta = 3$.

It was noted during the experiments that unlike the PID, the DA controller does not guarantee a zero steady state position error in the presence of non-negligible biases in the acceleration and velocity measurements. This is due to the post integration of e_y in the DA controller as opposed to the pre-integration of $\boldsymbol{e}_p$ in the PID controller, where the former can reach a steady state with non zero error. However, such biases have been easily practically reduced to zero using a standard calibration procedure. Therefore such aspect does not constitute a real problem in practice.

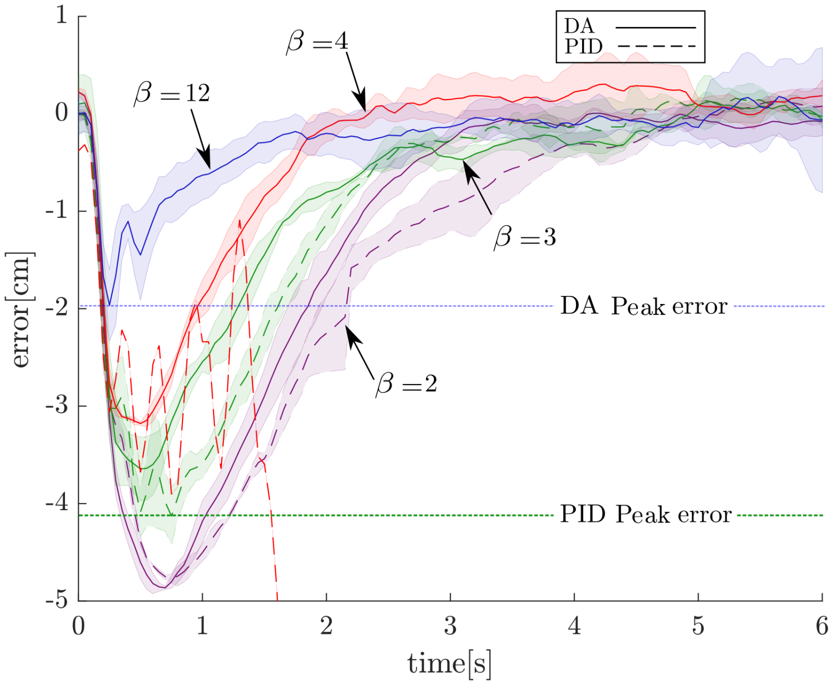

Figure 8.8 – Step response of DA vs PID following a 4 [N] ($\simeq 0.407$ [Kg]) step function while varying β, with lines of the same color corresponding to the same β, solid lines to DA, and dashed lines to PID. Each of the plots show the statistics of 3 identical flights, with the exception of the PID at $\beta = 4$ showing only one flight to avoid possible crashes.

8.3.4 Dynamic Maneuver

Finally, we assess the performance of DA while performing high speed maneuvers. While our system does not ameliorate the attitude controller, but rather is designed to be robust to external disturbances, we conduct these flights to show that the lateral motion is not deteriorated by our controller.

To this end, we fly our controller in a lemniscate pattern, with a radius of 2 [m] and at a maximum speed of 2.8 [m.s^{-1}] as shown in Fig. 8.9. The performance of the controller while following the lemniscate path is shown in Fig. 8.10. During these flights, our controller follows the desired state defined by the equation of the lemniscate with the corresponding derivatives. The controller exhibits a maximum error of 0.1 [m] along the trajectory, which is equivalent to the PID error for the same flight.

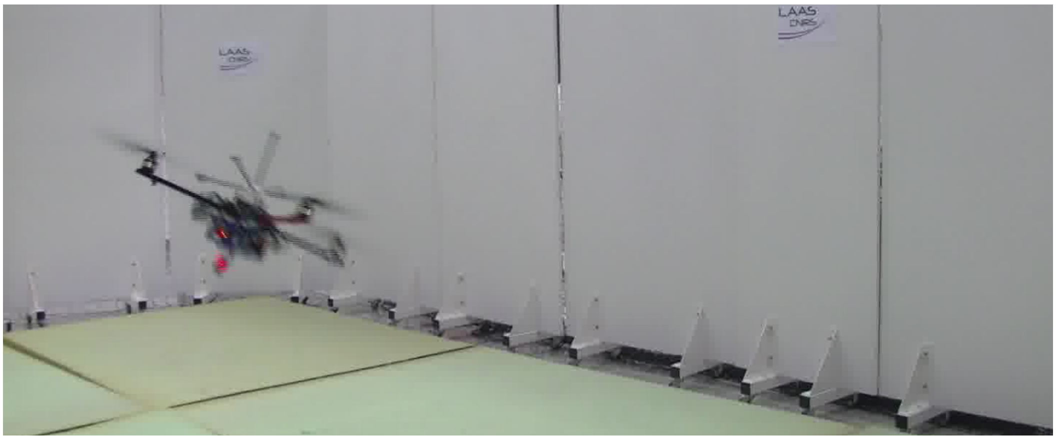

Figure 8.9 – showing the platform flying in a lemniscate maneuvre at a max velocity of 2.8 [m.s^{-1}].

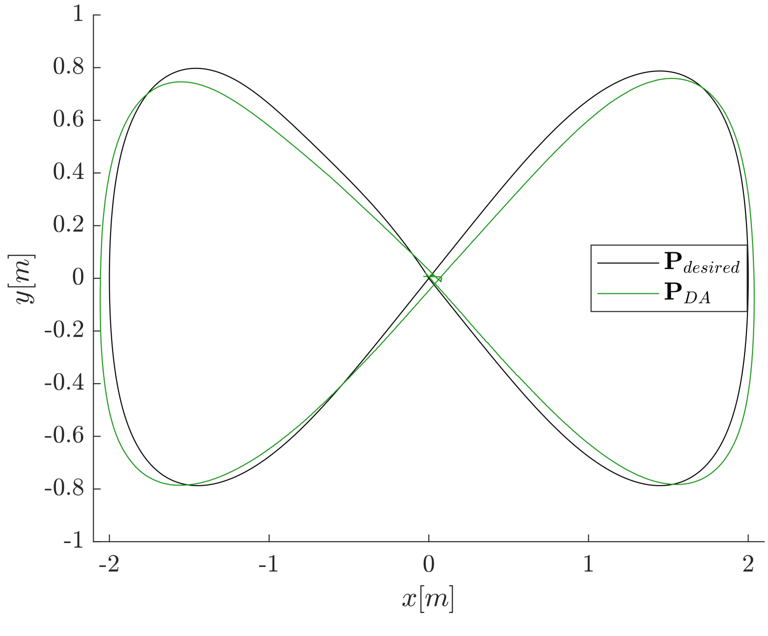

Figure 8.10 – position tracking of the quadrotor while following a high speed lemniscate maneuvre.

8.4 Conclusion

In this chapter we proposed a novel quadrotor controller concept based on direct acceleration (DA) feedback. The controller does not require any knowledge of the platform's mass or propeller efficiency, while can still benefit from such knowledge.

In simple terms, the controller aims to close the loop between the computed desired acceleration and the measured one. The derived controlled was proved to outperform a PID, where the difference between the used measurements between the two controllers allows the DA to be stable for higher gains.

On the other hand, the DA controller requires a specific IMU filter that was introduced earlier in Chapt. 7. As the filter reduces the high amplitude vibrations from the measurements while introducing no phase shift, it was used with this controller. The absence of this filter, or its replacement with a classical low-pass filter renders the presented controller unstable.

To validated the claimed robustness of the controller, we conducted an experimental campaign that demonstrates the performance of the new controller in various challenging scenarios, and compares its performance to a well tuned PID. During these experiments, the DA controller exhibits more accurate position tracking conditions, when compared to a PID, in reaction to sudden disturbances.

While we were able to present the robustness of the controller in theory and experimentally, we were not able to provide a formal proof of this stability. Moreover, the presented controller was derived only for the thrust controller of a quadrotor, while using 'off the shelf' attitude and motor controllers. As such, in the future the following improvements are required for the presented controller:

1) Derivation of formal proof of the presented controller, which would help us better understand its limitations.

2) Derivation of a similar controller that robustifies the attitude controller by closing the loop on the gyroscope measurements, similar to the robustification made with the thrust controller.

3) Employment of the controller on **FA** platforms, where we believe the same controller might be applicable even for the lateral force control thanks to the decoupling between the attitude and position dynamics.

4) Finally, the controller should be tested with a $\ddot{\boldsymbol{p}}_B^\star$ computed using some of the robust controllers discussed before.

Part IV

Conclusions

Chapter 9

Conclusions

This final chapter serves as a conclusion for the manuscript. The chapter serves three objectives, where first it provides a comprehensive summary of the presented material throughout the manuscript. Then it presents some of the lessons learned throughout the work on this manuscript and from the material therein. Finally, it provides prospective future work that entail from the current one.

9.1 Summary of the Thesis

The overall goal of this thesis has been to understand the effect of Multi-Rotor Aerial Vehicle (MRAV) design and actuation capabilities on the platform's ensuing abilities. These abilities being robustness to propeller failure, hovering ability and finally trajectory tracking. The aim of this study was to cover the topic from an extensive point of view (i.e., understanding this relation in the most general way), however, it was not aimed to be exhaustive (i.e., covering every possible aspect of the topic). As such, this manuscript

- first covered the theoretical modeling to bring the relation between actuation capabilities and abilities into perspective;
- then it demonstrated this relation on a large group of MRAV designs from the literature, where the chosen designs represent most of the ones that could be found in the literature.
- The manuscript then tackles a few example contributions in each field, first introducing a systematic method to understand a platform's robustness to propeller failure;
- then introducing a novel prototype **OD** platform with only 7 uni-directional thrusters;
- and finally, analyzing the effect of lateral force capability on a platform's trajectory tracking ability.
- Following the above three abilities, the manuscript also analyzes Inertial Measurement Unit (IMU) vibrations on-board different MRAVs, and shows the effect of different designs on the resulting vibration;
- and finally, introduces a filter for the above vibration and
- a controller that leverages the filtered measurements for the robust control of quadrotors.

The first part of this manuscript attempts to introduce an "all-encompassing" MRAV modeling. Since different designs from the literature use different nomenclature, we attempted in our modeling part to present a taxonomy that could easily and accurately represent any of such designs. The taxonomy relies largely on modeling platforms around their *full allocation matrix*, which maps the effect of the change in control inputs on the change in the applied forces and moments. We showed that following the presented modeling, the *full allocation matrix* for any platform (fixed or actuated propellers) can be derived, and then attempted to study the effect of the *full allocation matrix* on different properties and abilities. After the modeling part, we first grouped multirotors into actuation classes, where each of these classes can be formally defined by the platform's *full allocation matrix*. These classes reflect the platforms' feasible wrench space, where each reflect the degree of decoupling between the platform's applied forces and moments. Then we defined different platform abilities and showed the relation between these abilities and the *full allocation matrix*. 1) The first ability that we discussed is the ability of the platform to hover in different orientations. It is obvious to see that the hovering ability is directly related to the platform's class, where as the platform can decouple its forces and moments, it would be able to hover in different orientations. Within this ability we also discussed the platform's ability to sustain its hovering after the failure of one of its propellers, where we summarized the necessary conditions for robustness to propeller failure from the literature, and later studied these conditions and their computation more thoroughly. 2) The second ability that we discussed is the platform's ability to track different trajectories, i.e., trajectories with different Degrees of Freedom (DoF). 3) The third ability that we discussed is the platform's ability to interact with the environment. This ability is different from the other two, since it relies on the platform's wrench space, in addition to any attachments the platform could be endowed with. Indeed, even if the platform's design allows it to interact with the environment, if the adequate tools are not attached to the platform, it will not be able to interact. Finally, we presented a detailed method to compute and plot force and moment sets for different MRAV designs. The force (or moment) plots serve as yet another method to understand the feasible wrench set of a platform given its design.

Following the presented taxonomy, this manuscript demonstrates how this taxonomy could describe different platform designs. As such, it proposed a complete review of such designs from the literature, and showed how each of these designs could be described using the proposed taxonomy. The review then classified each platform in one of the proposed actuation classes, and discussed the possible abilities of each. Finally, the review showed force set plots for a representative number of the reviewed designs to demonstrate the feasible force set for a different number of platform's actuators. The review itself serves as a reference that we[1] hope to help researchers achieve new state-of-the-art MRAV designs. As such, the review was structured in way to highlight the different actuation capabilities possible for different design parameters. Moreover, it highlighted design limitations that we believe could be hindering the advancement of MRAV design, or for which, further advancement could help advance MRAV design.

Following the review, we tackled three different cases where each showcases one of the above mentioned abilities with respect to the platform design or the ensuing

---

[1] The use of first plural person throughout this thesis is motivated by the fact that most of the presented results have been achieved together with colleagues and collaborators from different affiliations. However, in the context referred to in this paragraph, the proposed considerations are probably more personal, although they might be shared with some of my colleagues.

platform capabilities. The first case that we tackled is the effect of platform design on its robustness to propeller failure. More specifically, we studied the effect of coplanar/collinear hexarotors' propeller failure on its hovering ability. Our study first summarized the conditions that ensure robustness to propeller failure, then introduced a geometrical tool that can calculate numerically the ability of a platform to hover (while healthy or after the propeller failure). The geometrical tool computes if the origin of the platform's moment set is an interior point of the set, where we showed this to be a sufficient condition for hovering. We applied this tool to validate the robustness of Y-shaped hexarotor platforms and the vulnerability of Star-shaped hexarotor platforms. Moreover, we studied the conditions that could allow a Star-shaped hexarotor to hover following the loss of some of its propellers, despite its vulnerability to propeller failure. Our theoretical hypotheses were finally validated with an extensive experimental campaign on two platforms (a Y-shaped and a Star-shaped hexarotor) with identical components and properties.

The second case that we tackled is the effect of platform design on its hovering ability, and the corresponding actuation class. In this part of the manuscript we studied the feasibility of an omnidirectional platform with minimal fixed uni-directional thrusters. While the theory on such feasibility was previously studied in the literature, it was never validated on a working prototype. As such, the corresponding chapter of the manuscript studied if it is possible, with the technology currently used in our lab, to build such a minimalistic omnidirectional platform. Our first attempt to the problem consisted of building a prototype platform, which aims to confirm the possibility of such design. We demonstrated that the prototype is capable of hovering in multiple different orientations, and thus we could confirm the omnidirectionality of the prototype. While this confirmed that it is possible to build an omnidirectional platform with only 7 fixed uni-directional thrusters, the prototype had multiple drawbacks, such as propellers' flow interaction, and the use of open-loop motor controllers due to the required high rotational speed. As such, we conducted another study where we showed the relation, between the possible platform weight and the maximum possible thrust per thruster. This study also relied on the analysis of the feasible force set of the proposed design. From this relation, we could confirm our practical findings, where the relation proves the omnidirectionality of the built prototype. However, aiming at an improved prototype, we found that it is not possible to build such an omnidirectional platform while using the motor controllers that we already use in our lab (which ensure closed-loop control of the motors), where we found that in order to achieve such an omnidirectional design, propellers have to rotate at a rotational velocity higher than the one where we could actively close the loop on the control of the motor rotational speed.

The third case that we tackled is the effect of platform actuation property on its trajectory tracking ability. Our study relied on a platform with Bounded Lateral Forces (BLF), with a corresponding controller that allows varying the maximum possible lateral force via a single key parameter, denoted $\overline{f_{xy}}$. As the presented controller allows changing numerically $\overline{f_{xy}}$, it allows the platform to shift between different actuation properties (Uni-directional thrust to Full Actuation) without any change of the platform and controller setup. This setup allowed us to achieve a fair comparison between the different actuation capabilities, and the corresponding change in the trajectory tracking ability. To achieve a consistent behavior of the controller while changing $\overline{f_{xy}}$, we presented an auto-tuning method that guarantees a consistent desired behavior of the platform for different actuation properties; the tuning method tunes the controller gains to guarantee the desired trajectory tracking behavior. This study shows that as $\overline{f_{xy}}$ of the platform increases, the platform's trajectory tracking ability approached **TT.4**, and as it decreases its trajectory tracking ability approaches **TT.2**. As such, the study shows that if the platform is UDT, the tuning method has to choose (depending on the desired behavior) either to track the desired position accurately, or to track the desired attitude accurately.

Following the above three cases, we studied vibration noise in IMU measurements. Vibration noise in MRAV platforms is a particular one, where these vibrations are caused by propellers vibrating the body of the platform, and are considered of high amplitude as compared to white noise present in the corresponding measurements. We studied, through frequency domain analysis of these measurements, the relation between the propeller rotational speeds and the vibration frequencies. This study showed that for a simple quadrotor these vibrations have a frequency equal (or very close) to the propeller rotational speeds. However, for a tilted propeller hexarotor, we showed that in addition to vibrations with frequencies near the propeller rotational speeds, the IMU measurements have vibrations at a fixed frequency, in addition to the aforementioned vibrations at frequencies near the propeller rotational speeds. We analyzed this vibration for two titled propeller hexarotors with different material composition, and showed that this vibration frequency is due to the platform geometry, and is independent from the platform material. This study of the vibration frequencies allowed us to then propose a novel, real-time, on-board IMU filter that can leverage the knowledge of the propeller rotational speeds to filter 'just' the vibration noise. We showed experimentally the advantage of the presented filter over classically used filters, as the presented one does not induce any phase lag, removes completely the vibration noise instead of attenuating it, and finally, does not remove any signal components at frequencies other than those corresponding to the vibration noise.

We leverage the presented filter by presenting a robust quadrotor position controller, that applies direct loop closure on the acceleration measurements. More specifically, the controller closes the loop between the desired quadrotor thrust and the applied one. We showed theoretically and experimentally that the proposed controller can mitigate variances in platform weight and aerodynamic coefficients, where the presented controller does not require the knowledge of the platform mass. We showed the advantage of the presented controller against a PID controller both theoretically and experimentally. While the two controllers can be written in equivalent forms, the difference between the two controllers (one relying on high frequency IMU measurements, and the other on the latent position and velocity measurements) allows the proposed controller to have much higher equivalent controller gains while still robustly controlling the platform; thus achieving better trajectory tracking and robustness to external disturbances and parameter modifications. Finally, while the controller's robustness was not formally proven, it was proven in an extensive experimental campaign, that showed its behavior while we systematically vary the platform mass, the platform aerodynamic coefficients, and while the platform picks up an unknown mass, and flies in an aerodynamically disturbed environment.

9.2 Lessons Learned

In the context of the problems presented throughout this thesis, there is a clear interplay between theoretical analysis and practical experiments. We believe that the theoretical study is a fundamental part of the scientific work, which allows a better analysis of the root problems and the derivation of adequate solutions; moreover, it allows the analysis of the presented solutions, to better understand the underlying limitations and advantages. However, most theoretical studies for systems as complex as the ones dealt with in this thesis require simplifying assumptions to be made; thus the need for experimental validation. Experimental validation is an important part of robotics research, as it allows first of all to understand the limitations of the system that was simplified in the theoretical study, then it allows in some circumstances to find solutions that could be further analyzed theoretically, and finally, it allows the validation of the presented theory on a physical system, and as such, ensure the validity of the assumptions made in theoretical analyses.

Along these lines, we believe that the theoretical study about the correlation between platform design and the ensuing actuation properties from one side, and the platform ability from the other side is an important one. As it can be seen throughout the rest of the thesis, it is very difficult to provide enough experiments to fully understand all these relations, where the experiments we provided in the other chapters of Part II cover only a single ability of MRAV platforms, while doing so on only one family of platforms (i.e., while modifying a limited number of design parameters). As such, the theoretical definitions were important to provide a complete understanding of these actuation properties and abilities. However, it was equally important in this context to provide adequate examples that could help the reader understand concretely the presented properties and abilities, as the theoretical definitions, while they could encompass all such design, were general and vague in some points. As such, we presented as many examples from the literature to provide a better understanding of the definitions instead of experiments.

The interplay between theoretical and experimental work is also visible in the omnidirectional platform design, where we first validated the theory from the literature by building a working prototype. We believe that it was important to finally show, on a working prototype the theory that was previously presented in the literature. However, after building the prototype, we had to conduct a new theoretical study to understand the limitations of the built design, and study the feasibility of a new and improved one. As such, this shows that there should always be a back and forth interplay between presenting theoretical background, validating the presented theory experimentally, and then re-iterating with the newly found limitations.

Such an approach was also followed in the case of the hexarotor robustness to propeller failure. As we studied the literature on the topic we found the contradictions between the presented theory and experiments conducted in the literature, where the Star-shaped platform was proven to be fully vulnerable to propeller failure ([Michieletto–2018]), while we could find some experiments from the literature, and experiments conducted at our lab where the Star-shaped hexarotor could in fact hover following the failure of some of its propellers. As such, we studied the theoretical conditions that could allow the platform to hover following the failure of some of its propellers. And again in this case, we validated the presented hypothesis through an extensive experimental campaign.

From this thesis we also learned that while formal proofs are important, sometimes they are hard to find. On the other hand, we believe that experimental validation of robotic systems is of equal importance to the formal proofs. However, we also learned that when an experimental campaign is being used as a proof, it is important for this campaign to be extensive enough to validate the proposed method for any condition for which it is intended to work, and to understand its limits. This lesson was obvious from the proposed direct acceleration feedback controller. While we did define formally the controller, and proved its robustness and advantage against the PID controller in an informal way, it proved very difficult to prove formally its robustness due to the unfamiliar form of the controller. As such, we relied on an extensive experimental campaign that aimed to study statistically the limits and robustness of the proposed controller. In addition, we had to provide experiments were the controller is tested in realistic scenarios where it might be later used.

Finally, we learned from this thesis that simple solutions, that are easily visible for the researcher, might sometimes be better than complex ones, that require extensive derivations and tuning to work. While this lesson was not visible in the thesis, it is one that I[2] learned personally while deriving two of the methods presented in this thesis. The first method was the presented direct acceleration feedback controller. While searching for a controller that can mitigate the variance in the platform parameters, I searched within classical controllers, and spent a significant time implementing and comparing those controllers. However, eventually we came up with the presented controller that is not similar to any of the tested controllers. The second method was the IMU filter for platforms other than the quadrotor. For this filter, I also spent a significant time deriving multiple methods that study the signal as a non-stationary stochastic signal using classical pattern recognition methods, deep learning methods and reinforcement learning methods. What I learned eventually that while some of the above methods do not work (while intuitively they should have worked), those that do work provide a filter that can remove less vibrations than the simple one presented in Chapt. 7. However, what I learned from this search for the best method, and the iterative testing of different methods is that, in robotics research, that's how lessons are learned.

---

[2] The use of first singular person is intentional in this paragraph to show that this paragraph is rather subjective, conversely to the objective tense used throughout the manuscript.

9.3 Future Work

Every conclusion of a scientific work is just the beginning of another one; similar to how this work followed from the collective of literature cited below, the following are future directions that could be pursued by future works to overcome some of the limitations of the work done in this thesis, and advance the literature on the topics in this thesis in general.

Regarding Part II, we presented a generalized modeling and analysis of the various designs from the literature. In this part we were able to fully describe some of the platform abilities, such as hovering and trajectory tracking, as these abilities have matured in the literature enough to be described in the scope of this manuscript. However, we realized that the literature as a whole is still missing some theoretical analyses necessary for the full understanding of the relation between MRAVs' design and their capabilities. One such study, mentioned in Chapt. 3, is the relation between the platform design and its APhI ability. As mentioned in Chapt. 3, the literature on the topic is not fully developed yet, where, to our knowledge, only one work in the literature attempted to study the relation between the force/moment decoupling of a platform and its APhI ability. However, the study was not exhaustive enough to allow us to understand based on a given design its APhI ability, and thus we reported in our review the demonstrated APhI abilities. We believe that such study could rely on the manipulability/maneuverability indexes of the platform and could help advance the literature on APhI as a whole.

MRAV Design Future Work Another future direction from this thesis is one that we described in Chapt. 3, were we believe that multiple design prospectives deserve further exploration in the literature. First, we believe that non-symmetric MRAV designs should be further explored; as we have seen in the literature review, most MRAV designs assume a certain symmetry to facilitate manufacturing and control of the platform. However, we have also seen that the few designs that attempted to break such symmetry were able to achieve a larger actuation capability than the one achieved by platforms with the same number of actuators that assume symmetry. As such, we believe that further analysis in this direction should be further explored.

Moreover, we also found very few works from the literature that incorporate the aerodynamic interaction between adjacent propellers into consideration, and almost no work incorporate these interactions in the platform design. We also believe that along these lines, the literature as a whole could benefit from such study from two perspectives: 1) first the understanding of such interactions should allow for their cancellation in the platform control, 2) and second, their incorporation could help achieve more stable designs, where the aerodynamic interaction between propellers is attenuated, or allocated in favor of the desired platform behavior.

Finally, in this work we attempted to study how the actuator limits could affect the feasibility of a design, by analyzing the ensuing force set. However, the actuator limits are usually dismissed in the design process of MRAVs. We expect this to be due to the fact that the design of the classical platforms (coplanar/collinear platforms) is forgiving in the sense that the used propellers usually allow a large range of forces to be applied, since eventually all of the platform's thrusters apply forces in the same direction. However, for platforms that apply forces in different orientations, such assumptions do not hold anymore, and the actuator limits could determine the feasibility of the proposed design. As such, we believe that the actuator limits have to be taken into consideration while designing platforms with a force set larger than that of a coplanar/collinear platform.

It has to be noted that we believe that the above three lines of design research should be accomplished in synchronization, and we believe that such conditions could be best enforced by following an optimization-based design approach.

Regarding the development of the omnidirectional platform with minimal unidirectional thrusters, we also believe that the topic requires further analysis. While we did demonstrate that it is possible to build a working prototype, the prototype has a low maturity level, as its purpose was only to prove the presented theory. However, once we studied the platform actuation limits we found that its impossible with the technology used in our lab to achieve the same platform design with better stability and higher maturity level. As such, we believe that future work could be done to the design, while focusing on smart materials that could help decrease the platform weight. Moreover, further analysis could be done from the actuators side; it would be interesting to test new Electronic Speed Controller (ESC) technology that could allow the allocation of the required high-speed rotational velocity while closing the loop on the motor control.

Finally, from the analysis of the failure robustness of coplanar/collinear hexarotors, we were able to understand that each of the Star-shaped and the Y-shaped hexarotors have some advantages over the other design. While the former is more efficient than the latter, the latter is robust to propeller failures while the former is not. As such, we believe that the study of a hybrid platform that can assume either configuration, or configurations in between could achieve the best of both designs. Such a platform could optimize its configuration to balance flight efficiency and robustness to propeller failure, where efficiency could be calculated from the overlap between adjacent propellers, or experimentally. A robustness metric could be introduced that reflects the size of the intersection between the interior of the platform moment set following the failure of each individual propeller, where the larger this set is, the more the platform could resist propeller failures and external disturbances after the loss of the corresponding propeller. This metric could be coupled with the efficiency calculation presented in the Chapt. 4 to optimize the configuration of the new platform mid-flight.

IMU Centered Control and Analysis Future Work We presented in this work an IMU filter that removes vibration noise from the IMU measurements, and runs on-board a platform in real time. Following this filter, we presented a controller that closes the loop between the desired accelerations and the filtered ones. While the filter work seems complete in the sense that the method used could be theoretically used for any platform (following adequate adaptation), it would be interesting to see its implementation on different platforms that are less linear than the ones it was tested on. From the controller perspective, we believe that the controller requires a formal proof of its robustness in order to better understand its limits. Following the formal proof, we believe the controller to be transferable to fully actuated platforms, where forces are applied along the three dimensions; as such, the controller could be incorporated along all the force directions of the platform, and not only along the thrust direction as was done in the quadrotor case. We believe the expansion of the controller to FA platforms to be a significant contribution to the literature, since it might be useful for disturbance rejection of fully actuated platforms, in addition to the contribution it could entail w.r.t. to the APhI literature.

Appendix

Appendix A

Introduction of the FiberTHex platform: design and implementation

This chapter summarizes the design and technical implementation of the FiberTHex platform. While this thesis does not contribute to the design or implementation of the FiberTHex platform, it analyzes the IMU measurements of this platform in Chapt. 7, and references this platform for the analysis of a new omnidirectional heptarotor design in Chapt. 5.

A.1 Actuation design

The FiberTHex can be considered as an upgraded version of the TiltHex ([Ryll–2017a]). The two platforms consist of Fully Actuated (FA) tilted propeller hexarotors. Propellers in each of the platforms are placed equally spaced about the platform's Center of Mass (CoM) in a star formation, and actuated by the same motor (MK3638 from MikroKopter). To be able to achieve FA, each propeller in the FiberTHex is rotated about it radial axes with an angle $\alpha = 20°$. Some of the FiberTHex important actuation parameters are listed in Tab. A.1.

Parameters	**Notation**	**Values**
Arm length [m]	d	0.389
Propeller radial tilting [degrees]	α	20
Propeller tangential tilting [degrees]	β	0
Propeller diameter [inches]	–	12"
Propeller lift coefficient [N/Hz^2]	c_f	1.920e-2

Table A.1 – FiberTHex actuation parameters.

A.2 Manufactured design

The major difference between the FiberTHex and its TiltHex predecessor is in the manufacturing of the two platforms. While the TiltHex is manufactured from aluminum bars, the former is built mostly from carbon-fiber parts (thus its name). The built platform is shown in Fig. A.1.

This platform has an inertia matrix as follows:

$$\boldsymbol{J}_B = \begin{pmatrix} 0.3969 & 1.446e-04 & -1.149e-05 \\ 1.446e-04 & 0.3972 & -1.168e-04 \\ -1.149e-05 & -1.168e-04 & 0.2549 \end{pmatrix} \tag{A.1}$$

The platform estimated mass is estimated in Tab. A.2 shown below.

Component	weight per unit [g]	# units	weight [g]
Motors	100	6	600
Propellers	15	6	90
Motor Mountings	22	6	132
Electronics	391	–	391
Mechanical parts	549	–	549
Battery	398	–	398
Total			2160

Table A.2 – FiberTHex estimated weight.

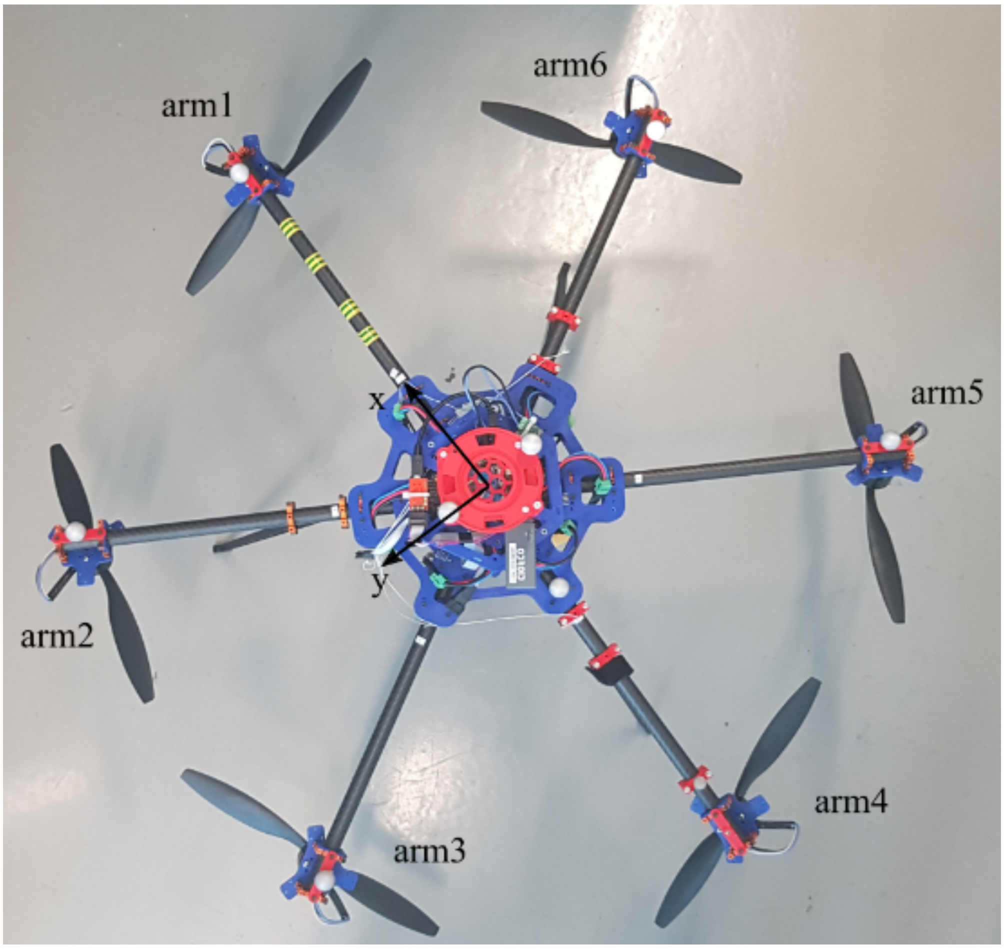

Figure A.1 – FiberTHex platform.

Bibliography

[Aerones–2016] Aerones. *Heavy duty drone for high paylaod transportation.* `https://www.aerones.com/`. Online, accessed: 31-August-2020. 2016 (cited on page 75).

[Ahmad–2013] N. Ahmad, R. Ghazilla, N. Khairi, and V. Kasi. “Reviews on various inertial measurement unit (IMU) sensor applications”. In: *International Journal of Signal Processing Systems* 1.2 (2013), pp. 256–262 (cited on page 7).

[Albers–2010] A. Albers, S. Trautmann, T. Howard, T. Nguyen, M. Frietsch, and C. Sauter. “Semi-autonomous flying robot for physical interaction with environment”. In: *2010 IEEE Conference on Robotics, Automation and Mechatronics.* June 2010, pp. 441–446 (cited on pages 63, 64, 65 and 75).

[Alexis–2011] K. Alexis, G. Nikolakopoulos, and A. Tzes. “Switching model predictive attitude control for a quadrotor helicopter subject to atmospheric disturbances”. In: *Control Engineering Practice* 19.10 (2011), pp. 1195–1207 (cited on page 163).

[Allenspach–2020] M. Allenspach, K. Bodie, M. Brunner, L. Rinsoz, Z. Taylor, M. Kamel, R. Siegwart, and J. Nieto. “Design and optimal control of a tiltrotor micro-aerial vehicle for efficient omnidirectional flight”. In: *The International Journal of Robotics Research* 39.10-11 (2020), pp. 1305–1325 (cited on page 78).

[Amiri–2011] N. Amiri, A. Ramirez-Serrano, and R. Davies. “Modelling of opposed lateral and longitudinal tilting dual-fan unmanned aerial vehicle”. In: *IFAC Proceedings Volumes* 44.1 (2011), pp. 2054–2059 (cited on pages 46 and 48).

[Antonelli–2018] G. Antonelli, E. Cataldi, F. Arrichiello, P. Robuffo Giordano, S. Chiaverini, and A. Franchi. “Adaptive Trajectory Tracking for Quadrotor MAVs in Presence of Parameter Uncertainties and External Disturbances”. In: *IEEE Trans. on Control Systems Technology* 26.1 (2018), pp. 248–254 (cited on page 163).

[Anzai–2017] T. Anzai, M. Zhao, X. Chen, F. Shi, K. Kawasaki, K. Okada, and M. Inaba. “Multilinked multirotor with internal communication system for multiple objects transportation based on form optimization method”. In: *2017 IEEE/RSJ Int. Conf. on Intelligent Robots and Systems.* Vancouver, Canada, Sept. 2017, pp. 5977–5984 (cited on page 19).

[Arthur–2015] M. K. Arthur. *Point picking and distributing on the disc and sphere.* Tech. rep. 2015 (cited on page 121).

[Badr–2016] S. Badr, O. Mehrez, and A. Kabeel. “A novel modification for a quadrotor design”. In: *2016 Int. Conf. on Unmanned Aircraft Systems.* Arlington, VA, USA, June 2016, pp. 702–710 (cited on pages 57, 58 and 62).

[Barber–1996] C. Barber, D. Dobkin, and H. Huhdanpaa. “The quickhull algorithm for convex hulls”. In: *ACM Transactions on Mathematical Software (TOMS)* 22.4 (1996), pp. 469–483 (cited on page 29).

[Baskaya–2021] E. Baskaya, M. Hamandi, M. Bronz, and A. Franchi. “A Novel Robust Hexarotor Capable of Static Hovering in Presence of Propeller Failure”. In: *IEEE Robotics and Automation Letters* 6.2 (2021), pp. 4001–4008. DOI: `10.1109/LRA.2021.3067182` (cited on page 12).

[Bernard–2018] D. D. C. Bernard, M. Giurato, F. Riccardi, and M. Lovera. “Ground effect analysis for a quadrotor platform”. In: *Advances in Aerospace Guidance, Navigation and Control*. Springer, 2018, pp. 351–367 (cited on page 172).

[Besnard–2012] L. Besnard, Y. B. Shtessel, and B. Landrum. “Quadrotor vehicle control via sliding mode controller driven by sliding mode disturbance observer”. In: *Journal of the Franklin Institute* 349.2 (2012), pp. 658–684 (cited on page 163).

[Bicego–2019] D. Bicego. “Design and Control of Multi-Directional Thrust Multi-Rotor Aerial Vehicles with applications to Aerial Physical Interaction Tasks”. Ph.D. thesis. Université de Toulouse, 2019 (cited on pages 67, 72 and 129).

[Bicego–2020] D. Bicego, J. Mazzetto, M. Farina, R. Carli, and A. Franchi. “Nonlinear Model Predictive Control with Enhanced Actuator Model for Multi-Rotor Aerial Vehicles with Generic Designs”. In: *Journal of Intelligent & Robotics Systems* 100 (2020), pp. 1213–1247. DOI: `10.1007/s10846-020-01250-9` (cited on pages 28, 81 and 127).

[Blouin–2014] C. Blouin and E. Lanteigne. “Pitch control of an Oblique Active Tilting bi-rotor”. In: *2014 Int. Conf. on Unmanned Aircraft Systems*. Oralndo, FL, USA, May 2014, pp. 791–799 (cited on pages 48 and 49).

[Bouabdallah–2004] S. Bouabdallah, A. Noth, and R. Siegwart. “PID vs LQ control techniques applied to an indoor micro quadrotor”. In: *2004 IEEE/RSJ Int. Conf. on Intelligent Robots and Systems*. Sendai, Japan, Sept. 2004, pp. 2451–2456 (cited on pages 55 and 62).

[Bouabdallah–2005] S. Bouabdallah and R. Siegwart. “Backstepping and sliding-mode techniques applied to an indoor micro quadrotor”. In: *2005 IEEE Int. Conf. on Robotics and Automation*. Barcelona, Spain, Apr. 2005, pp. 2247–2252 (cited on pages 55 and 62).

[Brescianini–2016a] D. Brescianini and R. D’Andrea. “Design, Modeling and Control of an Omni-Directional Aerial Vehicle”. In: *2016 IEEE Int. Conf. on Robotics and Automation*. Stockholm, Sweden, May 2016, pp. 3261–3266 (cited on page 104).

[Brescianini–2016b] D. Brescianini and R. D’Andrea. “Design, modeling and control of an omni-directional aerial vehicle”. In: *2016 IEEE Int. Conf. on Robotics and Automation*. Stockholm, Sweden, May 2016, pp. 3261–3266 (cited on pages 36, 76, 77, 78 and 79).

[Bronz–2017] M. Bronz, E. Smeur, H. Garcia de Marina, and G. Hattenberger. “Development of A Fixed-Wing mini UAV with Transitioning Flight Capability”. In: *35th AIAA Applied Aerodynamics Conference*. June 2017 (cited on page 19).

[Byrd–2000] R. H. Byrd, J. C. Gilbert, and J. Nocedal. “A trust region method based on interior point techniques for nonlinear programming”. In: *Mathematical programming* 89.1 (2000), pp. 149–185 (cited on page 31).

[Cardoso–2016] D. Cardoso, G. Raffo, and S. Esteban. “A robust adaptive mixing control for improved forward flight of a tilt-rotor UAV”. In: *2016 IEEE 19th International Conference on Intelligent Transportation Systems (ITSC)*. Rio de Janeiro, Brazil, 2016, pp. 1432–1437 (cited on pages 48 and 49).

[Castillo–2002] P. Castillo, R. Lozano, I. Fantoni, and A. Dzul. “Control design for the PVTOL aircraft with arbitrary bounds on the acceleration”. In: *Proceedings of the 41st IEEE Conference on Decision and Control, 2002.* Vol. 2. 2002, 1717–1722 vol.2. DOI: `10.1109/CDC.2002.1184768` (cited on page 28).

[Chowdhury–2012] A. Chowdhury, A. Kulhare, and G. Raina. “A generalized control method for a Tilt-rotor UAV stabilization”. In: *2012 IEEE International Conference on Cyber Technology in Automation, Control, and Intelligent Systems (CYBER)*. Bangkok, Thailand, 2012, pp. 309–314 (cited on pages 46, 47 and 48).

[Crowther–2011] B. Crowther, A. Lanzon, M. Maya-Gonzalez, and D. Langkamp. “Kinematic analysis and control design for a nonplanar multirotor vehicle”. In: *Journal of Guidance, Control, and Dynamics* 34.4 (2011), pp. 1157–1171 (cited on pages 69 and 72).

[Czapla–2013] T. Czapla and J. Wrona. “Technology development of military applications of unmanned ground vehicles”. In: *Vision Based Systemsfor UAV Applications*. Springer, 2013, pp. 293–309 (cited on page 3).

[De Martini–2017] D. De Martini, G. Gramazio, A. Bertini, C. Rottenbacher, and T. Facchinetti. “Design and Modeling of a Quadcopter with Double Axis Tilting Rotors”. In: *Unmanned Systems* 5.03 (2017), pp. 169–180 (cited on pages 60, 62 and 79).

[Devlin–2018] T. Devlin, R. Dickerhoff, K. Durney, A. Forrest, P. Pansodtee, A. Adabi, and M. Teodorescu. “ElbowQuad: Thrust Vectoring Quadcopter”. In: *2018 AIAA Information Systems-AIAA Infotech@ Aerospace*. 2018, p. 0893 (cited on pages 58 and 62).

[Donadel–2014] R. Donadel, G. Raffo, and L. Becker. “Modeling and control of a tiltrotor uav for path tracking”. In: *IFAC Proceedings Volumes* 47.3 (2014), pp. 3839–3844 (cited on pages 48 and 49).

[Dyer–2019] E. Dyer, S. Sirouspour, and M. Jafarinasab. “Energy optimal control allocation in a redundantly actuated omnidirectional UAV”. In: *2019 IEEE Int. Conf. on Robotics and Automation*. Montreal, Canada, May 2019 (cited on page 104).

[Elkhatib–2017] O. Elkhatib. “Control Allocation of a Tilting Rotor Hexacopter”. B.S. thesis. 2017 (cited on pages 67, 69 and 72).

[Escareno–2008] J. Escareno, A. Sanchez, O. Garcia, and R. Lozano. “Triple tilting rotor mini-UAV: Modeling and embedded control of the attitude”. In: *2008 American Control Conference*. Seattle, WA, USA, June 2008, pp. 3476–3481 (cited on pages 51 and 53).

[Faessler–2017] M. Faessler, A. Franchi, and D. Scaramuzza. “Differential flatness of quadrotor dynamics subject to rotor drag for accurate tracking of high-speed trajectories”. In: *IEEE Robotics and Automation Letters* 3.2 (2017), pp. 620–626 (cited on pages 27 and 166).

[Faessler–2018] M. Faessler, A. Franchi, and D. Scaramuzza. “Differential Flatness of Quadrotor Dynamics Subject to Rotor Drag for Accurate Tracking of High-Speed Trajectories”. In: *IEEE Robotics and Automation Letters* 3.2 (2018), pp. 620–626 (cited on pages 103, 163 and 165).

[Falanga–2017] D. Falanga, E. Mueggler, M. Faessler, and D. Scaramuzza. “Aggressive quadrotor flight through narrow gaps with onboard sensing and computing using active vision”. In: *2017 IEEE Int. Conf. on Robotics and Automation*. Marina Bay Sands, Singapore, May 2017, pp. 5774–5781 (cited on pages 57 and 62).

[Falconi–2012] R. Falconi and C. Melchiorri. “Dynamic model and control of an over-actuated quadrotor uav”. In: *IFAC Proceedings Volumes* 45.22 (2012), pp. 192–197 (cited on pages 57 and 62).

[Franchi–2017] A. Franchi and A. Mallet. “Adaptive Closed-loop Speed Control of BLDC Motors with Applications to Multi-rotor Aerial Vehicles”. In: *2017 IEEE Int. Conf. on Robotics and Automation*. Singapore, May 2017, pp. 5203–5208 (cited on pages 133, 167 and 171).

[Franchi–2018a] A. Franchi, R. Carli, D. Bicego, and M. Ryll. “Full-Pose Tracking Control for Aerial Robotic Systems with Laterally-Bounded Input Force”. In: *IEEE Trans. on Robotics* 34.2 (2018), pp. 534–541. DOI: `10.1109/TRO.2017.2786734` (cited on pages 6, 10, 28, 125, 126, 127, 128, 130, 133, 137 and 138).

[Franchi–2018b] A. Franchi, R. Carli, D. Bicego, and M. Ryll. “Full-Pose Tracking Control for Aerial Robotic Systems with Laterally-Bounded Input Force”. In: *IEEE Trans. on Robotics* 34.2 (2018), pp. 534–541 (cited on page 79).

[Frigo–1998] M. Frigo and S. G. Johnson. “FFTW: An adaptive software architecture for the FFT”. In: *Proceedings of the 1998 IEEE International Conference on Acoustics, Speech and Signal Processing, ICASSP’98 (Cat. No. 98CH36181)*. Vol. 3. IEEE. 1998, pp. 1381–1384 (cited on page 150).

[Fu–2017] Z. Fu, B. X. J. Yang, C. Wu, and Y. Wei. “Modeling and control of a new multicopter”. In: *2017 36th Chinese Control Conference (CCC)*. Liaoning, China, 2017, pp. 6495–6500 (cited on pages 76 and 78).

[Genov–2015] B. Genov. “The convex hull problem in practice: improving the running time of the double description method”. In: (2015) (cited on page 29).

[Giernacki–2019] W. Giernacki, D. Horla, T. Báča, and M. Saska. “Real-Time Model-Free Minimum-Seeking Autotuning Method for Unmanned Aerial Vehicle Controllers Based on Fibonacci-Search Algorithm”. In: *Sensors* 19.2 (2019), p. 312 (cited on page 130).

[Giribet–2016a] J. Giribet, R. Sanchez-Pena, and A. Ghersin. “Analysis and design of a tilted rotor hexacopter for fault tolerance”. In: *IEEE Transactions on Aerospace and Electronic Systems* 52.4 (2016), pp. 1555–1567 (cited on pages 69 and 72).

[Giribet–2016b] J. I. Giribet, R. S. Sanchez-Pena, and A. S. Ghersin. “Analysis and design of a tilted rotor hexacopter for fault tolerance”. In: *IEEE Trans. on Aerospace and Electronic System* 52.4 (2016), pp. 1555–1567 (cited on page 81).

[Grau–2017] A. Grau, M. Indri, L. L. Bello, and T. Sauter. “Industrial robotics in factory automation: From the early stage to the Internet of Things”. In: *IECON 2017-43rd Annual Conference of the IEEE Industrial Electronics Society*. IEEE. 2017, pp. 6159–6164 (cited on page 3).

[Gress–2002] G. Gress. “Using dual propellers as gyroscopes for tilt-prop hover control”. In: *2002 Biennial International Powered Lift Conference and Exhibit*. 2002, p. 5968 (cited on pages 46, 47 and 48).

[Hamandi–2020a] M. Hamandi, K. Sawant, M. Tognon, and A. Franchi. “Omni-Plus-Seven (O7+): An Omnidirectional Aerial Prototype with a Minimal Number of Unidirectional Thrusters”. In: *2020 Int. Conf. on Unmanned Aircraft Systems*. IEEE. 2020, pp. 754–761 (cited on page 12).

[Hamandi–2020b] M. Hamandi, M. Tognon, and A. A. Franchi. “Direct acceleration feedback control of quadrotor aerial vehicles”. In: *2020 IEEE Int. Conf. on Robotics and Automation*. IEEE. 2020, pp. 5335–5341 (cited on page 13).

[Hamandi–2020c] M. Hamandi, F. Usai, Q. Sablé, N. Staub, M. Tognon, and A. Franchi. “Survey on Aerial Multirotor Design: a Taxonomy Based on Input Allocation”. working paper or preprint. Jan. 2020. URL: `https://hal.archives-ouvertes.fr/hal-02433405` (cited on page 12).

[Hamandi–2021] M. Hamandi, Q. Sable, M. Tognon, and A. Franchi. “Understanding the omnidirectional capability of a generic multi-rotor aerial vehicle”. In: *submitted to IEEE AIRPHARO 2021*. IEEE. 2021 (cited on page 12).

[Hattenberger–2014] G. Hattenberger, M. Bronz, and M. Gorraz. “Using the paparazzi UAV system for scientific research”. In: 2014 (cited on page 92).

[Haus–2016] T. Haus, M. Orsag, and S. Bogdan. “Design considerations for a large quadrotor with moving mass control”. In: *2016 Int. Conf. on Unmanned Aircraft Systems*. Arlington, VA, USA, June 2016, pp. 1327–1334 (cited on page 19).

[Haus–2017] T. Haus, M. Orsag, and S. Bogdan. “A concept of a non-tilting multirotor-UAV based on moving mass control”. In: *2017 Int. Conf. on Unmanned Aircraft Systems*. Miami, FL, USA, June 2017, pp. 1618–1624 (cited on page 19).

[Horla–2021] D. Horla, M. Hamandi, W. Giernacki, and A. Franchi. “Optimal Tuning of the Lateral-Dynamics Parameters for Aerial Vehicles With Bounded Lateral Force”. In: *IEEE Robotics and Automation Letters* 6.2 (2021), pp. 3949–3955. DOI: `10.1109/LRA.2021.3067229` (cited on page 12).

[Hou–2020] Z. Hou, P. Lu, and Z. Tu. “Nonsingular terminal sliding mode control for a quadrotor UAV with a total rotor failure”. In: *Aerospace Science and Technology* 98 (2020), p. 105716 (cited on page 82).

[Hua–2015] M. Hua, T. Hamel, P. Morin, and C. Samson. “Control of VTOL vehicles with thrust-tilting augmentation”. In: *Automatica* 52 (2015), pp. 1–7 (cited on pages 60, 61 and 62).

[Invernizzi–2017] D. Invernizzi and M. Lovera. “Geometric tracking control of a quadcopter tiltrotor UAV”. In: *IFAC-PapersOnLine* 50.1 (2017), pp. 11565–11570 (cited on page 79).

[Invernizzi–2018] D. Invernizzi and M. Lovera. “Trajectory tracking control of thrust-vectoring UAVs”. In: *Automatica* 95 (2018), pp. 180–186 (cited on page 126).

[Jiang–2014] G. Jiang and R. Voyles. “A nonparallel hexrotor UAV with faster response to disturbances for precision position keeping”. In: *2014 IEEE Int. Symp. on Safety, Security and Rescue Robotics*. Toyako-cho, Hokkaido, Japan, Oct. 2014, pp. 1–5 (cited on pages 67 and 72).

[Jiang–2017] G. Jiang, R. Voyles, K. Sebesta, and H. Greiner. “Estimation and optimization of fully-actuated multirotor platform with nonparallel actuation mechanism”. In: *2017 IEEE/RSJ International Conference on Intelligent Robots and Systems (IROS)*. IEEE. 2017, pp. 6843–6848 (cited on page 79).

[Kamel–2015] M. Kamel, K. Alexis, M. Achtelik, and R. Siegwart. “Fast nonlinear model predictive control for multicopter attitude tracking on SO(3)”. In: *2015 IEEE Conf. on Control Applications*. Sydney, Australia, Sept. 2015 (cited on page 81).

[Kamel–2018] M. Kamel, S. Verling, O. Elkhatib, C. Sprecher, P. Wulkop, Z. Taylor, R. Siegwart, and I. Gilitschenski. “The Voliro Omniorientational Hexacopter: An Agile and Maneuverable Tiltable-Rotor Aerial Vehicle”. In: *IEEE Robotics & Automation Magazine* 25.4 (2018), pp. 34–44 (cited on pages 67, 69, 72 and 78).

[Kastelan–2015] D. Kastelan, M. Konz, and J. Rudolph. “Fully Actuated Tricopter with Pilot-Supporting Control This work is supported in part by the German Research Foundation (DFG) in the framework of project”. In: *IFAC-PapersOnLine* 48.9 (2015), pp. 79–84 (cited on pages 53 and 54).

[Kataoka–2011] Y. Kataoka, K. Sekiguchi, and M. Sampei. “Nonlinear control and model analysis of trirotor UAV model”. In: *IFAC Proceedings Volumes* 44.1 (2011), pp. 10391–10396 (cited on page 49).

[Kawasaki–2015] K. Kawasaki, Y. Motegi, M. Zhao, K. Okada, and M. Inaba. “Dual connected Bi-Copter with new wall trace locomotion feasibility that can fly at arbitrary tilt angle”. In: *2015 IEEE/RSJ Int. Conf. on Intelligent Robots and Systems*. Hamburg, Germany, Sept. 2015, pp. 524–531 (cited on pages 39, 61 and 62).

[Kendoul–2006] F. Kendoul, I. Fantoni, and R. Lozano. “Modeling and control of a small autonomous aircraft having two tilting rotors”. In: *IEEE Trans. on Robotics* 22.6 (2006), pp. 1297–1302 (cited on pages 46, 47 and 48).

[KG–2016] F. A. C̃. KG. *FreeMotionHandling*. `https://www.festo.com/net/SupportPortal/Files/443122/50017_Brosch_FreeMotionHandling_en_160329_lo_ES.pdf`. Online, accessed: 11-July-2018. 2016 (cited on page 19).

[Khalil–2001] H. K. Khalil. *Nonlinear Systems*. 3rd. Prentice Hall, 2001. ISBN: 978-0130673893 (cited on page 171).

[Khan–2013] W. Khan and M. Nahon. “Toward an accurate physics-based UAV thruster model”. In: *IEEE/ASME Transactions on Mechatronics* 18.4 (2013), pp. 1269–1279 (cited on pages 89 and 90).

[Khoo–2017] S. Khoo, M. Norton, J. Kumar, J. Yin, X. Yu, T. Macpherson, D. Dowling, and A. Kouzani. “Robust control of novel thrust vectored 3D printed multicopter”. In: *2017 36th Chinese Control Conference (CCC)*. Liaoning, China, 2017, pp. 1270–1275 (cited on pages 60 and 62).

[Kleder–2020] M. Kleder. *CON2VERT - constraints to vertices, MATLAB Central File Exchange*. 2020. URL: `https://www.mathworks.com/matlabcentral/fileexchange/7894-con2vert-constraints-to-vertices` (cited on page 29).

[Landau–2007] I. D. Landau and G. Zito. *Digital control systems: design, identification and implementation*. Springer Science & Business Media, 2007 (cited on page 171).

[Lee–2010] T. Lee, M. Leoky, and N. H. McClamroch. “Geometric tracking control of a quadrotor UAV on SE(3)”. In: *49th IEEE Conf. on Decision and Control*. Atlanta, GA, Dec. 2010, pp. 5420–5425 (cited on page 168).

[Loianno–2015] G. Loianno, G. Cross, C. Qu, Y. Mulgaonkar, J. Hesch, and V. Kumar. “Flying Smartphones: Automated Flight Enabled by Consumer Electronics”. In: *IEEE Robotics Automation Magazine* 22.2 (2015), pp. 24–32. DOI: `10.1109/MRA.2014.2382792` (cited on page 5).

[Long–2012] Y. Long, S. Lyttle, N. Pagano, and D. Cappelleri. “Design and quaternion-based attitude control of the omnicopter mav using feedback linearization”. In: *ASME International Design Engineering Technical Conference (IDETC)*. Chicago, Illinois, USA, 2012, pp. 1413–1421 (cited on pages 58, 59 and 62).

[Long–2013] Y. Long and D. J. Cappelleri. “Omnicopter: A Novel Overactuated Micro Aerial Vehicle”. In: *Advances in Mechanisms, Robotics and Design Education and Research*. Heidelberg: Springer International Publishing, 2013, pp. 215–226 (cited on page 103).

[Long–2014] Y. Long, A. Gelardos, and D. Cappelleri. “A novel micro aerial vehicle design: The evolution of the omnicopter MAV”. In: *ASME 2014 International Design Engineering Technical Conferences and Computers and Information in Engineering Conference*. Buffalo, NY, USA, 2014, V05AT08A092 (cited on pages 58, 59 and 62).

[Lu–2018] Y. Lu, Z. Xue, G.-S. Xia, and L. Zhang. “A survey on vision-based UAV navigation”. In: *Geo-spatial information science* 21.1 (2018), pp. 21–32 (cited on page 7).

[Lynch–2017] K. M. Lynch and F. C. Park. *Modern Robotics: Mechanics, Planning, and Control*. Cambridge University Press, 2017 (cited on page 21).

[Mahony–2012] R. Mahony, V. Kumar, and P. Corke. “Multirotor Aerial Vehicles: Modeling, Estimation, and Control of Quadrotor”. In: *IEEE Robotics & Automation Magazine* 19.3 (2012), pp. 20–32 (cited on pages 23, 27, 55, 62, 103, 163, 165 and 168).

[Mallet–2010] A. Mallet, C. Pasteur, M. Herrb, S. Lemaignan, and F. Ingrand. “GenoM3: Building middleware-independent robotic components”. In: *2010 IEEE International Conference on Robotics and Automation* (2010), pp. 4627–4632 (cited on pages 117 and 172).

[Martin–2010] P. Martin and E. Salaün. “The True Role of Accelerometer Feedback in Quadrotor Control”. In: *2010 IEEE Int. Conf. on Robotics and Automation*. Anchorage, AK, May 2010, pp. 1623–1629 (cited on page 168).

[McArthur–2017] D. McArthur, A. Chowdhury, and D. Cappelleri. “Design of the I-BoomCopter UAV for environmental interaction”. In: *2017 IEEE Int. Conf. on Robotics and Automation*. Singapore, May 2017, pp. 5209–5214 (cited on pages 62 and 63).

[Mehmood–2016] H. Mehmood, T. Nakamura, and E. Johnson. “A maneuverability analysis of a novel hexarotor UAV concept”. In: *2016 Int. Conf. on Unmanned Aircraft Systems*. Arlington, VA, USA, June 2016, pp. 437–446 (cited on page 70).

[Michieletto–2017] G. Michieletto, M. Ryll, and A. Franchi. “Control of Statically Hoverable Multi-Rotor Aerial Vehicles and Application to Rotor-Failure Robustness for Hexarotors”. In: *2017 IEEE Int. Conf. on Robotics and Automation*. Singapore, May 2017, pp. 2747–2752 (cited on page 81).

[Michieletto–2018] G. Michieletto, M. Ryll, and A. Franchi. “Fundamental Actuation Properties of Multi-rotors: Force-Moment Decoupling and Fail-safe Robustness”. In: *IEEE Trans. on Robotics* 34.3 (2018), pp. 702–715. DOI: `10.1109/TRO.2018.2821155` (cited on pages 10, 28, 41, 42, 65, 70, 81, 82, 85, 86, 88 and 188).

[Michini–2011] B. Michini, J. Redding, N. K. Ure, M. Cutler, and J. P. How. “Design and flight testing of an autonomous variable-pitch quadrotor”. In: *2011 IEEE Int. Conf. on Robotics and Automation*. Shanghai, China, May 2011, pp. 2978–2979 (cited on page 19).

[Mistler–2001] V. Mistler, A. Benallegue, and N. K. M'Sirdi. "Exact linearization and noninteracting control of a 4 rotors helicopter via dynamic feedback". In: *10th IEEE Int. Symp. on Robots and Human Interactive Communications.* Bordeaux, Paris, France, Sept. 2001, pp. 586–593 (cited on page 55).

[Mochida–2021] S. Mochida, R. Matsuda, T. Ibuki, and M. Sampei. "A Geometric Method of Hoverability Analysis for Multirotor UAVs With Upward-Oriented Rotors". In: *IEEE Transactions on Robotics* (2021) (cited on page 82).

[Mohamed–2012] M. Mohamed and A. Lanzon. "Design and control of novel tri-rotor UAV". In: *2012 UKACC International Conference on control (CONTROL).* Cardiff, United Kingdom, 2012, pp. 304–309 (cited on pages 51 and 53).

[Morbidi–2018] F. Morbidi, D. Bicego, M. Ryll, and A. Franchi. "Energy-Efficient Trajectory Generation for a Hexarotor with Dual-Tilting Propellers". In: *2018 IEEE/RSJ Int. Conf. on Intelligent Robots and Systems.* Madrid, Spain, Oct. 2018, pp. 6226–6232 (cited on pages 71 and 72).

[Mueller–2014] M. W. Mueller and R. D'Andrea. "Stability and control of a quadrocopter despite the complete loss of one, two, or three propellers". In: *2014 IEEE Int. Conf. on Robotics and Automation.* IEEE. 2014, pp. 45–52 (cited on page 93).

[Muñoz–2013] L. Muñoz, O. Santos, P. Castillo, and I. Fantoni. "Energy-based nonlinear control for a quadrotor rotorcraft". In: *2013 American Control Conference.* IEEE. 2013, pp. 1177–1182 (cited on page 28).

[Myeong–2019] W. Myeong, S. Jung, B. Yu, T. Chris, S. Song, and H. Myung. "Development of Wall-climbing Unmanned Aerial Vehicle System for Micro-Inspection of Bridges". In: *2019 IEEE Int. Conf. on Robotics and Automation.* Montreal, Canada, May 2019 (cited on pages 71 and 72).

[Nemati–2014] A. Nemati and M. Kumar. "Modeling and control of a single axis tilting quadcopter". In: *2014 American Control Conference.* Portlan, OR, USA, June 2014, pp. 3077–3082 (cited on pages 57 and 62).

[Nemati–2016] A. Nemati, N. Soni, M. Sarim, and M. .Kumar. "Design, Fabrication and Control of a Tilt Rotor Quadcopter". In: *2016 ASME Dynamic Systems and Control Conference.* American Society of Mechanical Engineers. Minneapolis, MN, USA, Oct. 2016, V002T29A005 (cited on pages 57 and 62).

[Nikou–2015] A. Nikou, G. Gavridis, and K. Kyriakopoulos. "Mechanical design, modelling and control of a novel aerial manipulator". In: *2015 IEEE Int. Conf. on Robotics and Automation.* Seattle, WA, USA, May 2015, pp. 4698–4703 (cited on pages 73, 74, 78 and 79).

[Odelga–2016] M. Odelga, P. Stegagno, and H. Bülthoff. "A fully actuated quadrotor UAV with a propeller tilting mechanism: Modeling and control". In: *2016 IEEE/ASME Int. Conf. on Advanced Intelligent Mechatronics.* Banff, Alberta, Canada, July 2016, pp. 306–311 (cited on pages 27, 60, 61 and 62).

[Ollero–2018] A. Ollero, G. Heredia, A. Franchi, G. Antonelli, K. Kondak, A. Sanfeliu, A. Viguria, J. R. Martinez-de Dios, F. Pierri, J. Cortés, A. Santamaria-Navarro, M. A. Trujillo, R. Balachandran, J. Andrade-Cetto, and A. Rodriguez. “The AEROARMS Project: Aerial Robots with Advanced Manipulation Capabilities for Inspection and Maintenance”. In: *IEEE Robotics & Automation Magazine, Special Issue on Floating-base (Aerial and Underwater) Manipulation* 25.4 (2018), pp. 12–23 (cited on page 5).

[Oosedo–2016] A. Oosedo, S. Abiko, S. Narasaki, A. Kuno, A. Konno, and M. Uchiyama. “Large attitude change flight of a quad tilt rotor unmanned aerial vehicle”. In: *Advanced Robotics* 30.5 (2016), pp. 326–337 (cited on pages 57 and 62).

[Papachristos–2011] C. Papachristos, K. Alexis, and A. Tzes. “Design and experimental attitude control of an unmanned tilt-rotor aerial vehicle”. In: *2011 Int. Conf. on Robotics*. Tallinn, Estonia, June 2011, pp. 465–470 (cited on pages 26, 47 and 48).

[Papachristos–2013] C. Papachristos and A. Tzes. “Large object pushing via a direct longitudinally-actuated unmanned tri-tiltrotor”. In: *2013 Mediterranean Conf. on Control and Automation*. Crete, Greece, June 2013, pp. 173–178 (cited on pages 50 and 53).

[Papachristos–2014] C. Papachristos, K. Alexis, and A. Tzes. “Efficient force exertion for aerial robotic manipulation: Exploiting the thrust-vectoring authority of a tri-tiltrotor uav”. In: *2014 IEEE Int. Conf. on Robotics and Automation*. Hong Kong, China, Aug. 2014, pp. 4500–4505 (cited on pages 50 and 53).

[Papachristos–2016] C. Papachristos, K. Alexis, and A. Tzes. “Dual-authority thrust-vectoring of a tri-tiltrotor employing model predictive control”. In: *Journal of Intelligent & Robotic Systems* 81.3-4 (2016), p. 471 (cited on pages 50 and 53).

[Park–2016a] S. Park, J. Her, J. Kim, and D. Lee. “Design, modeling and control of omni-directional aerial robot”. In: *2016 IEEE/RSJ Int. Conf. on Intelligent Robots and Systems*. Daejeon, Korea, Oct. 2016, pp. 1570–1575 (cited on pages 76, 77 and 79).

[Park–2016b] S. Park, J. J. Her, J. Kim, and D. Lee. “Design, Modeling and Control of Omni-Directional Aerial Robot”. In: *2016 IEEE/RSJ Int. Conf. on Intelligent Robots and Systems*. Daejeon, South Korea, 2016, pp. 1570–1575 (cited on page 104).

[Park–2018] S. Park, J. Lee, J. Ahn, M. Kim, J. Her, G. H. Yang, and D. Lee. “ODAR: Aerial Manipulation Platform Enabling Omni-Directional Wrench Generation”. In: *IEEE/ASME Transactions on Mechatronics* 23.4 (2018), pp. 1907–1918 (cited on pages 76, 77, 78 and 79).

[Politis–2017] I. Politis, P. Langdon, M. Bradley, L. Skrypchuk, A. Mouzakitis, and P. J. Clarkson. “Designing autonomy in cars: A survey and two focus groups on driving habits of an inclusive user group, and group attitudes towards autonomous cars". In: *International Conference on Applied Human Factors and Ergonomics.* Springer. 2017, pp. 161–173 (cited on page 3).

[Pose–2017] C. Pose, J. Giribet, and A. Ghersin. "Hexacopter fault tolerant actuator allocation analysis for optimal thrust". In: *2017 Int. Conf. on Unmanned Aircraft Systems.* Miami, FL, USA, June 2017, pp. 663–671 (cited on pages 69 and 72).

[Pose–2020] C. Pose, J. Giribet, and I. Mas. "Fault tolerance analysis for a class of reconfigurable aerial hexarotor vehicles". In: *IEEE/ASME Transactions on Mechatronics* 24.4 (2020), pp. 1851–1858 (cited on page 82).

[Pounds–2002] P. Pounds, R. Mahony, P. Hynes, and J. M. Roberts. "Design of a four-rotor aerial robot". In: *Proceedings of the 2002 Australasian Conference on Robotics and Automation (ACRA 2002).* Australian Robotics & Automation Association. 2002, pp. 145–150 (cited on page 54).

[Pounds–2010] P. Pounds, R. Mahony, and P. Corke. "Modelling and control of a large quadrotor robot". In: *Control Engineering Practice* 18.7 (2010), pp. 691–699 (cited on page 55).

[Powers–2013] C. Powers, D. Mellinger, A. Kushleyev, B. Kothmann, and V. Kumar. "Influence of aerodynamics and proximity effects in quadrotor flight". In: *Experimental robotics.* Springer. 2013, pp. 289–302 (cited on page 169).

[Prothin–2013] S. Prothin and J.-M. Moschetta. "A Vectoring Thrust Coaxial Rotor for Micro Air Vehicle: Modeling, Design and Analysis". In: *ERCOFTAC international symposium 'Unsteady separation in fluid-structure'.* Mykonos, Greece, June 2013 (cited on pages 47 and 48).

[Rajappa–2015] S. Rajappa, M. Ryll, H. Bülthoff, and A. Franchi. "Modeling, Control and Design Optimization for a Fully-actuated Hexarotor Aerial Vehicle with Tilted Propellers". In: *2015 IEEE Int. Conf. on Robotics and Automation.* Seattle, WA, May 2015, pp. 4006–4013 (cited on pages 70, 71 and 72).

[Ramp–2015] M. Ramp and E. Papadopoulos. "On modeling and control of a holonomic vectoring tricopter". In: *2015 IEEE/RSJ Int. Conf. on Intelligent Robots and Systems.* Hamburg, Germany, Sept. 2015, pp. 662–668 (cited on pages 52, 53 and 54).

[Rashad–2017] R. Rashad, P. Kuipers, J. Engelen, and S. Stramigioli. "Design, Modeling, and Geometric Control on SE (3) of a Fully-Actuated Hexarotor for Aerial Interaction". In: *arXiv preprint arXiv:1709.05398* (2017) (cited on pages 71, 72 and 79).

[Rashad–2019] R. Rashad, J. Engelen, and S. Stramigioli. "Energy tank-based wrench/impedance control of a fully-actuated hexarotor: A geometric port-hamiltonian approach". In: *2019 IEEE Int. Conf. on Robotics and Automation.* Montreal, Canada, May 2019, pp. 6418–6424 (cited on pages 71 and 72).

[Reid–2021] C. Reid. *Prepare For Gridlock If Future For Autonomous Vehicles Is Plentiful Cheap Journeys.* Feb. 2021. URL: `https://www.forbes.com/sites/carltonreid/2021/02/18/prepare-for-gridlock-if-future-for-autonomous-vehicles-is-plentiful-cheap-journeys/?sh=3143eb071434` (cited on page 3).

[Romero–2007a] H. Romero, S. Salazar, A. Sanchez, and R. Lozano. “A new UAV configuration having eight rotors: Dynamical model and real-time control”. In: *2007 46th IEEE Conference on Decision and Control.* New Orleans, LA, USA, 2007, pp. 6418–6423 (cited on pages 75, 76 and 78).

[Romero–2007b] H. Romero, S. Salazar, A. Sanchez, and R. Lozano. “A new UAV configuration having eight rotors: dynamical model and real-time control”. In: *46th IEEE Conf. on Decision and Control.* New Orleans, LA, Dec. 2007, pp. 6418–6423 (cited on page 103).

[Rongier–2005] P. Rongier, E. Lavarec, and F. Pierrot. “Kinematic and dynamic modeling and control of a 3-rotor aircraft”. In: *2005 IEEE Int. Conf. on Robotics and Automation.* Barcelona, Spain, Apr. 2005, pp. 2606–2611 (cited on pages 49 and 53).

[Ryll–2012] M. Ryll, H. Bülthoff, and P. Giordano. “Modeling and control of a quadrotor UAV with tilting propellers”. In: *2012 IEEE Int. Conf. on Robotics and Automation.* Paul, MN, USA, May 2012, pp. 4606–4613 (cited on pages 24, 56, 57 and 62).

[Ryll–2013] M. Ryll, H. Bülthoff, and P. Giordano. “First flight tests for a quadrotor UAV with tilting propellers”. In: *2013 IEEE Int. Conf. on Robotics and Automation.* Karlsruhe, Germany, May 2013, pp. 295–302 (cited on pages 57 and 62).

[Ryll–2015a] M. Ryll, H. Bülthoff, and P. Giordano. “A novel overactuated quadrotor unmanned aerial vehicle: Modeling, control, and experimental validation”. In: *IEEE Trans. on Control Systems Technology* 23.2 (2015), pp. 540–556 (cited on pages 28, 57 and 62).

[Ryll–2015b] M. Ryll, H. H. Bülthoff, and P. Robuffo Giordano. “A novel overactuated quadrotor unmanned aerial vehicle: modeling, control, and experimental validation”. In: *IEEE Trans. on Control Systems Technology* 23.2 (2015), pp. 540–556 (cited on page 103).

[Ryll–2016a] M. Ryll, D. Bicego, and A. Franchi. “Modeling and Control of FAST-Hex: a Fully-Actuated by Synchronized-Tilting Hexarotor”. In: *2016 IEEE/RSJ Int. Conf. on Intelligent Robots and Systems.* Daejeon, South Korea, Oct. 2016, pp. 1689–1694 (cited on pages 67, 68 and 72).

[Ryll–2016b] M. Ryll, D. Bicego, and A. Franchi. “Modeling and Control of FAST-Hex: a Fully-Actuated by Synchronized-Tilting Hexarotor”. In: *2016 IEEE/RSJ Int. Conf. on Intelligent Robots and Systems.* Daejeon, South Korea, Oct. 2016, pp. 1689–1694 (cited on page 103).

[Ryll–2017a] M. Ryll, G. Muscio, F. Pierri, E. Cataldi, G. Antonelli, F. Caccavale, and A. Franchi. "6D Physical Interaction with a Fully Actuated Aerial Robot". In: *2017 IEEE Int. Conf. on Robotics and Automation.* Singapore, May 2017, pp. 5190–5195 (cited on pages 41, 70, 71, 72 and 195).

[Ryll–2017b] M. Ryll, G. Muscio, F. Pierri, E. Cataldi, G. Antonelli, F. Caccavale, and A. Franchi. "6D Physical Interaction with a Fully Actuated Aerial Robot". In: *2017 IEEE Int. Conf. on Robotics and Automation.* Singapore, May 2017, pp. 5190–5195 (cited on page 151).

[Ryll–2019] M. Ryll, G. Muscio, F. Pierri, E. Cataldi, G. Antonelli, F. Caccavale, D. Bicego, and A. Franchi. "6D Interaction Control with Aerial Robots: The Flying End-Effector Paradigm". In: *The International Journal of Robotics Research* 38.9 (2019), pp. 1045–1062. DOI: `10.1177/0278364919856694` (cited on pages 7, 103 and 164).

[Saeed–2015] A. Saeed, A. Younes, S. Islam, J. Dias, L. Seneviratne, and G. Cai. "A review on the platform design, dynamic modeling and control of hybrid UAVs". In: *2015 Int. Conf. on Unmanned Aircraft Systems.* Denver, CO, USA, June 2015, pp. 806–815 (cited on page 19).

[Saied–2015] M. Saied, B. Lussier, I. Fantoni, C. Francis, and H. Shraim. "Fault tolerant control for multiple successive failures in an octorotor: Architecture and experiments". In: *2015 IEEE/RSJ International Conference on Intelligent Robots and Systems (IROS).* IEEE. 2015, pp. 40–45 (cited on page 82).

[Saied–2017] M. Saied, H. Shraim, B. Lussier, I. Fantoni, and C. Francis. "Local controllability and attitude stabilization of multirotor UAVs: Validation on a coaxial octorotor". In: *Robotics and Autonomous Systems* 91 (2017), pp. 128–138 (cited on page 82).

[SalazarCruz–2005] S. Salazar-Cruz and R. Lozano. "Stabilization and nonlinear control for a novel trirotor mini-aircraft". In: *2005 IEEE Int. Conf. on Robotics and Automation.* Barcelona, Spain, Apr. 2005, pp. 2612–2617 (cited on pages 50 and 53).

[SalazarCruz–2009] S. Salazar-Cruz, R. Lozano, and J. Escareño. "Stabilization and nonlinear control for a novel trirotor mini-aircraft". In: *Control Engineering Practice* 17.8 (2009), pp. 886–894 (cited on pages 50, 51 and 53).

[Sanchez–2008] A. Sanchez, J. Escareno, O. Garcia, and R. Lozano. "Autonomous hovering of a noncyclic tiltrotor UAV: Modeling, control and implementation". In: *IFAC Proceedings Volumes* 41.2 (2008), pp. 803–808 (cited on pages 47 and 48).

[Sarkisov–2019] Y. Sarkisov, M. J. Kim, D. Bicego, D. Tsetserukou, C. Ott, A. Franchi, and K. Kondak. "Development of SAM: cable-Suspended Aerial Manipulator". In: *2019 IEEE Int. Conf. on Robotics and Automation.* Montreal, Canada, May 2019 (cited on page 19).

[Scaramuzza–2014] D. Scaramuzza, M. C. Achtelik, L. Doitsidis, F. Friedrich, E. Kosmatopoulos, A. Martinelli, M. W. Achtelik, M. Chli, S. Chatzichristofis, L. Kneip, et al. “Vision-controlled micro flying robots: from system design to autonomous navigation and mapping in GPS-denied environments”. In: *IEEE Robotics & Automation Magazine* 21.3 (2014), pp. 26–40 (cited on page 93).

[Scholz–2016] G. Scholz, M. Popp, J. Ruppelt, and G. Trommer. “Model independent control of a quadrotor with tiltable rotors”. In: *2016 IEEE/ION Position, Location and Navigation Symposium (PLANS).* Savannah, Georgia, USA, 2016, pp. 747–756 (cited on pages 58 and 62).

[SeguiGasco–2014] P. Segui-Gasco, Y. Al-Rihani, H. Shin, and A. Savvaris. “A novel actuation concept for a multi rotor UAV”. In: *Journal of Intelligent & Robotics Systems* 74.1-2 (2014), pp. 173–191 (cited on pages 61 and 62).

[Şenkul–2013] F. Şenkul and E. Altuğ. “Modeling and control of a novel tilt—Roll rotor quadrotor UAV”. In: *2013 Int. Conf. on Unmanned Aircraft Systems.* Atlanta, USA, May 2013, pp. 1071–1076 (cited on pages 60 and 62).

[Şenkul–2014] F. Şenkul and E. Altuğ. “Adaptive control of a tilt-roll rotor quadrotor UAV”. In: *2014 Int. Conf. on Unmanned Aircraft Systems.* Orlando, FL, USA, May 2014, pp. 1132–1137 (cited on pages 60 and 62).

[Servais–2015a] É. Servais, B. d’Andréa-Novel, and H. Mounier. “Ground control of a hybrid tricopter”. In: *2015 Int. Conf. on Unmanned Aircraft Systems.* Denver, CO, USA, June 2015, pp. 945–950 (cited on pages 53 and 54).

[Servais–2015b] É. Servais, H. Mounier, and B. d’Andréa-Novel. “Trajectory tracking of trirotor UAV with pendulum load”. In: *2015 20th International Conference on Methods and Models in Automation and Robotics (MMAR).* Międzyzdroje, Poland, 2015, pp. 517–522 (cited on pages 53 and 54).

[SGuerrero–2018] D. S.-Guerrero and J. G. R.-Torres. “The Hexapodopter: A Hybrid Flying Hexapod—Holonomic Flying Analysis”. In: *Journal of Mechanisms and Robotics* 10.5 (June 2018), pp. 1–1 (cited on pages 40, 69 and 72).

[Shakhatreh–2019] H. Shakhatreh, A. H. Sawalmeh, A. Al-Fuqaha, Z. Dou, E. Almaita, I. Khalil, N. S. Othman, A. Khreishah, and M. Guizani. “Unmanned aerial vehicles (UAVs): A survey on civil applications and key research challenges”. In: *Ieee Access* 7 (2019), pp. 48572–48634 (cited on page 5).

[Shepherd–1965] C. M. Shepherd. “Design of primary and secondary cells: II. An equation describing battery discharge”. In: *Journal of the Electrochemical Society* 112.7 (1965), p. 657 (cited on page 92).

[Siciliano–2010] B. Siciliano, L. Sciavicco, L. Villani, and G. Oriolo. *Robotics: modelling, planning and control.* Springer Science & Business Media, 2010 (cited on page 21).

[Siciliano–2016] B. Siciliano and O. Khatib. *Springer handbook of robotics.* Springer, 2016 (cited on page 21).

[Smeur–2015] E. J. Smeur, Q. Chu, and G. C. de Croon. “Adaptive incremental nonlinear dynamic inversion for attitude control of micro air vehicles”. In: *Journal of Guidance, Control, and Dynamics* 38.12 (2015), pp. 450–461 (cited on pages 7 and 164).

[Smeur–2018a] E. J. Smeur, G. C. de Croon, and Q. Chu. “Cascaded incremental nonlinear dynamic inversion for MAV disturbance rejection”. In: *Control Engineering Practice* 73 (2018), pp. 79–90 (cited on page 164).

[Smeur–2018b] J. Smeur, G. de Croon, and Q. Chu. “Cascaded incremental nonlinear dynamic inversion for MAV disturbance rejection”. In: *Control Engineering Practice* 73 (2018), pp. 79–90 (cited on pages 7 and 93).

[Spica–2013] R. Spica, P. Robuffo Giordano, M. Ryll, H. H. Bülthoff, and A. Franchi. “An Open-Source Hardware/Software Architecture for Quadrotor UAVs”. In: *IFAC Proceedings Volumes*. Compiegne, France, Nov. 2013 (cited on page 128).

[Spong–2006] M. W. Spong, S. Hutchinson, M. Vidyasagar, et al. *Robot modeling and control*. 2006 (cited on page 21).

[Staub–2018] N. Staub, D. Bicego, Q. Sablé, V. Arellano-Quintana, S. Mishra, and A. Franchi. “Towards a Flying Assistant Paradigm: the OTHex”. In: *2018 IEEE Int. Conf. on Robotics and Automation*. Brisbane, Australia, May 2018, pp. 6997–7002 (cited on pages 70 and 72).

[Tadokoro–2017] Y. Tadokoro, T. Ibuki, and M. Sampei. “Maneuverability analysis of a fully-actuated hexrotor UAV considering tilt angles and arrangement of rotors”. In: *IFAC-PapersOnLine* 50.1 (2017), pp. 8981–8986 (cited on page 70).

[Tal–2018] E. Tal and S. Karaman. “Accurate tracking of aggressive quadrotor trajectories using incremental nonlinear dynamic inversion and differential flatness”. In: *2018 IEEE Conference on Decision and Control (CDC)*. IEEE. 2018, pp. 4282–4288 (cited on pages 7, 157, 158 and 164).

[Techradar–2021] Techradar. *what is industry 4.0? everything you need to know / techradar 2021*. 2021. URL: `%7Bhttps://www.techradar.com/news/what-is-industry-40-everything-you-need-to-know%7D` (visited on 05/10/2021) (cited on page 3).

[Theys–2016] B. Theys, G. Dimitriadis, P. Hendrick, and J. D. Schutter. “Influence of propeller configuration on propulsion system efficiency of multi-rotor unmanned aerial vehicles”. In: *2016 Int. Conf. on Unmanned Aircraft Systems*. IEEE. 2016, pp. 195–201 (cited on page 88).

[Tognon–2018] M. Tognon and A. Franchi. “Omnidirectional Aerial Vehicles with Unidirectional Thrusters: Theory, Optimal Design, and Control”. In: *IEEE Robotics and Automation Letters* 3.3 (2018), pp. 2277–2282. DOI: `10.1109/LRA.2018.2802544` (cited on pages 40, 73, 74, 76, 78, 103, 104 and 105).

[Tognon–2019] M. Tognon, H. A. Tello Chávez, E. Gasparin, Q. Sablé, D. Bicego, A. Mallet, M. Lany, G. Santi, B. Revaz, J. Cortés, and A. Franchi. "A Truly Redundant Aerial Manipulator System with Application to Push-and-Slide Inspection in Industrial Plants". In: *IEEE Robotics and Automation Letters* 4.2 (2019), pp. 1846–1851. DOI: `10.1109/LRA.2019.2895880` (cited on page 6).

[Tognon–2021] M. Tognon, R. Alami, and B. Siciliano. "Physical human-robot interaction with a tethered aerial vehicle: Application to a force-based human guiding problem". In: *IEEE Transactions on Robotics* (2021) (cited on page 5).

[Tomić–2017] T. Tomić, C. Ott, and S. Haddadin. "External wrench estimation, collision detection, and reflex reaction for flying robots". In: *IEEE Trans. on Robotics* 33.6 (2017), pp. 1467–1482 (cited on page 164).

[video01–2020a] **video01**. *Direct acceleration feedback control of quadrotor aerial vehicle.* `https://youtu.be/UKtHYjHEuyM`. 2020 (cited on page 164).

[video01–2020b] **video01**. *Omni-Plus-Seven O7+: Omnidirectional Aerial Vehicle with Minimal Number of Uni-directional Thrusters.* `https://youtu.be/Rv58JE6R2nE`. 2020 (cited on page 104).

[video01–2021a] **video01**. *A Novel Robust Hexarotor Capable of Static Hovering in Presence of Propeller Failure.* `https://youtu.be/GWrOIMyP-UA`. 2021 (cited on page 82).

[video01–2021b] **video01**. *Optimal Tuning of the Lateral-Dynamics Parameters for Aerial Vehicles with Bounded Lateral Force.* `https://youtu.be/yFSonGtvTsM`. 2021 (cited on page 125).

[Vischer–1995] D. Vischer and O. Khatib. "Design and development of high-performance torque-controlled joints". In: *IEEE Trans. on Robotics and Automation* 11.4 (1995), pp. 537–544 (cited on page 164).

[Wan–2000] E. A. Wan and R. Van Der Merwe. "The unscented Kalman filter for nonlinear estimation". In: *Proceedings of the IEEE 2000 Adaptive Systems for Signal Processing, Communications, and Control Symposium (Cat. No. 00EX373).* Ieee. 2000, pp. 153–158 (cited on page 114).

[Waslander–2009] S. Waslander and C. Wang. "Wind disturbance estimation and rejection for quadrotor position control". In: *AIAA Infotech@ Aerospace conference and AIAA unmanned... Unlimited conference.* 2009, p. 1983 (cited on page 79).

[Wu–2014] H. Wu, W. Su, and Z. Liu. "PID controllers: Design and tuning methods". In: *IEEE Conference on Industrial Electronics and Applications.* 2014, pp. 808–813 (cited on pages 128 and 129).

[Wüest–2019] V. Wüest, V. Kumar, and G. Loianno. "Online estimation of geometric and inertia parameters for multirotor aerial vehicles". In: *2019 IEEE Int. Conf. on Robotics and Automation.* 2019, pp. 1884–1890 (cited on page 128).

[Yih–2016] C. Yih. “Flight control of a tilt-rotor quadcopter via sliding mode”. In: *2016 InternationalAutomatic Control Conference (CACS)*. Taichung, Taiwan, 2016, pp. 65–70 (cited on pages 57 and 62).

[Yoon–2013] S. Yoon, S. Lee, B. Lee, C. Kim, Y. Lee, and S. Sung. “Design and flight test of a small tri-rotor unmanned vehicle with a LQR based onboard attitude control system”. In: *International Journal of Innovative Computing, Information and Control* 9.6 (2013), pp. 2347–2360 (cited on pages 50 and 53).

[Yoshikawa–1985] T. Yoshikawa. “Manipulability of robotic mechanisms”. In: *The International Journal of Robotics Research* 4.2 (1985), pp. 3–9 (cited on page 67).

[Young–1982] W. R. Young. *The Helicopters: The Epic of Flight*. Time-Life Books, 1982 (cited on page 54).

[Yüksel–2019] B. Yüksel, C. Secchi, H. H. Bülthoff, and A. Franchi. “Aerial Physical Interaction via IDA-PBC”. In: *The International Journal of Robotics Research* 38.4 (2019), p. 403421. DOI: `10.1177/0278364919835605` (cited on page 164).

[Zhang–2013] Y. Zhang, A. Chamseddine, C. A. Rabbath, B. W. Gordon, C.-Y. Su, S. Rakheja, C. Fulford, J. Apkarian, and P. Gosselin. “Development of advanced FDD and FTC techniques with application to an unmanned quadrotor helicopter testbed”. In: *Journal of the Franklin Institute* 350.9 (2013), pp. 2396–2422 (cited on page 93).

[Zhang–2016] W. Zhang, M. Mueller, and R. D’Andréa. “A controllable flying vehicle with a single moving part”. In: *2016 IEEE Int. Conf. on Robotics and Automation*. Stockholm, Sweden, May 2016, pp. 3275–3281 (cited on pages 26 and 46).

[Zhao–2017] M. Zhao, K. Kawasaki, X. Chen, S. Noda, K. Okada, and M. Inaba. “Whole-body aerial manipulation by transformable multirotor with two-dimensional multilinks”. In: *2017 IEEE Int. Conf. on Robotics and Automation*. Singapore, May 2017, pp. 5175–5182 (cited on pages 19 and 55).

[Zhou–1996] K. Zhou, J. Doyle, and K. Glover. *Robust and Optimal Control*. Prentice-Hall, 1996 (cited on pages 140 and 144).